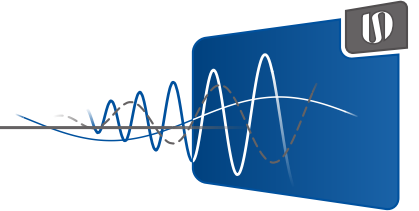


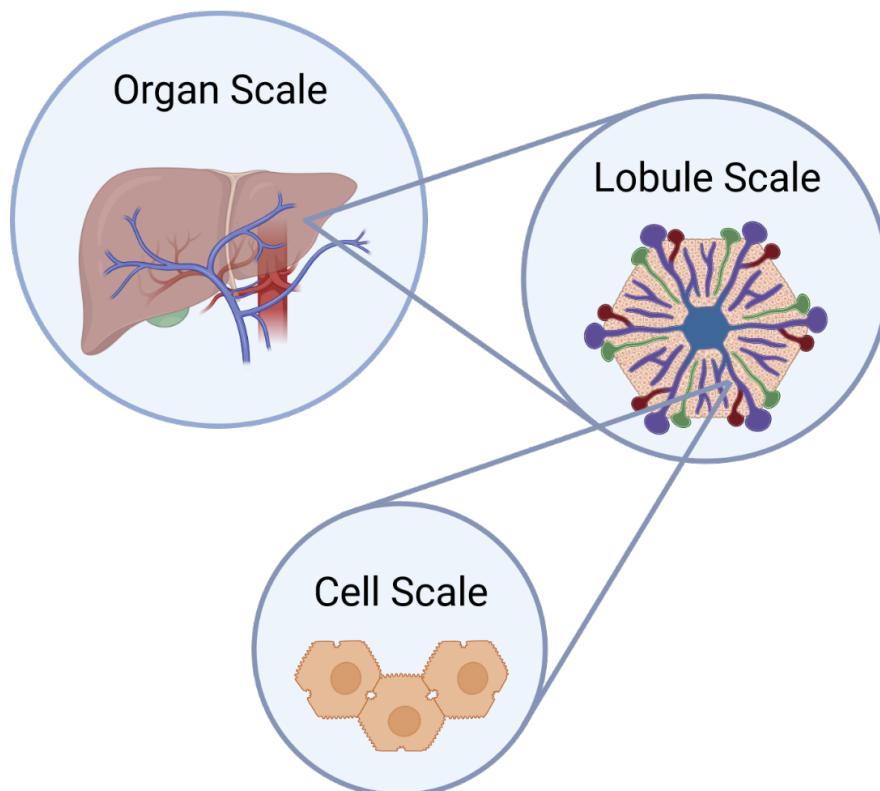
Universität Stuttgart

Institut für Statik und Dynamik
der Luft- und Raumfahrtkonstruktionen



Multiscale and Multiphase Modeling and Numerical Simulation of Function-Perfusion Processes in the Liver

Lena Lambers



Multiscale and Multiphase Modeling and Numerical Simulation of Function-Perfusion Processes in the Liver

A thesis accepted by the Faculty of Aerospace Engineering and Geodesy of the University of Stuttgart and the Stuttgart Center for Simulation Science in fulfillment of the requirements for the degree of Doctor of Engineering Sciences (Dr.-Ing.)

by
Lena Lambers, M. Sc.
born in Nordhorn

Main referee: Prof. Dr.-Ing. Tim Ricken
Co-referee: Prof. Dr. med. Uta Dahmen
Day of defense: March 21, 2023

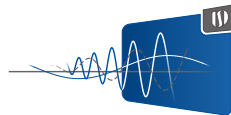
Institute of Structural Mechanics and
Dynamics in Aerospace Engineering
University of Stuttgart
2023

Publikationsreihe des
Instituts für Statik und Dynamik
der Luft- und Raumfahrtkonstruktionen (ISD)
Universität Stuttgart (D 93)

Bericht Nr. 3

Herausgeber: Univ.-Prof. Dr.-Ing. Tim Ricken

© Lena Lambers, 2023



Berichte können bezogen werden über:

Institut für Statik und Dynamik
der Luft- und Raumfahrtkonstruktionen
Universität Stuttgart
Pfaffenwaldring 27
70569 Stuttgart

Tel.: 0711 - 685 63612
Fax.: 0711 - 685 63706
E-Mail: office@isd.uni-stuttgart.de
URL: www.isd.uni-stuttgart.de

Alle Rechte, insbesondere das der Übersetzung in andere Sprachen, vorbehalten. Ohne Genehmigung des Autors ist es nicht gestattet, diesen Bericht ganz oder teilweise auf photomechanischem, elektronischem oder sonstigem Wege zu kommerziellen Zwecken zu vervielfältigen.

ISBN 978-3-942807-10-4

Contents

Kurzfassung	v
Abstract	vii
Symbols and Acronyms	ix
Acronyms	ix
Greek Symbols	xi
Roman Symbols	xii
Sub- and Superscripts	xiv
List of Figures	xvii
List of Tables	xxi
1 Introduction	1
1.1 Motivation	2
1.2 Scope and Aims	3
1.3 Outline	4
2 Liver Biology and Diseases	7
2.1 Liver Biology	8
2.1.1 Hepatic Macroanatomy	8
2.1.2 Hepatic Circulation	9
2.1.3 Hepatic Microanatomy	10
2.2 Hepatic Disease and Surgical Interventions	11
2.2.1 Non-alcoholic Fatty Liver Disease	12
2.2.2 Hepatocellular Carcinoma	15
2.2.3 Intoxication due to Paracetamol	18
2.2.4 Perfusion Disturbance in Surgical Interventions	19
3 Liver Simulation	23
3.1 State of the Art Liver Modeling	23
4 Generation of Experimental, Clinical and <i>In Silico</i> Data	29
4.1 Generation of Experimental and Clinical Data	30
4.1.1 Doppler-US, fMRI	30
4.1.2 Flow Measurements	30

4.1.3	Histology	30
4.1.4	Blood Serum Analysis	33
4.1.5	MRI	34
4.1.6	Transient Elastography	34
4.1.7	Liver Function Tests	35
4.2	Generation of <i>In Silico</i> Data	35
5	Fundamental eTPM	37
5.1	Theory of Porous Media	37
5.2	Mixture Theory and Concept of Volume Fraction	38
5.3	Density, Mass and Volume	40
5.4	Description of Solvent Substances using eTPM	41
5.5	Kinematics	42
5.5.1	Motion of a Spatial Body	42
5.5.2	Deformation and Strain of a Spatial Body	44
5.6	Extended Theory of Porous Media	46
5.6.1	Balance Equation	46
5.6.2	Constitutive Modeling for a Tetra-Phasic Model for NAFLD and Tumor Development	55
5.6.3	Field Equation	59
5.6.4	Mechanical and Thermodynamical Axioms: Thermodynamical Derivation	64
5.6.5	Evaluation of the Entropy Inequality	66
5.6.6	Stress	69
5.6.7	Seepage Velocity	71
5.6.8	Growth and Remodeling	76
5.6.9	Necrosis resulting from Paracetamol Overdose	84
6	Multiscale Modelling	85
6.1	Metabolic Processes on Cell Scale	86
6.1.1	Lipid Metabolism	86
6.1.2	Tumor Development	88
6.1.3	Detoxification	90
6.2	Macroscopic Perfusion on Organ Scale	91
6.3	Coupling Schemes	95
6.4	Numerical Implementation	97
6.4.1	Weak Forms	97
6.4.2	Boundary Value Problem	102
6.4.3	Stabilization Scheme for Concentration	103
7	Numerical Simulation of Function-Perfusion Processes in the Liver	107
7.1	Boundary Conditions	107

7.2	Microscopic Perfusion through Liver Lobules	109
7.2.1	Evaluation of Microperfusion	109
7.2.2	Integration of Realistic Liver Lobule Geometries	110
7.3	Simulation of Hepatic Diseases	114
7.3.1	Zonated Accumulation of Steatosis during NAFLD	114
7.3.2	Development of Liver Tumor	120
7.3.3	Evaluation of Growth Processes	125
7.3.4	Detoxification of Paracetamol and necrosis	127
7.4	Simulation of Perfusion Changes after Extended Liver Resection . . .	131
7.5	Function-Perfusion Relationship	136
7.5.1	Evaluation of Function during Perfusion Changes	136
7.5.2	Evaluation of Microperfusion during Diseases	137
7.6	Non-Linear Model Order Reduction	141
7.7	Numerical Sensitivity Analysis	143
7.7.1	Morris Method	146
7.7.2	Extended Fourier Amplitude Sensitivity Test	149
7.7.3	Regional Sensitivity Analysis	153
8	Summary, Conclusion, and Future Work	157
8.1	Summary	157
8.2	Conclusion	158
8.3	Future Aspects	159
	Bibliography	161

Kurzfassung

Lebererkrankungen sind weltweit für über 2 Millionen Todesfälle verantwortlich. Durch eine signifikante Erhöhung der Risikofaktoren, wie Alkoholkonsum, Übergewicht und Diabetes, steigt die Zahl der chronischen Lebererkrankungen in den letzten Jahren kontinuierlich an und stellt ein enormes soziales und ökonomisches Problem weltweit dar. Um das ärztliche Personal bei der Diagnose, Prognose und Therapieentscheidungen zu unterstützen, wurde in den letzten Jahren vermehrt die computergestützte kontinuumsbiomechanische Modellierung verwendet. Hierbei werden komplexe biologische Prozesse mit Hilfe mathematischer Modelle auf Basis der Kontinuumsmechanik modelliert und untersucht.

Zur Beschreibung von gekoppelten Funktions-Perfusionsbeziehungen in der Leber wird ein kontinuumsbiomechanisches Modell mit Hilfe der Theorie poröser Medien hergeleitet, verifiziert und validiert. Dieses Modell ermöglicht eine grundlagenbasierte Simulation der hepatischen Vorgänge, wie den Blutfluss durch das Gewebe, aber auch die Entstehung und die Auswirkungen verschiedener Leberkrankheiten. Zudem wird der Einfluss dieser Krankheiten auf die Perfusion, also den Blutfluss, durch eine Kopplung verschiedener Skalen untersucht. Des Weiteren werden Perfusionsstörungen durch chirurgische Interventionen, wie einer Tumorresektion, einbezogen.

Zur Berechnung der gekoppelten Funktions-Perfusionsprozesse müssen die makroskopische Perfusion im gesamten Organ, die Mikroperfusion durch das Gewebe der Leberläppchen und die Funktion in Form von metabolischen Prozessen in den Leberzellen berücksichtigt werden. Hierzu wird ein Mehrskalenansatz mit geeigneten Kopplungsstrategien zwischen den unterschiedlichen Längenskalen verwendet. Die Leberläppchen werden als durchströmtes poröses Medium mit gelösten Stoffen mit Hilfe der erweiterten Theorie poröser Medien beschrieben. Hierbei erfolgt die Einbeziehung einer Fett-, Tumor- und Nekrose-Phase sowie den Metabolismen zur Entstehung einer zonierten nicht-alkoholischen Fettleber, eines Lebertumors und einer Paracetamol-induzierten Nekrose. Unter Verwendung der Kontinuumsbiomechanik und der Grundlagen der Thermodynamik wird ein mathematisches Modell unter

Berücksichtigung physikalischer und thermodynamischer Randbedingungen hergeleitet. Durch konstitutive Gleichungen wird die Materialmodellierung von biologischem Gewebe in das Modell integriert. Die hepatischen Vorgänge werden dabei mit Hilfe von Wechselwirkungen zwischen den Phasen und gelösten Stoffen unter Verwendung phänomenologischer Ansätze und biochemischer Zellmodelle integriert. Das resultierende gekoppelte PDE-ODE-Gleichungssystem wird mit Hilfe der Finiten Elemente Methode gelöst.

Um die Auswirkungen makroskopischer Perfusionsstörungen durch chirurgische Eingriffe einzubeziehen, erfolgt eine Erweiterung um die Organskala auf ein dreiskaliges Modell. Hierbei wird die sich verzweigende Struktur des Gefäßbaums innerhalb der Leber mit der Bernoulli-Theorie berechnet. Dabei werden biologische Vorgänge wie die resultierende Gefäßweite bei Resektionen einbezogen.

Rein wissenschaftliche Modelle sind jedoch zu allgemeingültig, um individuelle, verlässliche und effiziente Vorhersagen im klinischen Alltag treffen zu können. Aus diesem Grund werden patienten-spezifische Daten unterschiedlicher Herkunft und Formate zur Parametrisierung und Validierung des Modells verwendet. Die Verlässlichkeit und Effizienz der Modelle wird mit Hilfe einer Sensitivitätsanalyse der Eingangsparameter untersucht. Zur Reduzierung der Rechenzeit und -leistung erfolgt eine vereinfachte Modellreduktion zur Entwicklung eines Ersatzmodells der Leberläppchen.

Es wird somit ein daten- und wissensgetriebenes, dreiskaliges, mehrphasiges kontinuumbiomechanisches Modell zur Beschreibung gekoppelter Perfusions-Funktionsprozesse in der Leber entwickelt. Dies ermöglicht die Simulation von hepatischer Funktion, Perfusion und deren Wechselwirkung zur Diagnose und Prognose von Leberkrankheiten und deren Therapien.

Abstract

Liver diseases are responsible for over 2 million deaths worldwide. Due to a significant increase in risk factors, such as alcohol consumption, obesity, and diabetes, the number of chronic liver diseases has been steadily increasing in recent years and represents an enormous social and economic problem worldwide. To assist physicians in diagnosis, prognosis, and therapeutic decisions, computational continuum-biomechanical modeling has been increasingly used in recent years. This involves modeling and studying complex biological processes using mathematical models based on continuum mechanics.

To describe coupled function-perfusion relationships in the liver, a continuum-bio-mechanical model is derived, verified, and validated using the Theory of Porous Media. This model enables a fundamental-based simulation of hepatic processes, such as blood flow through the tissue, as well as the development and effects of various liver diseases. In addition, the influence of these diseases on perfusion, i.e. blood flow, is investigated by coupling different scales. Furthermore, perfusion disturbances due to surgical interventions such as tumor resection are included.

To calculate the coupled function-perfusion processes, macroscopic perfusion in the whole organ, microperfusion through the tissue of the liver lobules, and function through metabolic processes in the liver cells have to be considered. For this purpose, a multiscale approach with appropriate coupling strategies between the different length scales is used. The liver lobules are described as a blood saturated porous medium with solutes using the extended Theory of Porous Media. Here, a tumor and necrosis phase as well as the metabolites for the development of zoned nonalcoholic fatty liver, liver tumor, and paracetamol-induced necrosis are incorporated. Using continuum-biomechanics and the fundamentals of thermodynamics, a mathematical model is derived considering physical and thermodynamic constraints. Material modeling of biological tissue is integrated into the model through constitutive equations. Hepatic processes are integrated by phase-solute interactions using phenomenological approaches and biochemical cell models. The resulting coupled PDE-ODE system of equations is solved using the finite element method.

To incorporate the effects of macroscopic perfusion perturbations due to surgical procedures, an extension to a three-scale model is performed to include the organ scale. Here, the branching structure of the vascular tree within the liver is calculated using Bernoulli theory. Biological processes such as the resulting vessel dilation during resections are included.

However, purely knowledge-based models are too generic to provide individual, reliable and efficient predictions in clinical practice. For this reason, patient-specific data of different origins and formats are used to parameterize and validate the model. The reliability and efficiency of the models will be investigated using a sensitivity analysis of the input parameters. To reduce computational time and power, model reduction is performed to develop a surrogate model of the liver lobules.

Thus, a data- and knowledge-driven, three-scale, multiphase continuum-biomechanical model is developed to describe coupled function-perfusion processes in the liver. This enables the simulation of hepatic function, perfusion and their interaction for the diagnosis and prognosis of liver diseases and their therapies.

Symbols and Acronyms

Acronyms

(e)PHx extended partial hepatectomy

AAT All-At-a-Time

AFLD alcoholic fatty liver disease

ALPPS associating liver partition and portal vein ligation for staged Hepatectomy

ANN artificial neural network

BC boundary condition

BMI body mass index

BVP boundary value problem

CCO constrained constructive optimization

CDF cumulative distribution function

CFD Computational Fluid Dynamics

CT computed tomography

CV central vein

CVP central vein pressure

eFAST extended Fourier Amplitude Sensitivity Test

eTPM extended Theory of Porous Media

FAST Fourier Amplitude Sensitivity Test

FE Finite Element

FEM Finite Element Method

FFA free fatty acid

fMRI functional magnetic resonance imaging

Glu glucose

GS glutamine synthetase

H&E hematoxylin and eosin

HA hepatic artery

HABR hepatic arterial buffer response

HCC hepatocellular carcinoma

ICG indocyanine green

IRI ischemia reperfusion injury

LRPC liver representative periodic unit cell

LTx liver transplantation

MELD Model of End-Stage Liver Disease Score

ML Machine Learning

MOR model order reduction

MR magnetic resonance

MRE magnetic resonance elastography

MRI magnetic resonance imaging

NAC N-acetyl cysteine

NAFLD Non-alcoholic Fatty Liver Disease

NAPQI N-acetyl-p-benzoquinonimide

NASH non-alcoholic steatohepatitis

OAT One-At-a-Time

ODE ordinary differential equation

OPS orthogonal polarization spectral imaging

PDE partial differential equation

PF portal field

PV portal vein

PVL portal vein ligation

RSA Regional Sensitivity Analysis

RVE representative volume element

SA sensitivity analysis

TC testcompound

TG triglyceride

TPM Theory of Porous Media

US ultrasound

VEGF vascular endothelial growth factor

WSS wall shear stress

Greek Symbols

Symbol	Unit	Description
α		index for immiscible solvent phases
$\alpha\beta$		dual index for solute β solved in phase α
β		miscible solutes
χ		motion function
δ		test function
ε	J/kg	specific internal energy
η	J/K kg	specific entropy
λ^α	N/m ²	2. Lamé constant for phase α
λ		Lagrange multiplier/ pressure
μ^α	N/m ²	1. Lamé constant for phase α
$\mu^{\alpha\beta}$	J/mol	chemical potential
φ	–	constituent
ψ	J/kg	Helmholtz free energy
$\rho^{\alpha R}$	kg/m ³	real density
$\hat{\rho}$	kg/m ³ s	mass production term
ρ	kg/m ³	density
θ	řK	absolute temperature
ζ	–	resistance coefficient

Roman Symbols

Symbol	Unit	Description
B		spatial body
d	m/s	diffusion velocity

Symbol	Unit	Description
R	J/molK	gas constant
k_D	m^4/Ns	isotropic Darcy permeability
Grad(.)		partial derivative of (.) with respect to \mathbf{X}_α
grad(.)		partial derivative of (.) with respect to \mathbf{x}
J	–	Jacobian determinant
E	N/m ²	Young's modulus
K	mJ	kinetic energy
M	kg	mass
Q	mJ/s	non-mechanical work
V	m ³	volume
W	mJ/s	mechanical work
A	–	Almansi strain tensor
B	–	left Cauchy deformation tensor
C	–	right Cauchy deformation tensor
D	s ⁻¹	symmetric deformation velocity tensor
E	–	Green-Lagrange strain tensor
F	–	deformation gradient
I	–	identity tensor
K	–	Karni-Reiner strain tensor
L	s ⁻¹	deformation velocity tensor
P	N/m ²	1. Piola-Kirchhoff stress tensor
T	N/m ²	Cauchy stress tensor
W	–	skew-symmetric deformation velocity tensor
X	m	reference position vector
b	m/s ²	external acceleration
$\hat{\mathbf{h}}$		change of momentum of momentum
h		momentum of momentum
j	mol/m ² s	solute flux
k	N	momentum
l	Ns	external forces
m	Nm	external angular momentum
n	–	unit normal vector

Sub- and Superscripts

Symbol	Unit	Description
$\hat{\mathbf{p}}$	N/m ³	momentum production term
\mathbf{p}	Pa	pressure
\mathbf{q}	J/m ² s	heat flux vector
\mathbf{t}	N/m ²	surface traction vector
\mathbf{u}	m	displacement vector
\mathbf{w}	m/s	seepage velocity
\mathbf{x}	m	actual position vector
$c^{\alpha\beta}$	mol/m ³	solute concentration
l	m	length
p	Pa	pressure
$M_{\text{mol}}^{\alpha\beta}$	kg/mol	molar mass
r	J/kg s	specific heat supply
\mathbf{M}	–	structural tensor
t	s	time
dt	s	time increment
v	m/s	velocity (one-dimensional)
n	–	volume fraction

Sub- and Superscripts

Symbol	Description
$(.)^{\alpha}$	non-kinematic quantity attached to solvent phase α
$(.)^{\alpha}$	non-kinematic quantity attached to solvent phase α
$(.)_{\alpha}$	kinematic quantity attached to solvent phase α
$(.)^{\beta}$	non-kinematic quantity attached to miscible solute β
$(.)_{\beta}$	kinematic quantity attached to miscible solute β
$\partial(.)$	partial derivative

Symbol	Description
$(\cdot)'_{\alpha}$	material-time derivation with respect to φ^{α}
$(\cdot)'_{\alpha}$	material-time derivation with respect to φ^{α}
$(\cdot)_{ae}$	quantity with relation to elastic deformation
$(\cdot)_{ag}$	quantity with relation to growth deformation
$(\cdot)_0$	quantity in reference position at time $t = 0$

List of Figures

2.1	Overview of the structure and circulation of the human liver	7
2.2	Composition of hepatic lobular scale and subdivision into different functional units	11
2.3	Global prevalence of obesity at the age over 18 in 2016 for males and females	13
2.4	Clinical presentation of steatosis	14
2.5	Development of liver disease from a healthy liver to hepatic tumor as well as possible treatments.	14
2.6	Abdominal CT showing a patient with liver mass ¹	15
2.7	Worldwide incidence rates of liver cancer in 2020 for both sexes in ages over 50.	16
2.8	Cancer incidence cases and deaths worldwide for both sexes and all ages.	17
2.9	Schematic overview of surgical interventions affecting the hepatic perfusion	20
2.10	Overview of liver transplantation	21
4.1	Workflow from tissue sampling to histological scan.	31
4.2	H&E staining of a human liver sample	33
5.1	Mixture approach: outline of the homogenization of solid phase and a fluid phase.	38
5.2	Geometrical interpretation of the motion for liver tissue (S), fat tissue (F), tumor tissue (C), blood (F) and solved microscopic substances ($\alpha\beta$).	43
5.3	Overview of the composition of the total aggregate for the simulation of fat accumulation and tumor growth in the liver.	56
5.4	Mixture approach of liver lobule	59
5.5	Benchmark of a rectangle representing a sinusoid from periportal to pericentral zone	74
5.6	Spatial and temporal distribution of glucose and FFA concentration for different Fick's parameters	74
5.7	Spatial and temporal distribution of glucose and FFA concentration for different Darcy parameters	75
5.8	Evaluation of seepage velocity and spatial pressure distribution for different time steps and different anisotropic factors α	78
5.9	Benchmark for the evaluation of different growth approaches	83
5.10	Overview of the composition of the total aggregate for the simulation of fat accumulation and necrosis in the liver.	84

List of Figures

6.1	Overview of different size scales of the human liver	85
6.2	Overview of processes during hepatic fat metabolism	87
6.3	Overview of processes during tumor development.	88
6.4	Overview of processes during paracetamol degeneration.	90
6.5	Comparison of two different approaches for vascular tree geometry in the liver	94
6.6	Evaluation of the pressure and the blood velocity over 16 generations in a healthy liver vascular tree	94
6.7	Coupling Procedure between different size scales of the human liver. .	95
6.8	Coupling Procedure between cell and lobule.	95
6.9	Boundary values on Dirichlet boundary ∂B_D and Neumann boundary ∂B_N	103
6.10	Progression of the concentration of a solute within a sinusoid without and with stabilization algorithm	104
6.11	Evaluation of concentrations using a stabilization algorithm	105
7.1	Applied boundary conditions of the pressure for one lobule and for a group of lobules for three conditions	108
7.2	Evaluation of microperfusion in a group of liver lobules	111
7.3	Semi-automatic workflow for including realistic liver lobule geometries in the simulation	112
7.4	Comparison of blood pressure in a group of ideally hexagonally and a group of realistically shaped liver lobules	112
7.5	Evaluation of lobule geometry using sinusoidal remodeling	113
7.6	Evolution of blood flow distribution over time illustrated by streamlines. .	114
7.7	Spatial distribution of fat volume fraction with periportal and pericentral zonation	115
7.8	Distribution of fat volume fraction along the liver lobule	116
7.9	Zonated accumulation of fat in histological images	117
7.10	Deposition of nutrients and fat accumulation after 1610 seconds of simulation time	119
7.11	Evaluation of fat volume fraction for different rates of oxygen	120
7.12	Evaluation of combined NAFLD and tumor development at different time points	123
7.13	Evaluation of volume fractions during the development of HCC	124
7.14	Evaluation of glucose concentration during the development of HCC .	124
7.15	Histological images of HCC	125
7.16	Evaluation of Jacobian and its growth part over time	126
7.17	Evaluation of paracetamol and glutathione concentration for different doses	128
7.18	Evaluation of volume fractions during necrosis after different doses of paracetamol.	129

7.19	Evaluation of volume fractions during necrosis with and without additional NAFLD	130
7.20	Evaluation of paracetamol and glutathione concentration with additional NAFLD	130
7.21	Validation of necrosis simulation	132
7.22	Evaluation of the resulting pressure plotted over the generation at which the system is disturbed	133
7.23	Evaluation of the resulting velocity plotted over the generation at which the system is disturbed	134
7.24	Validation of simulation with experimental results for pressure after different resections	135
7.25	Evaluation of fat volume fraction for various CVPs	137
7.26	Numerical simulation of the relation between the fat accumulation and the seepage velocity in relation to the initial one	138
7.27	Evaluation of relationship between NAFLD and microperfusion	139
7.28	Evaluation of relationship between tumor growth and microperfusion	140
7.29	Identification of decisive influencing parameters on fat accumulation	142
7.30	Evaluation of lobular processes using an ANN	143
7.31	Morris Method for NAFLD	148
7.32	Morris Method for tumor growth	150
7.33	eFAST for NAFLD	151
7.34	eFAST for tumor growth	153
7.35	Regional Sensitivity Analysis for NAFLD	154
7.36	Regional Sensitivity Analysis for tumor growth	155

List of Tables

2.1	Detection and treatment options for liver tumors	17
5.1	Overview of (thermo-)mechanical balance relations	54
7.1	Input and Output parameters for local and global simulation of liver lobules.	108
7.2	Material parameters of a liver lobule for the simulation of NAFLD . .	115
7.3	Material parameters of a liver lobule for the simulation of tumor development	122
7.4	Range of Parameters in Morris Method for fat accumulation	147
7.5	Range of Parameters in Morris Method for tumor growth	149
7.6	Range of Parameters in eFAST Method for fat accumulation	151
7.7	Range of Parameters in eFAST Method for tumor growth	152

1 Introduction

The human liver is a unique organ and, as the body's power plant, primarily responsible for the metabolic processes in the body that are essential for survival. These complex processes result from a highly specialized interaction between the perfusion, i.e. the blood flow through the tissue, and the function in the liver cells. In the latter, metabolic processes such as fat metabolism, protein metabolism, but also detoxification processes are performed. These interactions and thus the functioning of the liver can be impaired by diseases. Due to a fatty diet and an unhealthy lifestyle, the fat metabolism is disturbed, leading to excess fat being deposited in the liver cells, and subsequently to the development of a Non-alcoholic Fatty Liver Disease (NAFLD). This disease already affects 25% of adults in industrialized societies [164]. NAFLD can lead to severe diseases such as cirrhosis and ultimately liver tumors. An overdose of medications such as paracetamol can also have serious consequences for the functioning of the liver. The gold standard for smaller, single-sided tumors is liver resection, whereas end-stage liver diseases are mostly treated with liver transplantation. However, these lead to significant disturbances in perfusion and can therefore also have a negative impact on the hepatic functioning. In order to minimize the suffering of patients and, at the same time, the socioeconomic consequences, the liver has become the subject of research aimed at improving the diagnosis, prognosis, and treatment of hepatic diseases. One approach in this regard is the use of mathematical models to simulate hepatic properties and processes. This provides the advantage of a fast and non-invasive method to visualize liver function or disease progression using physical and mathematical principles. These models can be perspective applied as support for clinical decision making. To ensure this, however, the models must first be developed for the respective areas of application. Furthermore, a clinical application requires a multitude of constraints concerning accuracy, reliability, speed and individualization of the models. For this reason, further research in the development and improvement of mathematical models of the liver is required.

1.1 Motivation

Although mathematical models to describe processes in the liver already exist, these usually only describe a specific use case or a specific scale of the liver. However, in addition to simulating a single disease, the interaction between various diseases is also essential. For example, tumor development in the liver may arise from and be influenced by pre-existing NAFLD. Treatment of terminal liver diseases results in significant perfusion disturbances, which may also have an impact on the hepatic functioning or the development of diseases. For this reason, macroscopic pressure and flow conditions at the organ level must also be considered in a multiscale model. Effects of resections in which a part of the liver is removed can thus be incorporated into tissue and cell scale calculations.

Mathematical deterministic models rely on physical and mathematical principles. While these knowledge-based approaches allow the representation of processes in the liver, they are too generic to make a patient-specific prediction. Since this is indispensable for clinical application, models need to be extended to include data-driven approaches that incorporate experimental, clinical, or *in silico* data. Moreover, due to the complex models with many degrees of freedom to be processed, the computational time has so far been significantly too high and a fast simulation is usually only possible on special hardware such as high performance clusters. In addition, the models need to be simplified to reduce computational time and power, so that they can perspectivevely be used for clinical applications. Furthermore, the clinical use requires a reliability of the results. Statements about the efficiency of the model and its parameters will also enable a more targeted selection of experimental and clinical parameters. This leads to a reduction of the necessary experimental animal studies as well as interventions on patients.

Resulting from these unresolved questions in research, four main research questions are derived:

- 1) How can a multiscale and multiphase continuum-biomechanical model be derived to incorporate the prediction the development of NAFLD, tumor growth and necrosis after paracetamol overdose?
- 2) How can vascular perfusion changes be incorporated?

- 3) How can a purely knowledge-driven prediction be made more accurate and patient specific?
- 4) How can the simulation be made more efficient?

1.2 Scope and Aims

This thesis addresses the main open research questions in the simulation of selected processes of hepatic diseases. For this purpose, a continuum-biomechanical approach is developed and implemented. In detail, four objectives of this thesis are identified to address the respective research questions.

How can a model including the identified relevant phenomena of zoned NAFLD, tumor growth and necrosis resulting from paracetamol overdose be derived? How can the different scales of the model be coupled?

The model first requires an implementation of specific metabolic processes on the cell scale. For this purpose, a cellular model for zoned fat metabolism has been incorporated. For the metabolism of tumor growth and paracetamol degradation, different phenomenological approaches from literature and experiments/clinic has been investigated and a suitable cell scale approach has been implemented. On the tissue scale, components such as fat tissue, tumor tissue or necrotic tissue have been considered and the model has been derived using these components and their interactions. To couple the processes on both scales, a coupling approach has been developed and implemented. Finally, the different diseases have been investigated separately as well as their interaction with each other and the influence on perfusion.

How can the vascular perfusion during resection in the total organ be calculated?

In this thesis, macroscopic perfusion at the organ level has been implemented into the model. For this purpose, a mathematical approach has been developed to calculate the perfusion of the vascular tree and its evolutions over different branching generations. First, this approach has been compared to the boundary conditions in healthy livers. Subsequently, this approach was able to determine the altered flow and pressure conditions during a liver resection. In addition, the effect of increased central vein pressure (CVP) after cardiac problems and thus disturbed outflow from the liver has been considered.

How can selected data from different sources be integrated into the coupled model?

The implementation of the selected data into the mathematical model poses many challenges. For example, the data are available in different data formats: histological sections as image data, perfusion measurements as numerical values or *in silico* data as specific output files of different programs. Methods have been developed to use specific heterogeneous data relevant for a first parameterization and validation of the continuum-biomechanical model.

How can computational time of the simulation be reduced to increase the efficiency?

How can the uncertainty of the data and input parameters be quantified to make the model more efficient?

An initial model reduction approaches has been applied to reduce computation time. Here, a simplified surrogate model for the processes in the liver lobules has been developed on the basis of simulation data. To increase efficiency, a numerical sensitivity analysis has been performed. This has identified the relevant parameters and their influence on different output variables and thus quantified the uncertainty of the parameters.

1.3 Outline

To accomplish the objectives formulated in the previous section, Chapter 2 explains the relevant basics of the liver and its function in more detail. In addition, the disease patterns and surgical interventions addressed in this thesis are briefly introduced. To gain an overview of the current state in liver modeling, a selection of previously published models describing the relevant liver scales and processes is presented in Chapter 3. Since first data-driven approaches will be developed, Chapter 4 discusses the different data formats and the possibilities of generation for the used data. A distinction is made between experimental, clinical and *in silico* data. These selected data will then be incorporated in the multiphase model, which is derived in Chapter 5 for the liver lobules. As a modeling approach, the extended Theory of Porous Media (eTPM) is applied. In order to obtain a thermodynamically consistent model, the thermodynamic derivation is performed. From the evaluation of the entropy inequality, restrictions for the stresses and the seepage velocity are generated before the applied mechanical growth approach is described. Finally, this chapter extends

the model to necrosis after paracetamol intoxication. To incorporate also other scales, Chapter 6 is dedicated to the multi-scale consideration of the model. First, the relevant processes on the cell scale are considered, an approach to describe the organ scale is developed and all scales are coupled. This is followed by a description of the numerical implementation. Chapter 7 shows the results from the model, derived in the previous chapters, with selected incorporation of data. First, the general perfusion in the healthy liver is discussed, before the simulation results of the development of the considered liver diseases follow. The function-perfusion relationship of the liver is then examined for specific cases. Finally, a first approach for a model order reduction (MOR) as well as a sensitivity analysis (SA) is performed to make the derived model more efficient. The thesis and results are summarized in Chapter 8 and an outlook on further research questions is provided.

2 Liver Biology and Diseases

The human liver is a unique organ and, as the body's power plant, it is primarily responsible for the metabolic processes in the body that are essential for survival. These highly complex processes result from a highly specialized interaction between the perfusion, i.e. the blood flow through the tissue, and the function in the liver cells. In order to represent these processes in mathematical models, an understanding of anatomy, biology, and hepatic perfusion and function is first necessary. In addition, the basic characteristics of the liver diseases NAFLD, tumor growth and necrosis due to paracetamol overdose are explained. For more detailed information about the liver biology, the reader is referred to MACSWEEN et al. [96].

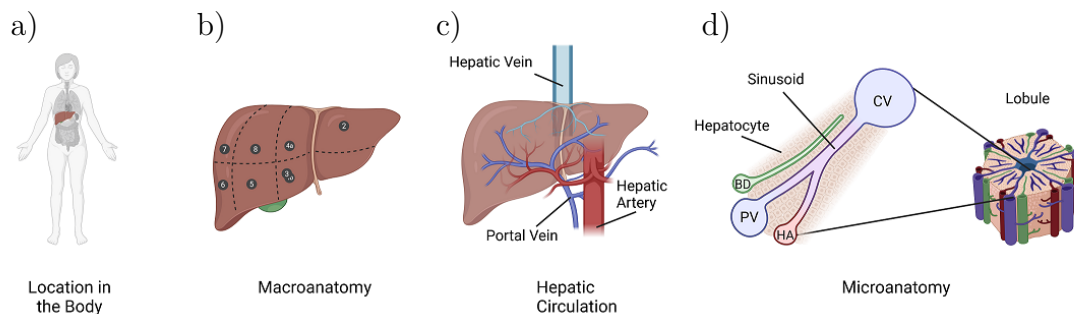


Figure 2.1: Overview of the structure and circulation of the human liver. From left to right: a) Location in the right upper abdomen, b) Macroanatomy with different segments, c) Hepatic circulation with blood supply from portal vein, hepatic artery and outflow via the hepatic vein, d) Hepatic microanatomy with liver lobules. The blood flow is directed from the terminal branches of portal vein and hepatic artery through sinusoids to the central vein. PV = portal vein, HA = hepatic artery, CV = central vein, BD = bile duct.

2.1 Liver Biology

Due to a complex interaction of many individual components and organs of the organism, human life is possible. Vital metabolic processes in particular play a decisive role here. These processes, including glucose metabolism, fat metabolism, bile formation and detoxification, are carried out by the liver, the largest endocrine gland in the body. Weighing about 1.5 kg, it occupies 2% of the body mass of an adult human and is located in the right upper abdomen. It is almost completely covered by the rib cage and thus optimally protected. The central task of the liver is to carry out vital metabolic processes, such as protein and fat metabolism. In addition, the liver stores the glucose contained in food in the form of glycogen. This can be released again as needed to regulate the blood glucose level. The liver is also the main detoxification organ, as it filters various toxins and pollutants from the blood and metabolizes drugs. Furthermore, bile is also produced in the liver. [42]

2.1.1 Hepatic Macroanatomy

The liver is located in the right upper abdomen, nearly completely covered by the ribcage and is bounded on the upper side by the diaphragm as shown in Figure 2.1. Since it touches the diaphragm directly, the liver moves during respiration. The liver is surrounded by the peritoneum viscerale and thus has a glistening peritoneal surface and a brown-red color. A macroscopic division of the liver can be traditionally obtained by an externally, topographical classification. Thus, the liver is divided into a right and a left liver lobe, which are separated by a midline falciform ligament, as well as a caudate and a quadrate liver lobe. A broader and more detailed classification of the liver can be achieved by the internal branching of the supply vessels, the Couinaud system [32], depicted in Figure 2.1. The vessels enter the liver through the porta hepatis and branch to form a vascular tree. Starting from this branching, two identically sized physiological lobes of the liver are formed, the right and the left, which are supplied independently by the vessels. In each of the two liver lobes, a further branching of the vessels occurs, thus dividing each lobe into two subregions. A further horizontal subdivision of the resulting subregions ultimately results in a division of the liver into eight segments, each of which has an independent vascular supply as well as biliary drainage. The caudate lobe is located between the left

and right vascular systems and is supplied from both branches. The macroanatomy of the liver segments allows for surgical partial hepatectomy and thus living liver transplantation (LTx), see Section 2.2.4. Here, haemostasis of the remnant liver can be ensured as the different segments are supplied independently and no intersegmental connections exist. In addition, the vascular structure allows the procedure of portal vein ligation (PVL), see Section 2.2.4, in which a specific inflow of the liver is clamped off so that a liver segment is undersupplied. [96]

2.1.2 Hepatic Circulation

The liver is responsible for essential metabolism of nutrients as well as detoxification of toxic substances. To perform these tasks, nutrient rich blood in which these substances are dissolved as well as oxygen rich blood must be transported to the liver, passed through the liver parenchyma and subsequently removed from the liver. In normal, healthy adults at rest, this results in a blood flow of 1500 to 1900 ml/min, which corresponds to about 25% of cardiac output [96]. Two-thirds of the inflowing blood comes from the portal vein (PV), which transports nutrient-rich but oxygen-poor blood from the digestive tract to the liver. Portal venous blood flow thus increases after food intake and decreases during sleep or exertion. The remaining blood is delivered via the hepatic artery (HA) as oxygenated blood [96]. The blood supplying system is illustrated in Figure 2.1.

Thus, the liver contains about 20% of the total amount of oxygen in the body, which, however, is supplied not only by the HA, but also by the PV due to the rapid flow rate [156]. The two vascular systems reach the liver along with a branch of the bile duct, lymphatic vessels, and nerve cords at the portal fields (PFs). Even though both systems are autonomous and independent of each other, there is a relationship between the two systems, the hepatic arterial buffer response (HABR) [156]. This process describes the compensatory ability of the HA to initiate flow changes that result in portal flow changes as a direct consequence. Thus, the HA has the ability to control the microcirculation within the liver by dilatation or reduction to the portal flow and regulating it. Hepatic perfusion exhibits differentially triggered heterogeneities at the various scales of the liver. Sinusoidal perfusion is mainly influenced by the composition of the tissue and the blood and its change over time due to remodeling processes. The perfusion in the liver lobes and the total organ is also affected by

heterogeneities. The liver capsule receives approximately 25% more arterial flow than the deeper tissue leading to a different perfusion [89]. Within the liver lobes, portal flow shows a pattern with higher flow on the top, than at the bottom, whereas the degree of this heterogeneity appears to be under dynamic and multiple interacting forces [89]. Hepatic perfusion also varies with disease state [47] such as during fibrosis and cirrhosis due to inhomogeneous collagen material or during NAFLD with focal accentuation of fat accumulation [76].

2.1.3 Hepatic Microanatomy

Microscopically, the entire organ consists of liver parenchyma consisting of different types of liver cells. The blood enters the tissue scale at the PFs where the terminal branches of the PV and the HA as well as the bile duct are located, see Figure 2.1 and 2.2. The oxygenated blood from the HA and the nutrient-rich one from the PV are mixed and flow through small capillaries, the so called sinusoids to the central veins (CVs), where the blood is drained from the liver and directed to the heart. Along the sinusoids, the liver cells called hepatocytes are located, so that the blood is directed along and into the cells enabling the metabolic processes. The bile duct is also located directly at the liver cells on the opposite side to the sinusoids. After production of the bile in the cells, it is discharged into the gallbladder via the bile canaliculus, this process being opposite to the direction of flow of the blood in the direction of the PFs. On the lobular scales different spatial functional units can be classified, where the most famous one is the liver lobule, see Figure 2.2. This functional unit has a hexagonally shaped geometry with the CV located in the middle and the PF describing the outer corners of the hexagon. After WEPFER described the hepatic lobules for the first time in 1664 [23], several descriptions of the functional unit evolved, which differ mainly in the consideration of the center of the structure. The main subdivisions of the hepatic lobular scale are indicated in Figure 2.2.

The hepatic acinus, which was first explored by RAPPAPORT et al. [113] experimentally, describes a rhombus, bounded by two terminal branches of the PVs and two terminal branches of the CVs. According to the blood flow, the acinus is divided into three zones, which are oriented according to the distance to the inflowing blood at the PFs.

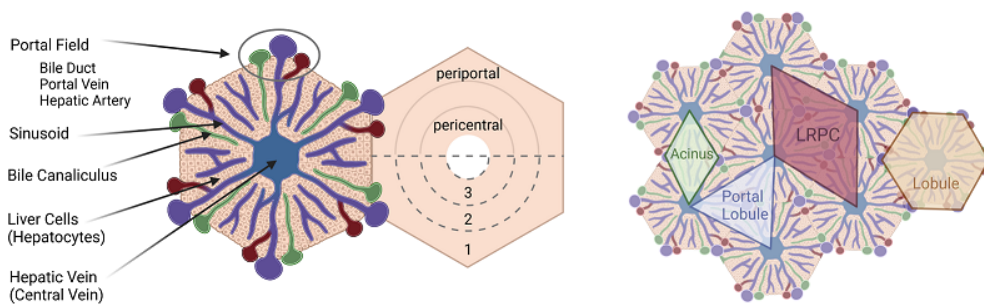


Figure 2.2: Composition of hepatic lobular scale and subdivision into different functional units: hepatic lobule (beige), acinus (green), portal lobule (blue) and liver representative periodic unit cells (red). Additionally, characteristic zones, namely zone 1, 2 and 3, as well as a periportal or pericentral zone, are highlighted.

These zones are either declared numerically (Zone 1 - Zone 3) or according to their location in the acinus as periportal or pericentral zone, see also Figure 2.2.

In contrast to the classical hepatic lobule, where the center is assumed to be the terminal branch of the CV, the portal lobule describes the PF with blood flow to the origin of the substructure. This results in a considered region bounded by three CVs and containing the PF in the center, see Figure 2.2 marked in blue. Another subunit of the liver was presented by ROHAN et al. [124]. This structure describes a periodically repeating region of the lobular scale, namely the liver representative periodic unit cell (LRPC), consisting of two adjacent portal lobules. Because of its geometry, this structure also contains a complete acinus. More detailed information on the hepatic microarchitecture can be found in MACSWEEN et al. [96].

2.2 Hepatic Disease and Surgical Interventions

In a healthy person, the liver performs the vital metabolic processes, allowing the body to function. However, the functionality of the liver can be impaired by various diseases [96]. These include infectious liver diseases such as hepatitis, which are triggered by viruses or bacteria in the body. Due to the centrality of the liver in the human circulatory system, as well as metabolic processes, the liver is responsible for the degradation of potentially toxic substances. Depending on the dose, various medications, fungi, but also herbal preparations can lead to a permanent damage

of the liver. Furthermore, the degradation of alcohol is one of the central tasks of the liver, whereby excessive consumption can lead to toxic diseases such as alcoholic fatty liver disease (AFLD) or alcoholic hepatitis. A NAFLD, which is characterized by the accumulation of fatty vacuoles in the liver cells, can be caused not only by alcohol, but also by a disturbed lipid metabolism or the excessive intake of free fatty acids (FFAs) through nutrition. Depending on the etiology and the habits of the patient, a distinction is made between AFLD and NAFLD. In the final stage of chronic liver disease, liver cirrhosis develops, which is characterized by tissue transformation to a connective tissue-like structure and the loss of the liver lobule architecture. Pathological tissue alterations from pre-existing diseases as well as metastatic lesions can also lead to the formation of liver tumors, whereby a distinction is made between benign and malignant tumors. In this work, the focus is on numerical computation of a NAFLD, primary liver tumor formation of hepatocellular carcinoma (HCC), and necrosis after paracetamol overdose. These diseases are very common in today's society and also have interactions with each other, which will be studied using mathematical models. The clinical pictures of these diseases will be explained in more detail in the following sections. Detailed information on hepatic diseases and their relevance in clinical practice can be found in [42]. The treatment of most hepatic diseases involves surgical intervention rather than medication. In this case, morbid parts of the liver are removed in a resection or the complete organ is replaced by a healthy donor organ in a LTx, see CHRIST et al. [37]. However, these surgical interventions directly alter perfusion and thus have an influence on the function-perfusion relationship in the liver, see CHRIST et al. [38]. In this work, some of these surgical interventions are numerically simulated and explained in detail in the following sections.

2.2.1 Non-alcoholic Fatty Liver Disease

Epidemiology and Etiology NAFLD describes one of the most common liver diseases worldwide with a prevalence of about 25% in adults [164]. It is characterized by the development of hepatic steatosis, with a critical threshold of 5-10% of steatotic liver weight [123]. In addition, the absence of other etiologies, such as hepatitis, the use of medications or chronic liver disease is mandatory [164]. As a distinction from the AFLD, the NAFLD indicates a formation of fatty vacuoles in the presence of a non-significant amount of alcohol, which is specified at more than 20 g of alcohol/day

in men and 10 g/day in women [123].

NAFLD is a non-communicable disease, which is not transmitted from one person to another. The most significant risk factors associated with NAFLD are obesity, type 2 diabetes, the metabolic syndrome, an unhealthy lifestyle characterized by mainly sedentary activities, low physical activity and poor dietary habits, and older age [123, 96]. In recent years, these risk factors have multiplied in large parts of the world, increasing the prevalence of the disease. The proportion of obese individuals with a body mass index (BMI) of over 30 kg/m², for instance, exceeds 20 % in many parts of the world, as shown in Figure 2.3.

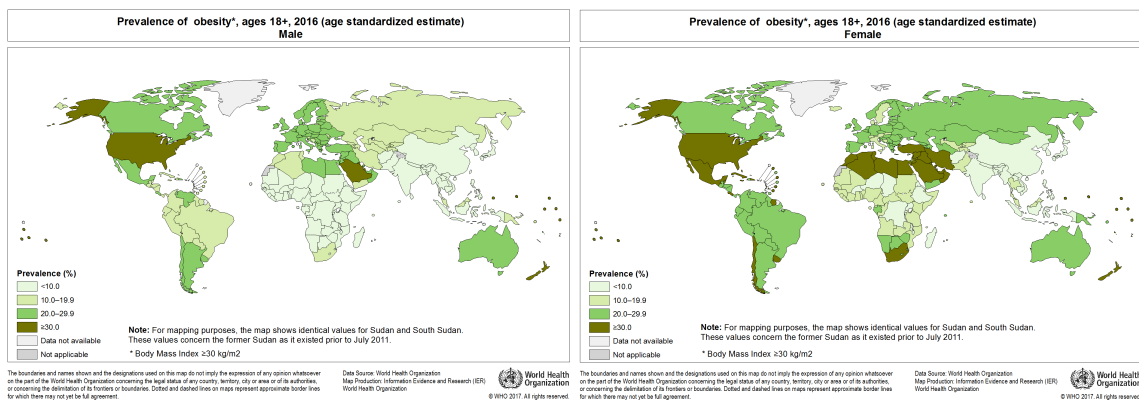


Figure 2.3: Global prevalence of obesity at the age over 18 in 2016 for males (left) and females (right)[114, 115].

Pathogenesis and Pathology NAFLD is characterized by FFA and triglyceride accumulation within the liver [16]. Due to an increased uptake of FFAs and a disturbed fat metabolism, fat droplets are deposited in the hepatocytes, recognizable by the yellowish color in Figure 2.4. A distinction is made between microvesicular steatosis, with small fat droplets, and macrovesicular steatosis, with the formation of large droplets that displace the cell nucleus of the hepatocytes and is most common during NAFLD [96, 16].

Fat formation is not homogeneously distributed over a liver lobule but occurs in a zoned pattern [96]. In NAFLD, an increased accumulation of fat droplets in the pericentral zone can be observed, as seen in Figure 2.4. However, an exact determination of the zonation is mostly difficult. For example, zonation in experimental studies often depends on the diet administered. In human livers, NAFLD usually occurs concomitantly with other etiologies such as alcohol consumption or hypertension,

so zonation from NAFLD is not always clearly delineated.



Figure 2.4: Clinical presentation of steatosis. Left: Explanted liver with NAFLD¹, Right: Histological section of a steatotic human liver sample with pericentral steatosis². CV = central vein, PF = portal field

The mostly symptom-free NAFLD can progress into non-alcoholic steatohepatitis (NASH), which is characterized by inflammation, steatosis and hepatocellular ballooning in the fatty liver but without fibrosis. The further progress to a cirrhotic liver, characterized by scar tissue, is - in contrast to the previous progresses - irreversible. Both hepatic cirrhosis and NASH can evolve into a HCC, a highly aggressive form of cancer [77]. For further information on HCC see Section 2.2.2. The whole spectrum of NAFLD can be seen in Figure 2.5.

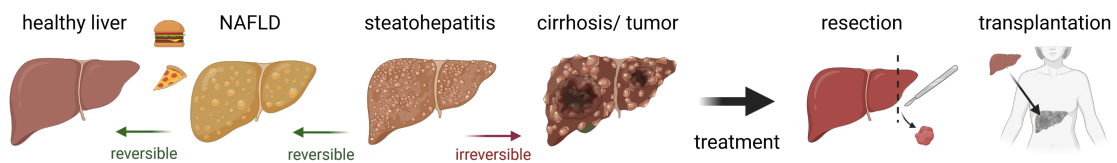


Figure 2.5: Development of liver disease from a healthy liver to hepatic tumor as well as possible treatments.

Diagnosis and Treatment Due to the mostly asymptomatic course, many disease progressions are only noticed belatedly. The clear definition of NAFLD requires, on the one hand, the presence of steatosis within the liver. In addition, other etiologies leading to the same clinical pattern must be excluded. These include AFLD induced by significant consumption of alcohol or chemotherapy-based steatohepatitis [36]. A

¹© PD Dr. med. Hans-Michael Tautenhahn, Jena University Hospital

²© Prof. Dr. med. Uta Dahmen, Jena University Hospital, UKJ-19_050_Human+_J-19-0712_HE.ndpi

liver biopsy is one method to determine hepatic steatosis in liver lobules, cf. Section 4.1.3. However, the invasive procedure can lead to health complications for patients and is costly and resource-intensive.

For noninvasive determination, screening by ultrasound (US) can be used, but this is also associated with high costs and has relatively low sensitivity in non-risk patients. [123, 36]. For these reasons, comprehensive screening of both healthy and high risk patients is currently not recommended [123, 36]. Furthermore, the fat content can be detected using the magnetic resonance imaging (MRI), in which fat and water portions of the liver tissue can be separated and quantified, cf. Section 4.1.5 [123].

2.2.2 Hepatocellular Carcinoma

Epidemiology and Etiology In the global view of cancer incidence, liver tumors represent the sixth most common cancer type and the fourth leading cancer type resulting in cancer related deaths [31]. However, a wide variation in the geographic distribution of incidences is evident here. A particularly frequent occurrence of this tumor type occurs in the African as well as the Asian area [31, 161]. Figure 2.7 illustrates the geographical distribution of liver cancer incidence in 2020 for both sexes in ages over 50.



Figure 2.6: Abdominal CT showing a patient with liver mass³.

The global imbalance can be explained by the various etiology of the disease. One of the most common causes of liver tumors is infection with the hepatitis B or hepatitis C virus, which is increasingly found on the African and Asian continents. In Europe and the American continent, the main cause of liver cancer is excessive alcohol consumption and an unhealthy lifestyle with associated obesity. Furthermore, aflatoxin exposure or liver fluke infection are a trigger for liver cancer, see [161].

A variety of benign or malignant tumors can arise in the liver. In this context, a distinction is made between primary tumors, which arise from liver cells, and metastatic tumors, which form from metastases from tumors in other organs. The

³© PD Dr. med. Hans-Michael Tautenhahn, Jena University Hospital

most common form of primary a hepatic tumor is HCC, which arises in the hepatocytes and is caused mainly by chronic liver disease. An example of a large tumor mass in the right liver lobe and a small metastasis in the left liver lobe using an abdominal computed tomography (CT) (arterial phase) in axial plane is shown in Figure 2.6.

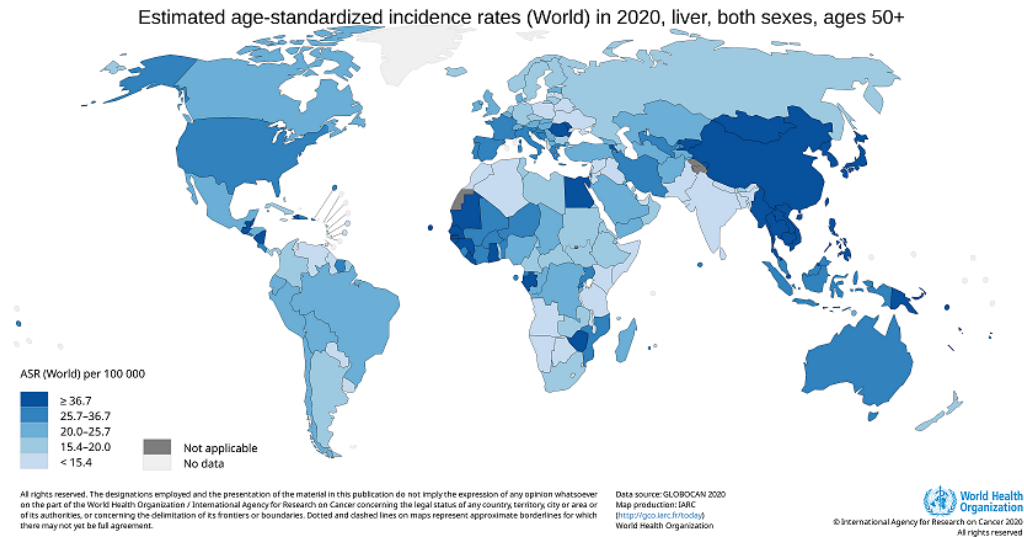


Figure 2.7: Worldwide incidence rates of liver cancer in 2020 for both sexes in ages over 50. [53]

Pathogenesis HANAHAN et al. [67] proposed six hallmarks of cancer identifying traits that all human tumors share. According to these, the core hallmarks are sustaining proliferative signaling, evading growth suppressors, activating invasion and metastasis, enabling replicative immortality, inducing angiogenesis and resisting cell death. These hallmarks were later expanded by two emerging hallmarks (reprogramming energy metabolism and evading immune destruction) and two enabling characteristics (namely genome instability and mutation as well as tumor-promoting inflammation) [66].

Diagnosis and Treatment The development of tumors in the human liver does not trigger any symptoms in an early stage, unlike other types of cancer such as a brain tumor. In addition, they are usually not externally palpable [96]. Nevertheless, there are different ways of detecting liver tumors, either by imaging, blood analysis, or (minimally) invasive procedures, as shown in Table 2.1 [42].

Table 2.1: Detection and treatment options for liver tumors

Detection	Treatment
CT scan	resection/ partial hepatectomy
MRI	LTx
Ultrasonography	Radiofrequency ablation
blood analysis	Radiotherapy
Angiogram	Radioembolization
Labroscopy	Chemoembolization
Biopsy	Targeted therapy
	Immunotherapy

Due to the mostly asymptomatic course and the consequent delayed detection of liver masses, a complete cure is hampered and liver cancer has one of the worst chances of survival when comparing the incidence and mortality rate, see Figure 2.7.

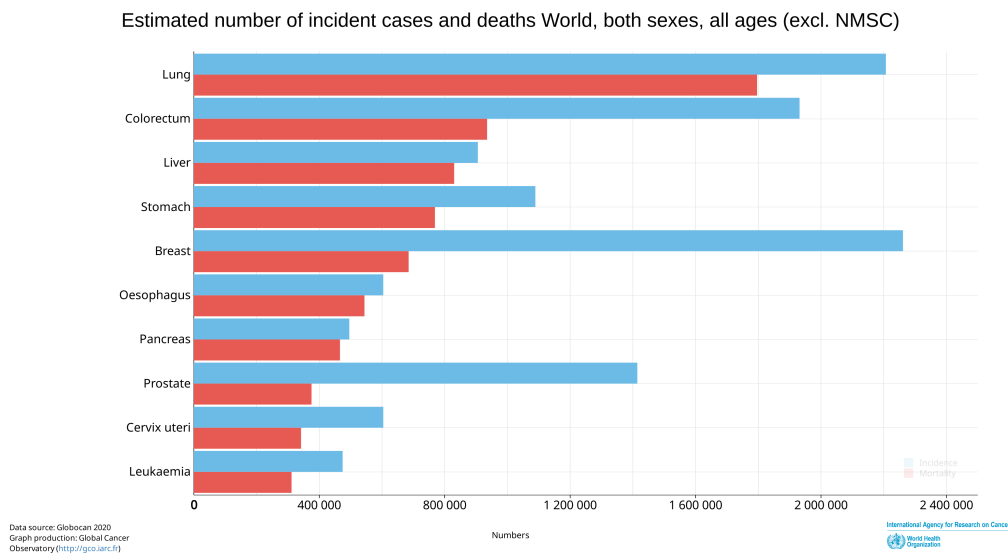


Figure 2.8: Cancer incidence cases and deaths worldwide for both sexes and all ages. [53]

The tumors are mostly treated with extended partial hepatectomy ((e)PHx), but this procedure also bears risks. During (e)PHx, the detection of tumor margins is an important criterion to ensure a complete resection of the tumor but also to ensure enough remnant liver mass at the same time, see THELEN et al. [149]. Another method for complete surgical removal of tumor tissue is LTx. In addition to invasive methods also Radiotherapy or Chemoembolization can be taken into account [161]. However, since the liver is the main organ for detoxification processes in the body, drugs that are supposed to access and target the tumor tissue are often metabolized beforehand.

This requires the intake of high concentrations of the chemical substances, which can lead to serious side effects.

2.2.3 Intoxication due to Paracetamol

As a central organ for metabolic and detoxification processes, the liver is mainly responsible for the degradation of the analgesic and antipyretic medication paracetamol, which is used for the symptomatic treatment of fever and mild to moderate pain. While a therapeutic dose rarely causes side effects, an overdose can lead to severe toxification of the liver characterized by necrosis of the tissue. [69]

Epidemiology and Etiology Due to its toxic effect and its simultaneous numerous and easy procurement possibilities, the drug paracetamol is one of the most frequently overdosed medications. It is responsible for a large number of poisoning reports, hospitalizations and even acute liver failure in various countries [33, 69, 88]. The toxic amount of the drug ranges and can be quantified with about 7.5 g for adults and 150 mg/kg body weight for children. The tolerated dose depends on age, body type and previous diseases. Thus, liver damage in patients with acute hepatitis, renal dysfunction or malnutrition occurs at a lower dose. Simultaneous use with alcohol also promotes liver damage and influences the toxicity of paracetamol. [69]

Pathogenesis Overdose of the drug paracetamol predictably and dose-dependently results in hepatic necrosis. The metabolization of paracetamol occurs in two different pathways, with the majority being degraded to non-toxic metabolites by association with sulfates and glucuronic acids and excreted via the kidney. Only 10% of the dose oxidizes to the toxic metabolite N-acetyl-p-benzoquinonimide (NAPQI) [69]. The reaction to the toxic degradation product is accelerated by the endogenous cytochrome CYP2E1. A high concentration of CYP2E1 therefore also means a high concentration of NAPQI and thus greater damage to the liver. The molecule NAPQI is usually rendered harmless directly by combining with the antioxidant glutathiones and excreted by the kidney. Glutathiones are endogenous metabolites that are present in the liver and are capable of binding and thus neutralizing free radicals. An increase in paracetamol concentration due to an overdose leads to a greater degradation of

glutathiones in the liver. If their concentration decreases below 70% of the initial value, the concentration is exhausted and no further NAPQI can be degraded. The free NAPQI molecules bind with the cell proteins of the hepatocytes and cause damage to the liver cells called hepatocellular necrosis. [69]

Diagnosis and Treatment As an overdose does not directly produce spontaneous symptoms, an early clinical diagnosis is often difficult. First symptoms appear within 24 hours in the form of nausea, vomiting or abdominal pain. After preliminary improvement of these conditions, initial clinical symptoms and abnormalities in liver function values can usually be detected after 24 to 48 hours. If left untreated, an overdose of paracetamol leads to acute hepatocellular necrosis, which ultimately results in death [69]. One possible therapy to curb liver damage is the administration of N-acetyl cysteine (NAC), which, as a precursor of glutathiones, replenishes the glutathione store, allowing further toxic metabolites to be degraded. [42]

2.2.4 Perfusion Disturbance in Surgical Interventions

Surgical interventions, in which parts of the liver ((e)PHx) or the entire liver (LTx) are removed, are mostly performed for the treatment of liver diseases. These surgical interventions are accompanied by clamping or severing of the vessels from the vascular tree. This procedure directly results in changes in hepatic perfusion, which vice versa have an influence on the hepatic function. Also perfusion changes in the vena cava can affect hepatic function. The surgical interventions and perfusion disturbances are shown in Figure 2.9.

Liver resection

Liver resection ((e)PHx) is used to treat many serious liver diseases, in which severely damaged parts of the liver are surgically removed. Different resection techniques exist, which are based on the anatomy of the liver, on the basis of the liver segments or only on the damaged structure to be removed, for example delimited by the edges of a tumor [146]. An (e)PHx is characterized by the removal of large parts of the vascular bed, which directly leads to portal hypertension and hyperperfusion of the liver.

This results from the adaption of the blood pressure and the volume flow, since the inflowing blood flows completely into the remaining liver. (e)PHx is associated with high morbidity and mortality rates, since up to 80 % of the liver mass is removed and significant blood loss occurs during surgery. The associating liver partition and portal vein ligation for staged Hepatectomy (ALPPS), which is a two-stage hepatectomy process, was developed to increase the remaining liver volume after resection and is applied in surgical removal of liver tumors [38].

Portal Vein Ligation

During the ALPPS procedure, the first step include the dissection of the liver parenchyma and a PVL, the occlusion of the PV, that supplies the liver lobe carrying the tumor. The interruption of the blood supply leads to a direct hypertrophy in the remnant liver mass due to the changed pressure and velocity conditions as well as the resulting remodeling of blood flow [146, 117]. Several days after the first step of ALPPS the remaining blood vessels of the clamped lobe namely the HA as inflow and CV as outflow are occluded. Afterwards the effected liver lobe can be dissected and removed. This techniques leads to an increase in liver volume in the remnant liver mass of about 50-80% in contrast to classical liver resection. [132]

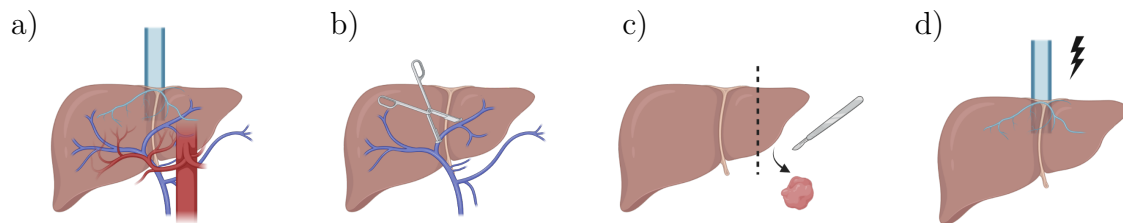


Figure 2.9: Schematic overview of surgical interventions affecting the hepatic perfusion: a) normal healthy liver, with blood perfusion from portal vein and hepatic artery, b) portal vein ligation with clamping of one vessel of the portal vein and resulting change in perfusion, c) resection with removal of parts of the liver with resulting changed perfusion in the remnant liver, d) change in CVP due to cardiovascular disturbances.

Liver Transplantation

The only established curative method for the treatment of acute and chronic end-stage liver diseases is LTx and thus the implantation of a healthy (partial) liver. However, the shortage of available organs is an enormous problem and leads to an imbalance between patients on the waiting list and available organs. In addition, the organ quality of donors is affected by the demographic change and an unhealthy lifestyle, so that the number of elderly, multi-morbid donors is increasing. The clinician is faced with the decision to accept or reject such a marginal graft. In this case, there may be altered perfusion due to pre-existing conditions, for example, NAFLD. The transplantation process starts with the procurement, where the perfusion of the organ is interrupted, see Figure 2.10. The organ is then stored in a cold preservation solution and transported to the transplant hospital (cold ischemia time) as seen on the right in Figure 2.10. During this process, an ischemia reperfusion injury (IRI) may occur, which may also have an impact on function and perfusion. During implantation, the vessels are reconnected and reperfusion of the organ occurs.

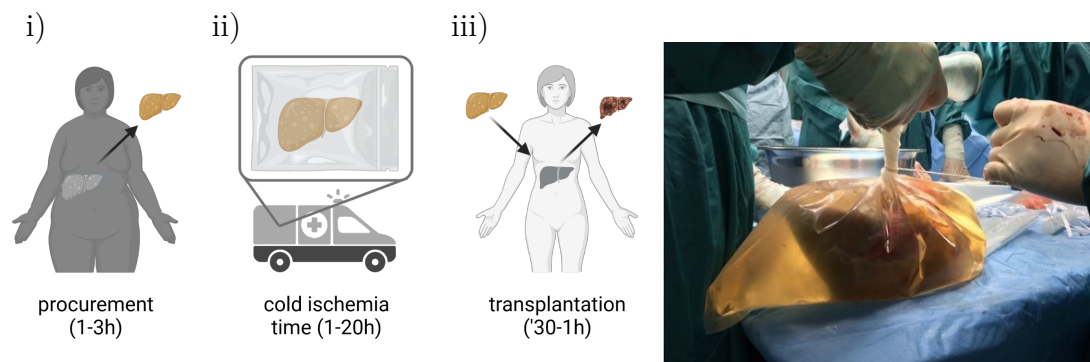


Figure 2.10: Overview of liver transplantation. Left: Key steps of LTx: i) Organ procurement. Donor condition (e.g. obesity) affects graft quality (e.g. hepatic steatosis). ii) Organ transport in a cold preservation solution for the transport (cold ischemia time). iii) Organ transplantation. Right: Storage of a explanted liver in cold preservation solution⁴.

Changes in CVP

The CVP characterizes the pressure in the vena cava, which carries blood from the circulation to the right atrium of the heart. It thus also receives the blood from the

⁴© PD Dr. med. Hans-Michael Tautenhahn, Jena University Hospital

liver after flowing through the hepatic lobules and hepatocytes and draining into the CV. Disturbances in this pressure can be triggered, for example, by underlying cardiovascular diseases or cardiac surgery of the patients. A retrospective study by SCHIEFENHÖVEL et al. [129] showed an increased Model of End-Stage Liver Disease Score (MELD), a quantification of liver disease, in patients with high CVP. Furthermore, fully or partial outflow obstructions can be a post-operative complication after liver transplantation [151]. If the pressure within the vena cava increases, this has a direct effect on the perfusion gradient in the hepatic lobules and the blood is no longer adequately drained from the liver. This is clinically evident in a backlog of blood in the hepatic lobules and an associated increased fatty degeneration of the liver due to altered function of the lipid metabolism. The study of the influence of impaired CVP on fat metabolism is also clinically important, because the etiology of cardiovascular disease is based on the same risk factors as NAFLD, and therefore the diseases often occur together. Additionally, obesity is not only a risk factor for NAFLD, but also for an increased pressure in the vena cava [90].

3 Liver Simulation

3.1 State of the Art Liver Modeling

In recent years, computational modeling has been increasingly applied to describe biological processes. Due to the complex functioning and the major importance for the human organism, the modeling of processes in the liver was an important aspect of the research. The models can be differentiated according to method, scale and application.

Simulation on the Organ Scale

Organ scale models describe perfusion throughout the total organ. The organ scale includes macroscopic perfusion represented by a vascular tree throughout the organ. There are different approaches to describe the perfusion within these vessels. Neglecting the spatial dimensions, 0D models determine to represent the macroscopic blood flow and its time course. Here the models use electronic components to describe the resistance within the vascular tree. These models can evaluate the influence of liver resection on the hemodynamics of the liver for different species such as humans [63], rats [45] or pigs [10] or for the simulation of HABR [68].

The geometry of the vascular tree can also be determined by optimization algorithms. For this purpose, different approaches have been used, such as the constrained constructive optimization (CCO) approach [134, 14] or extensions [73], Murry's law [82] or constructal law of design evolution [94].

Models using Computational Fluid Dynamics (CFD) have been used to describe blood flow within vessels at the organ level, based for example on tumor-infested

livers [7, 26] as well as real geometry from CT scans of humans [43, 147] or mice [43, 110]. Furthermore, blood flow can be determined by classical flow equations such as Bernoulli equations [125] or coupled Navier-Stokes/Darcy equations [144] and thus an estimation of the hepatic macrocirculation can be made.

Simulation on the Lobular Scale

Models on the lobule scale describe the liver tissue of the hepatic lobules as well as the microperfusion of the blood flowing through them. The liver has a complex morphology with a blood saturated porous structure, where a lot of biochemical reactions take place in the liver cells. Therefore, a large number of mathematical models have been developed in recent years using different approaches to describe the phenomena on this scale, where an overview can be found in [120] and [38]. MESCAM et al. [99] have developed a hepatic fluid flow model of the total organ for the investigation of tumor complexity in images. Another model that focuses only on the fluid flow and neglects the solid-fluid interaction is the work presented by RANI et al. [112], that focuses in the vascular bed and the circulation in the liver. The simulation of perfusion in respective sinusoid has been presented by MA et al. [95]. The inclusion of ultrasound measurements of arterial flow enables the simulation of perfusion in healthy livers as well as after hepatectomy. To include not only hepatic perfusion but also geometric effects, DEBBAUT et al. [44] have developed a CFD model and included the hexagonal structure of liver lobules to simulate spatial perfusion and microcirculation.

The porous structure of the liver and the resulting effects are captured by porous media approaches. With respect to the mechano-elastic behavior of the porous liver tissue, BONFIGLIO et al. [27] have described the liver as an anisotropic porous medium and the blood flow after resection using a Darcy approach. This model was also taken as a basis in the work of AHMADI-BADEJANI et al. [3] in combination with a Biot approach, where the realistic geometry of the liver lobules was determined from experimental histological images. DEBBAUT et al. [44] have presented a 3D CFD model with respect to the vascular septa. This work also focuses on the anisotropy in liver tissue. Using a homogenization approach for the porous liver tissue, SIGGERS et al. [138] investigated the permeability parameters as well as the microcirculation in the liver. The lobular perfusion in one sinusoid was also investigated in normal

livers [5, 21] or with respect to fibrosis or cirrhosis [70]. An overview of models on the lobular scale can also be found in CHRIST et al. [38].

Simulation on the Cellular Scale

To get an insight of the mechanisms and the coupling between hepatic function, perfusion and deformation, cellular models describing the processes in cells or hepatocytes help to understand the underlying processes including metabolism, signaling and mechanotransduction. This work focuses on the coupling of metabolism and perfusion, an overview of cellular models for signaling and mechanotransduction can be found in CHRIST et al. [38]. Changes in perfusion can effect metabolic pathways like glucose metabolism, lipid metabolism or the detoxification of drugs and toxins. GILLE et al. [61] have developed the comprehensive metabolic model HepatoNet1 including 777 metabolites and 2539 reactions to describe metabolism in hepatocytes based on a constraint-based modeling approach. This approach has also been used by MARDINOGLU et al. [97] for a genome scale metabolic model of liver hepatocytes for lipid metabolism. Kinetic models based on ordinary differential equation (ODE) have been developed to simulate central metabolic processes using a comprehensive biochemistry-based kinetic model [19], the detailed human hepatic glucose metabolism with application to disease [81, 80] or metabolism of caffeine [65] or indocyanine green (ICG) [79] for liver functions test. Lipid metabolism has been simulated in various models focusing on lipid oxidation and export as well as fatty acid uptake [130], zonation [131] or lipid metabolism during HCC [18]. Smaller cellular models have been included in multiscale models for a detailed description of hepatic processes on all relevant length scales. SLUKA et al. [140] and FU et al. [55] describe paracetamol detoxification using a multiscale model.

Multiscale Simulation

The previous models referred to perfusion in the liver lobules or the cellular processes. A link between perfusion and function can be established by multiscale models that include not only the liver lobules but also other scales such as the hepatocytes or the entire organ. SLUKA et al. [140] have simulated the paracetamol detoxification by coupling the tissue scale with the sub-scale and the whole body scale which

is validated with human *in vivo* data. A comparable model has been presented by DIAZ OCHOA et al. [48] to describe the paracetamol uptake and detoxification. NISHII et al. [104] have applied a multiscale approach for natural and decellularized livers and validated the results with flow rates from ferret livers. Another multiscale approach has been presented by BERNDT et al. [17] by applying a sinusoidal tissue unit composed of a representative sinusoid with the surrounding space of Disse and one layer of hepatocytes. The model is able to simulate carbohydrate metabolism, hepatic glucose exchange and hormone clearance during inhomogeneous blood perfusion. Due to the hierarchically organized structure of the liver with different functional units, a multiscale model can be used to describe the processes on each scale. In this approaches, the transfer of parameters and processes between the different length scales is investigated. For the coupling of the different scales, various solutions exist, cf. BLEILER [22].

Weak and Strong Coupling

Coupled problems with multiple fields require a weak or strong coupling approach [98]. Using the monolithic approach, the whole problem is solved monolithically in time by using the same integration scheme. In contrast, the iterative approach separates the variables and solves each one individually, for example with its own solution method. Since there are different subproblems in the multiscale simulation, a staggered algorithm is usually used to solve them. With this algorithm both subproblems are considered separately. Here a variable of a problem is frozen and passed to the other problem and assumed to be known. Since this algorithm leads to a reduction of the magnitude of the subsystem, this method reduces the computational cost required for the calculation.

Multiscale and Multiphase Models Using the Theory of Porous Media

In order to describe the complex porous structure of liver lobules, the tissue can be described at the lobule level using the Theory of Porous Media (TPM). RICKEN et al. [119] have presented a model to simulate outflow obstructions in liver lobules using an anisotropic permeability approach. To delineate the processes in liver cells as well as the function-perfusion relationship between scales, this model has

been extended to include glucose metabolism in RICKEN et al. [118]. To describe the development of NAFLD, a first cell-scale metabolism has been implemented and previously developed approaches to growth and remodeling have been adapted and extended to the lobule level by RICKEN et al. [121] and WERNER [160].

Simulation of Hepatic Disease

The zoned processes taking place during a steatosis in the liver have been described by ASHWORTH et al. [8] using a multicompartiment model. The authors divide the sinusoid in eight compartments with different concentrations of substances leading to a zoned metabolism of fat accumulation in the liver. In addition, they have introduced a whole body compartment, to simulate the processes in the complete body. WALLSTAB et al. [158] have presented a kinetic model for the description of the processes leading to an accumulation of fat in steatotic livers. The model simulates the dynamics of lipid droplet including the result of *in vivo* and *in vitro* experiments. For the simulation of tumor-parenchyma interaction during seeding and growth of colorectal cancer metastasis in the liver, WANG et al. [159] have developed a poroviscoelastic model of liver lobules. A central task of the liver is the detoxification of toxic substances in the blood. The transport and degradation of these substances can be performed using a multi-scale approach [140, 48], a lattice model [116], a compartment model [55] or with a focus on hemodynamics [25] or cell damage [2].

4 Generation of Experimental, Clinical and *In Silico* Data

A mathematical model aims to mimic the behavior of given natural processes. The first task of model development is a detailed observation of that processes, since the model quality is directly linked with the available data quality. In order to apply the liver lobular model in a patient-specific setting, information on the specific liver is required, which provides information on the liver geometry, heterogeneity of the liver lobules, damage such as degree of fatty tissue, hyperperfusion and, if necessary, degree of resection. Methods such as imaging techniques, biopsy or blood serum analysis are available, which will be briefly explained in the following sections.

The collection of data for parameterization and validation always requires experimental as well as clinical trials, for which special attention must be paid to a resource-saving experimental set-up as well as to the smallest possible number of samples required. Experiments on animals, such as rats or mice, are therefore planned according to the 3R principle [127], namely (1) Replace: The animal experiments are not replaceable by experiments using cell lines or primary hepatocytes, (2) Reduce: Only the absolute number of animals needed for the intended results should be studied, (3) Refine: The conditions of the veterinary care and treatment has to be under optimal conditions and be constantly improved. All clinical study are conducted in accordance with the Declaration of Helsinki [162] and the International Conference on Harmonization Guidelines for Good Clinical Practice [49].

4.1 Generation of Experimental and Clinical Data

4.1.1 Doppler-US, fMRI

The Doppler-US can be used to measure the macroscopic blood flow velocity in arteries and veins in the liver. PISCAGLIA et al. [111] used Doppler-US to measure the portal hemodynamics in chronic liver diseases and ZEKANOVIC et al. [165] invested the PV flow using this non-invasive method. Another way to determine hepatic hemodynamics is the non-invasive functional magnetic resonance imaging (fMRI), cf. BARASH et al. [13]. This method is based on the MRI technique with the extension of gradients in the magnetic field. These gradients are caused by changes in the blood flow, oxygen concentration or blood volume and can be measured as different signal intensities during the magnetic resonance (MR) image. The changes in signal intensity are then converted to the changed hepatic macroperfusion.

4.1.2 Flow Measurements

The orthogonal polarization spectral imaging (OPS) is a non-invasive video-based method to identify changes in microcirculation in human organs by illuminating the organ with a polarized light and illustration via a orthogonal installed polarizer, cf. GRONER et al. [64]. The OPS enables an examination of the blood microcirculation via the parameters of the vessel diameter and the functional capillary density. LANGER et al. [87] investigated the applicability of this method to study the microcirculation of the liver. The generated images using OPS imaging are suitable for the quantification of the microcirculatory parameters.

4.1.3 Histology

An important criterion for determining the condition of the liver and any diseases that may be present is histology, i.e. the assessment of human tissue. Histology investigations of liver tissue are necessary for diagnosis and evaluation of a NAFLD, cf. BEDOSSA [15]. This methods provides an overview of the tissue morphology and delivers the shape of the liver lobules. Further, the patterns of the steatosis can

be determined as well as zonation patterns. The process of tissue evaluation using histological images is shown in Figure 4.1.

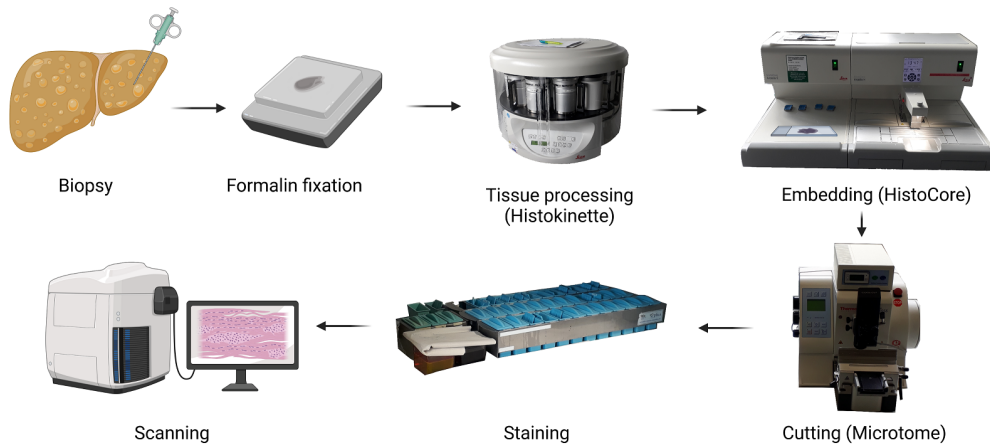


Figure 4.1: Workflow from tissue sampling to histological scan.

Tissue samples

The first step is to obtain parts of the tissue, that should be analysed, which involves taking small tissue samples from the liver during a biopsy. To investigate the histology of liver tissue, liver biopsies are necessary and are normally obtained by a transcutaneous approach. Tissue samples are taken for clinical assessment of the liver condition of patients as well as in the experimental context of large and small animals.

Tissue processing

Accurate analysis of histology requires fixation directly after dissection of the specimen to prevent premature degradation. In addition, fixation allows long-term storage of the specimens. In this process, the structure of the tissue is preserved, but stops all cellular processes by denaturing the proteins, thus preventing any subsequent structural change. The different fixation methods have to be chosen based on different points of view, e.g. tissue alteration, shrinkage or swelling as well as changes in the quality of the subsequent staining may occur. In addition, the loss of cellular components by,

for example, rinsing should be minimized. The most common method in classical pathology is formaldehyde fixation, other methods are among others glutaraldehyde fixation, osmium tetroxide fixation or mercuric chloride fixation. Detailed information on fixation methods can be found in SUVARNA et al. [145]. The tissue sample is then dehydrated, displacing both the previously prepared fixation and the cellular water. During dehydration, only the free water should be removed, the bound water as a component of the cells should remain. This is achieved by rinsing the solution with ethanol solutions of different concentrations. Here, the concentration is increased continuously, thus ensuring the dehydration of the sample. To clear the sample, it is then necessary to bathe the sample in a clearing agent, for which xylene can be used among others. Subsequently, in the microtomy, extremely thin sections are created from the paraffin-embedded specimens using a microtome and located on glass slides. The sections are then placed in a cold water bath to eliminate tissue ribbons. Afterwards, the paraffin is melted in a warm water bath. After a few minutes, the sections can be mounted on labeled slides. Complete removal of the paraffin is achieved by heating the sections for several hours. [145]

Staining

In order to subsequently examine the sample, the histological sections are stained. This means that the biological components that are of interest are made visible with the help of markers in certain color or shape. The choice of markers used depends on the desired result, as different markers react differently to certain biological components, such as fat. The most common staining is hematoxylin and eosin (H&E) staining, where the hematoxylin stains the nucleus in blue-black and eosin stains the cytoplasm and connective tissue in pink [145], as shown in Figure 4.2 a).

Since the color appears in different shades due to the stained compartment, also other tissue structures can be detected. H&E staining allows a general tissue analysis as well as the detection of pathologically altered tissue such as fibrosis or the existence of fat vacuoles, which can be recognized as white round circles. Since in the liver many processes as well as the distribution of different proteins and markers do not occur homogeneously but in a zonated manner, the stainings in hepatic tissue are also used to detect the different zones, which are described in more detail in Section 2.1.3. Here, the hepatocytes in the pericentral zone of the liver lobules react to

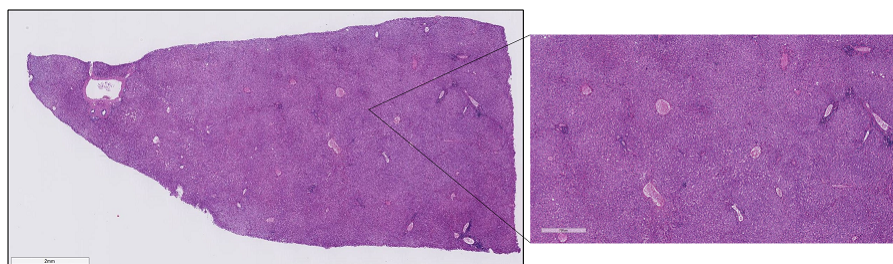


Figure 4.2: H&E staining of a human liver sample¹ and close-up with higher magnification showing the lobular structure with central veins and portal fields.

the marker glutamine synthetase (GS) [57]. Staining with this marker leads to a brownish staining near the CV within the lobules and to a pink staining of the PFs. In contrast, periportally located hepatocytes respond to the marker anti-arginase 1 and respectively the liver mitochondrial marker CPS1, allowing staining with it to identify the periportal zone [163, 60]. In addition to classical H&E staining, other staining methods exist, such as hematoxylin staining or nuclear red staining. Furthermore, the binding of antibodies to antigens in the tissue can be visualized by colored histochemical reactions which enables a location of the respective important molecules. This method called immunohistochemistry can be used to study various metabolisms in the liver, e.g. carbohydrate, lipid or testcompound (TC) metabolisms [145].

4.1.4 Blood Serum Analysis

In NAFLD, the concentration of lipid in the blood plays an important role for the lipid metabolism and accumulation in liver lobules. In addition to the invasive method of liver biopsy, the analysis of the blood serum also can be used for the diagnosis of NAFLD. GITTO et al. [62] have presented an overview of different serum analysis methods, like metabolomics. Here a distinction can be made between different fields of application, such as lipid metabolism or glucose metabolism.

¹© Prof. Dr. med. Uta Dahmen, Jena University Hospital, UKJ_16_016_J-19-0469_HE.ndpi

4.1.5 MRI

MRI represents an additional experimental and clinical method for generating hepatic tissue and flow data. This is a non-ionizing technique used in clinical practice mainly for tumor detection [93]. A detailed overview of the role of MRI in liver biomechanics is presented in the review article by SEYEDPOUR et al. [136] or CHRIST et al. [38]. The hepatic perfusion can be evaluated with four-dimensional flow MRI, which also provides pertinent data on spatial and temporal flow with velocities and blood volumes [12], which can be used to extract wall shear stress (WSS) [126]. Pathological alterations in tissues can occur during diseases and are closely associated with modifications in their biomechanical characteristics, such as stiffness [52, 137]. To examine the biomechanical parameters of liver tissue, elastography can be used for diagnosis. By encoding tissue motion over location and time inside the organ, tissue deformation is externally produced and monitored. The elastography techniques are already in clinical practice for the diagnosis of liver cancer [56] or liver fibrosis [35]. A technique, which is potentially more independent from the operator and therefore more reliable is magnetic resonance elastography (MRE) [103]. This is due to the use of specific frequency ranges that can illuminate the entire body with shear waves, better phase contrast, and the ability to examine the entire liver, even in obese and injured patients [155]. Another clinical challenge is the recognition of liver morphology and geometry. Here, MRI can be used to reconstruct the characteristics of the tissue as well as the blood vessels, their length and diameter. MRI provides the additional benefit of offering an impartial tool for fat estimation in the evaluation of NAFLD. [166]

4.1.6 Transient Elastography

An essential point to determine the material behavior of the liver is the elasticity. To assess the elasticity of liver tissue, e.g. UNTAROIU et al. [154] experimentally determined the material parameters relating to the Ogden model for an isotropic hyper-elastic formulation of the stress energy function of human liver samples in tensile tests with different strain rates. A qualitative statement on the elasticity of the liver can be made on the basis of a non-invasive transient elastography (FibroScan®), cf. JUNG et al. [74]. US is used to measure the condition of the liver and can be used to diagnose diseases such as NAFLD.

4.1.7 Liver Function Tests

The measurement of liver function is essential for the assessment of patient condition as well as prediction of post operative liver failure and selection of possible treatments. Therefore different non-invasive liver function tests are used in clinical practice to measure the hepatic reserve capacity and to prevent hepatic failure. One possible decision criterion is the ICG clearance of the liver. As a non-invasive monitoring system the LiMON® serves as a measurement for ICG elimination using pulse spectrophotometry [106]. Advantages of this test are the cost-effective, bedside implementation, its rapidity and the measurement of the ICG plasma disappearance rate and the ICG retention rate. To determine liver function capacity, the LiMAX (maximum liver function capacity) test [143] can also be used, which is based on the decomposition of ^{13}C -methacetin to assess the remaining liver function. Here, the intravenous administration of ^{13}C -methacetin and following a dose of sodium chloride takes place directly at the patient's bedside. The initiated substance is metabolized within the liver by the enzyme P450 1A2 resulting in the degradation products paracetamol and $^{13}\text{CO}_2$. This metabolic process is dependent on the function of the liver, which is reduced after surgical procedures such as hepatectomy. Since $^{13}\text{CO}_2$ is subsequently transported to the lungs and excreted via the respiratory air, it can be determined in the exhaled air with the aid of a breath test. This results in a calculated LiMAX value, which depends on the patient's body weight and can be used to analyze liver function.

4.2 Generation of *In Silico* Data

In addition to experimental and clinical data, which represent the real conditions in the liver, *in silico* or numerically generated data are also incorporated into the developed multiphase model. Here, computationally critical parts of the calculation are substituted with the help of these data. On the one hand, a substitution can be done by implementing external mathematical models to describe the processes in the liver cells. The biochemical processes in the hepatocytes proceed in many different reactions with different biological and chemical reaction partners as well as catalysts. These complex relations are described, for example, by mathematical modeling using

pharmacokinetic approaches or systems biology models and can thus represent a broad spectrum of reactions and biological dependencies. A selection of models for simulating biochemical processes in hepatocytes is shown in Section 3.1. By integrating these approaches into the perfusion model at the liver lobule scale, functioning in hepatocytes is also delineated by validated, highly complex models. The coupling of both scales allows a detailed description of the perfusion-function relationship without oversimplifying the biochemical processes in the primarily continuum-biomechanical model. To ensure a promising biological as well as numerical coupling of the models, the cellular models are individually tailored to the continuum-biomechanical model in co-design. A more detailed description of the coupling of pharmacokinetic models with the perfusion model is given in Section 6.3. Furthermore, cellular models can also be obtained from previously published publications, see Section 6.1.1.

Another use of *in silico* data for integration into numerical models is the development of surrogate models as non-linear MOR to reduce runtime and computational costs. The basis for this is provided by a ready-to-use simulation model, which is calculated on a previously defined selection of output variables. Defined input variables are varied in order to achieve a statistically relevant scatter. On the basis of the generated data, substitute models for this type of boundary value problem (BVP) can be generated with the help of Machine Learning (ML) methods, so that the resulting results can be determined in a short time for a variation of input values. A more detailed description as well as application of this implementation of *in silico* data for non-linear MOR is shown in Section 7.6.

5 Fundamental eTPM

To describe hepatic function-perfusion processes, the liver is considered as a porous medium with included blood flow. This consideration as a multiphase material allows the application of the TPM, in which the liver is divided into different phases. Therefore, the liver is separated into a tissue phase, a fat phase, a tumor tissue phase, a necrotic tissue phase, as well as a fluid blood phase. The derivation for a model to calculate fat accumulation and tumor development is shown in the following. In the further course, a model for the simulation of detoxification of paracetamol and resulting necrosis will also be discussed.

5.1 Theory of Porous Media

As biological soft tissue consists of a porous skeleton with blood flow, a porous medium approach is appropriate for the detailed description of mechanical and biological processes in the liver. Initially, porous structures were considered as one component materials, leading to averaging of mechanical values such as stress. However, this classical continuum mechanics approach does not provide detailed information about the characteristics of the different components, such as the distribution and change of the pore structure or the different motion of the solid and the blood perfusing it. One computational approach for fluid-saturated porous structures is based on the exact description of the individual components. Thus, the different components are considered separately from one another and physical axioms of mechanics and thermodynamics as well as boundary and initial conditions are applied for each phase individually. However, this requires a detailed knowledge of the complex underlying microstructure of the geometry. In addition, engineering problems often require a description on the macroscopic level, where all measured values are statistical averages.

This leads to an alternative calculation method, where a surrogate model is created based on the mixture theory [30, 9] and interaction forces between the individual constituents are accounted for. Moreover, the extension by the concept of volume fractions allows an estimation of the partial volumes of the individual phases related to the total volume of the considered body without knowledge of the exact location of pores and solid skeleton. This approach is described in the Theory of Porous Media [24, 51]. The combination of the mixture theory and the concept of volume fractions can be evaluated on a microscale level as well as on the macroscopic level, where both considerations of scale are feasible. A microscopic description of the problem requires an exact observation of the interactions so that the representation of the coupling behavior is required. However, this is limited by the unknown and irregular microscopic geometry of porous materials and the need for a macroscopic view arises. In a macroscale calculation, average values replace the material characteristics on the microscale, thus avoiding a high calculation effort on the microscale.

5.2 Mixture Theory and Concept of Volume Fraction

The mixture theory aims at a description of the real structure on the macroscopic level including microscopic properties. In this context, the various components of the structure are assumed to be in an ideal disorder over the entire control domain. The resulting physical and chemical properties of the microstructure are replaced at the macroscopic level with average values. This homogenization of the constituents leads to a smeared surrogate model as shown in Figure 5.1.

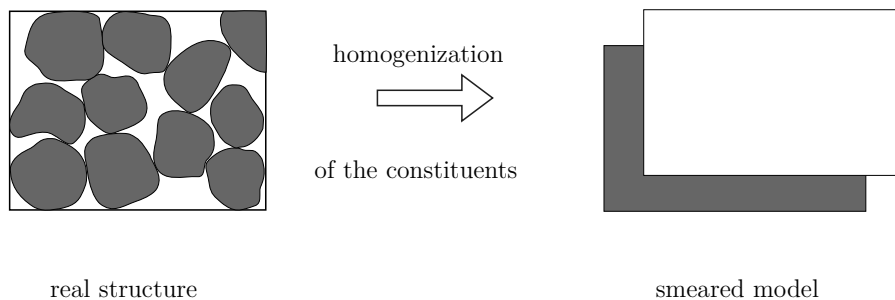


Figure 5.1: Mixture approach: outline of the homogenization of solid phase and a fluid phase.

Using this description, the motion, deformation and stress can also be calculated as

statistical average values of the structure. We assume the coherent and impenetrable control body B_S with the surface ∂B_S in current configuration at time $t = t_1$ and the control body B_{0S} with its surface ∂B_{0S} in reference configuration at time $t = t_0$, where the index 0 represents quantities in reference placement. The immiscible mixture is then composed of κ main phases φ^α with their particles X_α and α describing the individual constituents, which leads to the total description of the body

$$\varphi = \sum_{\alpha=1}^{\kappa} \varphi^\alpha. \quad (5.1)$$

Here the description of a multiphase body originates from the metaphysical principles of TRUESDELL [152]. These state that

- 1) All properties of a considered mixture must result of properties of the individual constitute.
- 2) If we properly account for how the other constituents will interact with it, we can imaginatively isolate a constituent from the rest of the mixture in order to describe its motion.
- 3) The same equations that govern the motion of a single body also govern the motion of a mixture.

Therefore, to describe the interactions between the individual constituents, supply terms for the density $\hat{\rho}^\alpha$, the interaction forces $\hat{\mathbf{p}}^\alpha$ and the energy \hat{e}^α of the constituents are introduced. Their sum over all κ constituents results in zero.

$$\sum_{\alpha=1}^{\kappa} \hat{\rho}^\alpha = 0, \quad \sum_{\alpha=1}^{\kappa} \hat{\mathbf{p}}^\alpha = 0, \quad \sum_{\alpha=1}^{\kappa} \hat{e}^\alpha = 0. \quad (5.2)$$

The mixture theory is enhanced by the concept of volume fractions to control the masses of solid and fluid to the total body in the control space. When considering porous bodies, it is assumed that the pores of the solid are statistically distributed over the control body and that only the fluid or gases contained in the pores can leave the control body. This results in an representative volume element (RVE) in both the reference and the current configuration, which consists of the real constituents. The concept of volume fractions is based on an averaging of the microscopic values, which are integrated over an average volume dv . Volume fractions n^α for each constituent α are introduced in current and reference configuration that represent the ratio of the

partial volumes of the individual constituents dv^α relative to the total volume of the body dv .

$$\text{Current config.: } n^\alpha(\mathbf{x}, t) = \frac{dv^\alpha}{dv}; \quad \text{Reference config.: } n_{0\alpha}^\alpha(\mathbf{X}_\alpha, t) = \frac{dV_{0\alpha}^\alpha}{dV_{0\alpha}} \quad (5.3)$$

The introduced volume fractions satisfy the saturation condition with

$$\text{Current configuration: } \sum_{\alpha=1}^{\kappa} n^\alpha = 1; \quad \text{Reference configuration: } \sum_{\alpha=1}^{\kappa} n_{0\alpha}^\alpha = 1. \quad (5.4)$$

5.3 Density, Mass and Volume

By averaging the densities of the individual constituents on the microscale, the macroscopic real density $\rho^{\alpha R}$ as well as the partial density ρ^α can be determined. Here, the partial density ρ^α describes the mass of a constituent dm^α related to the total volume dv , whereas the real density of a constituent $\rho^{\alpha R}$ relates the mass of a constituent dm^α to the partial volume dv^α .

$$\rho^\alpha = \frac{dm^\alpha}{dv} \quad \rho^{\alpha R} = \frac{dm^\alpha}{dv^\alpha} \quad (5.5)$$

Both densities are connected via the volume fractions.

$$\begin{aligned} \text{Current configuration: } \rho^\alpha(\mathbf{x}, t) &= n^\alpha(\mathbf{x}, t) \rho^{\alpha R}(\mathbf{x}, t) \\ \text{Reference configuration: } \rho_{0\alpha}^\alpha(\mathbf{X}_\alpha, t = t_0) &= n_{0\alpha}^\alpha \rho_{0\alpha}^{\alpha R} \end{aligned} \quad (5.6)$$

Assuming that the pores are homogeneously distributed over the volume, the initial volume fractions $n_{0\alpha}^\alpha$ are independent of the position in the reference configuration \mathbf{X}_α with $n_{0\alpha}^\alpha = n_{0\alpha}^\alpha(t = t_0)$.

The volume fractions can also be used to derive the total volume and the total mass

of the mixture.

Current configuration:

$$V = \int_{B_S} dv = \sum_{\alpha=1}^{\kappa} V^{\alpha} = \int_{B_S} \sum_{\alpha=1}^{\kappa} dv^{\alpha} = \int_{B_S} \sum_{\alpha=1}^{\kappa} n^{\alpha} dv$$

$$M = \sum_{\alpha=1}^{\kappa} M^{\alpha} = \int_{B_S} \sum_{\alpha=1}^{\kappa} \rho^{\alpha} dv$$

Reference configuration:

$$V_0 = \int_{B_{0S}} dV_{0\alpha} = \sum_{\alpha=1}^{\kappa} V_0^{\alpha} = \int_{B_{0S}} \sum_{\alpha=1}^{\kappa} dV_{0\alpha}^{\alpha} = \int_{B_{0S}} \sum_{\alpha=1}^{\kappa} n_{0\alpha}^{\alpha} dV_{0\alpha}$$

$$M_0 = \sum_{\alpha=1}^{\kappa} M_0^{\alpha} = \int_{B_{0S}} \sum_{\alpha=1}^{\kappa} \rho_{0\alpha}^{\alpha} dV_{0\alpha}$$
(5.7)

5.4 Description of Solvent Substances using eTPM

Within the main phases microscopic substances, such as free fatty acids or paracetamol, are solved, which exert an influence on the carrier phases and must therefore be taken into account in the TPM. For this purpose, a description of the volume is necessary, which is described by dv in the TPM. When dividing the volume among the phases, a distinction is made between the partial volume of the phase φ^{α} , denoted by dv^{α} with a bold index, and the partial volume of the carrier phase φ^{α} , denoted by dv^{α} . If the solute $\varphi^{\alpha\beta}$ is present only to a small extent in the volume of the phase dv^{α} the volume of the phase φ^{α} can be equated with the volume of the carrier phase φ^{α} .

$$dv^{\alpha} = dv^{\alpha} \quad (5.8)$$

Although the effect of the substances $\varphi^{\alpha\beta}$ on the total volume of a phase φ^{α} is negligible small, the substances nevertheless influence the mass of the phase $\varphi^{\alpha\beta}$, since the partial molar density $\rho^{\alpha\beta}$ depends on the fluid molar concentration $c^{\alpha\beta}$. The inclusion of a formulation for concentrations of solutes allows a description of the interactions between the different phases, the solutes and the fluids in a mixture.

The concentration of a solute can also be described by the molar concentration present

in the mixture volume. Here, the number of particles of the respective substance dn_{mol}^β is represented in relation to the total volume dv .

$$c^\beta = \frac{dn_{\text{mol}}^\beta}{dv} \quad (5.9)$$

A further description of the concentrations is given by the molar mass M_{mol}^β of a substance. This results in

$$M_{\text{mol}}^\beta = \frac{dm^\beta}{dn^\beta}. \quad (5.10)$$

In order to enable the volume fractions to be linked to the balance equations, the partial density $\rho^{\alpha\beta}$ is determined.

$$\rho^{\alpha\beta} = n^\alpha c^{\alpha\beta} M_{\text{mol}}^\beta \quad (5.11)$$

5.5 Kinematics

The kinematics deals with the geometrical aspects of the motion of a material body, such as translation, rotation or deformations in the case of deformable bodies. We define a body B_S consisting of a set of connected material points and its surface ∂B_S . Two configurations are introduced to describe the deformations. The reference configuration indicates the initial state of the body at time t_0 , while the state at the current time t is described by the current configuration.

5.5.1 Motion of a Spatial Body

Actions of the environment on a continuum cause deformations, which are described mathematically in kinematics. In the analysis of the TPM, independent motion functions χ_α are assumed for each constituent α . As an additional assumption, each spatial point \mathbf{x} in the current configuration is occupied by all material points X_α of all κ constituents at any time t . This results in the kinematic relations shown in Figure 5.2. For the description of hepatic processes, the same motion function is assumed for all solid constituents namely liver tissue, fat tissue and tumor tissue, as also explained in detail in Section 5.6.2.

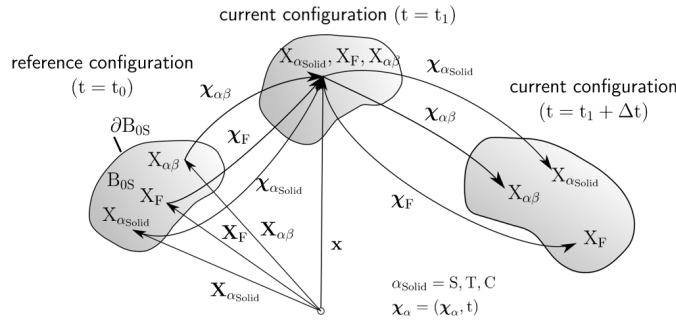


Figure 5.2: Geometrical interpretation of the motion for liver tissue (S), fat tissue (F), tumor tissue (C), blood (F) and solved microscopic substances ($\alpha\beta$).

The continuum mechanics differentiates between two ways of consideration with which a change of the material body can be described, namely the Lagrangian and the Eulerian approach. These serve a mathematically as exact as possible reproduction of the processes in different materials, such as solids or fluids, but do not change the underlying physics. In the Lagrangian approach, a certain particle and its change over time is considered. The position of this particle is defined by the position vector \mathbf{X}_α of the reference configuration. In contrast, the current position of the point in the Lagrangian approach can be determined with the help of the motion function, insofar as the point is located at point X_α at the time t_0 . All quantities refer to the location vector \mathbf{X}_α .

Here, the position vector \mathbf{x} of the material points X_α in the current configuration is prescribed using the motion function of the constituent χ_α that is unique and unambiguous invertible.

$$\mathbf{x} = \chi_\alpha(\mathbf{X}_\alpha, t). \quad (5.12)$$

The velocity \mathbf{x}'_α and the acceleration \mathbf{x}''_α result in

$$\mathbf{x}'_\alpha = \frac{\partial \chi_\alpha(\mathbf{X}_\alpha, t)}{\partial t} \quad \mathbf{x}''_\alpha = \frac{\partial^2 \chi_\alpha(\mathbf{X}_\alpha, t)}{\partial t^2}. \quad (5.13)$$

Alternatively, the Eulerian approach provides the description of a certain location and its change and thus refers to the position vector \mathbf{x} of the current configuration. All quantities refer to the location vector of the current position \mathbf{x} . The starting point of a particle located at point X_α at time t_0 can be determined by the inverse of the motion function.

$$\mathbf{X}_\alpha = \chi_\alpha^{-1}(\mathbf{x}, t) \quad (5.14)$$

The velocity \mathbf{x}'_α and the acceleration \mathbf{x}''_α result in

$$\mathbf{x}'_\alpha = \mathbf{x}'_\alpha(\mathbf{x}, t) = \mathbf{x}'_\alpha[\chi_\alpha^{-1}(\mathbf{x}, t), t] \quad \mathbf{x}''_\alpha = \mathbf{x}''_\alpha(\mathbf{x}, t) = \mathbf{x}''_\alpha[\chi_\alpha^{-1}(\mathbf{x}, t), t]. \quad (5.15)$$

5.5.2 Deformation and Strain of a Spatial Body

The existence of the inverse function of the equation of motion in Equation (5.14) requires mathematically a non-singular Jacobian J_α , which maps the spatial points of the reference configuration to the current configuration, so that

$$J_\alpha = \det \mathbf{F}_\alpha \neq 0. \quad (5.16)$$

The Jacobian J_α is derived from the determinant of the deformation gradient \mathbf{F}_α of the constituent, which describes the local deformations of a material point, that has to be greater than 0 during deformation processes.

$$\mathbf{F}_\alpha = \frac{\partial \mathbf{x}}{\partial \mathbf{X}_\alpha} = \frac{\partial \chi_\alpha(\mathbf{X}_\alpha, t)}{\partial \mathbf{X}_\alpha} = \text{Grad}_\alpha \chi_\alpha \quad \mathbf{F}_\alpha^{-1} = \frac{\partial \mathbf{X}_\alpha}{\partial \mathbf{x}} = \frac{\partial \chi_\alpha^{-1}(\mathbf{x}, t)}{\partial \mathbf{x}} = \text{grad} \mathbf{X}_\alpha \quad (5.17)$$

Herein the operator „Grad“ denotes the differential derivation with respect to the reference configuration position \mathbf{X}_α and the operator „grad“ the differential derivation with respect to the current configuration position \mathbf{x} .

In order to capture the individual motion function for the constituents, individual material time derivatives have to be considered.

The material time derivative specifies the time derivative of a quantity in the material points of the considered body, where the material points are fixed. The material time derivative of a quantity provides a local part, which describes the temporal change at a fixed place, as well as a convective part, which shows the change of the material point due to its movement.

The convective part is omitted in the Lagrangian approach, since this approach assumes fixed material points and thus has no time dependence. The Eulerian approach, however, provides a local and a convective part, so that the general form of

the material time derivative of an arbitrary scalar function $\phi(\mathbf{x}, t)$ results in

$$\phi'_{\alpha} = \frac{\partial \phi}{\partial t} + \left(\frac{\partial \phi}{\partial \mathbf{x}} \right) \frac{\partial \mathbf{x}}{\partial t} = \underbrace{\frac{\partial \phi}{\partial t}}_{\text{local part}} + \underbrace{(\text{grad} \phi) \cdot \mathbf{x}'_{\alpha}}_{\text{convective part}}. \quad (5.18)$$

The derivation of the deformation gradient yield the material velocity gradient $(\mathbf{F}_{\alpha})'_{\alpha}$ in Lagrangian formulation and the spatial velocity gradient \mathbf{L}_{α} in Eulerian formulation

$$(\mathbf{F}_{\alpha})'_{\alpha} = \frac{\partial \mathbf{x}'_{\alpha}}{\partial \mathbf{X}_{\alpha}} = \text{Grad}_{\alpha} \mathbf{x}'_{\alpha} \quad \mathbf{L}_{\alpha} = (\text{Grad}_{\alpha} \mathbf{x}'_{\alpha})(\mathbf{F}_{\alpha})'_{\alpha} = \text{grad} \mathbf{x}'_{\alpha}. \quad (5.19)$$

The spatial velocity gradient \mathbf{L}_{α} can be split additively into a symmetrical part \mathbf{D}_{α} and a skew-symmetrical part \mathbf{W}_{α} .

$$\mathbf{L}_{\alpha} = \mathbf{D}_{\alpha} + \mathbf{W}_{\alpha} \quad \mathbf{D}_{\alpha} = \frac{1}{2}(\mathbf{L}_{\alpha} + \mathbf{L}_{\alpha}^T) \quad \mathbf{W}_{\alpha} = \frac{1}{2}(\mathbf{L}_{\alpha} - \mathbf{L}_{\alpha}^T) \quad (5.20)$$

Since the deformation gradient still contains rigid body motions, it is not sufficient to describe the deformed state of the body with this variable. For this reason, deformation measures are derived from the line elements, more precisely their squares, which exclude these rigid body motions and thus allow valid evaluations. Transport theorems are applied to extract strain tensors from the square of line elements. The transport theorems represent the shape change of the material body from the reference configuration to the current configuration and can be evaluated since the deformation gradient changes between both configurations. The relationship of the position vector at the reference configuration $d\mathbf{X}$ to the current configuration is represented by the tangent mapping

$$d\mathbf{x} = \mathbf{F}_{\alpha} d\mathbf{X} \quad \mathbf{x} \in B_S. \quad (5.21)$$

The surface mapping gives the transformation of the surface of the reference $d\mathbf{A}$ into the current configuration

$$d\mathbf{a} = \det \mathbf{F}_{\alpha} \mathbf{F}_{\alpha}^{-1} d\mathbf{A} = J_S \mathbf{F}_{\alpha}^{-1} d\mathbf{A} \quad (5.22)$$

and the change of the volume describes the volume mapping

$$dv = \det \mathbf{F}_{\alpha} dV = J_{\alpha} dV. \quad (5.23)$$

The deformation of a body in reference configuration can be represented by the right Cauchy-Green tensor \mathbf{C}_α and in current configuration by the left Cauchy-Green tensor \mathbf{B}_α , with

$$\mathbf{C}_\alpha = \mathbf{F}_\alpha^T \mathbf{F}_\alpha \quad \mathbf{B}_\alpha = \mathbf{F}_\alpha \mathbf{F}_\alpha^T. \quad (5.24)$$

The evaluation of these deformation tensors at the position \mathbf{X}_α , so in reference configuration, yield the identity \mathbf{I} . However, from the physical point of view the deformation does not exist in the absence of any loads and thus must become 0. Therefore, the introduction of strain tensors is performed, which is not a physical quantity, but a conceptual approach. As a measure of the material strain, the Green-Lagrange strain tensor \mathbf{E}_α is derived from the right Cauchy-Green tensor \mathbf{C}_α and thus describes the strain in the reference configuration.

$$\mathbf{E}_\alpha = \frac{1}{2} (\mathbf{F}_\alpha^T \mathbf{F}_\alpha - \mathbf{I}) = \frac{1}{2} (\mathbf{C}_\alpha - \mathbf{I}) \quad (5.25)$$

In current configuration the Almansi strain tensor \mathbf{A}_α derived from the left Cauchy-Green tensor \mathbf{B}_α measures the spatial strain.

$$\mathbf{A}_\alpha = \frac{1}{2} (\mathbf{I} - (\mathbf{F}_\alpha \mathbf{F}_\alpha^T)^{-1}) = \frac{1}{2} (\mathbf{I} - (\mathbf{B}_\alpha)^{-1}) \quad (5.26)$$

These strain tensors are invariant to rotation and yield $\mathbf{F}_S = \mathbf{I}$ in the reference configuration and under deformations $\mathbf{F}_S \neq \mathbf{0}$. By including a forward or backward rotation, the Karni-Reiner tensors in reference and current configuration are obtained as

$$\mathbf{K}_\alpha^R = \frac{1}{2} (\mathbf{I} - \mathbf{C}_\alpha^{-1}), \quad \mathbf{K}_\alpha = \frac{1}{2} (\mathbf{B}_\alpha - \mathbf{I}). \quad (5.27)$$

5.6 Extended Theory of Porous Media

5.6.1 Balance Equation

In continuum mechanics, the behavior of the extensive quantities mass, momentum, momentum of momentum and energy can be described with the help of balance equations, which must be satisfied for each body. Here, the balance equations describe

the effect of the environment on a body as well as the resulting change in physical quantities.

In the TPM, these balance equations are based on those of a one-component body and are therefore set up individually for each constituent φ^α . According to TRUESDELL's third metaphysical rule [152], the balance equations set up for the constituents correspond to that of a comparable one-component body. Furthermore, all proportions that have an influence on the individual constituents must be taken into account, as well as the interactions between the phases. These interactions between the constituents are represented by the exchange terms, which must sum up to zero. The balance equations are derived both in the Lagrangian and the Eulerian approach. The focus here is on the Lagrangian approach, since this is primarily used for solid mechanics. Global balance equations apply to the entire body, while local balance equations apply to all local areas within the body and have to be fulfilled for all local material points.

The general form of balance equations consists of the temporal change of the respective quantity ψ , that is equal to the production $\hat{\psi}$ and the supply composed of inflow σ and outflow ϕ of this quantity.

This results for scalar- and vector-valued functions in

$$\text{scalar: } \dot{\psi} + \psi \operatorname{div} \dot{\mathbf{x}} = \operatorname{div} \boldsymbol{\phi} + \sigma + \hat{\psi}, \quad \text{vector: } \dot{\boldsymbol{\psi}} + \boldsymbol{\psi} \operatorname{div} \dot{\mathbf{x}} = \operatorname{div} \boldsymbol{\Phi} + \boldsymbol{\sigma} + \hat{\boldsymbol{\psi}}. \quad (5.28)$$

Balance of Mass

The mass balance is determined for each constituent φ^α separately and equates the change in mass M^α over time with the mass term $\int_{B_\alpha} \hat{\rho}^\alpha$. The mass supply is described by the interaction terms of the mass exchange $\hat{\rho}^\alpha$. It is also assumed that there are no external sources of mass:

$$(M^\alpha)'_\alpha = \left(\int_{B_\alpha} \rho^\alpha \operatorname{d}v \right)'_\alpha = \int_{B_\alpha} \hat{\rho}^\alpha \operatorname{d}v. \quad (5.29)$$

The mass supply $\hat{\rho}^\alpha$ is caused by the interaction of a constituent φ^α with the $(\kappa - 1)$ remaining constituents, which are at the same place X_α at time t . Using the transport

theorem of a volume element $(dv)'_\alpha = \text{div } \mathbf{x}'_\alpha dv$, the mass for one constituent results in

$$(M^\alpha)'_\alpha = \int_{B_\alpha} [(\rho^\alpha)'_\alpha + \rho^\alpha \text{div } \mathbf{x}'_\alpha] dv \quad (5.30)$$

and thus the balance of mass equals

$$\int_{B_\alpha} [(\rho^\alpha)'_\alpha + \rho^\alpha \text{div } \mathbf{x}'_\alpha] dv = \int_{B_\alpha} \hat{\rho}^\alpha dv. \quad (5.31)$$

This expression describes the global form of the mass balance in integral form. The local expression can be obtained to

$$(\rho^\alpha)'_\alpha + \rho^\alpha \text{div } \mathbf{x}'_\alpha = \hat{\rho}^\alpha, \quad \text{respectively : } \frac{\partial \rho^\alpha}{\partial t} + \text{div } (\rho^\alpha \mathbf{x}'_\alpha) = \hat{\rho}^\alpha. \quad (5.32)$$

By considering the same velocity for the phases, we can sum up the local expression in Equation (5.32) to

$$\sum_{\alpha=1}^{\kappa} [(\rho^\alpha)'_\alpha + \rho^\alpha \text{div } \mathbf{x}'_\alpha] = \sum_{\alpha=1}^{\kappa} \hat{\rho}^\alpha. \quad (5.33)$$

Considering TRUESDELL's metaphysical principle [152], this equation is only satisfied if the sum of the mass transfer term $\hat{\rho}^\alpha$ over all constituents vanishes:

$$\sum_{\alpha=1}^{\kappa} \hat{\rho}^\alpha \stackrel{!}{=} 0. \quad (5.34)$$

Equation (5.6) can now be used to convert the local form of the mass balance into a formulation including the volume fractions:

$$(\mathbf{n}^\alpha)'_\alpha + \frac{\mathbf{n}^\alpha}{\rho^{\alpha R}} (\rho^{\alpha R})'_\alpha + \mathbf{n}^\alpha \text{div } \mathbf{x}'_\alpha = \frac{1}{\rho^{\alpha R}} \hat{\rho}^\alpha. \quad (5.35)$$

Balance of momentum

The momentum balance describes the relation between the temporal change of the momentum $(\mathbf{I}^\alpha)'_\alpha$ and the external forces \mathbf{k}^α acting on the body. Here, the interaction of the individual constituents φ^α is also required by considering the interaction forces $\hat{\mathbf{p}}^\alpha$.

In the general form, the moment balance is given by

$$(\mathbf{l}^\alpha)' = \mathbf{k}^\alpha + \int_{B_\alpha} \hat{\mathbf{p}}^\alpha dv, \quad (5.36)$$

with the momentum \mathbf{l}^α and the external forces \mathbf{k}^α defined with

$$\mathbf{l}^\alpha = \int_{B_\alpha} \rho^\alpha \mathbf{x}'_\alpha dv, \quad \mathbf{k}^\alpha = \int_{B_\alpha} \rho^\alpha \mathbf{b}^\alpha dv + \int_{\partial B_\alpha} \mathbf{t}^\alpha da. \quad (5.37)$$

The external forces are composed of the volume forces $\rho^\alpha \mathbf{b}^\alpha$ and the surface forces. The surface forces can be converted into the Cauchy's stress tensor \mathbf{T}^α using the Cauchy theorem with

$$\int_{\partial B_\alpha} \mathbf{t}^\alpha da = \int_{\partial B_\alpha} \mathbf{T}^\alpha \mathbf{n} da = \int_{\partial B_\alpha} \mathbf{T}^\alpha d\mathbf{a}, \quad (5.38)$$

where $d\mathbf{a} = \mathbf{n} da$ is representing the external surface element in current configuration and \mathbf{n} is the unit normal at the surface of each constituent. To convert a surface integral of a vector field within a closed surface to a volume integral with the corresponding surface as boundary, the Gauss theorem can be applied. For Equation (5.38) this reads

$$\int_{\partial B_\alpha} \mathbf{T}^\alpha d\mathbf{a} = \int_{B_\alpha} \text{div } \mathbf{T}^\alpha dv. \quad (5.39)$$

The interaction force $\hat{\mathbf{p}}^\alpha = \hat{\mathbf{p}}^\alpha(\mathbf{x}, t)$ in addition describes the local increase of the momentum resulting from the interactions of the constituents.

Using Equation (5.37), the Gauss theorem (5.39) as well as the local form of mass balance (5.32) the balance of momentum results in

$$\int_{B_\alpha} (\rho^\alpha \mathbf{x}''_\alpha + \hat{\rho}^\alpha \mathbf{x}'_\alpha) dv = \int_{B_\alpha} (\text{div } \mathbf{T}^\alpha + \rho^\alpha \mathbf{b}^\alpha) dv + \int_{B_\alpha} \hat{\mathbf{p}}^\alpha dv, \quad (5.40)$$

with its local form

$$\text{div } \mathbf{T}^\alpha + \rho^\alpha (\mathbf{b}^\alpha - \mathbf{x}''_\alpha) + \hat{\mathbf{p}}^\alpha - \hat{\rho}^\alpha \mathbf{x}'_\alpha = \mathbf{0}. \quad (5.41)$$

The exchange of linear momentum caused by mass supply is characterized by $\hat{\rho}^\alpha \mathbf{x}'_\alpha$. To describe the momentum balance for the entire mixture, the local form is summed

up over all constituents:

$$\sum_{\alpha=1}^{\kappa} [\operatorname{div} \mathbf{T}^{\alpha} + \rho^{\alpha} (\mathbf{b}^{\alpha} - \mathbf{x}''_{\alpha}) + \hat{\mathbf{p}}^{\alpha} - \hat{\rho}^{\alpha} \mathbf{x}'_{\alpha}] = \mathbf{0}. \quad (5.42)$$

By TRUESDELL's constraint [152], the sum of the interaction forces $\hat{\mathbf{p}}^{\alpha}$ must add up to zero, so that the balance equation of the mixture is the same as that of a single component material:

$$\sum_{\alpha=1}^{\kappa} \hat{\mathbf{p}}^{\alpha} \stackrel{!}{=} \mathbf{0}. \quad (5.43)$$

Balance of angular momentum

The balance of angular momentum requires the equilibrium between the time derivative of the moment of momentum $\mathbf{h}_{(0)}^{\alpha}$ with respect to a spatially fixed reference point 0 and the momentum $\mathbf{m}_{(0)}^{\alpha}$ resulting from the forces acting on the body. The consideration of the interactions between the constituents is incorporated by the interaction forces $\hat{\mathbf{h}}_{(0)}^{\alpha}$.

The angular momentum balance is obtained as follows

$$(\mathbf{h}_{(0)}^{\alpha})'_{\alpha} = \mathbf{m}_{(0)}^{\alpha} + \hat{\mathbf{h}}_{(0)}^{\alpha}, \quad (5.44)$$

with the momentum of momentum $\mathbf{h}_{(0)}^{\alpha}$ and the momentum $\mathbf{m}_{(0)}^{\alpha}$ resulting from the forces defined as

$$\mathbf{h}_{(0)}^{\alpha} = \int_{\mathring{B}_{\alpha}} \mathbf{x} \times \rho^{\alpha} \mathbf{x}'_{\alpha} \, dv, \quad \mathbf{m}_{(0)}^{\alpha} = \int_{\mathring{B}_{\alpha}} \mathbf{x} \times \rho^{\alpha} \mathbf{b}^{\alpha} \, dv + \int_{\partial \mathring{B}_{\alpha}} \mathbf{x} \times \mathbf{T}^{\alpha} \, da, \quad (5.45)$$

as well as the interaction forces $\hat{\mathbf{h}}_{(0)}^{\alpha}$ as

$$\hat{\mathbf{h}}_{(0)}^{\alpha} = \int_{\mathring{B}_{\alpha}} \mathbf{x} \times \hat{\mathbf{p}}^{\alpha} \, dv. \quad (5.46)$$

Using the material time derivative of momentum of momentum

$$(\mathbf{h}_{(0)}^{\alpha})'_{\alpha} = \int_{\mathring{B}_{\alpha}} \mathbf{x} \times (\rho^{\alpha} \mathbf{x}''_{\alpha} + \hat{\rho}^{\alpha} \mathbf{x}'_{\alpha}) \, dv \quad (5.47)$$

and the Gauss theorem (5.39), the balance of angular momentum results in

$$\int_{B_\alpha} \mathbf{x} \times (\rho^\alpha \mathbf{x}_\alpha'' + \hat{\rho}^\alpha \mathbf{x}_\alpha') = \int_{B_\alpha} [\mathbf{x} \times (\operatorname{div} \mathbf{T}^\alpha + \rho^\alpha \mathbf{b}^\alpha) + \mathbf{I} \times \mathbf{T}^\alpha] \, dv + \int_{B_\alpha} \mathbf{x} \times \hat{\mathbf{p}}^\alpha \, dv. \quad (5.48)$$

By rewriting the Cauchy surface stress to volume integrals, and inserting the local form of the momentum balance (5.41), it reduces to

$$\mathbf{I} \times \mathbf{T}^\alpha = \mathbf{0}. \quad (5.49)$$

The angular momentum balance can only be satisfied if the stress tensor \mathbf{T}^α is symmetrical. This results in the symmetry of the Cauchy stress tensor \mathbf{T}^α as the central statement of the balance of angular momentum:

$$\mathbf{T}^\alpha = (\mathbf{T}^\alpha)^T. \quad (5.50)$$

Balance of energy

The balance of energy states that the internal and kinetic energy of a physical body must be equal to the sum of the change in mechanical and thermal energy. In addition, analogous to the previous balance equations the interactions between the different phases are captured in the form of energy exchange terms \hat{e}^α . From the energy balance it can be deduced that in a self-contained system no energy is lost, but can only be present in another energy form through an energy exchange. This requirement is also known as the first law of thermodynamics. On the basis of the TPM, the energy balance results in

$$(\mathbf{E}^\alpha)'_\alpha + (\mathbf{K}^\alpha)'_\alpha = \mathbf{W}^\alpha + \mathbf{Q}^\alpha + \int_{B_\alpha} \hat{e}^\alpha \, dv, \quad (5.51)$$

with the internal energy \mathbf{E}^α , the kinetic energy \mathbf{K}^α , the rate of mechanical energy \mathbf{W}^α , the rate of heat \mathbf{Q}^α and the energy supply \hat{e}^α from the other constituents. The different parts of the balance of energy can be derived to

$$\begin{aligned}
 E^\alpha &= \int_{B_\alpha} \rho^\alpha \varepsilon^\alpha \, dv, & K^\alpha &= \int_{B_\alpha} \frac{1}{2} \hat{\rho}^\alpha \mathbf{x}'_\alpha \cdot \mathbf{x}'_\alpha \, dv, \\
 W^\alpha &= \int_{B_\alpha} \mathbf{x}'_\alpha \cdot \rho^\alpha \mathbf{b} \, dv + \int_{\partial B_\alpha} \mathbf{x}'_\alpha \cdot \mathbf{T}^\alpha \, da, & Q^\alpha &= \int_{B_\alpha} \rho^\alpha r^\alpha - \int_{\partial B_\alpha} \mathbf{q}^\alpha \cdot d\mathbf{a},
 \end{aligned} \tag{5.52}$$

with internal energy $\varepsilon^\alpha = \varepsilon^\alpha(\mathbf{x}, t)$, partial energy sources r^α and partial heat flux vector \mathbf{q}^α .

In combination with the interaction forces $\hat{\varepsilon}^\alpha$ this results in the global form of the balance of energy

$$\begin{aligned}
 &\int_{B_\alpha} \left[\hat{\rho}^\alpha \varepsilon^\alpha + \rho^\alpha (\varepsilon^\alpha)'_\alpha + (\rho^\alpha \mathbf{x}''_\alpha + \frac{1}{2} \hat{\rho}^\alpha \mathbf{x}'_\alpha) \cdot \mathbf{x}'_\alpha \right] \, dv \\
 &= \int_{B_\alpha} [(\operatorname{div} \mathbf{T}^\alpha + \rho^\alpha \mathbf{b}^\alpha) \cdot \mathbf{x}'_\alpha + \mathbf{T}^\alpha \cdot \mathbf{L}_\alpha + (\rho^\alpha r^\alpha - \operatorname{div} \mathbf{q}^\alpha) + \hat{\varepsilon}^\alpha] \, dv
 \end{aligned} \tag{5.53}$$

with its local form

$$\rho^\alpha (\varepsilon^\alpha)'_\alpha + \hat{\rho}^\alpha (\varepsilon^\alpha + \frac{1}{2} \mathbf{x}'_\alpha \cdot \mathbf{x}'_\alpha) = [\operatorname{div} \mathbf{T}^\alpha + \rho^\alpha (\mathbf{b}^\alpha - \mathbf{x}''_\alpha)] \cdot \mathbf{x}'_\alpha + \mathbf{T}^\alpha \cdot \mathbf{L}_\alpha + \rho^\alpha r^\alpha - \operatorname{div} \mathbf{q}^\alpha + \hat{\varepsilon}^\alpha. \tag{5.54}$$

Using the local form of the momentum balance (5.41), as well as the symmetry of the Cauchy stress tensor from (5.50), by which the motion gradient \mathbf{L}_α can be replaced by its symmetric part \mathbf{D}_α , it follows that

$$\rho^\alpha r^\alpha = \rho^\alpha (\varepsilon^\alpha)'_\alpha + \hat{\rho}^\alpha (\varepsilon^\alpha - \frac{1}{2} \mathbf{x}'_\alpha \cdot \mathbf{x}'_\alpha) + \hat{\mathbf{p}}^\alpha \cdot \mathbf{x}'_\alpha - \mathbf{T}^\alpha \cdot \mathbf{D}_\alpha + \operatorname{div} \mathbf{q}^\alpha - \hat{\varepsilon}^\alpha. \tag{5.55}$$

Summed up over all constituents, the energy balance for the entire mixture thus results in

$$\sum_{\alpha=1}^{\kappa} [\rho^\alpha r^\alpha] = \sum_{\alpha=1}^{\kappa} [\rho^\alpha (\varepsilon^\alpha)'_\alpha + \hat{\rho}^\alpha (\varepsilon^\alpha - \frac{1}{2} \mathbf{x}'_\alpha \cdot \mathbf{x}'_\alpha) + \hat{\mathbf{p}}^\alpha \cdot \mathbf{x}'_\alpha - \mathbf{T}^\alpha \cdot \mathbf{D}_\alpha + \operatorname{div} \mathbf{q}^\alpha - \hat{\varepsilon}^\alpha]. \tag{5.56}$$

Analogous to the previous balance equations, the energy balance also requires that the interaction terms summed over all components must be zero:

$$\sum_{\alpha=1}^{\kappa} \hat{\varepsilon}^\alpha = 0. \tag{5.57}$$

Entropy Inequality

Constitutive relations are introduced in order to be able to consider not only the physical conditions but also the material behavior of the investigated property. However, these require restrictions, which can be obtained from the evaluation of the entropy inequality. The entropy inequality describes the second law of thermodynamics and results from the energy balance together with some manipulations. Its application ensures the thermodynamic consistency of the model. The successful application of the entropy inequality was developed by COLEMAN et al. [39] and subsequently modified by MÜLLER [102] and LIU [91].

To account for the existence of dissipative mechanisms within the mathematical model, a common entropy inequality is required for the sum of all constituents. This leads to the formulation for the entropy inequality

$$\sum_{\alpha=1}^{\kappa} (\mathbf{H}^{\alpha})'_{\alpha} \geq \sum_{\alpha=1}^{\kappa} \int_{\mathbf{B}_{\alpha}} \frac{1}{\theta^{\alpha}} \rho^{\alpha} \mathbf{r}^{\alpha} \, \mathrm{d}v - \sum_{\alpha=1}^{\kappa} \int_{\partial \mathbf{B}_{\alpha}} \frac{1}{\theta^{\alpha}} \mathbf{q}^{\alpha} \cdot \mathbf{d}a, \quad (5.58)$$

with the absolute temperature θ^{α} of the constituent and the entropy \mathbf{H}^{α} of the constituent dependent on the specific entropy η^{α} with

$$\mathbf{H}^{\alpha} = \int_{\mathbf{B}_{\alpha}} \rho^{\alpha} \eta^{\alpha} \, \mathrm{d}v. \quad (5.59)$$

Using the material time derivation of (5.59), the local form of the balance of mass (5.32) and the Gauss theorem (5.39), the entropy results in

$$\sum_{\alpha=1}^{\kappa} \int_{\mathbf{B}_{\alpha}} [\rho^{\alpha} (\eta^{\alpha})'_{\alpha} + \hat{\rho}^{\alpha} \eta^{\alpha}] \, \mathrm{d}v \geq \sum_{\alpha=1}^{\kappa} \int_{\mathbf{B}_{\alpha}} \left[\frac{1}{\theta^{\alpha}} \rho^{\alpha} \mathbf{r}^{\alpha} - \operatorname{div} \left(\frac{1}{\theta^{\alpha}} \mathbf{q}^{\alpha} \right) \right] \, \mathrm{d}v \quad (5.60)$$

or in the local form

$$\sum_{\alpha=1}^{\kappa} [\rho^{\alpha} (\eta^{\alpha})'_{\alpha} + \hat{\rho}^{\alpha} \eta^{\alpha} - \frac{1}{\theta^{\alpha}} \rho^{\alpha} \mathbf{r}^{\alpha} + \operatorname{div} \left(\frac{1}{\theta^{\alpha}} \mathbf{q}^{\alpha} \right)] \geq 0. \quad (5.61)$$

A thermodynamic equilibrium of a system always requires a maximum entropy, which cannot decrease by itself. In order to consider this, the Helmholtz free energy is introduced. The free Helmholtz energy is a thermodynamic potential used to describe the energy of a material. It is independent on the existing deformation of the body

and is defined as

$$\psi^\alpha = \varepsilon^\alpha - \theta^\alpha \eta^\alpha \quad (5.62)$$

with its material time derivation

$$(\psi^\alpha)'_\alpha = (\varepsilon^\alpha)'_\alpha - (\theta^\alpha)'_\alpha \eta^\alpha - \theta^\alpha (\eta^\alpha)'_\alpha. \quad (5.63)$$

By including (5.63) and assuming constant temperature for all phases in the mixture

$$\theta^\alpha = \theta = \text{constant}, \quad \rightarrow (\theta^\alpha)'_\alpha = 0, \quad \rightarrow \text{grad } \theta = 0, \quad (5.64)$$

the entropy inequality can be formulated as the Clausius-Duhem inequality

$$\sum_{\alpha=1}^{\kappa} [-\rho^\alpha (\psi^\alpha)'_\alpha - \hat{\rho}^\alpha (\psi^\alpha - \frac{1}{2} \mathbf{x}'_\alpha \cdot \mathbf{x}'_\alpha) + \mathbf{T}^\alpha \cdot \mathbf{D}_\alpha - \hat{\mathbf{p}}^\alpha \cdot \mathbf{x}'_\alpha] \geq 0. \quad (5.65)$$

All balance equations can be summed up in Table 5.1.

Table 5.1: Overview of (thermo-)mechanical balance relations

	$\psi^\alpha, \boldsymbol{\psi}^\alpha$	$\phi^\alpha, \boldsymbol{\Phi}^\alpha$	$\sigma^\alpha, \boldsymbol{\sigma}^\alpha$	$\hat{\psi}^\alpha, \hat{\boldsymbol{\psi}}^\alpha$
mass	ρ^α	0	0	$\hat{\rho}^\alpha$
momentum	$\rho^\alpha \mathbf{x}'_\alpha$	\mathbf{T}^α	$\rho^\alpha \mathbf{b}^\alpha$	$\hat{\mathbf{p}}^\alpha$
ang. momentum	$\mathbf{x} \times (\rho^\alpha \mathbf{x}'_\alpha)$	$\mathbf{x} \times \mathbf{T}^\alpha$	$\mathbf{x} \times (\rho^\alpha \mathbf{b}^\alpha)$	$\hat{\mathbf{h}}^\alpha$
energy	$\rho^\alpha (\varepsilon^\alpha + \frac{1}{2} \mathbf{x}'_\alpha \cdot \mathbf{x}'_\alpha)$	$\mathbf{T}^\alpha \mathbf{x}'_\alpha - \mathbf{q}^\alpha$	$\rho^\alpha (\mathbf{b}^\alpha \cdot \mathbf{x}'_\alpha) + r^\alpha$	\hat{e}^α
entropy	$\rho^\alpha \eta^\alpha$	$-\frac{1}{\theta^\alpha} \mathbf{q}^\alpha$	$\frac{1}{\theta^\alpha} \rho^\alpha r^\alpha$	$\hat{\eta}^\alpha$

Closure Problem

To close the physical problem, the number of unknown fields must be as large as that of the balance equations and the constitutive relations. In the TPM, there are less equations than unknowns due to the introduction of the additional volume fractions. To solve this problem, it is necessary to introduce complementary fields, however, this is difficult as the volume fractions involve not only the macroscale but also the microscale. Therefore, in order to account for the saturation condition, this equation

is introduced into the entropy evaluation in the form of its rates. The evaluation of the derivation of the saturation condition with respect to the solid phase results in

$$\begin{aligned} (n^S)'_S + (n^F)'_S &= 0 \\ -(n^S)'_S - (n^F)'_F + \text{grad } n^F \cdot \mathbf{w}_{FS} &= 0 \end{aligned} \quad (5.66)$$

or in the form of balance of mass without mass exchange

$$n^S \mathbf{D}_S \cdot \mathbf{I} + n^F \mathbf{D}_F \cdot \mathbf{I} + \text{grad } n^F \cdot \mathbf{w}_{FS} = 0. \quad (5.67)$$

5.6.2 Constitutive Modeling for a Tetra-Phasic Model for NAFLD and Tumor Development

As described in the previous chapters, various physical conditions must be included in the description of mechanical problems. On the one hand, these are the basic physical equations of kinetics with the balance equations. On the other hand, the kinematics are considered by looking at the deformation under the influence of certain forces. For the connection of the two fields and thus for the comprehensive description of the problem, the constitutive modeling is necessary. In addition to the general and material-independent conditions, this also includes the material relations. Depending on the selected material, a material model or constitutive model is developed, which reflects the material behavior and shows the relationship between the resulting stress and the strain. Even if each material behaves individually and a generally valid relationship is not possible, the material theory tries to find the commonalities in the behavior of a material and to describe this behavior mathematically. For this purpose different principles are introduced, which were developed from experience and plausibility. Some of these principles will be explained in the following, cf. BERTRAM [20].

Principle of determinism states that there is a relationship between the stresses prevailing in a body and the motion and temperature of the body. However, this does not include statistical and probabilistic assumptions. The history of the material point can be expressed, for example, via history functionals or internal variables containing the history.

Principle of local action states that the stress, which appears in a material point, depends only on the direct, finite neighborhood. This means that only the movements of directly neighboring points have an influence on the considered material point and further distant points are negligible.

Principle of equipresence states that all constitutive equations describing a material must depend on the same set of process variables. Process variables are quantities, that describe a systems path through equilibrium space. They depend on the path taken from one state to the next. Conversely, an independent variable that occurs in one constitutive equation must also occur in the other equations, cf. TRUESDELL et al. [153].

Material frame indifference (objectivity) states that all process variables and all constitutive equations must be independent of the observer. Measured physical quantities, such as time, are observer dependent and change with different choices of observed time or observed location. Certain kinematic and dynamic quantities, such as stress tensors, are observer independent, which leads to objectivity of the material equations. This also implies that the equations must not change with different configurations and are therefore invariant.

Assumptions

With regard to the use of eTPM, various assumptions are made for the detailed description of liver processes and to reduce numerical effort of the simulation. The general overview of the derived model for the description of NAFLD and tumor development is depicted in Figure 5.3. We consider a tetra-phasic model with three solid main

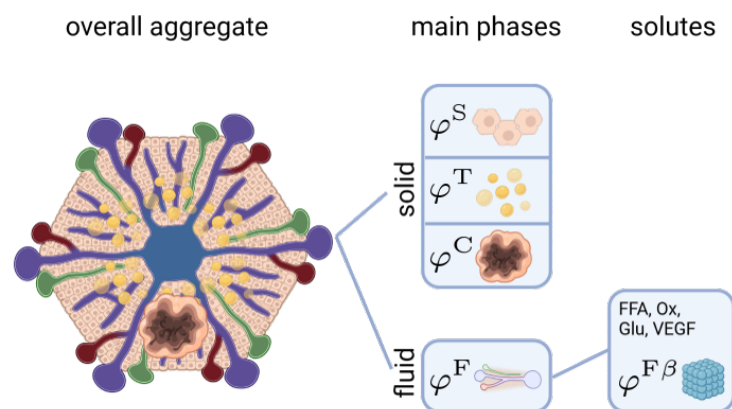


Figure 5.3: Overview of the composition of the total aggregate for the simulation of fat accumulation and tumor growth in the liver.

phases, namely solid liver tissue φ^S , as well as fat tissue φ^T and tumor tissue φ^C both with the ability to grow and deplete and a fluid main phase describing the blood φ^F . We assume the same motion function for all three solid phases. Since the blood flows through the liver lobule, this phase gets its own motion function, which is different from that of the solid phases:

$$\chi_S = \chi_T = \chi_C, \quad \chi_F \neq \chi_S. \quad (5.68)$$

In addition, microscopic substances can be dissolved in the main phases, which are required for metabolism within the liver cells. These are blood dissolved substances like FFAs and oxygen for lipid metabolism and glucose (Glu) and vascular endothelial growth factor (VEGF) for tumor growth. Solutes in liver tissue are also assumed to have the same motion as the solid phases whereas solutes within the blood phase have their own motion independent of the blood.

$$\chi_S = \chi_{S\beta} \quad \chi_F \neq \chi_{F\beta}. \quad (5.69)$$

Furthermore, the partial volume $dv^{\alpha\beta}$ of the microscopic substances β solved in the component α with respect to the phase is negligibly small, so that

$$dv^{\alpha\beta} \ll dv^\alpha. \quad (5.70)$$

With this assumption, we can assume the carrier phase φ^α to be equal to the total phase φ^α . The temperature in the liver is assumed to be equal in all components and the processes to be described are isothermal, so that there is no change in temperature:

$$\theta^S = \theta^F = \theta^T = \theta^C, \quad (\theta^\alpha)'_\alpha = 0. \quad (5.71)$$

This also implies that there is no energy exchange between the individual constituents

$$\hat{e}^\alpha = 0. \quad (5.72)$$

Liver tissue is also described as being materially incompressible, since the volume change of the tissue is significantly smaller compared to the volume change of the overall porous medium. The blood flowing through it can also be assumed to be materially

incompressible, since no change in density occurs with a change in pressure.

$$(\rho^{\text{SR}})'_{\text{S}} = (\rho^{\text{TR}})'_{\text{S}} = (\rho^{\text{CR}})'_{\text{S}} = (\rho^{\text{FR}})'_{\text{F}} = 0 \quad (5.73)$$

In the TPM, velocities \mathbf{x}'_{α} are mainly assumed to be small, so that the square of velocities can be regarded as negligible and a transient but quasi-static description is used with no acceleration, so it holds

$$\mathbf{x}''_{\alpha} = \mathbf{0}. \quad (5.74)$$

Furthermore, the body forces have an negligible influence on the blood flow in the liver. For this reason, no external forces on the liver are assumed

$$\mathbf{b}^{\alpha} = \mathbf{0}. \quad (5.75)$$

The metabolic exchanges between substances that occur in liver cells as well as phase transformations, require mass exchanges between constituents $\hat{\rho}^{\alpha}$ or substances $\hat{\rho}^{\alpha\beta}$. Since the exchange processes in the liver are comparatively slow and there are no explosive processes or chemical reactions, the mass transfer rate can be assumed to be sufficiently low, which leads to the assumption of a negligible mass exchange moment with

$$\hat{\rho}^{\alpha} \mathbf{x}'_{\alpha} = \hat{\rho}^{\alpha\beta} \mathbf{x}'_{\alpha} \approx \mathbf{0}. \quad (5.76)$$

The detailed mass exchange processes are explained in more detail in the description of the cell scale in Section 6.1. During the formation of fat vacuoles as well as a liver tumor, growth processes take place in the tissue. These imply an increase in volume and thus have direct effects on the adjacent tissue. Growth approaches describe these volume changes, which will be described in more detail in Section 5.6.8.

Using the eTPM the whole body φ can be described as

$$\varphi = \sum_{\alpha=1}^{\kappa} \varphi^{\alpha} := \sum_{\alpha=1}^{\kappa} \left[\sum_{\beta=1}^{\nu-1} (\varphi^{\alpha\beta}) + \varphi^{\alpha} \right]. \quad (5.77)$$

with $\kappa = 4$ main immiscible phases φ^{α} with $\alpha = \{\text{S, T, C, F}\}$, see Figure 5.4, and $(\nu - 1)$ miscible substances $\varphi^{\alpha\beta}$ with $\beta = \text{FFA, ox, Glu, VEGF}$, that are solved in the carrier phase α . Note that we assume the phases of solved components to be

negligible in Equation (5.70).

$$\begin{aligned}\varphi^{S\beta} &= \text{VEGF} &= \beta_i \mid i = 1 \\ \varphi^{F\beta} &= \text{FFA, Ox, Glu} &= \beta_i \mid i = 1, 2\end{aligned}\quad (5.78)$$

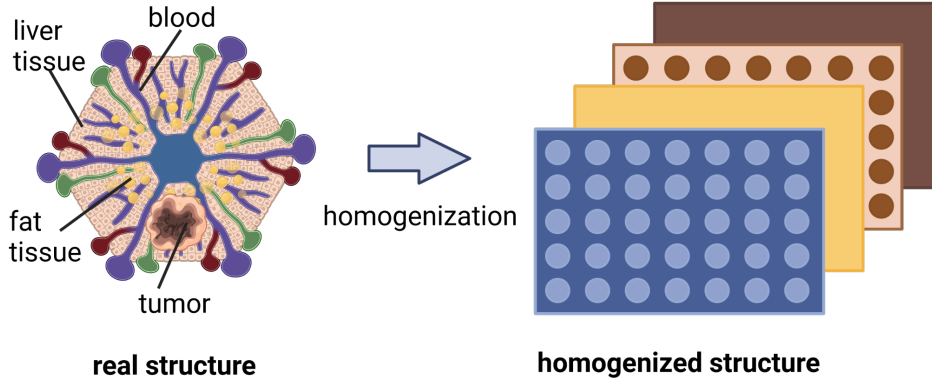


Figure 5.4: Mixture approach of liver lobule with the solid phases liver tissue (S), fat tissue (T), tumor tissue (C) and a fluid blood phase (F). Additionally, the phases can contain miscible substances.

The overall volume V of the whole mixture can be calculated via the sum of the partial volume dv^α as

$$V = \sum_{\alpha=1}^{\kappa} dv^\alpha = \int_{B_S} \sum_{\alpha=1}^{\kappa} dv^\alpha = \int_{B_S} \sum_{\alpha=1}^{\kappa} n^\alpha dv, \quad (5.79)$$

with $\kappa \in \{S, T, C, F\}$.

5.6.3 Field Equation

In order to fulfill physical requirements, the macroscopic description of the liver lobules has to satisfy the balance equations. Since no energy exchange, see Equation (5.72), and equal temperature, see Equation (5.71), is considered, the evaluation of the balance of mass, momentum and angular momentum is required. These balance equations are stated for the incompressible solid phases for liver tissue φ^S , fat tissue φ^T and tumor tissue φ^C , a fluid blood phase φ^F as well as for each microscopic

substances $\varphi^{\alpha\beta}$ solved in the phases. Furthermore, additional mixture conditions according to TRUESDELL [152] are included for the multiphase model, including the mass exchanges for liver tissue $\hat{\rho}^S$, fat tissue $\hat{\rho}^T$ and tumor tissue $\hat{\rho}^C$ as well as for substances $\hat{\rho}^{\alpha\beta}$ and interaction forces $\hat{\mathbf{p}}^\alpha$ and $\hat{\mathbf{p}}^{\alpha\beta}$ between the constituents.

Balance of mass

For the multiphase liver lobule model based on the eTPM, the balance equations of mass are applied in their local form. Here it is distinguished between each main phase and microscopic substance analogously to Equation (5.32) as following

$$\begin{aligned}
 \text{solid : } \quad (n^S)'_S + n^S \operatorname{div} \mathbf{x}'_S &= \frac{1}{\rho_{SR}} \hat{\rho}^S, & \text{fat : } (n^T)'_S + n^T \operatorname{div} \mathbf{x}'_S &= \frac{1}{\rho_{TR}} \hat{\rho}^T, \\
 \text{tumor : } \quad (n^C)'_S + n^C \operatorname{div} \mathbf{x}'_S &= \frac{1}{\rho_{CR}} \hat{\rho}^C, & \text{fluid : } (n^F)'_F + n^F \operatorname{div} \mathbf{x}'_F &= 0.
 \end{aligned}
 \tag{5.80}$$

The evaluation of the balance of mass for microscopic substances requires the material time derivation of the the partial density with respect to the solvent's kinematic. This leads to the following general local form of balance of mass for components

$$\begin{aligned}
 (\rho^{\alpha\beta})'_{\alpha\beta} + \rho^{\alpha\beta} \operatorname{div} \mathbf{x}'_\alpha &= \hat{\rho}^{\alpha\beta} & \text{with (5.11)} \\
 (n^\alpha c^{\alpha\beta} M_{\text{mol}}^\beta)'_{\alpha\beta} + n^\alpha c^{\alpha\beta} M_{\text{mol}}^\beta \operatorname{div} \mathbf{x}'_\alpha &= \hat{\rho}^{\alpha\beta} \\
 (n^\alpha)'_{\alpha\beta} c^{\alpha\beta} M_{\text{mol}}^\beta + n^\alpha (c^{\alpha\beta})'_{\alpha\beta} M_{\text{mol}}^\beta + n^\alpha c^{\alpha\beta} M_{\text{mol}}^\beta \operatorname{div} \mathbf{x}'_\alpha &= \hat{\rho}^{\alpha\beta}
 \end{aligned}
 \tag{5.81}$$

For the balance of mass for the fluid components we consider the seepage velocity \mathbf{w}_{FS} , that describes the relation between the fluid velocity \mathbf{x}'_F and the solid velocity \mathbf{x}'_S with

$$\mathbf{w}_{FS} = \mathbf{x}'_F - \mathbf{x}'_S.
 \tag{5.82}$$

Accordingly the seepage velocity for fluid components $\mathbf{w}_{F\beta S}$ depicts the velocity of fluid components $\mathbf{x}'_{F\beta}$ to the solid velocity \mathbf{x}'_S :

$$\mathbf{w}_{F\beta S} = \mathbf{x}'_{F\beta} - \mathbf{x}'_S.
 \tag{5.83}$$

By regarding the components velocity with respect to the velocity of the fluid, the diffusion velocity $\mathbf{d}_{F\beta S}$ results in

$$\mathbf{d}_{F\beta S} = \mathbf{w}_{F\beta S} - \mathbf{w}_{FS} = \mathbf{x}'_{F\beta} - \mathbf{x}'_F. \quad (5.84)$$

Since components solved in the solid are assumed to move collectively with the solid phase, there is no seepage velocity for solid components $\mathbf{w}_{S\beta S} = \mathbf{0}$. According to THOM [150] the total flux can be divided into an advective part, where the particles are transported via the solute velocity and a diffusive part, that describes the particle's own motion. The diffusive flux results in

$$\mathbf{j}_{\text{diff}}^{\alpha\beta} = \rho^{\alpha\beta} \mathbf{d}_{F\beta S} = \rho^{\alpha\beta} (\mathbf{w}_{F\beta S} - \mathbf{w}_{FS}). \quad (5.85)$$

Additionally, the material time derivation of the volume fraction of the main phases n^α with respect to the solvent's kinematic $(n^\alpha)'_{\alpha\beta}$ has to be evaluated. Therefore, the material time derivation for main phases results in

$$\begin{aligned} (n^\alpha)'_{F\beta} &= \frac{\partial n^\alpha}{\partial t} + \frac{\partial n^\alpha}{\partial \mathbf{x}(\mathbf{X}_F, t)} \frac{\partial \mathbf{x}(\mathbf{X}_F, t)}{\partial t} = \frac{\partial n^\alpha}{\partial t} + \text{grad } n^F \mathbf{x}'_F \\ \frac{\partial n^\alpha}{\partial t} &= (n^\alpha)'_{F\beta} - \text{grad } n^F \mathbf{x}'_F \end{aligned} \quad (5.86)$$

With Equation (5.86) and the seepage velocity of fluid components $\mathbf{w}_{F\beta F}$ in Equation (5.83) the material time derivation with respect to the solvent yields

$$\begin{aligned} (n^\alpha)'_{F\beta} &= \frac{\partial n^\alpha}{\partial t} + \frac{\partial n^\alpha}{\partial \mathbf{x}(\mathbf{X}_{F\beta}, t)} \frac{\partial \mathbf{x}(\mathbf{X}_{F\beta}, t)}{\partial t} \\ &= (n^\alpha)'_{F\beta} - \text{grad } n^F \mathbf{x}'_F + \text{grad } n^F \mathbf{x}'_{F\beta} \\ &= (n^\alpha)'_{F\beta} + \text{grad } n^F (\mathbf{x}'_{F\beta} - \mathbf{x}'_F) \\ &= (n^\alpha)'_{F\beta} + \text{grad } n^F \mathbf{w}_{F\beta F} \end{aligned} \quad (5.87)$$

Finally the local forms of the balance equation of mass for the microscopic components stored either in the solid or in the fluids can be derived to

$$\begin{aligned} \text{solid comp.} \quad & (n^S)'_S c^{S\beta} M_{\text{mol}}^{S\beta} + n^S (c^{S\beta})'_{S\beta} M_{\text{mol}}^{S\beta} + n^S c^{S\beta} M_{\text{mol}}^{S\beta} \text{div } \mathbf{x}'_S = \hat{\rho}^{S\beta}, \\ \text{fluid comp.} \quad & (n^F)'_F c^{F\beta} M_{\text{mol}}^{F\beta} + n^F (c^{F\beta})'_{F\beta} M_{\text{mol}}^{F\beta} + \text{grad } n^F \mathbf{w}_{F\beta S} c^{F\beta} M_{\text{mol}}^{F\beta} \\ & - \text{grad } n^F \mathbf{w}_{FS} c^{F\beta} M_{\text{mol}}^{F\beta} + n^F c^{F\beta} M_{\text{mol}}^{F\beta} \text{div } \mathbf{x}'_{F\beta} = \hat{\rho}^{F\beta}. \end{aligned} \quad (5.88)$$

Balance of Momentum

In addition, the balance equation of momentum must be satisfied, which represents the relationship between the material time derivatives of the motion quantities and the external forces. In the context of eTPM, the interactions between the constituents are also included as interaction forces for the main phases $\hat{\mathbf{p}}^\alpha$ and for solved components $\hat{\mathbf{p}}^{\alpha\beta}$, cf. TRUESDELL [152]. The local forms of the balance of momentum according to Equation (5.41) for each main phase and components using assumption (5.75) and (5.76) result in

$$\begin{array}{llll}
 \text{solid} & \operatorname{div} \mathbf{T}^S + \hat{\mathbf{p}}^S & = \mathbf{0}, & \text{fat} & \operatorname{div} \mathbf{T}^T + \hat{\mathbf{p}}^T & = \mathbf{0}, \\
 \text{tumor} & \operatorname{div} \mathbf{T}^C + \hat{\mathbf{p}}^C & = \mathbf{0}, & \text{fluid} & \operatorname{div} \mathbf{T}^F + \hat{\mathbf{p}}^F & = \mathbf{0}, \\
 \text{solid comp.} & \operatorname{div} \mathbf{T}^{S\beta} + \hat{\mathbf{p}}^{S\beta} & = \mathbf{0}, & \text{fluid comp.} & \operatorname{div} \mathbf{T}^{F\beta} + \hat{\mathbf{p}}^{F\beta} & = \mathbf{0},
 \end{array} \tag{5.89}$$

where \mathbf{T}^α and $\mathbf{T}^{\alpha\beta}$ characterizes the partial Cauchy stress tensor for main phases and solutes, whose divergence is included in the balance equation of momentum with divergence operator div .

Balance of Angular Momentum

The balance equation of angular momentum demands the symmetry of the Cauchy stress tensor, see Equation (5.50). This is also required for all partial stress tensors $\mathbf{T}^\alpha = (\mathbf{T}^\alpha)^T$ and $\mathbf{T}^{\alpha\beta} = (\mathbf{T}^{\alpha\beta})^T$.

Physical Requirements

In addition to the evaluation of the balance equations, the saturation condition according to Equation (5.4) must also be fulfilled. To describe the volume fractions of the main phases, the relations between partial and real density are applied, see Equation (5.6):

$$n^S + n^T + n^C + n^F = 1, \tag{5.90}$$

with

$$n^S = \frac{\rho^S}{\rho^{SR}}, \quad n^T = \frac{\rho^T}{\rho^{TR}}, \quad n^C = \frac{\rho^C}{\rho^{CR}}, \quad n^F = \frac{\rho^F}{\rho^{FR}}. \tag{5.91}$$

As additional physical requirements, it is considered that the mass exchanges as well as the interaction forces for main phases and components annul each other.

$$\hat{\rho}^S + \hat{\rho}^T + \hat{\rho}^C + \hat{\rho}^F + \hat{\rho}^{\alpha\beta} = 0, \quad \hat{\mathbf{p}}^S + \hat{\mathbf{p}}^T + \hat{\mathbf{p}}^C + \hat{\mathbf{p}}^F + \hat{\mathbf{p}}^{\alpha\beta} = \mathbf{0}. \quad (5.92)$$

Setup of equation system

In summary, the balance equations as well as the physical restrictions result in 49 field equations. There are 151 unknown quantities, but with the real density $\rho^{\alpha R}$, the molar mass of the substances M_{mol}^β and the external forces \mathbf{b}^α , 23 quantities are already known. This results in a difference of 79 unknown quantities, which must be determined by the choice of suitable constitutive quantities to close the system. Therefore, the Cauchy stress tensors \mathbf{T}^α and $\mathbf{T}^{\alpha\beta}$, the Helmholtz free energy ψ^α and $\psi^{\alpha\beta}$, the mass exchanges $\hat{\rho}^\alpha$ and $\hat{\rho}^{\alpha\beta}$ and the interaction forces $\hat{\mathbf{p}}^\alpha$ and $\hat{\mathbf{p}}^{\alpha\beta}$ are chosen as constitutive quantities. Taking into account the symmetry of the stress tensor, see Equation (5.50), there are thus 80 constitutive quantities for closing the system of equations, resulting in a redundant equation system with one overcount. This results in a coupled variational problem where the different fields are interrelated caused by the additional introduction of the volume fractions as unknown quantities, for whose calculation, however, a suitable balance equation is missing. To take this into account in the mathematical description of the model, additional equations are considered as constraints with the help of the Lagrange multiplier in the evaluation of the entropy equation [24]. In order to physically consider the saturation condition as a constraint when evaluating the problem, it is added to the entropy equation in its rate formulation using the mass balance. In order to close the system of equations, we introduce the following set of constitutives:

$$C = [\mathbf{T}_{\text{sym}}^S, \mathbf{T}_{\text{sym}}^F, \mathbf{T}_{\text{sym}}^{F\beta}, \hat{\mathbf{p}}^F, \hat{\mathbf{p}}^{F\beta}, \hat{\rho}^{\alpha\beta}]. \quad (5.93)$$

A requirement of the material theory is the principle of equipresence according to TRUESDELL [152], according to which all constitutive functions depend on the same set of process variables \mathcal{P} . This also guarantees compliance with the entropy inequality according to the thermomechanically consistent approach. The material behavior depends on an independent set of process variables P as well as on the derivations of

the process variables A :

$$\begin{aligned} P &:= [\mathbf{C}_S, \mathbf{n}^S, \mathbf{n}^F, \mathbf{n}^T, \mathbf{n}^C, \mathbf{w}_{F\beta S}, \mathbf{w}_{FS}, c^{S\beta}, c^{F\beta}, \text{grad } c^{S\beta}, \text{grad } c^{F\beta}, \text{grad } \mathbf{n}^F] \\ A &:= [\mathbf{D}_S, \mathbf{D}_F, \mathbf{D}_{F\beta}, (\mathbf{n}^F)'_F, (\mathbf{n}^T)'_S, (\mathbf{n}^C)'_S, (c^{S\beta})'_{S\beta}, (c^{F\beta})'_{F\beta}]. \end{aligned} \quad (5.94)$$

We assume the Helmholtz free energies of the phases ψ^α and microscopic components $\psi^{\alpha\beta}$ depending on the process variables as follows:

$$\begin{aligned} \psi^S &= \psi^S(\mathbf{C}_S), & \psi^T &= \psi^T(\mathbf{C}_S), & \psi^C &= \psi^C(\mathbf{C}_S), & \psi^F &= \psi^F(-), \\ \psi_S^{S\beta} &= \psi_S^{S\beta}(c^{S\beta}), & \psi_F^{F\beta} &= \psi_F^{F\beta}(c^{F\beta}). \end{aligned} \quad (5.95)$$

where $\psi_S^{S\beta}$ and $\psi_F^{F\beta}$ describe the energies depending on the realistic volume of the microscopic components. This leads to the relation of partial energy $\psi^{\alpha\beta}$ and the volume-specific energy $\psi_\alpha^{\alpha\beta}$ as:

$$\psi_S^{S\beta} = \rho^{S\beta R} \psi^{S\beta} \quad \psi_F^{F\beta} = \rho^{F\beta R} \psi^{F\beta}. \quad (5.96)$$

5.6.4 Mechanical and Thermodynamical Axioms: Thermodynamical Derivation

The evaluation of the entropy inequality requires additional constraints besides the adaptation of the general entropy equation to the given phases and assumptions. The eTPM is based on the concept of volume fractions and requires the saturation condition in Equation (5.4). To achieve thermodynamic consistency of the material law, the saturation condition must be added to the entropy equation and evaluated, cf. B. MARKERT [11]. According to the method of Lagrange multipliers presented by LIU [91], additional restrictions can be implemented as linear combination of field equation, that are weighted by the Lagrange multiplier. Since the saturation condition in its rate formulation with respect to the solid skeleton results in zero, see Equation (5.66), this formulation can be added to the entropy equation as a constraint using the Lagrangian multiplier λ :

$$\lambda \left[(\mathbf{n}^S)'_S + (\mathbf{n}^T)'_S + (\mathbf{n}^C)'_S + (\mathbf{n}^F)'_S \right]. \quad (5.97)$$

Since the TPM introduces the concept of volume fractions as an additional representation of the porosity and the distribution of the microstructure, no direct balance equations exist for solving the volume fractions. However, in the developed material model, the solid and the fluid phases are assumed to be materially incompressible, as stated in Equation (5.73), so that a statement about the volume fractions can be obtained from this. For the evaluation of the entropy inequality, the material time derivatives of the volume fractions are therefore replaced with the corresponding mass balances of the individual phases in their local forms (5.80).

$$\begin{aligned}
 \text{solid : } \quad (\mathbf{n}^S)'_S &= \frac{1}{\rho_{SR}} \hat{\rho}^S - \mathbf{n}^S \operatorname{div} \mathbf{x}'_S, & \text{fat : } (\mathbf{n}^T)'_S &= \frac{1}{\rho_{TR}} \hat{\rho}^T - \mathbf{n}^T \operatorname{div} \mathbf{x}'_S, \\
 \text{tumor : } \quad (\mathbf{n}^C)'_S &= \frac{1}{\rho_{CR}} \hat{\rho}^C - \mathbf{n}^C \operatorname{div} \mathbf{x}'_S, & \text{fluid : } (\mathbf{n}^F)'_F &= -\mathbf{n}^F \operatorname{div} \mathbf{x}'_F.
 \end{aligned} \tag{5.98}$$

Adapting this equation together with the relations

$$(\mathbf{n}^F)'_S = (\mathbf{n}^F)'_F - \operatorname{grad} \mathbf{n}^F \cdot \mathbf{w}_{FS}, \quad \operatorname{div} \mathbf{x}'_\alpha = \mathbf{D}_\alpha \cdot \mathbf{I}. \tag{5.99}$$

the final constraint for the entropy inequality reads

$$\begin{aligned}
 \lambda \left[\frac{\hat{\rho}^S}{\rho_{SR}} - \mathbf{D}_S \cdot \mathbf{I} \mathbf{n}^S + \frac{\hat{\rho}^T}{\rho_{TR}} - \mathbf{D}_S \cdot \mathbf{I} \mathbf{n}^T + \frac{\hat{\rho}^C}{\rho_{CR}} - \mathbf{D}_S \cdot \mathbf{I} \mathbf{n}^C - \mathbf{D}_F \cdot \mathbf{I} \mathbf{n}^F \right. \\
 \left. - \operatorname{grad} \mathbf{n}^F \cdot \mathbf{w}_{FS}. \right] \tag{5.100}
 \end{aligned}$$

In order to derive a thermodynamical consistent material model, the entropy inequality has to be considered. By adding an assumption for the Helmholtz free energy ψ^α , that ensures the entropy to be as large as possible and that entropy can never decrease in a closed system, the Clausius-Duhem inequality was derived in Equation (5.65). This inequality is adapted to the TPM and tailored to each constituent. In addition, the further constraints in Equation (5.100) is applied so that the extended entropy

inequality for the mixture of all phases and substances is obtained:

$$\begin{aligned}
 & - \rho^S (\psi^S)'_S - \rho^T (\psi^T)'_S - \rho^C (\psi^C)'_S - \rho^F (\psi^F)'_F - \rho^{S\beta} (\psi^{S\beta})'_{S\beta} - \rho^{F\beta} (\psi^{F\beta})'_{F\beta} \\
 & - \hat{\rho}^S (\psi^S - \frac{1}{2} \mathbf{x}'_S \cdot \mathbf{x}'_S) - \hat{\rho}^T (\psi^T - \frac{1}{2} \mathbf{x}'_S \cdot \mathbf{x}'_S) - \hat{\rho}^C (\psi^C - \frac{1}{2} \mathbf{x}'_S \cdot \mathbf{x}'_S) \\
 & - \hat{\rho}^{S\beta} (\psi^{S\beta} - \frac{1}{2} \mathbf{x}'_S \cdot \mathbf{x}'_S) - \hat{\rho}^{F\beta} (\psi^{F\beta} - \frac{1}{2} \mathbf{x}'_{F\beta} \cdot \mathbf{x}'_{F\beta}) \\
 & + \mathbf{T}^S \cdot \mathbf{D}_S + \mathbf{T}^T \cdot \mathbf{D}_S + \mathbf{T}^C \cdot \mathbf{D}_S + \mathbf{T}^F \cdot \mathbf{D}_F + \mathbf{T}^{S\beta} \cdot \mathbf{D}_S + \mathbf{T}^{F\beta} \cdot \mathbf{D}_{F\beta} \\
 & - \hat{\mathbf{p}}^S \cdot \mathbf{x}'_S - \hat{\mathbf{p}}^T \cdot \mathbf{x}'_S - \hat{\mathbf{p}}^C \cdot \mathbf{x}'_S - \hat{\mathbf{p}}^F \cdot \mathbf{x}'_F - \hat{\mathbf{p}}^{S\beta} \cdot \mathbf{x}'_S - \hat{\mathbf{p}}^{F\beta} \cdot \mathbf{x}'_{F\beta} \\
 & - \lambda (-\mathbf{D}_S \cdot \mathbf{I} \mathbf{n}^S - \mathbf{D}_S \cdot \mathbf{I} \mathbf{n}^T - \mathbf{D}_S \cdot \mathbf{I} \mathbf{n}^C - \mathbf{D}_F \cdot \mathbf{I} \mathbf{n}^F \\
 & - \frac{\hat{\rho}^S}{\rho^{SR}} - \frac{\hat{\rho}^T}{\rho^{TR}} - \frac{\hat{\rho}^C}{\rho^{CR}} - \text{grad } \mathbf{n}^F \cdot \mathbf{w}_{FS}) \geq 0.
 \end{aligned} \tag{5.101}$$

5.6.5 Evaluation of the Entropy Inequality

The derived entropy inequality for the whole aggregate can now be evaluated under the condition of thermodynamic consistency. For this, first the temporal change of the free Helmholtz energy $(\psi^\alpha)'_\alpha$ is considered, which result from the dependencies of the Helmholtz energy according to the process variables shown in Equation (5.95):

$$\begin{aligned}
 \rho^S (\psi^S)'_S &= 2 \rho^S \mathbf{F}_S \frac{\partial \psi^S}{\partial \mathbf{C}_S} \mathbf{F}_S^T \cdot \mathbf{D}_S, & \rho^T (\psi^T)'_S &= 2 \rho^T \mathbf{F}_S \frac{\partial \psi^T}{\partial \mathbf{C}_S} \mathbf{F}_S^T \cdot \mathbf{D}_S, \\
 \rho^C (\psi^C)'_S &= 2 \rho^C \mathbf{F}_S \frac{\partial \psi^C}{\partial \mathbf{C}_S} \mathbf{F}_S^T \cdot \mathbf{D}_S, & \rho^F (\psi^F)'_F &= 0.
 \end{aligned} \tag{5.102}$$

Furthermore, the entropy inequality can be sorted according to the different process variables that are found in the individual terms. Here, a distinction is made between the elastic components, which do not cause entropy, and the dissipative and thus entropy-generating components. The terms with dependence on the deformation velocity gradient in the form of the symmetric spatial velocity gradient are classified

as elastic components.

$$\begin{aligned}
 \mathbf{D}_S & \cdot [\mathbf{T}^S + \mathbf{T}^T + \mathbf{T}^C + \mathbf{T}^{S\beta} + \lambda \mathbf{I}(\mathbf{n}^S + \mathbf{n}^T + \mathbf{n}^C) \\
 & \quad - 2\rho^S \mathbf{F}_S \frac{\partial \psi^S}{\partial \mathbf{C}_S} \mathbf{F}_S^T - 2\rho^T \mathbf{F}_S \frac{\partial \psi^T}{\partial \mathbf{C}_S} \mathbf{F}_S^T - 2\rho^C \mathbf{F}_S \frac{\partial \psi^C}{\partial \mathbf{C}_S} \mathbf{F}_S^T] \\
 + \mathbf{D}_F & \cdot [\mathbf{T}^F + \frac{\partial \psi_F^{F\beta}}{\partial \mathbf{c}^{F\beta}} \mathbf{n}^F \mathbf{c}^{F\beta} \mathbf{I} - \psi_F^{F\beta} \mathbf{n}^F \mathbf{I} + \lambda \mathbf{I} \mathbf{n}^F] \\
 + \mathbf{D}_{F\beta} & \cdot [\mathbf{T}^{F\beta} - \frac{\partial \psi_F^{F\beta}}{\partial \mathbf{c}^{F\beta}} \mathbf{n}^F \mathbf{c}^{F\beta} \mathbf{I} + \psi_F^{F\beta} \mathbf{n}^F \mathbf{I}] = 0.
 \end{aligned} \tag{5.103}$$

Here, all Cauchy stresses for the solid phases can be summarized to an overall solid Cauchy stress tensor \mathbf{T}^S with

$$\mathbf{T}^S = \mathbf{T}^S + \mathbf{T}^T + \mathbf{T}^C + \mathbf{T}^{S\beta}. \tag{5.104}$$

Therefore, under the assumption of existing deformation and the requirement that elastic components do not contribute to the evolution of entropy, restrictions for the stresses can be evaluated using the volume fraction for the pore space $\mathbf{n}^P = \mathbf{n}^S + \mathbf{n}^T + \mathbf{n}^C$.

$$\begin{aligned}
 \mathbf{T}^S & = 2\rho^S \mathbf{F}_S \frac{\partial \psi^S}{\partial \mathbf{C}_S} \mathbf{F}_S^T + 2\rho^T \mathbf{F}_S \frac{\partial \psi^T}{\partial \mathbf{C}_S} \mathbf{F}_S^T + 2\rho^C \mathbf{F}_S \frac{\partial \psi^C}{\partial \mathbf{C}_S} \mathbf{F}_S^T - \lambda \mathbf{I}(1 - \mathbf{n}^P) \\
 \mathbf{T}^F & = -\frac{\partial \psi_F^{F\beta}}{\partial \mathbf{c}^{F\beta}} \mathbf{n}^F \mathbf{c}^{F\beta} \mathbf{I} + \psi_F^{F\beta} \mathbf{n}^F \mathbf{I} - \lambda \mathbf{I} \mathbf{n}^F \\
 \mathbf{T}^{F\beta} & = \frac{\partial \psi_F^{F\beta}}{\partial \mathbf{c}^{F\beta}} \mathbf{n}^F \mathbf{c}^{F\beta} \mathbf{I} - \psi_F^{F\beta} \mathbf{n}^F \mathbf{I}
 \end{aligned} \tag{5.105}$$

In addition to the elastic components and the resulting restrictions, the dissipative components of the entropy inequality can also be identified with:

$$\begin{aligned}
 -\mathbf{w}_{\text{FS}} &\cdot [\hat{\mathbf{p}}^{\text{F}} - \lambda \text{grad } \mathbf{n}^{\text{F}} - \frac{\partial \psi_{\text{F}}^{\text{F}\beta}}{\partial \mathbf{c}^{\text{F}\beta}} \text{grad } \mathbf{n}^{\text{F}} \mathbf{c}^{\text{F}\beta} + \psi_{\text{F}}^{\text{F}\beta} \text{grad } \mathbf{n}^{\text{F}}] \\
 -\mathbf{w}_{\text{F}\beta\text{S}} &\cdot [\hat{\mathbf{p}}^{\text{F}\beta} + \frac{\partial \psi_{\text{F}}^{\text{F}\beta}}{\partial \mathbf{c}^{\text{F}\beta}} \text{grad } \mathbf{n}^{\text{F}} \mathbf{c}^{\text{F}\beta} - \psi_{\text{F}}^{\text{F}\beta} \text{grad } \mathbf{n}^{\text{F}}] \\
 -\hat{\rho}^{\text{S}} &\cdot [\psi^{\text{S}} - \frac{1}{2} \mathbf{x}'_{\text{S}} \cdot \mathbf{x}'_{\text{S}} + \frac{\lambda}{\rho^{\text{SR}}}] \\
 -\hat{\rho}^{\text{T}} &\cdot [\psi^{\text{T}} - \frac{1}{2} \mathbf{x}'_{\text{S}} \cdot \mathbf{x}'_{\text{S}} + \frac{\lambda}{\rho^{\text{TR}}}] \\
 -\hat{\rho}^{\text{C}} &\cdot [\psi^{\text{C}} - \frac{1}{2} \mathbf{x}'_{\text{S}} \cdot \mathbf{x}'_{\text{S}} + \frac{\lambda}{\rho^{\text{CR}}}] \\
 -\hat{\rho}^{\text{S}\beta} &\cdot [\psi^{\text{S}\beta} - \frac{1}{2} \mathbf{x}'_{\text{S}} \cdot \mathbf{x}'_{\text{S}} + \frac{\partial \psi_{\text{S}}^{\text{S}\beta}}{\partial \mathbf{c}^{\text{S}\beta}} \frac{1}{M_{\text{mol}}^{\text{S}\beta}} + \psi_{\text{S}}^{\text{S}\beta} \frac{1}{\rho^{\text{S}\beta\text{R}}}] \\
 -\hat{\rho}^{\text{F}\beta} &\cdot [\psi^{\text{F}\beta} - \frac{1}{2} \mathbf{x}'_{\text{F}\beta} \cdot \mathbf{x}'_{\text{F}\beta} + \frac{\partial \psi_{\text{F}}^{\text{F}\beta}}{\partial \mathbf{c}^{\text{F}\beta}} \frac{1}{M_{\text{mol}}^{\text{F}\beta}} + \psi_{\text{F}}^{\text{F}\beta} \frac{1}{\rho^{\text{F}\beta\text{R}}}] \geq 0
 \end{aligned} \tag{5.106}$$

Restrictions for the various process variables can also be evaluated from these dissipative parts of the entropy inequality. However, since the terms do not add up to zero due to the energy-destroying behavior, it must be ensured that they become positive at any given time. This is achieved by the suitable choice of the restrictions, by using the already existing parts for the dissipative variables and by ensuring the positivity of the quantities using squared terms. Furthermore, for the calculation of the interaction forces, the two parameters $\gamma_{\mathbf{w}_{\text{FS}}}^{\text{F}}$ and $\gamma_{\mathbf{w}_{\text{F}\beta\text{S}}}^{\text{F}}$ are introduced, which by

definition have the character to provide a positive result of the equation:

$$\begin{aligned}
 \bar{\psi}^{\text{F}\beta} &= \psi^{\text{F}\beta} - \frac{1}{2} \mathbf{x}'_{\text{F}\beta} \cdot \mathbf{x}'_{\text{F}\beta} + \frac{\partial \psi^{\text{F}\beta}}{\partial c^{\text{F}\beta}} \frac{1}{M_{\text{mol}}^{\text{F}\beta}} + \psi^{\text{F}\beta} \frac{1}{\rho^{\text{F}\beta\text{R}}} \\
 \bar{\psi}^{\text{S}\beta} &= \psi^{\text{S}\beta} - \frac{1}{2} \mathbf{x}'_{\text{S}} \cdot \mathbf{x}'_{\text{S}} + \frac{\partial \psi^{\text{S}\beta}}{\partial c^{\text{S}\beta}} \frac{1}{M_{\text{mol}}^{\text{S}\beta}} + \psi^{\text{S}\beta} \frac{1}{\rho^{\text{S}\beta\text{R}}} \\
 \bar{\psi}^{\text{S}} &= \psi^{\text{S}} - \frac{1}{2} \mathbf{x}'_{\text{S}} \cdot \mathbf{x}'_{\text{S}} + \frac{\lambda}{\rho^{\text{SR}}} \\
 \bar{\psi}^{\text{T}} &= \psi^{\text{T}} - \frac{1}{2} \mathbf{x}'_{\text{S}} \cdot \mathbf{x}'_{\text{S}} + \frac{\lambda}{\rho^{\text{TR}}} \\
 \bar{\psi}^{\text{C}} &= \psi^{\text{C}} - \frac{1}{2} \mathbf{x}'_{\text{S}} \cdot \mathbf{x}'_{\text{S}} + \frac{\lambda}{\rho^{\text{CR}}} \\
 \hat{\mathbf{p}}^{\text{F}} &= \lambda \text{grad } n^{\text{F}} + \frac{\partial \psi^{\text{F}\beta}}{\partial c^{\text{F}\beta}} \text{grad } n^{\text{F}} c^{\text{F}\beta} - \psi^{\text{F}\beta} \text{grad } n^{\text{F}} \\
 &\quad - \gamma_{\mathbf{w}_{\text{FS}}}^{\text{F}} \mathbf{w}_{\text{FS}} + \gamma_{\mathbf{w}_{\text{F}\beta\text{S}}}^{\text{F}} \mathbf{w}_{\text{F}\beta\text{S}} \\
 \hat{\mathbf{p}}^{\text{F}\beta} &= -\frac{\partial \psi^{\text{F}\beta}}{\partial c^{\text{F}\beta}} \text{grad } n^{\text{F}} c^{\text{F}\beta} + \psi^{\text{F}\beta} \text{grad } n^{\text{F}} \\
 &\quad - \gamma_{\mathbf{w}_{\text{F}\beta\text{S}}}^{\text{F}} \mathbf{w}_{\text{F}\beta\text{S}} - \gamma_{\mathbf{w}_{\text{FS}}}^{\text{F}} \mathbf{w}_{\text{FS}}.
 \end{aligned} \tag{5.107}$$

The entropy inequality is satisfied for fixed values of the process variables and their derivatives.

5.6.6 Stress

The evaluation of the entropy inequality delivers restriction for stresses. Together with this, the constitutive approach for the stresses is provided by the Neo-Hooke material law, which is dependent on the process variables. Here all solid phases possess the same material law, so that the energy functions differ only in the material parameters.

The Helmholtz free energy for the solid phases result in

$$\begin{aligned}
 \psi^S &= \frac{1}{\rho_{0S}^S} \left[\lambda^S \frac{1}{2} (\ln J_S)^2 - \mu^S \ln J_S + \frac{1}{2} \mu^S (\text{tr } \mathbf{C}_S - 3) \right], \\
 \psi^T &= \frac{1}{\rho_{0S}^T} \left[\lambda^T \frac{1}{2} (\ln J_S)^2 - \mu^T \ln J_S + \frac{1}{2} \mu^T (\text{tr } \mathbf{C}_S - 3) \right], \\
 \psi^C &= \frac{1}{\rho_{0S}^C} \left[\lambda^C \frac{1}{2} (\ln J_S)^2 - \mu^C \ln J_S + \frac{1}{2} \mu^C (\text{tr } \mathbf{C}_S - 3) \right],
 \end{aligned} \tag{5.108}$$

with λ^S , λ^T , λ^C and μ^S , μ^T , μ^C being the Lamé constants. Due to the dependence of the Helmholtz free energy on the process variable \mathbf{C}_S , the derivation according to the latter is as follows:

$$\begin{aligned}
 \frac{\partial \psi^S}{\partial \mathbf{C}_S} &= \frac{1}{\rho_{0S}^S} \left[\lambda^S \frac{1}{2} \mathbf{C}_S^{-1} \ln J_S - \mu^S \frac{1}{2} \mathbf{C}_S^{-1} + \frac{1}{2} \mu^S \mathbf{I} \right], \\
 \frac{\partial \psi^T}{\partial \mathbf{C}_S} &= \frac{1}{\rho_{0S}^T} \left[\lambda^T \frac{1}{2} \mathbf{C}_S^{-1} \ln J_S - \mu^T \frac{1}{2} \mathbf{C}_S^{-1} + \frac{1}{2} \mu^T \mathbf{I} \right], \\
 \frac{\partial \psi^C}{\partial \mathbf{C}_S} &= \frac{1}{\rho_{0S}^C} \left[\lambda^C \frac{1}{2} \mathbf{C}_S^{-1} \ln J_S - \mu^C \frac{1}{2} \mathbf{C}_S^{-1} + \frac{1}{2} \mu^C \mathbf{I} \right].
 \end{aligned} \tag{5.109}$$

Similarly, an approach according to ACARTÜRK [1], EHLERS [50] and WAGNER, A. [157] is adopted for the Helmholtz free energy of microscopic substances $\psi_F^{F\beta}$. This as well as the corresponding derivation according to the process variable $c^{F\beta}$ results as

$$\begin{aligned}
 \psi_F^{F\beta} &= c^{F\beta} \mu_0^{F\beta} + c^{F\beta} R \theta (\ln c^{F\beta} - 1), \\
 \frac{\partial \psi_F^{F\beta}}{\partial c^{F\beta}} &= \mu_0^{F\beta} + R \theta \ln c^{F\beta} = \mu^{F\beta}.
 \end{aligned} \tag{5.110}$$

Here R describes the gas constant and θ the temperature of the mixture, while $\mu_0^{F\beta}$ indicates the constant standard chemical potential. In contrast to the solid phases, the concentrations in the fluid have their own motion function, which is why the approach of the concentrations is set up for each one separately. The chemical potential derived from the entropy inequality is thus a function of the solute concentration, which is calculated with

$$c^{\alpha\beta} = e^{\left[\frac{M_{\text{mol}}^{\beta}}{R\theta} (\mu^{\text{F}} - \mu_0^{\alpha\beta}) \right]} c_0^{\alpha\beta}. \quad (5.111)$$

Analogous to ACARTÜRK [1], EHLERS [50], BOWEN [30, 29] and WAGNER, A. [157], the resulting stress of the external concentrations can be divided into an osmotic pressure Π with

$$\Pi = R\theta \sum_{\text{F}\beta} c^{\text{F}\beta}. \quad (5.112)$$

The osmotic component is caused by the effort of the microscopic substances to compensate for a concentration difference that arises. This results in concentration gradient which generates the osmotic pressure. Summing up the osmotic pressure Π and the hydraulic pressure p^{FR} , characterized by the Lagrange parameter, the total pressure p^{R} results in

$$p^{\text{R}} = p^{\text{FR}} + \Pi. \quad (5.113)$$

Inserting the approaches for the Helmholtz free energy functions (5.108, 5.110₍₁₎) and their derivations (5.109, 5.110₍₂₎) in the evaluation of the entropy inequality results in the following stress equations:

$$\begin{aligned} \mathbf{T}^{\text{S}} &= \left[\lambda^{\text{S}} \ln J_{\text{S}} \mathbf{I} + 2\mu^{\text{S}} \mathbf{K}_{\text{S}} \right] - \lambda \mathbf{I} (1 - n^{\text{P}}), \\ \mathbf{T}^{\text{F}} &= -n^{\text{F}} (\lambda + \Pi) \mathbf{I}, \\ \mathbf{T}^{\text{F}\beta} &= n^{\text{F}} c^{\text{F}\beta} R\theta \mathbf{I} = n^{\text{F}} \Pi \mathbf{I}, \end{aligned} \quad (5.114)$$

with the Karni-Reiner stress tensor $\mathbf{K}_{\text{S}} = \frac{1}{2} (\mathbf{B}_{\text{S}} - \mathbf{I})$ and the effective Lamé parameters for the solid phases weighted by the volume fractions of each phase with $\lambda^{\text{S}} = n^{\text{S}} \lambda^{\text{S}} + n^{\text{T}} \lambda^{\text{T}} + n^{\text{C}} \lambda^{\text{C}}$ and $\mu^{\text{S}} = n^{\text{S}} \mu^{\text{S}} + n^{\text{T}} \mu^{\text{T}} + n^{\text{C}} \mu^{\text{C}}$.

5.6.7 Seepage Velocity

In addition to the evaluation of the stresses, restrictions for the dissipative moment production can also be obtained from the evaluation of the entropy inequality. The

restrictions of the interaction forces of the fluid phase $\hat{\mathbf{p}}^F$ as well as the substances dissolved in it $\hat{\mathbf{p}}^{F\beta}$ result to:

$$\begin{aligned}\hat{\mathbf{p}}^F &= \text{grad } n^F \lambda + \Pi \text{grad } n^F + \gamma_{\mathbf{w}_{F\beta S}}^F \mathbf{w}_{F\beta S} - \gamma_{\mathbf{w}_{FS}}^F \mathbf{w}_{FS}, \\ \hat{\mathbf{p}}^{F\beta} &= -\Pi \text{grad } n^F - \gamma_{\mathbf{w}_{F\beta S}}^F \mathbf{w}_{F\beta S} - \gamma_{\mathbf{w}_{FS}}^F \mathbf{w}_{FS}.\end{aligned}\tag{5.115}$$

Here, the parameters $\gamma_{\mathbf{w}_{FS}}^F$ and $\gamma_{\mathbf{w}_{F\beta S}}^F$ describe factors that ensure a positive value of the dissipative fraction to ensure thermodynamic consistency.

The restrictions for the interaction forces enable the draft of a constitutive law for the filter velocity. First, we focus on the flux of the external concentrations $\mathbf{w}_{F\beta S}$ from miscible components solved within the fluid. For this, we apply the Cauchy stresses (5.114₍₃₎) and momentum production (5.115₍₂₎), to recalculate the balance of momentum for the fluid components to

$$\begin{aligned}\text{div } \mathbf{T}^{F\beta} + \hat{\mathbf{p}}^{F\beta} &= \text{div } (n^F \Pi \mathbf{I}) - \Pi \text{grad } n^F - \gamma_{\mathbf{w}_{F\beta S}}^F \mathbf{w}_{F\beta S} - \gamma_{\mathbf{w}_{FS}}^F \mathbf{w}_{FS} \\ &= \mathbf{I} \text{grad } (n^F \Pi) + n^F \Pi \text{div } \mathbf{I} - \Pi \text{grad } n^F - \gamma_{\mathbf{w}_{F\beta S}}^F \mathbf{w}_{F\beta S} - \gamma_{\mathbf{w}_{FS}}^F \mathbf{w}_{FS} \\ &= n^F \mathbf{I} \text{grad } \Pi + \mathbf{I} \Pi \text{grad } n^F - \Pi \text{grad } n^F - \gamma_{\mathbf{w}_{F\beta S}}^F \mathbf{w}_{F\beta S} - \gamma_{\mathbf{w}_{FS}}^F \mathbf{w}_{FS} \\ &= n^F \text{grad } \Pi - \gamma_{\mathbf{w}_{F\beta S}}^F \mathbf{w}_{F\beta S} - \gamma_{\mathbf{w}_{FS}}^F \mathbf{w}_{FS} = \mathbf{0},\end{aligned}\tag{5.116}$$

where the calculation for divergence with scalar ϕ and a vectorial value \mathbf{v} is used with

$$\text{div } (\phi \mathbf{v}) = \mathbf{v} \cdot \text{grad } \phi + \phi \text{div } \mathbf{v}.\tag{5.117}$$

From Equation (5.116) the seepage velocity of the external substances can be calculated to:

$$\mathbf{w}_{F\beta S} = \frac{1}{\gamma_{\mathbf{w}_{F\beta S}}^F} [n^F \text{grad } \Pi - \gamma_{\mathbf{w}_{FS}}^F \mathbf{w}_{FS}].\tag{5.118}$$

Equation (5.118) highlights the two different components that influence the motion of the external concentrations. On the one hand, the advective part, which describes the velocity of the particles caused by the velocity of the fluid and is driven by the seepage velocity of the blood \mathbf{w}_{FS} . The diffusive motion resulting from the concentration gradient is driven by the osmotic pressure Π . For this diffusive part of the external components a Fick approach for $\gamma_{\mathbf{w}_{F\beta S}}^F$ is adopted, which includes the diffusivity

parameter D_{Fick} :

$$\gamma_{\mathbf{w}_{F\beta S}}^F = -\frac{R\theta}{D_{\text{Fick}} M_{\text{mol}}^\beta}. \quad (5.119)$$

In a next step the advective part can be evaluated by applying the restrictions from the entropy inequality to the balance of momentum for the fluid (5.89) analogously to the evaluation of the seepage velocity for external components. We use the Cauchy stress for the fluid (5.114₍₂₎) as well as the momentum production (5.115₍₂₎):

$$\begin{aligned} \operatorname{div} \mathbf{T}^F + \hat{\mathbf{p}}^F &= \operatorname{div} (-n^F p^R \mathbf{I}) + \operatorname{grad} n^F \lambda + \Pi \operatorname{grad} n^F + \gamma_{\mathbf{w}_{F\beta S}}^F \mathbf{w}_{F\beta S} - \gamma_{\mathbf{w}_{FS}}^F \mathbf{w}_{FS} \\ &= -p^R \operatorname{grad} n^F - n^F \operatorname{grad} p^R + \operatorname{grad} n^F \lambda + \Pi \operatorname{grad} n^F + \gamma_{\mathbf{w}_{F\beta S}}^F \mathbf{w}_{F\beta S} \\ &\quad - \gamma_{\mathbf{w}_{FS}}^F \mathbf{w}_{FS} \\ &= -n^F \operatorname{grad} p^R + \gamma_{\mathbf{w}_{F\beta S}}^F \mathbf{w}_{F\beta S} - \gamma_{\mathbf{w}_{FS}}^F \mathbf{w}_{FS} = \mathbf{0}. \end{aligned} \quad (5.120)$$

By substituting the previously determined equation of the seepage velocity of the external concentrations $\mathbf{w}_{F\beta S}$ in (5.118) as well as the deviation of the total pressure into the hydraulic and osmotic pressure in (5.113), we obtain the simplified expression:

$$\begin{aligned} &-n^F \operatorname{grad} p^{\text{FR}} - n^F \operatorname{grad} \Pi + \gamma_{\mathbf{w}_{F\beta S}}^F \frac{1}{\gamma_{\mathbf{w}_{F\beta S}}^F} [n^F \operatorname{grad} \Pi - \gamma_{\mathbf{w}_{FS}}^F \mathbf{w}_{FS}] - \gamma_{\mathbf{w}_{FS}}^F \mathbf{w}_{FS} \\ &= -n^F \operatorname{grad} p^{\text{FR}} - 2\gamma_{\mathbf{w}_{FS}}^F \mathbf{w}_{FS}. \end{aligned} \quad (5.121)$$

The seepage velocity of the fluid follows with

$$n^F \mathbf{w}_{FS} = \mathbf{K}_F [-\operatorname{grad} \lambda]. \quad (5.122)$$

Note that the constitutive relation for the advective part derived in (5.122) is based on a Darcy approach. This results in a proportional dependence of the seepage velocity \mathbf{w}_{FS} to the hydraulic pressure p^{FR} .

Benchmark Concentrations

To visualize the influence of the diffusive and advective components of the solute seepage velocity, the inflowing concentrations are varied and the resulting effects are illustrated using a simplified benchmark problem, which is shown in Figure 5.5. Here,

we apply a feeding curve dependent on nutrition for the inflow concentration of FFA c^{FFFA} .

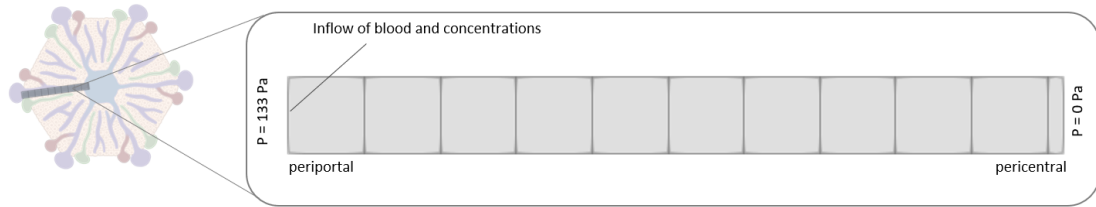


Figure 5.5: Benchmark of a rectangle representing a sinusoid from periportal to pericentral zone. A pressure of 133 Pa is applied on the left side, while the pressure on the right side is set to 0 Pa. A nutrient inflow is applied on the left side, while the nutrient concentration follow a predefined feeding curve.

To illustrate the influence of diffusion on the concentration distribution within the domain, we vary the Fick's coefficient $D_{\text{Fick}} = 0.5 \cdot 10^{-9}$ and plot the spatial as well as temporal distribution of FFA c^{FFFA} in Figure 5.6.

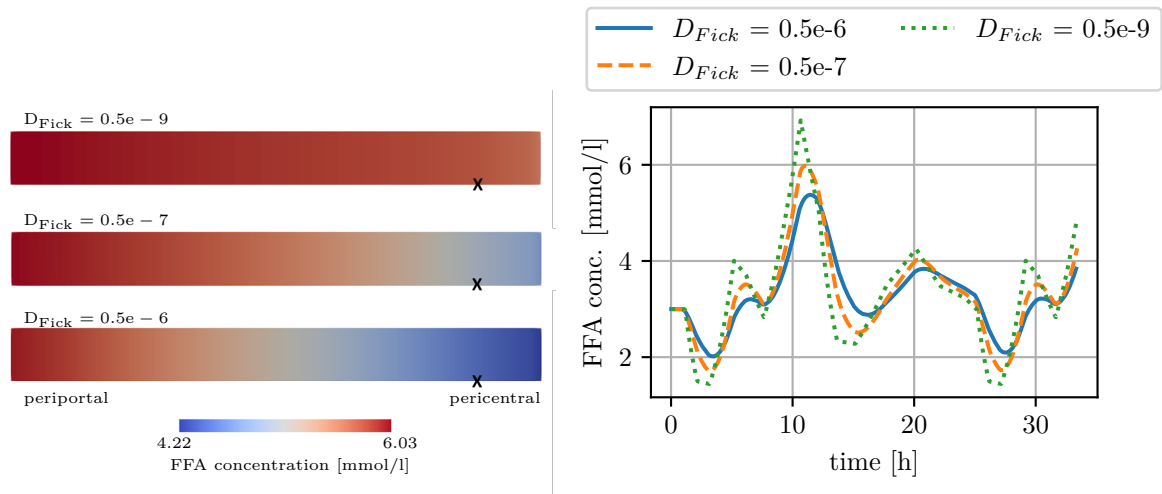


Figure 5.6: Left hand side: Spatial distribution of FFA concentration c^{FFFA} for different Fick's parameters D_{Fick} after 10h, right hand side: Temporal distribution of FFA concentration c^{FFFA} evaluated at the marked points in the domain for each simulation. The changes in concentration result from the initially applied feeding curve.

The changed diffusion coefficients have an influence on the concentration of nutrients. While the temporal course remains relatively identical, there are deviations in

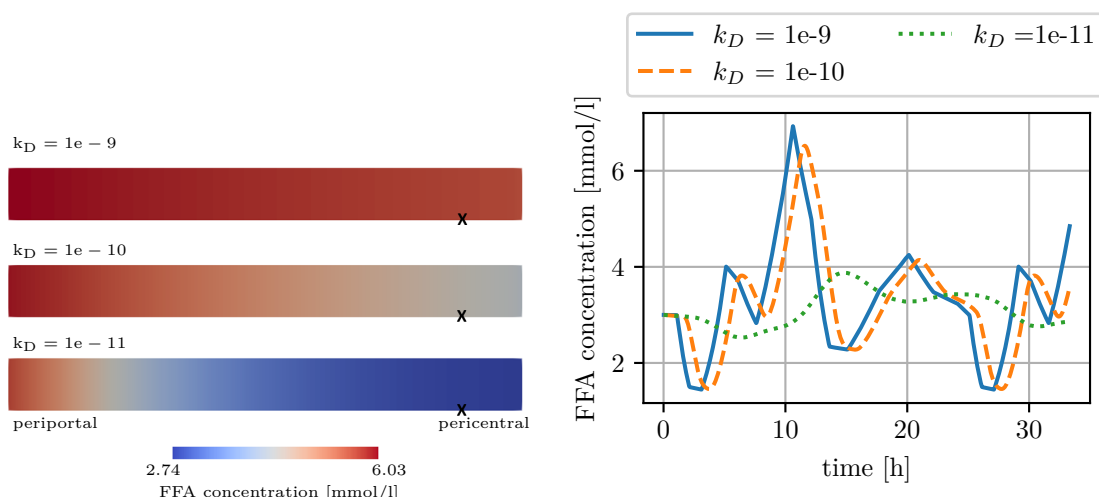


Figure 5.7: Left hand side: Spatial distribution of glucose concentration c^{FGl} for different Darcy parameters k_D after 10h, right hand side: Temporal distribution of glucose c^{FGl} and FFA concentration c^{FFFA} evaluated at the marked points in the domain for each simulation. The changes in concentration result from the initially applied feeding curve.

the concentration values. The changed diffusion properties of the blood hinder the transport of the nutrients and the amplitude of the feeding curve is lower, so that the maximum and minimum values of the nutrient concentrations are also reduced.

In addition to diffusion, advective processes are largely responsible for the transport and distribution of nutrients. These processes are influenced by permeability. Figure 5.7 shows the spatial and temporal distribution of FFA concentration c^{FFFA} considering different permeability coefficients k_D . A distortion of the concentration curves becomes apparent; the lower the coefficient, the worse the solutes are transported through the sinusoid by advection. On the one hand, this leads to a shift in the curves over time and to the maximum concentration being reached later. On the other hand, the range of concentration values is reduced and the characteristic feeding curve is clearly flattened, which shows a less favorable distribution and a slower transport of the nutrients. When considering the solute flux, it is therefore possible to distinguish between an advective and a diffusive part of the solute flux by calculating the Peclet number or the capillary number. The latter is a dimensionless number, that represents the relation between viscosity forces and forces due to surface or interfacial tension [128]. To investigate which of the two types is dominant in the

present example, the Peclet number P_e can be calculated with

$$P_e = \frac{\mathbf{v} \cdot \mathbf{l}}{n^F \cdot D}, \quad (5.123)$$

where \mathbf{v} describes the velocity of the fluid, l is the characteristic length of the problem and D describes the diffusion coefficient [71]. The calculation of the Peclet number for the described problem results in $P_e = 20 \gg 1$, which indicates a clearly advection dominated problem, that results from the pressure gradient in one lobule and a constant flow of the blood through the sinusoids. For this reason, a purely advective flow is assumed in the simulations.

5.6.8 Growth and Remodeling

During the development of various diseases and processes in the liver, growth and remodeling processes occur. Growth refers to processes that lead to an increase in the observed volume, while remodeling refers to a restructuring of the microstructure. For both processes, existing mechanical approaches are adapted and integrated into the model.

Sinusoidal Remodeling

When considering the microperfusion in the liver lobules, the permeability of the tissue is of particular importance. This is not isotropically distributed over the area of the lobules, but forms an anisotropic pattern. The proportionality factor \mathbf{K}_F in the advective part of the seepage velocity describes the anisotropic permeability of the liver tissue and can be described by different approaches. At first we apply an ansatz based on PIERCE et al. [109] with the permeability tensor \mathbf{K}_F dependent on a positive definite material parameter tensor \mathbf{M}^* :

$$\mathbf{K}_F = k_D \left(\frac{n^F}{1 - n_{0S}^S} \right)^{m_D} \mathbf{M}^*, \quad \text{with } \mathbf{M}^* = \alpha \mathbf{I} + \frac{(1 - 3\alpha)}{I_4} \mathbf{M}. \quad (5.124)$$

Due to the directional blood flow and the arrangement of sinusoids in the liver tissue, an anisotropic permeability is present and the seepage velocity of the blood is dependent on the solid structure as well as on its deformation. The permeability of

solid liver tissue is described with the permeability parameter k_D and m_D depicts the factor for the permeability deformation dependency. The dependency on deformation is included by adding the fluid volume fraction n^F as well as the initial solid volume fraction n_{0S}^S . The relation of the both volume fractions included describes the change of the pore space by deformation and thus changes the permeability of the tissue. Blood flow velocity is also affected by the development of fat vacuoles in liver tissue. This is ensured by the coupled multiscale and multiphase model, that ensures a direct relationship between hepatic function and perfusion.

Alternatively, the permeability of liver tissue can be assumed using literature values. DEBBAUT et al. [46] presented permeability values for liver tissue using flow simulation on liver lobules developed on experimental micro-CT data.

Liver tissue has anisotropic permeability due to its structure and directional blood flow. Within the hepatic lobules, blood flow is directed from the PFs to the CV by a pressure gradient, resulting in anisotropic microperfusion. To describe the anisotropic properties of the liver tissue, an approach for sinusoidal remodeling of RICKEN et al. [119] is adopted. Here, the structural tensor \mathbf{M} used to calculate the permeability tensor in Equation (5.124) depends on the preferred direction of blood flow. The distinguished flow direction is determined by minimizing the flow dissipation and finding the optimal state with less resistance to hepatic flow. This leads to a reorientation of the sinusoids in the direction of the normalized blood pressure gradient with

$$\mathbf{p}_0 = \frac{|\text{Grad } \lambda|}{|\text{Grad } \lambda|} \text{ with } |\mathbf{p}_0| = 1. \quad (5.125)$$

The structural tensor \mathbf{M} is then calculated using the preferred flow direction with $\mathbf{M} = \mathbf{a} \otimes \mathbf{a}$ with the preferred flow direction \mathbf{a} [119]. This leads to an adjustment of the permeability in case of changed pressure conditions within the liver parenchyma.

Figure 5.8 demonstrates the effects of anisotropic permeability under different boundary conditions.

Shown is an exemplary geometry of a simplified, angled blood vessel, through which the blood flows from the upper left to the upper right. The pressure and flow distribution within the geometry is considered. In the horizontal direction, four different time steps are examined over which the pressure and the flow are formed. In vertical direction a change of the anisotropy parameter α occurs, which indicates

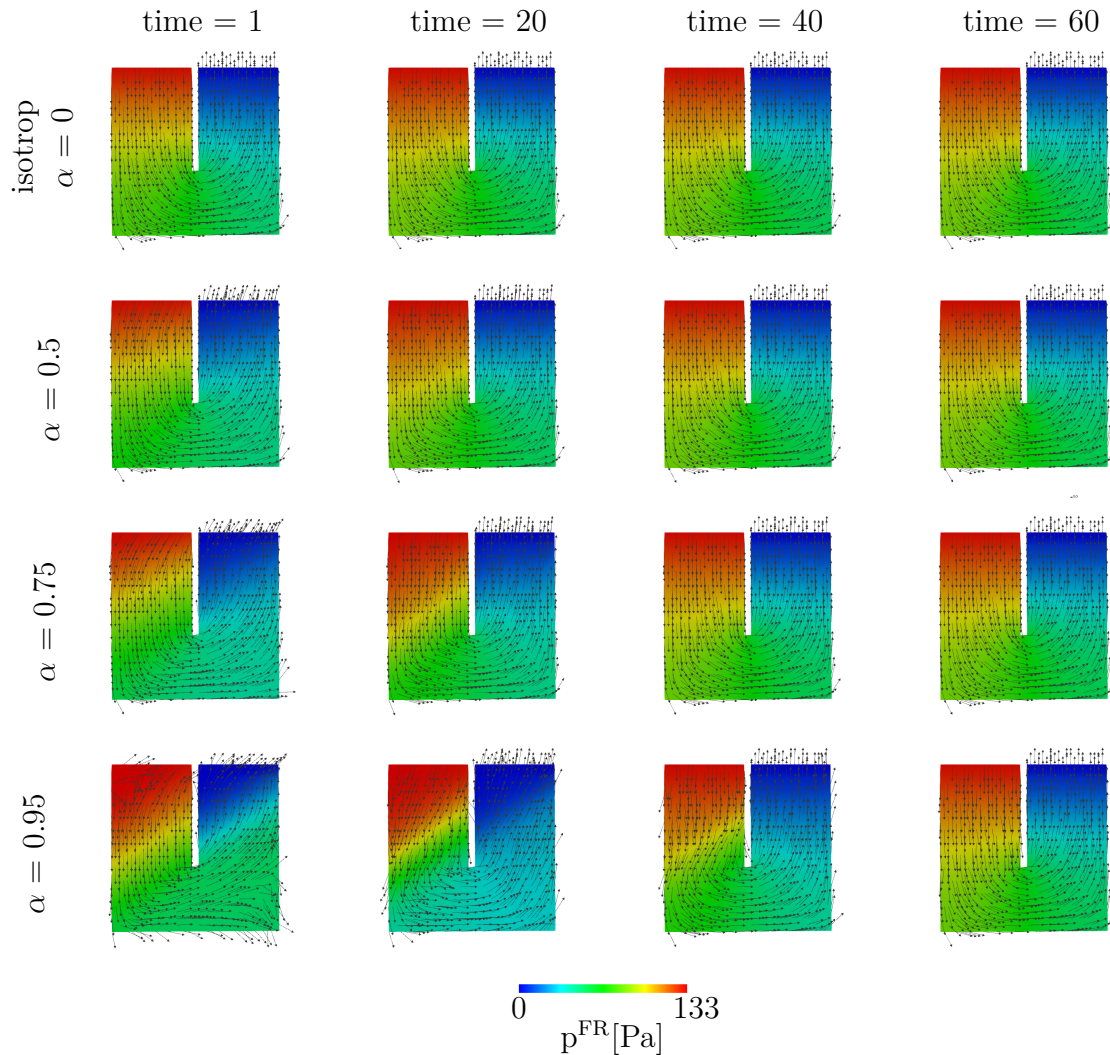


Figure 5.8: Evaluation of seepage velocity and spatial pressure distribution for different time steps and different anisotropic factors α .

the measure of the anisotropy, a high parameter corresponds thereby to a large influence of the anisotropy as indicated in Equation (5.124). It becomes clear that the flux distribution adapts over time to the preferred flow direction depending on the pressure distribution. Furthermore, the flow distribution changes significantly when the anisotropy parameter is increased. With a more anisotropic behavior, the pressure and thus the flow form more clearly in the given direction. The approach of a pressure dependent anisotropic permeability enables a sinusoidal remodeling with respect to the spatial pressure distribution in the lobular scale.

Mechanical Growth Approach

Growth processes in biological tissue can be described using numerous approaches and theoretical models. Basically, biological growth in porous tissue is divided into two types, interstitial growth and volumetric growth. If new material grows within the porous body only in its pores, it is defined as interstitial growth. In this case, there is no volumetric change in shape, only the density is increased by adding new material. This leads to a variation of stiffness in each growth generation, cf. ATESHIAN et al. [9] or CYRON et al. [40]. If, in contrast, the density is retained in the case of growth of new material, this results in an increase in the volume of the considered body. The resulting volume dilation can be represented by a multiplicative split of the deformation gradient, which takes into account the growth as well as the elastic part of the deformation, cf. RODRIGUEZ et al. [122].

During NAFLD fat vacuoles are stored in liver cells. In addition, ballooning of the liver cells is observed, in which the hepatocytes expand in shape. These two growth processes lead to an increase in the total liver volume. During the development of HCC, growth processes also occur within the hepatic tissue. However, the entire liver is not affected by a change in volume, but only the local area of the tumor tissue. The solid phase of the tissue therefore only experiences dilatation due to mechanical deformation of the tumor. The development of the tumor depends on various influential factors, such as the supply of nutrients or growth parameters. An increase of the tumor phase is described by mass exchange, which directly depends on the concentration of nutrients. A detailed description of these processes and their specification on the cell scale can be found in Section 6.1.2. In order to depict the development of fat and tumor tissue and the concomitant growth of the solid phase, an approach by WERNER [160] is adapted for combined growth of fat and tumor tissue. In the developed approach, the solid phase φ^S is only capable of growing by mechanical deformation or accumulation and thus growth of the fat phase φ^T and the tumor phase φ^C . The multiplicative split of the deformation gradient \mathbf{F}_S is used to describe these growth processes, which allows the elastic growth part \mathbf{F}_{Se} to be calculated using a constitutive approach to the growth part \mathbf{F}_{Sg} :

$$\mathbf{F}_S = \mathbf{F}_{Se} \mathbf{F}_{Sg}; \quad \mathbf{F}_{Sg} = (J_{Sg})^{1/3} \mathbf{I}; \quad \mathbf{F}_{Se} = \mathbf{F}_S \mathbf{F}_{Sg}^{-1}. \quad (5.126)$$

The basis for the general description of mechanical growth of a solid in the TPM is the balance equation of mass given by

$$(\mathbf{n}^\alpha \rho^{\alpha R})'_S + \rho \operatorname{div} \mathbf{x}'_S = \hat{\rho}^\alpha. \quad (5.127)$$

The evaluation of the material time derivation of the Jacobian yields

$$(\mathbf{J}_S)'_S = \frac{\partial \mathbf{J}_S}{\partial \mathbf{F}_S} \cdot \frac{\partial \mathbf{F}_S}{\partial t} = \frac{\partial \det \mathbf{F}_S}{\partial \mathbf{F}_S} \cdot (\mathbf{F}_S)'_S, \quad (5.128)$$

with

$$\frac{\partial \det \mathbf{F}_S}{\partial \mathbf{F}_S} = \mathbf{J}_S \mathbf{F}_S^{\mathbf{T}-1} \quad \text{and} \quad \mathbf{L}_S = (\mathbf{F}_S)'_S \mathbf{F}_S^{-1}, \quad (5.129)$$

we get

$$\begin{aligned} (\mathbf{J}_S)'_S &= \mathbf{J}_S \mathbf{F}_S^{\mathbf{T}-1} \cdot \mathbf{L}_S \mathbf{F}_S = \mathbf{J}_S \mathbf{F}^{\mathbf{T}} \mathbf{F}_S^{\mathbf{T}-1} \cdot \mathbf{L}_S \\ &= \mathbf{J}_S \operatorname{grad} \mathbf{x}'_S \cdot \mathbf{I} = \mathbf{J}_S \operatorname{div} \mathbf{x}'_S \end{aligned} \quad (5.130)$$

It follows that

$$\operatorname{div} \mathbf{x}'_S = \frac{1}{\mathbf{J}_S} (\mathbf{J}_S)'_S, \quad (5.131)$$

which results in the balance of mass

$$(\mathbf{n}^\alpha \rho^{\alpha R})'_S + \rho \frac{1}{\mathbf{J}_S} (\mathbf{J}_S)'_S = \hat{\rho}^\alpha. \quad (5.132)$$

The first part of the equation shows the influence of the changing partial density, while the second part represents the volumetric part.

Growth due to changed partial density

One factor that is influencing tissue growth is a change in partial density. To investigate this behavior, the first part of (5.132)

$$(\mathbf{n}^\alpha \rho^{\alpha R})'_S = \hat{\rho}^\alpha, \quad (5.133)$$

which includes the partial density $\rho^\alpha = \mathbf{n}^\alpha \rho^{\alpha R}$ is evaluated. Together with the restriction that the sum of the mass exchanges has to be zero in Equation (5.34) and so a change of mass from one phase to another, this leads to changes in volume fraction of the respective phases. By considering the relation of volume and mass in

Equation (5.7) and the general relation for the density $\rho = \frac{m}{V}$, Equation (5.132) can also lead to a change of volume through deformation of solid tissue. As long as the real density of the two substances of the mass transfer is identical, there is no change of the volume but only a change of the respective volume fraction, so a change of the microstructure and thus remodeling occurs. However, if the two substances are of different real densities, there is a change in the volume, while the mass remains the same, i.e. a component with a lower density grows with an increase in mass, while it would shrink with a density higher than that of the corresponding component. This relation also occurs by mass exchange between a solid phase and nutrients, see RICKEN et al. [117].

Growth due to volumetric split of deformation gradient

The volumetric split introduces a growth and an elastic part of the deformation gradient and therefore the Jacobian. The Jacobian growth part J_{Sg} can be calculated by evaluating the balance of mass for the solid phases for fat φ^T and tumor φ^C both capable of growing and depleting.

$$(\rho^T)'_T + \rho^T \frac{(J_T)'_T}{J_T} = \hat{\rho}^T, \quad (\rho^C)'_C + \rho^C \frac{(J_C)'_C}{J_C} = \hat{\rho}^C, \quad (5.134)$$

Evaluating the balance of mass for a mixture description results in a description for the Jacobian J^T of the fat-tissue and J^C for tumor tissue

$$\frac{\rho_{0S}^T}{\rho^T} \exp\left(\int \frac{\hat{\rho}^T}{\rho^T} dt\right) = J^T, \quad \frac{\rho_{0S}^C}{\rho^C} \exp\left(\int \frac{\hat{\rho}^C}{\rho^C} dt\right) = J^C. \quad (5.135)$$

With Equation (5.135), the division of the deformation into an elastic J_e^T/J_e^C and growth J_g^T/J_g^C part leads to

$$\begin{aligned} J^T &= J_e^T J_g^T, & J_e^T &= \frac{\rho_{0S}^T}{\rho^T}, & J_g^T &= \exp\left(\int \frac{\hat{\rho}^T}{\rho^T} dt\right). \\ J^C &= J_e^C J_g^C, & J_e^C &= \frac{\rho_{0S}^C}{\rho^C}, & J_g^C &= \exp\left(\int \frac{\hat{\rho}^C}{\rho^C} dt\right). \end{aligned} \quad (5.136)$$

where dt denotes the time increment of the simulation and $\hat{\rho}^T$ and $\hat{\rho}^C$ characterizes the mass supply of fat and tumor, that correlates with the supply of fat volume fraction

term as $\hat{\rho}^T = \hat{n}^T \rho^{TR}$ for fat and $\hat{\rho}^C = \hat{n}^C \rho^{CR}$ for tumor tissue.

Benchmark Growth

To examine and evaluate the differences between the two growth approaches in more detail, they are investigated using a simple benchmark.

For this purpose, a square geometry is simulated with a pressure boundary condition at the bottom, as well as an outflow at the top. A mass transfer between the fat and the solid is assumed, with the fat phase growing. The two approaches differ significantly in their description of growth kinematics. In Figure 5.9 (Plot 1), the split of the deformation gradient \mathbf{F}_S due to the increase of the growth fraction J_{Sg} becomes clear, it remains constant at 1 without the split and thus not cause any additional volume change. The split of the deformation gradient leads to a changed kinematic since it directly influences the deformation gradient. This results in changed stresses and strains, since these are dependent on the elastic part of the deformation gradient. Also an increased growth of the geometry and therefore of the pore volume follows from the changed kinematics. Due to the coupled system of multiple fields, a change in the kinematics and therein in stresses and strains also directly influences the other field variables. The formation of the fat volume fraction n^T also varies, since this depends on the geometry and the pore size, which is changed by the growth (Plot 2). Due to the increased amount of embedded fat, the flow velocity \mathbf{w}_{FS} is also negatively affected, as visible in Figure 5.9 (Plot 3). The different expression of the growth is also evident in the displacements both over time (Plot 4) and in Figure 5.9 (Bottom) during the spatial evaluation of n^T , where a clear increase in geometry can be observed when the split of the deformation gradient \mathbf{F}_S is applied. A detailed evaluation of the different forms of growth is conducted in section 7.3.3.

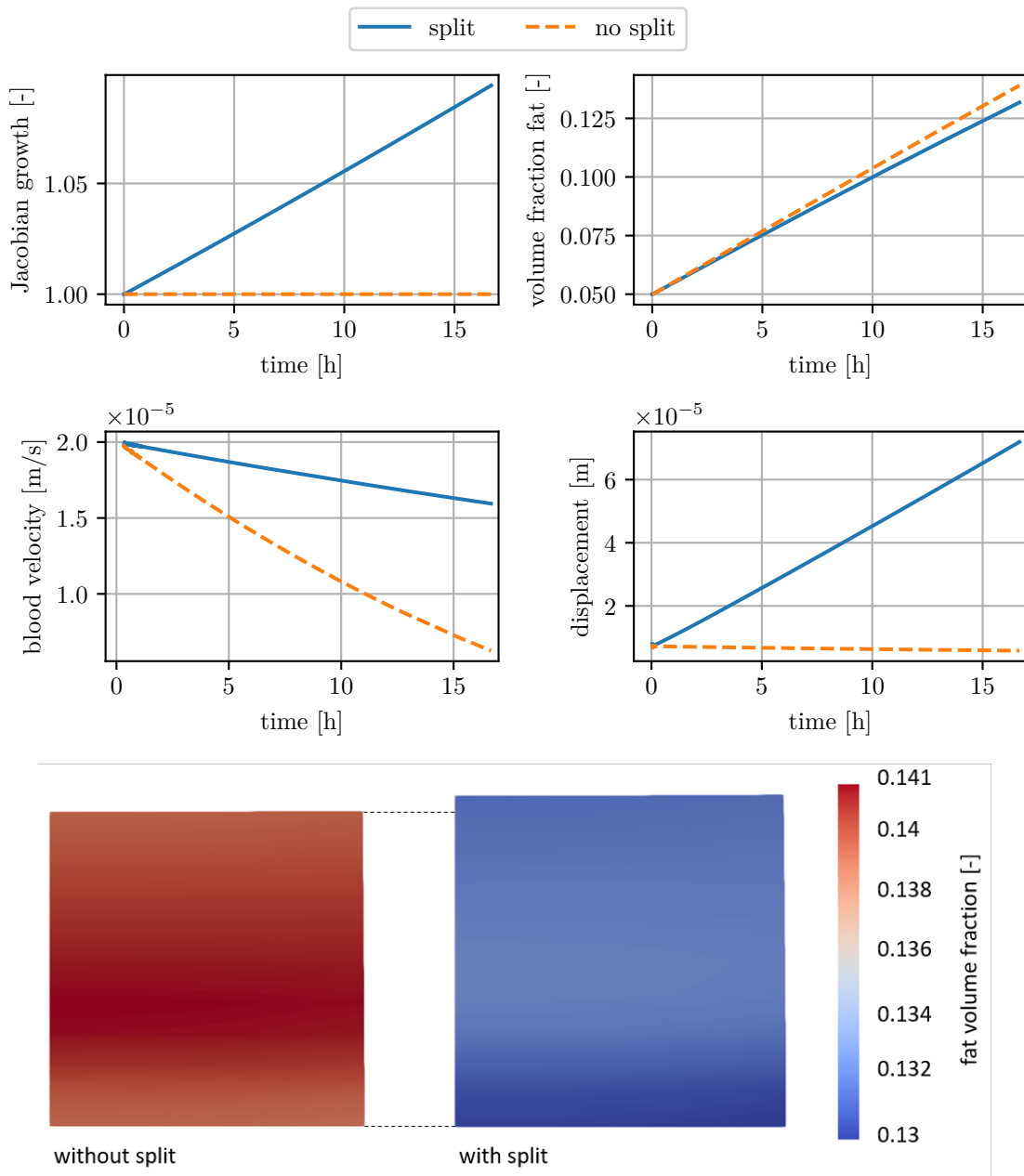


Figure 5.9: Benchmark for the evaluation of different growth approaches. Top: Progression of Jacobian growth J_{Sg} , fat volume fraction n^T , blood velocity \mathbf{w}_{FS} and magnitude of displacement \mathbf{u}_{mag} over time with and without split of deformation gradient \mathbf{F}_S . Bottom: Spatial distribution of fat volume fraction n^T without (left) and with (right) split of deformation gradient \mathbf{F}_S .

5.6.9 Necrosis resulting from Paracetamol Overdose

Analogous to deriving the liver model for calculating the accumulation of fat vacuoles and tumor growth, a model for simulating detoxification of paracetamol and necrosis was developed on the basis of eTPM [86, 85]. The basic procedure for the evaluation of the basic equations and the thermodynamically consistent evaluation of the entropy inequality corresponds to the procedure shown in the previous sections. The de-

veloped model describes the transport of an ingested dose of paracetamol as a solute within the fluid blood phase. Within the hepatocytes, the degradation of paracetamol and resulting necrosis is simulated on the microscale dependent on the internal glutathione concentration stored in the liver tissue and coupled to the perfusion scale. The necrosis of the liver tissue that as a consequence of a paracetamol overdose is described as an additional solid phase of the whole aggregate. This results in a 4-phase model with a solid phase of liver tissue (S) as well as fat tissue (T) and necrotic tissue (N). The blood is represented as a fluid phase with the solved microscopic substances FFAs, oxygen as well as paracetamol (Para) are dissolved while the glutathiones (Gt) are stored in the solid phase. The composition of the total aggregate for the simulation of necrosis is shown in Figure 5.10.

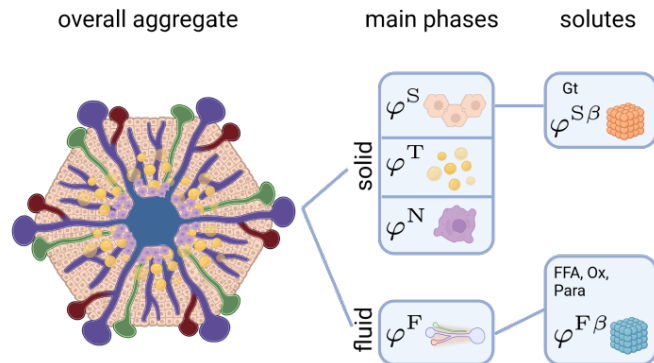


Figure 5.10: Overview of the composition of the total aggregate for the simulation of fat accumulation and necrosis in the liver.

6 Multiscale Modelling

To evaluate liver-specific processes using numerical simulation, consideration of different size scales is required by using a multiscale approach. The relevant scales range from the whole body scale to the hepatocytes, the liver cells, as shown in Figure 6.1. The whole body scale describes the interaction of the liver with the whole body through the systemic circulation. Macroscopic perfusion at the organ scale describes the hepatic vascular system through which the liver is supplied with oxygen-rich blood from the HA and nutrient-rich blood from the PV. The whole organ consists of smaller functional units called hepatic lobules with anisotropic microcirculation. The underlying cell scale describes the metabolic processes, mechanotransduction and signaling within the hepatocytes.

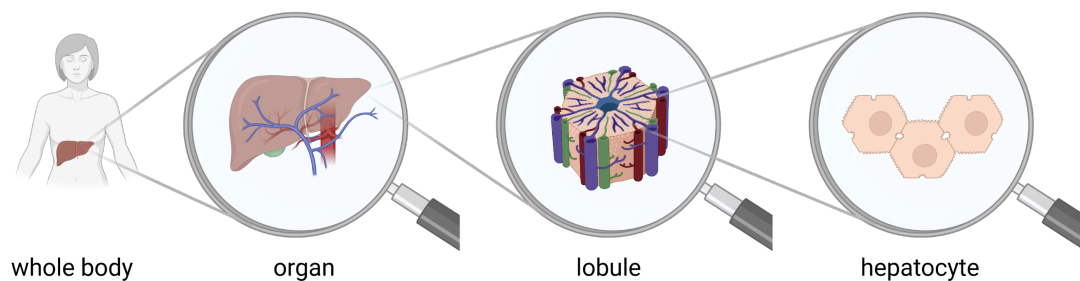


Figure 6.1: Overview of different size scales of the human liver. i) whole body scale with processes in the organism and other organs, ii) total organ with macroscopic vascular system, iii) liver lobule as functional unit of the liver with a porous structure and anisotropic perfusion, iv) hepatocytes, where metabolic processes take place.

To represent and investigate the interaction of the individual scales, the hepatic function-perfusion processes are calculated using a multiscale approach. The main focus is on the lobular scale, which is described with the help of the multiphase

approach introduced in Section 5. In order to consider the influences of macroperfusion as well as metabolism on microperfusion and tissue deformation, the processes of the total organ as well as the metabolic processes in the liver cells are integrated.

6.1 Metabolic Processes on Cell Scale

The function of the liver is significantly influenced by the metabolic processes taking place in the liver cells. This metabolism can be harmed by diseases as well as changes in liver lobule parameter, such as blood flow velocity or morphology. In this work, lipid metabolism, tumor tissue formation and detoxification of paracetamol are considered as exemplary liver-specific processes. With the help of ODEs as well as phenomenological considerations, the underlying processes are integrated in a simplified way on the cellular scale and coupled with the overlaying tissue level.

6.1.1 Lipid Metabolism

During NAFLD, the FFAs absorbed from nutrition cannot be adequately metabolized and are stored in the liver cells in the form of fatty vacuoles consisting of triglycerides (TGs). This accumulation is inhomogeneously distributed over the domain of the liver lobule and mostly occurs with a zonation in periportal or pericentral regions, cf. Figure 2.2. In order to integrate these processes into the introduced multiphasic perfusion model at the lobule level, a mathematical model by SCHLEICHER et al. [131] for the description of lipid metabolism is applied and adapted. This model represents the fatty acid metabolism and the resulting influence on blood flow by a set of ODEs. This is embedded in the multiphasic lobule perfusion model to gain a perfusion-dependent, spatial distribution of fat accumulation and nutrient deposition in the lobule. The equations are solved in each Gauss point during the calculation and are dependent on the actual concentrations of the microscopic substances ($c^{\alpha\beta}$) and actual volume fractions (n^α), that are transferred from the lobular scale. The mathematical model considers the uptake of FFA and oxygen to the hepatocytes, oxidative procedures, synthesis and secretion of triglyceride as shown in Figure 6.2.

The following reactions characterize the main solutes FFA and oxygen in the mathematical model:

$$\begin{aligned} c_{\text{FFA}}^{\text{int}} &= (v_{\text{FFA}}^{\text{up}}; v^{\text{syn}}; v^{\text{oxy}}) \\ c_{\text{Ox}}^{\text{int}} &= (v_{\text{Ox}}^{\text{up}}; v^{\text{oxy}}; v^{\text{deg}}), \end{aligned} \quad (6.1)$$

with $c_{\text{FFA}}^{\text{int}}$ and $c_{\text{Ox}}^{\text{int}}$ being the cellular concentrations of the respective solutes in the liver cells. The uptake processes contained therein are described with the help of Michaelis Menten kinetics [141] using the maximum rate v_{max} as well as the Michaelis Menten constant K_M . Furthermore, the intercellular concentration of FFA is dependent on the synthesis of TG, since FFAs are esterified to TG. The oxidation process v^{oxy} describes the mitochondrial FFA oxidation with consumption of FFAs as well as oxygen.

The degradation of oxygen v^{deg} describes not only the FFA oxidation happening during NAFLD, but also degradation through other oxidative processes like glucose metabolism.

To characterize the esterification of FFAs to TGs during NAFLD the underlying hepatic lipid dynamic process ($\hat{\rho}^T$) is represented by the synthesis rate v^{syn} and the export rate v^{exp} :

$$\hat{\rho}^T = (v^{\text{syn}}; v^{\text{exp}}). \quad (6.2)$$

In order to represent a supply of the liver lobules with the substances, their plasma concentration is applied by inflow boundary conditions (BCs). Due to the dependencies of the microscale, this results in a concentration gradient on the lobule scale. Since oxidative processes play a crucial role in the formation of fat vacuoles, fat accumulation may be enhanced in areas with low oxygen saturation. Thus, due to the inhomogeneous distribution of oxygen within the liver lobule, a zoned distribution of fat is obtained. The concentration gradients are caused and influenced by the advection and diffusion processes on the lobule scale.

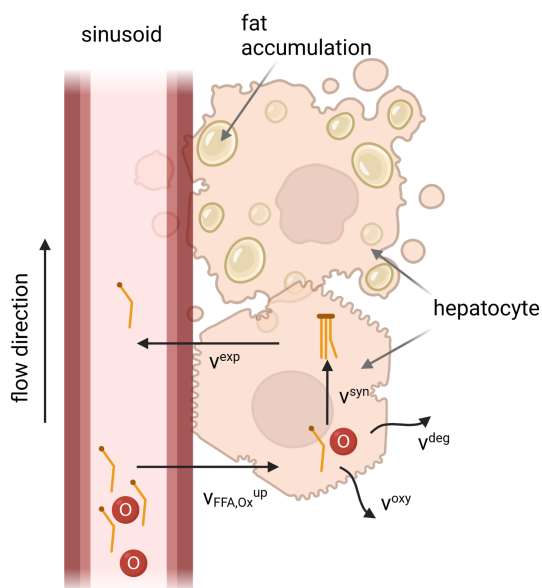


Figure 6.2: Overview of processes during hepatic fat metabolism according to [131].

6.1.2 Tumor Development

NAFLD, if left untreated, can further develop into cirrhosis and even HCC as shown in Figure 2.5. For this reason, an approach to describe function in terms of tumor growth in the liver is also implemented at the cellular level as shown in Figure 6.3.

Since many models have already been developed that focus exclusively on the cellular processes of tumor development, see Section 3.1, only a simplified model of tumor development is applied. This is sufficient since the focus of the presented model is on the connection of perfusion and function and the exact metabolic processes are not described in its full complexity. The development of the tumor depends on various factors, see Section 2.2.2. A significant factor is the supply of nutrients to the tumor. The Monod kinetics is applied to describe the development of a tumor in the liver, in which glucose as a nutrient is the limiting factor according to KATSUDA et al. [75]. The inclusion of the temporal change of tumor formation is realized in the mass balance of the mixture as well as the mass balance of the tumor tissue by the mass exchange term $\hat{\rho}^C$. This results in

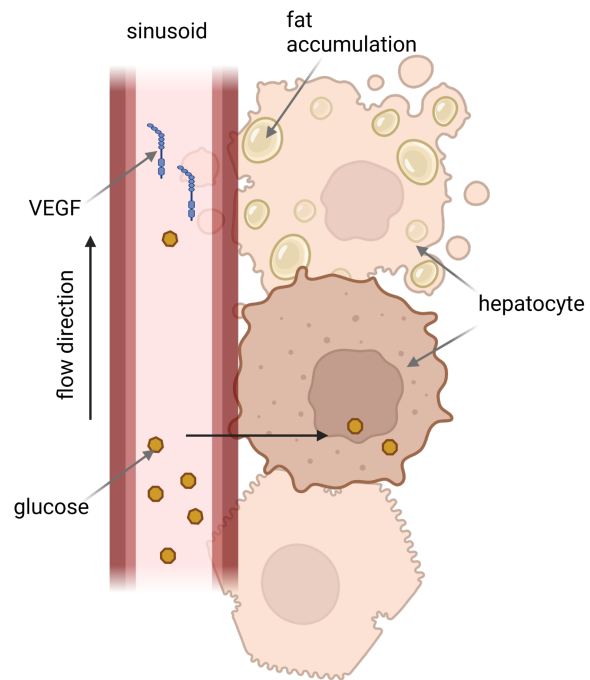


Figure 6.3: Overview of processes during tumor development.

$$\hat{\rho}^C = \mu_{\max} \frac{c^{\text{FGI}}}{K_S + c^{\text{FGI}}}, \quad (6.3)$$

with the maximal specific growth rate μ_{\max} , the current concentration of limiting substance glucose c^{FGI} and the Monod constant K_S . During tumor development, glucose is consumed leading to a reduction in glucose concentration. Based on an approach by KATSUDA et al. [75] the mass supply term for glucose concentration is

described with

$$\hat{\rho}^{\text{Gl}} = \frac{C_x n^S \hat{\rho}_{\text{max}}^C}{Y_{X/S}} \frac{c^{\text{FGI}}}{K_S + c^{\text{FGI}}} \quad \text{and} \quad \frac{1}{Y_{X/S}} = \frac{1}{Y_G} + \frac{m}{\hat{\rho}^C}, \quad (6.4)$$

where C_x describes the concentration in the tissue and Y_G and m represent the growth yield constant and a maintenance coefficient. The development of the hepatic tumor at the cellular level can occur both as an initial tumor and after a certain time. In addition, a coupling with the existing fat volume fraction n^T is implemented. Areas with a high proportion of fatty tissue are more prone to pathological changes in liver cells and thus to the development of a tumor. Since not every cell undergoes morbid changes and a certain probability distribution is present in this case, a simplified random algorithm is implemented. As soon as a cell is potentially at risk of progressing into a tumor cell, e.g. due to a high fat content or after a predefined exceeded time, a random value is calculated. If this value falls below a defined threshold, the metabolism of the tumor is activated.

6.1.3 Detoxification

To extend the numerical model to include the degradation of paracetamol and a resulting necrosis, the concentrations of paracetamol and glutathiones are included in the model to simulate the processes described in Section 6.1.3. The glutathione is included as an internal concentration, since it is an endogenous substance, whereas paracetamol is transported through the liver as an external concentration via the blood flow.

Here, the glutathione concentration c^{SGt} is directly dependent on the concentration of paracetamol. The external concentration of paracetamol c^{FPara} enters the liver via the bloodstream and is metabolized in the liver cells, see Figure 6.4. From the equation of the current paracetamol concentration obtained due to the pharmacokinetic, the rate for determining the change in concentration at each time step can be calculated based on an adaption of a model from GEENEN et al. [58]. However, since only the degradation of paracetamol is considered in the model and adsorption into the blood is neglected, the equation simplifies. In each blood cycle, only a portion of the paracetamol is metabolized, the remaining concentration leaves the liver unchanged and re-enters the bloodstream. To implement this numerically, the paracetamol concentration at the outflow of the CV at the current time point is determined and in the following time step applied as boundary condition for the initial concentration at the periportal field. To compensate for the differences from diffusion within the hepatic lobule and to obtain a realistic degradation, the rate is additionally multiplied by a degradation factor.

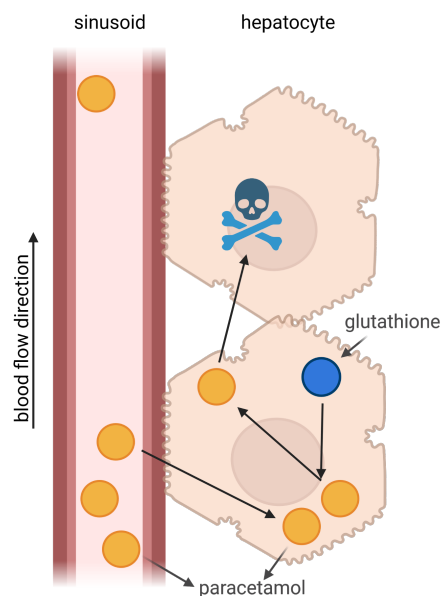


Figure 6.4: Overview of processes during paracetamol degeneration.

6.2 Macroscopic Perfusion on Organ Scale

To describe macroscopic perfusion on the organ scale, the hepatic vascular structure is also integrated into the model. Here, the liver is supplied with blood by the HA and the PV, as described in Section 2.1.2. The flow in the vascular tree at the organ level can be assumed to be longitudinal to the streamlines. This type of flow is described with the help of the Bernoulli equation according to DANIEL BERNOULLI (1700-1782), cf. [28]. This equation allows to calculate the total energy of the particles inside the flow, which remains constant inside a stream tube. The energy is composed of the parts of the potential, kinetic and pressure energy, which can change constantly within the flow, but must remain constant in total. The derivation can be done either via Newton's basic law or via the theorem of conservation of energies. More detailed information about the derivation of the Bernoulli equations for the calculation of flows along the streamlines can be found in BÖSWIRTH et al. [28]. The Bernoulli equation for the calculation of the total energy e_g results in

$$e_g = \frac{p - p_0}{\rho} + \frac{1}{2} v^2 + g h, \quad (6.5)$$

with the pressure p , density ρ , velocity v , gravity g and height h .

However, calculation of flow through the vascular tree of the liver requires further boundary conditions and assumptions. For example, the density ρ and height h are assumed to be constant along the length of a vessel and friction losses occur within the flow. These result from the wall friction p_w within a vessel and the branching friction p_b at the branching points of the vessels. Therefore, the BERNOULLI equation can be derived with

$$e_g = \frac{v_1^2}{2g} + \frac{p_1}{\rho g} = \frac{v_2^2}{2g} + \frac{p_2}{\rho g} + p_w + p_b \quad (6.6)$$

and the branching pressure loss p_b can be calculated with

$$p_b = \zeta \rho \frac{v^2}{2}, \quad (6.7)$$

where the resistance coefficient ζ is determined by the type of branching. For the straight Y-pipe branching type and a branching angle of 30° , it is $\zeta = 0.3$, if a curved

Y-pipe is assumed it results in $\zeta = 0.4$ [139].

This wall friction loss can be calculated using different approaches. The Darcy equation characterizes the pressure loss, the length l and the diameter d of the vessel, the Reynolds number R_e as well as a friction parameter λ and is given by

$$p_w = \lambda \frac{l}{d} \frac{v^2}{2} \rho \quad \text{with } \lambda = \frac{64}{R_e}. \quad (6.8)$$

Alternatively, the pressure loss can be derived from the flow resistance force F_w that is dependent on the experimentally obtained flow resistance parameter C_w and the blood viscosity ν [139]:

$$F_w = C_w A \frac{1}{2} \rho v^2 \quad \text{with } C_w = \frac{\ell v \rho}{\nu}. \quad (6.9)$$

To calculate a pressure from the flow resistance force F_w that acts approximately constant over the local cross-sectional area, the flow resistance force F_w is divided by the vessel area A . The local pressure loss over the local vessel length p_w is given by

$$p_w = \frac{\rho^2 v^3 \ell}{2\nu}. \quad (6.10)$$

The local energy at the end of the considered vessel is obtained by substituting the corresponding pressure losses and the local pressure into the previously derived Bernoulli energy equation. In both the PV and the HA, the energies over the number of vessels in the branched structure must be equal to the energy in the first vessel for the number of branches considered. Thus, by subtracting the energy from the pressure losses, the local energy at the end of the vessel h with the pressure in the local branch p is given with

$$h = \frac{\frac{v^2}{2g} + \frac{p}{\rho g}}{\#\text{branches}} \quad p = p_0 + \frac{(1 - (\frac{x}{2})^2) v^2 \rho}{2} - p_b - p_w. \quad (6.11)$$

Due to the branched structure, the blood pressure, blood velocity and blood flow change in each generation. These quantities are therefore calculated in each generation based on the values from the previous generations. For this purpose, the local areas, flow velocities and lengths of the vessels are important. Assuming a total number of lobules of one million, a division factor of $x = 1.85$ is chosen to calculate the

cross-sectional areas of the subsequent vessels. Assuming that one vessel branches into two further vessels, the flow velocity v_1 and the blood pressure p_1 for the subsequent vessel is given by

$$v_1 = \frac{x}{2} v_0 \quad p_1 = \frac{(1 - (\frac{x}{2})^2)}{2} v_0 \rho + p_0. \quad (6.12)$$

The organ scale approach is intended not only to calculate perfusion in healthy organs, but also to represent perfusion disturbances. These occur, for example, during PVL or (e)PHx. The clamped or removed vessels no longer deliver blood to the corresponding areas of the liver, so that the incoming blood must be distributed to fewer vessels. This leads to a direct change in macroscopic perfusion. Assuming that one vessel is impaired in flow, a vessel of the previous generation no longer branches into two vessels, but only into one. This thus absorbs the entire volume of blood. The increased volume flow results in a changed blood velocity and blood pressure of

$$v_1 = v_0 x \quad p_1 = \frac{(1 - x^2)}{2} v_0 \rho + p_0. \quad (6.13)$$

Furthermore, resection triggers a variety of other processes by which the liver compensates for altered blood flow, such as displacement of blood volume, increase in venous return, or activation of HABR [38]. Another important point to feature the flow and pressure conditions after resection is the dilation of the vessels to accommodate the increased blood flow. Here, the change in sinusoidal diameter depends, among other things, on the extent of the resection as shown in DAHMEN et al. [41]. This dilatation of the vessels and thus the change in diameter implies a change in the pressure conditions within the vascular tree. To account for this biological adaptation, a dilation factor is added to the calculation of the vessel area per generation starting from the disturbed generation and is adjusted for different percentages of dilatation of the vessel.

Experimental data from DEBBAUT [43] are used to describe the initial geometry of a hepatic vascular tree and specific the PV. These provide the radii, the length as well as the total number of vessels for 16 generations. In addition, a calculation of radii and vessel number using exponential functions is implemented. A comparison of both approaches is shown in Figure 6.5. Under the given assumptions, the pressure distribution as well as the blood velocity can be evaluated over the different generations.

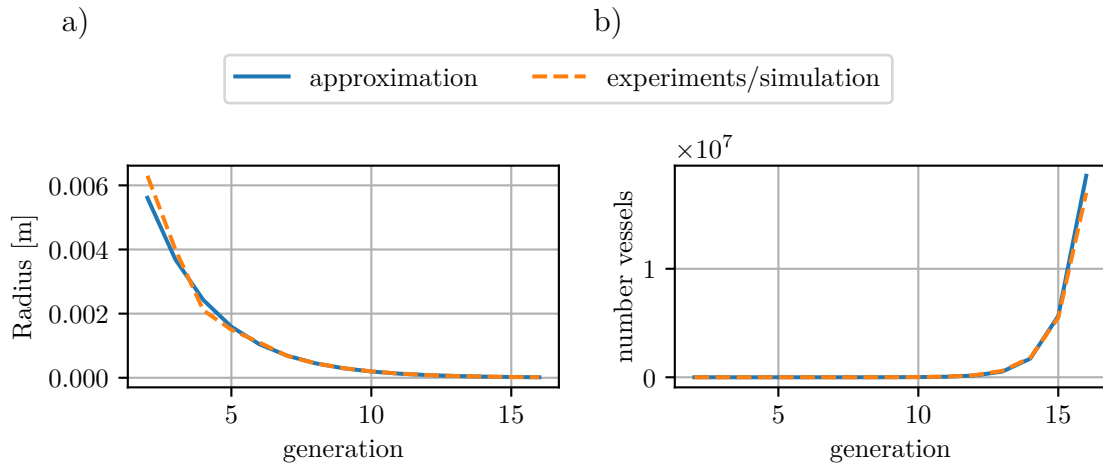


Figure 6.5: Comparison of two different approaches for vascular tree geometry in the liver: experimental data supplemented with approximations by DEBBAUT [43] (orange dashed line) and exponential approximation (blue line) for a) the vessel radius and b) the total number of vessels per generation.

Starting from 5 mmHG in the PV when leaving the gastrointestinal tract, the portal venous pressure reduces to around 1 mmHG at the terminal branches at the inlet of the hepatic lobules, see Figure 6.6. Assuming an ideal pressure of 0 mmHG in the vena cava, this results in a pressure gradient of 1 mmHG of microperfusion on the lobular scale, which corresponds to experimental and clinical evaluations, cf. DANCYGIER [42].

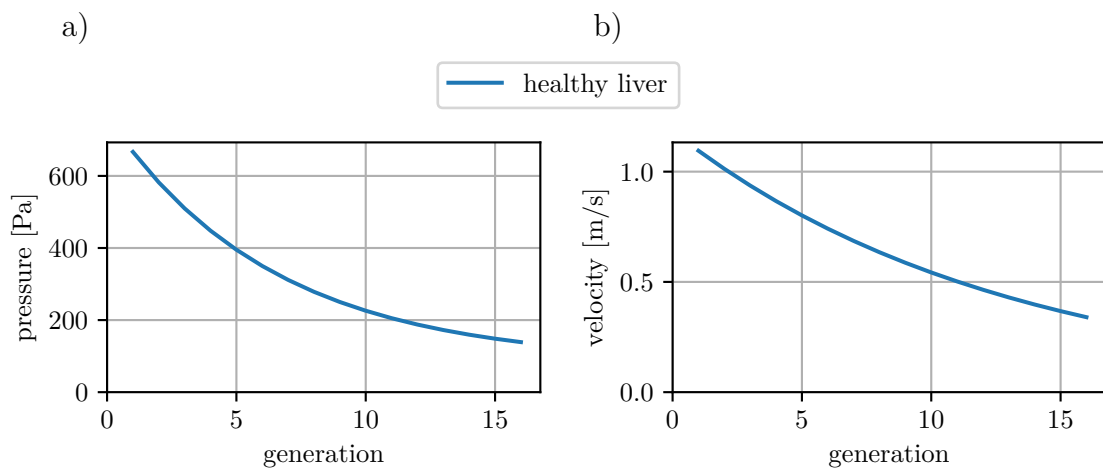


Figure 6.6: Evaluation of a) the pressure and b) the blood velocity over 16 generations in a healthy liver vascular tree.

6.3 Coupling Schemes

After deriving the partial differential equation (PDE) formulation at the lobular scale, the ODE formulation at the cellular scale, and the Bernoulli equation at the organ scale, the equation on the different scales must be coupled. Here, a transfer of the individual quantities between the scales as well as the consideration of possible differences in the time scales is crucial. Figure 6.7 illustrates the different scales and the coupling between the scales.

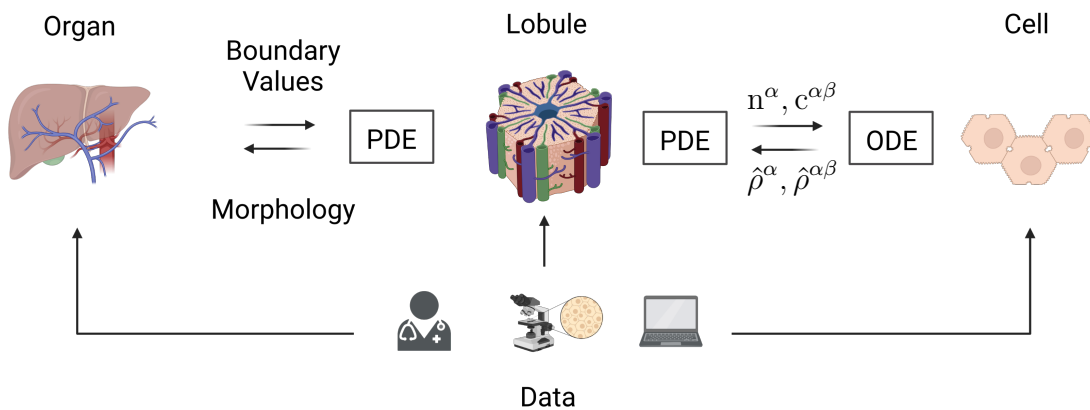


Figure 6.7: Coupling Procedure between different size scales of the human liver.

Coupling between Lobule and Cell Scale

A staggered algorithm is used to couple the biochemical models on cell scale from Sections 6.1.1, 6.1.2 and 6.1.3 and the Finite Element Method (FEM) code, see RICKEN et al. [118].

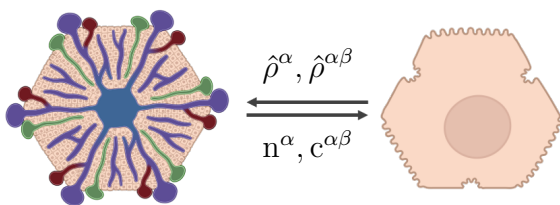


Figure 6.8: Coupling Procedure between cell and lobule.

This takes into account, that the metabolism of the entire liver is scaled down to one liver cell. The current values of the volume fractions n^α and concentrations $c^{\alpha\beta}$ of the individual substances are calculated on the macroscale and transferred to the cell scale, see Figure 6.8. Here they serve as inputs for the ODEs,

from which the current source and sink terms of the phases $\hat{\rho}^\alpha$ and concentrations $\hat{\rho}^{\alpha\beta}$ are derived. Returning these calculated quantities to the lobule scale allows them to be included in the PDEs and thus to calculate the new quantities in the next time step.

To couple the macroscale and the microscale, we assume a huge ratio between the length of both scales. We use the concept of RVEs, see [118], which leads to the connection

$$\{\cdot\} = \frac{1}{V} \int_{\partial B_S} \overline{\{\cdot\}} dv, \quad (6.14)$$

where $\{\cdot\}$ represents the scalar quantities on the macroscale and $\overline{\{\cdot\}}$ shows the scalar quantities on the microscale. This leads to the description of the rates

$$\begin{aligned} \hat{c}^{\text{FFA}} &= \frac{1}{V} \int_{\partial B_S} \overline{\hat{c}^{\text{FFA}}} dv, & \hat{c}^{\text{Ox}} &= \frac{1}{V} \int_{\partial B_S} \overline{\hat{c}^{\text{Ox}}} dv, & \hat{c}^{\text{Gl}} &= \frac{1}{V} \int_{\partial B_S} \overline{\hat{c}^{\text{Gl}}} dv, \\ \hat{c}^{\text{Gt}} &= \frac{1}{V} \int_{\partial B_S} \overline{\hat{c}^{\text{Gt}}} dv, & \hat{c}^{\text{Para}} &= \frac{1}{V} \int_{\partial B_S} \overline{\hat{c}^{\text{Para}}} dv, & & \\ \hat{\rho}^{\text{T}} &= \frac{1}{V} \int_{\partial B_S} \overline{\hat{\rho}^{\text{T}}} dv, & \hat{\rho}^{\text{N}} &= \frac{1}{V} \int_{\partial B_S} \overline{\hat{\rho}^{\text{N}}} dv. & & \end{aligned} \quad (6.15)$$

Regarding these dependencies, the ODE model is solved in each Gauss point by computing the concentration change for FFAs (\hat{c}^{FFA}) and oxygen (\hat{c}^{FOx}), glucose (\hat{c}^{FGl}), glutathione (\hat{c}^{SGt}), and paracetamol (\hat{c}^{FPara}) as well as the rate for the fat accumulation $\hat{\rho}^{\text{T}}$ and necrotic tissue $\hat{\rho}^{\text{N}}$.

Coupling between Lobule and Organ Scale

By calculating macroscopic perfusion at the organ level in Section 6.2, changes in total perfusion over generations can be calculated. These affect the processes in the liver lobules and thus also in the liver cells by altered pressure conditions and thus altered microperfusion. In this case, the pressure, that results at the terminal branch of the PV and thus at the connection to the sinusoids of the liver lobule is determined and applied as initial pressure boundary condition to the PFs of the lobule. The initial BVP is described in Section 7.1.

6.4 Numerical Implementation

The numerical implementation of the four-phase model is carried out using the FEM. Here, the PDEs are solved with an approximation, whereby only a numerical approach to the solution is produced. The principle of the FEM consists of the discretization of the entire area into finite subregions [105]. The finite elements have a uniquely describable geometry, which can be represented by simple ansatz functions. The approaches of the individual elements are then inserted into the differential equations, whereby these can be solved. The resulting non-linear equations system for the derived PDEs is solved using the Newton-Raphson approach, one of the most common implicit solution schemes for these equations systems. For further information on this scheme it is referred to [107]. To solve the problem, at first weak formulations from the derived balance equations and an initial BVP is set up and evaluated. For this purpose, boundary conditions are required, which are divided into the Neumann and the Dirichlet boundary conditions. In this respect, eTPM requires special attention to the numerical implementation of the concentrations as boundary values, which is why a special approach is used to apply these values. In order to use the FEM, spatial and temporal discretizations are then applied. The spatial discretization approximates the entire domain as well as the primary variables using appropriate functions on the finite elements. Here, the accuracy of the achieved solution is directly dependent on the meshing, since smaller finite elements approximate the solution more accurately. In this work, the isoparametric concept is used, which applies the same set of approximation functions for the geometry and the displacements. Analogous to the Bubnov-Galerkin method, the test functions are then also approximated with the same set of functions as the initial functions. For a discretization in time, the Newmark-beta approach is applied. To solve the strongly coupled problem in a numerically stable way, a mixed FEM formulation using Taylor-Hood elements [148] is employed. Here, the displacements are approximated with quadratic ansatz functions, while only linear ansatz functions are used for the remaining field quantities.

6.4.1 Weak Forms

The approaches and evaluations made in Section 5 directly result in a determination of the unknown quantities of the equation system and thus reduce the unknowns to

be solved. As a result, the following unknown quantities remain to be determined:

$$\bar{\mathcal{R}} = [\mathbf{u}_S, p^{\text{FR}}, \mathbf{w}_{\text{FS}}, \mathbf{w}_{\text{F}\beta\text{S}}, n^{\text{S}}, n^{\text{T}}, n^{\text{C}}, n^{\text{F}}, \mu^{\alpha\beta}]. \quad (6.16)$$

These unknown quantities can be further reduced by applying the equations for calculating the flow velocity of the blood in Equation (5.122) and solutes in Equation (5.118). The saturation condition in Equation (5.4) is applied for solving the volume fraction of the fluid n^{F} . Hereby, the final degrees of freedom of the system result in:

$$\mathcal{R} = [\mathbf{u}_S, p^{\text{FR}}, n^{\text{S}}, n^{\text{T}}, n^{\text{C}}, \mu^{\alpha\beta}]. \quad (6.17)$$

For the numerical solution of the degree of freedoms, governing equations are adopted. These are transformed into their integral weak form according to the Galerkin method [105] and then integrated over the domain. The previously established balance equations serve as governing equations. Here, the momentum balance of the entire aggregate after multiplication by the test function $\delta \mathbf{u}_S$ is used to solve the solid displacement \mathbf{u}_S . The degree of freedom of the fluid pressure p^{FR} is solved using the mass balance of the whole aggregate multiplied with the test function δp^{FR} . The volume fractions of the solid phases solid n^{S} , fat n^{T} , and tumor tissue n^{C} are determined by using the weak form of the mass balance of the respective solid phase multiplied by the respective test function δn^α . The chemical potential of the microscopic substances $\mu^{\alpha\beta}$ is provided by the mass balance of the respective substance, multiplied with the test function $\delta \mu^{\alpha\beta}$.

Weak form of balance of momentum for the mixture To evaluate the fluid pressure as a degree of freedom, the momentum balance of the entire aggregate is applied. For this purpose, the momentum balances of the individual phases derived in Equation (5.89) are summed up regarding assumptions (5.75), (5.76) as well as TRUESDELL'S constraint for the interaction forces $\hat{\mathbf{p}}^\alpha$ in Equation (5.43):

$$\mathbf{G}_{\text{Mom}}^{\text{M}} = \text{div} (\mathbf{T}^{\text{S}} + \mathbf{T}^{\text{T}} + \mathbf{T}^{\text{C}} + \mathbf{T}^{\text{F}} + \mathbf{T}^{\text{S}\beta} + \mathbf{T}^{\text{F}\beta}). \quad (6.18)$$

The momentum balance for the total aggregate is then multiplied by the test function δp^{FR} and integrated over the body B_S . This results in the weak form in the current

configuration.

$$\mathbf{G}_{\text{Mom}}^{\text{M}} = \int_{\text{B}_S} \text{div} (\mathbf{T}^{\text{S}} + \mathbf{T}^{\text{T}} + \mathbf{T}^{\text{C}} + \mathbf{T}^{\text{F}} + \mathbf{T}^{\text{S}\beta} + \mathbf{T}^{\text{F}\beta}) \delta \mathbf{p}^{\text{FR}} = \mathbf{0}. \quad (6.19)$$

This is followed by the pull-back of the weak form into the reference configuration using the transport theorems in Equation (5.22) and (5.23), the Cauchy Theorem and the transformation of the Cauchy stress tensor \mathbf{T}^α into the 1st Piola-Kirchhoff stress tensor \mathbf{P}^α with $\mathbf{T}^\alpha = \frac{1}{J_\alpha} \mathbf{P}^\alpha \mathbf{F}_\alpha^{\text{T}}$:

$$\mathbf{G}_{\text{Mom}}^{\text{M}} = \int_{\text{B}_{0\text{S}}} \left(\sum_{\alpha}^{\text{S,T,C,F,S}\beta,\text{F}\beta} \mathbf{P}^\alpha \text{Grad} \delta \mathbf{u}_S \right) dV = \int_{\partial \text{B}_{0\text{S}}} (t_0 \delta \mathbf{u}_S) dA. \quad (6.20)$$

Weak form of balance of mass for the mixture Analogous to the momentum balance of the mixture, the evaluation of the mass balance of the total aggregate is also obtained by summing up the mass balances of the individual phases:

$$\begin{aligned} \mathbf{G}_{\text{Mass}}^{\text{M}} = & (n^{\text{S}})'_{\text{S}} + n^{\text{S}} \text{div} \mathbf{x}'_{\text{S}} - \frac{\hat{\rho}^{\text{S}}}{\rho^{\text{SR}}} + (n^{\text{T}})'_{\text{S}} + n^{\text{T}} \text{div} \mathbf{x}'_{\text{S}} - \frac{\hat{\rho}^{\text{T}}}{\rho^{\text{TR}}} \\ & + (n^{\text{C}})'_{\text{S}} + n^{\text{C}} \text{div} \mathbf{x}'_{\text{S}} - \frac{\hat{\rho}^{\text{C}}}{\rho^{\text{CR}}} + (n^{\text{F}})'_{\text{F}} + n^{\text{F}} \text{div} \mathbf{x}'_{\text{F}}. \end{aligned} \quad (6.21)$$

This equation can be further simplified by including the material time derivations (5.86), the saturation condition (5.4) as well as the formulation for the seepage velocity (5.82). Furthermore, we assume a direct coupling between the mass exchange from solid and tumor tissue, see Section 6.1.2, with the relation $\hat{\rho}^{\text{S}} = -\hat{\rho}^{\text{C}}$:

$$\mathbf{G}_{\text{Mass}}^{\text{M}} = \text{div} \mathbf{x}'_{\text{S}} + n^{\text{F}} \text{div} \mathbf{w}_{\text{FS}} + \text{grad} n^{\text{F}} \mathbf{w}_{\text{FS}} - \frac{\hat{\rho}^{\text{T}}}{\rho^{\text{TR}}} - \hat{\rho}^{\text{S}} \left(\frac{1}{\rho^{\text{SR}}} - \frac{1}{\rho^{\text{CR}}} \right). \quad (6.22)$$

Reformulation with the calculation rule for divergence in (5.117) and Gauss theorem in (5.39) as well as multiplication with the test function $\delta \mathbf{p}^{\text{FR}}$ and integration over the body B_S leads to

$$\begin{aligned}
 & \int_{B_S} \left[-\mathbf{n}^F \mathbf{w}_{FS} \operatorname{grad} \delta p^{FR} + \mathbf{D}_S \cdot \mathbf{I} \delta p^{FR} - \left(\frac{\hat{\rho}^S}{\rho^{SR}} - \frac{\hat{\rho}^S}{\rho^{CR}} + \frac{\hat{\rho}^T}{\rho^{TR}} \right) \delta p^{FR} \right] dv \\
 &= \int_{\partial B_S} \left[(\mathbf{n}^F \mathbf{w}_{FS}) \cdot \mathbf{n} \delta p^{FR} \right] da.
 \end{aligned} \tag{6.23}$$

The transformation to the reference configuration using the transport theorems for a surface (5.22) and volume element (5.23) and the pull-back of the gradient operator with

$$\operatorname{grad}(\cdot) = \operatorname{Grad}(\cdot) \mathbf{F}_S^{-1} \tag{6.24}$$

leads to

$$\begin{aligned}
 & \int_{B_{0S}} \left[-J_S \mathbf{n}^F \mathbf{w}_{FS} \mathbf{F}_S^{T-1} \operatorname{Grad} \delta p^{FR} + J_S \mathbf{D}_S \cdot \mathbf{I} \delta p^{FR} \right. \\
 & \left. - J_S \left(\frac{\hat{\rho}^S}{\rho^{SR}} - \frac{\hat{\rho}^S}{\rho^{CR}} + \frac{\hat{\rho}^T}{\rho^{TR}} \right) \delta p^{FR} \right] dV = \int_{\partial B_{0S}} \left[J_S \mathbf{F}_S^{T-1} (\mathbf{n}^F \mathbf{w}_{FS}) \cdot \mathbf{n} \delta p^{FR} \right] dA.
 \end{aligned} \tag{6.25}$$

Weak form for Solid Phases To calculate the volume fractions of the solid phases, the respective mass balance of the phase is evaluated individually as a governing equation and converted into their weak form. The multiplication with the test function δn^α as well as the integral evaluation over the entire area B_S thus results in

$$\begin{aligned}
 G_{\text{Mass}}^{\text{Solid}} &= \int_{B_S} \left[(\mathbf{n}^S)'_S \delta n^S + \mathbf{n}^S \mathbf{D}_S \cdot \mathbf{I} \delta n^S - \frac{\hat{\rho}^S}{\rho^{SR}} \delta n^S \right] dv = 0 \\
 G_{\text{Mass}}^{\text{Fat}} &= \int_{B_S} \left[(\mathbf{n}^T)'_S \delta n^T + \mathbf{n}^T \mathbf{D}_S \cdot \mathbf{I} \delta n^T - \frac{\hat{\rho}^T}{\rho^{TR}} \delta n^T \right] dv = 0 \\
 G_{\text{Mass}}^{\text{Tumor}} &= \int_{B_S} \left[(\mathbf{n}^C)'_S \delta n^C + \mathbf{n}^C \mathbf{D}_S \cdot \mathbf{I} \delta n^C - \frac{\hat{\rho}^C}{\rho^{CR}} \delta n^C \right] dv = 0.
 \end{aligned} \tag{6.26}$$

Using the transport theorem for volume element (5.23), the weak form is pulled back to the reference configuration

$$\begin{aligned}
 G_{\text{Mass}}^{\text{Solid}} &= \int_{B_S} \left[J_S (n^S)'_S \delta n^S + J_S n^S \mathbf{D}_S \cdot \mathbf{I} \delta n^S - J_S \frac{\hat{\rho}^S}{\rho^{\text{SR}}} \delta n^S \right] dv = 0 \\
 G_{\text{Mass}}^{\text{Fat}} &= \int_{B_S} \left[J_S (n^T)'_S \delta n^T + J_S n^T \mathbf{D}_S \cdot \mathbf{I} \delta n^T - J_S \frac{\hat{\rho}^T}{\rho^{\text{TR}}} \delta n^T \right] dv = 0 \\
 G_{\text{Mass}}^{\text{Tumor}} &= \int_{B_S} \left[J_S (n^C)'_S \delta n^C + J_S n^C \mathbf{D}_S \cdot \mathbf{I} \delta n^C - J_S \frac{\hat{\rho}^C}{\rho^{\text{CR}}} \delta n^C \right] dv = 0
 \end{aligned} \tag{6.27}$$

To solve the chemical potential $\mu^{\alpha\beta}$ of the different microscopic substance β solved in the phase α , their mass balance is also evaluated. Here, a distinction is made between solutes in the solid without their own movement and solutes in the blood with the corresponding transport processes. For substances solved in the solid liver tissue the balance of mass is obtained:

$$\begin{aligned}
 G_{\text{Mass}}^{S\beta} &= \int_{B_S} \left[(n^S)'_S c^{S\beta} \delta\mu^{\alpha\beta} + n^S (c^{S\beta})'_S \delta\mu^{\alpha\beta} + n^S c^{S\beta} \text{div } \mathbf{x}'_S \delta\mu^{\alpha\beta} \right. \\
 &\quad \left. - \frac{\hat{\rho}^{S\beta}}{M_{\text{mol}}^{\alpha\beta}} \delta\mu^{\alpha\beta} \right] dv = 0.
 \end{aligned} \tag{6.28}$$

and transformed to the reference configuration using the transport theorems for a volume element (5.23)

$$\begin{aligned}
 G_{\text{Mass}}^{S\beta} &= \int_{B_{0S}} \left[J_S (n^S)'_S c^{S\beta} \delta\mu^{\alpha\beta} + J_S n^S (c^{S\beta})'_S \delta\mu^{\alpha\beta} + J_S n^S c^{S\beta} \text{div } \mathbf{x}'_S \delta\mu^{\alpha\beta} \right. \\
 &\quad \left. - J_S \frac{\hat{\rho}^{S\beta}}{M_{\text{mol}}^{\alpha\beta}} \delta\mu^{\alpha\beta} \right] dV = 0.
 \end{aligned} \tag{6.29}$$

For the solutes that are solved in the blood and thus have their own motion independent of the solid and the blood, the weak form can be derived to

$$\begin{aligned}
 G_{\text{Mass}}^{\text{F}\beta} &= \int_{B_S} \left[(n^{\text{F}})'_{\text{F}\beta} c^{\text{F}\beta} \delta\mu^{\alpha\beta} + n^{\text{F}} (c^{\text{F}\beta})'_{\text{F}\beta} \delta\mu^{\alpha\beta} + n^{\text{F}} c^{\text{F}\beta} \text{div } \mathbf{x}'_{\text{F}\beta} \delta\mu^{\alpha\beta} \right. \\
 &\quad \left. - \frac{\hat{\rho}^{\text{F}\beta}}{M_{\text{mol}}^{\alpha\beta}} \delta\mu^{\alpha\beta} \right] dv = 0.
 \end{aligned} \tag{6.30}$$

A reformulation using the relation for the seepage velocity of external substances in Equation (5.83) the weak form results in

$$\begin{aligned} G_{\text{Mass}}^{\text{F}\beta} = \int_{\text{B}_S} \left[(\mathbf{n}^{\text{F}})'_{\text{F}\beta} c^{\text{F}\beta} \delta\mu^{\alpha\beta} + \mathbf{n}^{\text{F}} (c^{\text{F}\beta})'_{\text{F}\beta} \delta\mu^{\alpha\beta} + \mathbf{n}^{\text{F}} c^{\text{F}\beta} \operatorname{div} \mathbf{w}_{\text{F}\beta\text{S}} \delta\mu^{\alpha\beta} \right. \\ \left. + \mathbf{n}^{\text{F}} c^{\text{F}\beta} \operatorname{div} \mathbf{x}'_S \delta\mu^{\alpha\beta} - \frac{\hat{\rho}^{\text{F}\beta}}{\text{M}_{\text{mol}}^{\alpha\beta}} \delta\mu^{\alpha\beta} \right] \text{d}v = 0. \end{aligned} \quad (6.31)$$

Here we can identify the concentration flux with $\mathbf{j}_{\text{F}\beta\text{S}} = \mathbf{n}^{\text{F}} c^{\alpha\beta} \operatorname{div} \mathbf{w}_{\text{FS}}$ and reformulate using the Gauss theorem (5.39) to obtain the final weak form in current configuration:

$$\begin{aligned} G_{\text{Mass}}^{\text{F}\beta} = \int_{\text{B}_S} \left[(\mathbf{n}^{\text{F}})'_{\text{F}\beta} c^{\text{F}\beta} \delta\mu^{\alpha\beta} + \mathbf{n}^{\text{F}} (c^{\text{F}\beta})'_{\text{F}\beta} \delta\mu^{\alpha\beta} - \mathbf{j}_{\text{F}\beta\text{S}} \operatorname{grad} \delta\mu^{\alpha\beta} \right. \\ \left. + \mathbf{n}^{\text{F}} c^{\text{F}\beta} \operatorname{div} \mathbf{x}'_S \delta\mu^{\alpha\beta} - \frac{\hat{\rho}^{\text{F}\beta}}{\text{M}_{\text{mol}}^{\alpha\beta}} \delta\mu^{\alpha\beta} \right] \text{d}v = \int_{\partial\text{B}_S} - [\mathbf{j}_{\text{F}\beta\text{S}} \cdot \mathbf{n} \delta\mu^{\alpha\beta}] \text{d}a. \end{aligned} \quad (6.32)$$

Transformation into reference configuration using the transport theorems for surface (5.22) and volume elements (5.23) as well as pull-back of the gradient operator (6.24) results in the weak form for balance of mass of the substances solved in the fluid with

$$\begin{aligned} G_{\text{Mass}}^{\text{F}\beta} = \int_{\text{B}_S} \left[\text{J}_S (\mathbf{n}^{\text{F}})'_{\text{F}\beta} c^{\text{F}\beta} \delta\mu^{\alpha\beta} + \text{J}_S \mathbf{n}^{\text{F}} (c^{\text{F}\beta})'_{\text{F}\beta} \delta\mu^{\alpha\beta} - \text{J}_S \mathbf{j}_{\text{F}\beta\text{S}} \mathbf{F}_S^{\text{T}-1} \cdot \operatorname{Grad} \delta\mu^{\alpha\beta} \right. \\ \left. + \text{J}_S \mathbf{n}^{\text{F}} c^{\text{F}\beta} \mathbf{D}_S \cdot \mathbf{I} \delta\mu^{\alpha\beta} - \text{J}_S \frac{\hat{\rho}^{\text{F}\beta}}{\text{M}_{\text{mol}}^{\alpha\beta}} \delta\mu^{\alpha\beta} \right] \text{d}V \\ = \int_{\partial\text{B}_S} - [\text{J}_S \mathbf{j}_{\text{F}\beta\text{S}} \mathbf{F}_S^{\text{T}-1} \delta\mu^{\alpha\beta} \cdot \mathbf{n}] \text{d}A. \end{aligned} \quad (6.33)$$

6.4.2 Boundary Value Problem

When solving physical problems using the FEM, these often exist in the form of a BVP. Here, the TPM involves PDEs in which the value of the primary variable at the edges of the domain to be solved is known. These boundary value conditions can be

divided into Dirichlet and Neumann boundary conditions. Conditions defined on the Dirichlet boundary ∂B_D are so-called first type boundaries, where the direct values of the solutions on the boundary are known. On the Neumann boundary ∂B_N , on the other hand, the derivative of these primary variables is known and is assumed to be the solution on the boundary [133], see Figure 6.9.

Thereby, both types of boundary values for a primary variable cannot be applied to the same section of the boundary at the same time. However, under the condition of different primary variables, overlapping Dirichlet and Neumann boundary conditions are not mutually exclusive. The boundary values of both Dirichlet boundary ∂B_D and Neumann boundary ∂B_N are characterized by the surface terms of the weak forms of a problem and depicted for the considered problem in Figure 6.9. According to the weak forms derived in Section 6.4.1, this results in the first-type boundary conditions of the solid displacement $\bar{\mathbf{u}}_S$, the fluid pressure \bar{p}^{FR} , the volume fractions of the solid phases $\bar{n}^S, \bar{n}^T, \bar{n}^N$ and the chemical potentials of the microscopic substances $\bar{\mu}^{\alpha\beta}$. The Neumann boundaries values result in the traction $\bar{\mathbf{t}}$, the fluid mass flow $\bar{\mathbf{w}}^{FR}$ and the molar flux for the microscopic substances $\bar{\mathbf{j}}^{\alpha\beta}$. The Neumann boundary conditions correspond directly to the Dirichlet conditions and represent their derivatives. Only in the mass balances of the solid phases there exist no second-type boundary conditions.

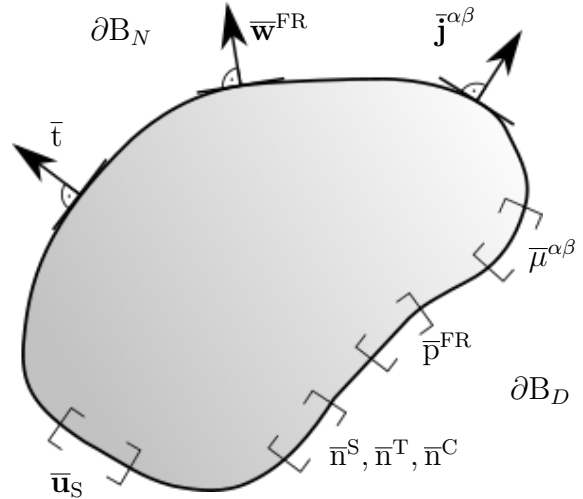


Figure 6.9: Boundary values on Dirichlet boundary ∂B_D and Neumann boundary ∂B_N

6.4.3 Stabilization Scheme for Concentration

The model based on eTPM includes a description for substances dissolved in the carrier phases, which have their own motion function independent of that of the fluid phase. The BVP of the hepatic lobules describes a flow problem, with an inflow of the blood at the PF as well as an outflow at the CV. Here a dependence of the outflow

of the solutes on the outflow of the carrier phase is necessary, to fulfill the Dirichlet boundary values for the concentrations $c^{F\beta}$ and chemical potential $\mu^{\alpha\beta}$ and Neumann boundaries for the flux $\mathbf{j}^{F\beta}$ and to avoid numerical instabilities in the Finite Element (FE) simulation. Therefore, an update algorithm according to WERNER [160] is implemented. In this approach, an explicit Euler algorithm is used to dynamically adjust the boundary values at the outflow boundary ∂B_D as depicted in Figure 6.10. Here the difference $\Delta \bar{c}^{F\beta}$ between the value, that would form in the simulation and the boundary value is calculated. The boundary value $\bar{c}_{t+1}^{F\beta}$ is then dependent on the actual solution for the inflow concentration $c_{in}^{F\beta}$ and $\bar{c}_t^{F\beta}$, which results in

$$\bar{c}_{t+1}^{F\beta} = \bar{c}_t^{F\beta} + \Delta \bar{c}^{F\beta}, \quad \Delta \bar{c}^{F\beta}(c_{in}^{F\beta}, \bar{c}_t^{F\beta}). \quad (6.34)$$

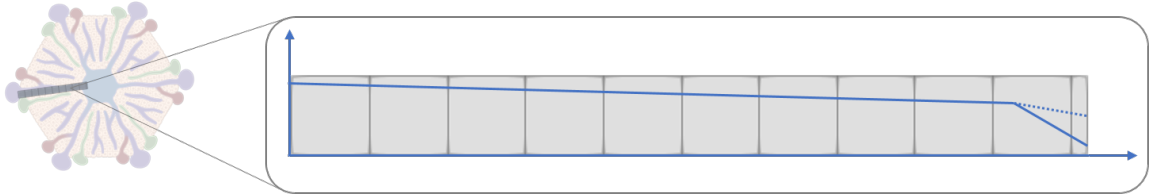


Figure 6.10: Progression of the concentration of a solute within a sinusoid without stabilization algorithm (solid line) and with stabilization algorithm (dashed line). The algorithm used here determines a difference $\Delta \bar{c}^{F\beta}$ between the boundary values. Adapted from [160].

Figure 6.11 a) shows the effects of the stabilization algorithm on the spatial progression of the glucose concentration c^{FGl} . While using such an algorithm the concentration decreases uniformly over the length of the geometry, without the stabilization an irregular distribution occurs in the last element. The concentration is forced to a too small value by the given gradient, which leads to numerical instabilities in addition to the deviating results. When looking at the time course in Figure 6.11 b), the concentrations of glucose c^{FGl} and FFA c^{FFFA} at two points within the geometry are considered. Here, the concentrations are applied using a time-varying load curve representing for example a feeding cycle. While there are only slight differences between the two curves at the center point, large fluctuations occur in the last element. Here the values deviate strongly from the expected values without a stabilizing algorithm and it comes to a false representation of the concentration distribution.

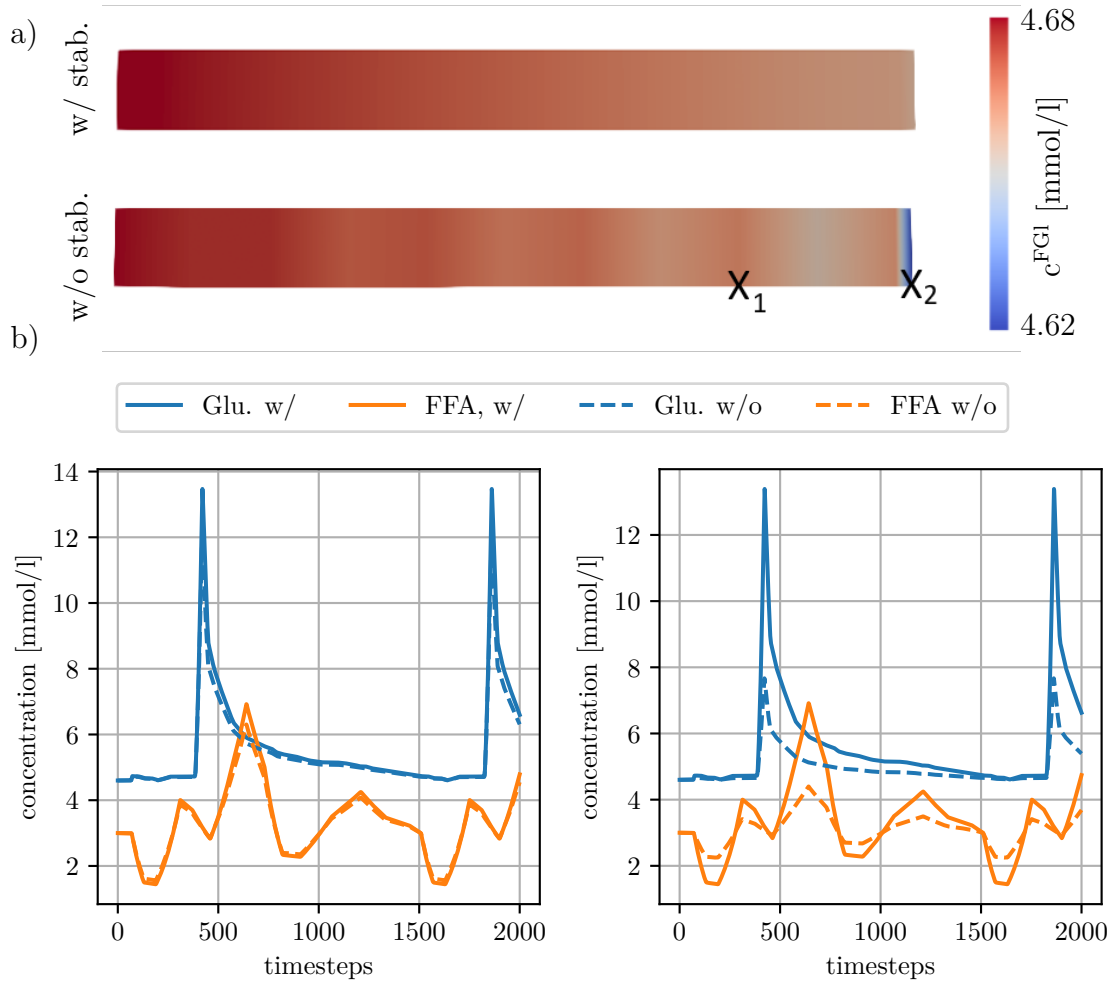


Figure 6.11: Evaluation of concentrations using a stabilization algorithm. a) Spatial distribution of glucose concentration c^{FGI} with and without stabilization algorithm in one sinusoid; b) Time course of glucose concentration c^{FGI} (blue) and FFA concentration c^{FFFA} (orange) with (solid line) and without (dashed line) stabilization algorithm evaluated at point X_1 (left) and X_2 (right).

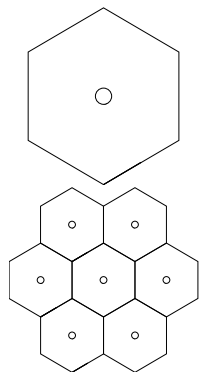
7 Numerical Simulation of Function-Perfusion Processes in the Liver

After deriving the multiphase and multiscale model in the previous chapters, it will now be applied to simulate selected function-perfusion processes in the liver. For this purpose, the liver is modeled by choosing appropriate material parameters and boundary conditions. Liver function and perfusion can be represented and evaluated in different geometries. By selecting a coupled model, the complex function-perfusion relationship can also be investigated. In order to take first steps towards a clinical application, a nonlinear MOR as well as a sensitivity analysis of the parameters will also be performed.

7.1 Boundary Conditions

To describe the function-perfusion-deformation relationship in the liver at the lobule scale, both the local processes within a single separated functional unit and global processes within multiple lobules will be considered, see Table 7.1. Input parameters are the chemical potentials $\mu^{F\beta}$ of the different metabolites β and the pressures at PFs and CVs to establish a pressure gradient within the lobule. On the local level of a single liver lobule, the formation of fat, tumors and necrosis as well as the concentration of metabolites in quantity and spatial distribution and the microperfusion in the lobule are evaluated. In a global view, heterogeneities in volume fractions and concentrations between individual liver lobules as well as interactions in perfusion conditions can be analysed.

Table 7.1: Input and Output parameters for local and global simulation of liver lobules.

	Input	Output
	concentration FFA concentration Ox blood pressure	% of fat and tumor volume fraction Zonation of fat accumulation Zonation of FFA and Ox Perfusion/ Resistance Change in concentration local
		% of Heterogeneity of fat accumulation Change in concentration global Change in concentration in relation to the area

The derived model will be tested and validated for several cases. Therefore, a single lobule is considered as the main geometry representing a ideally shaped hexagon, shown in Figure 7.1 a). The red line represents the inflow and the blue one the outflow area. As discussed in RICKEN ET AL. [121], the inflow area consists of the portal triad and additional venules, which are positioned on the lobule periphery.

An additional example is performed on the geometry of a group of lobules. Figure 7.1 b) illustrates the FE mesh of the group with three different BC, cf. LAMBERS ET AL. [85].

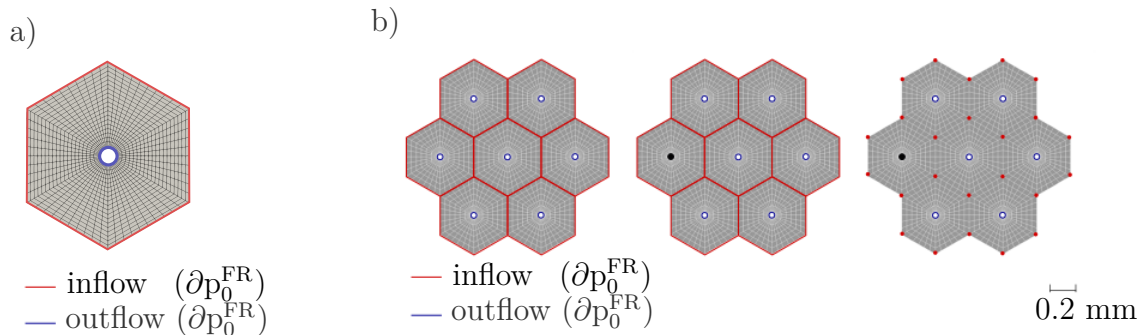


Figure 7.1: Applied boundary conditions of the pressure a) for one lobule and b) for a group of lobules for three conditions: (i) Undisturbed flux, (ii) Outflow obstruction, (iii) Outflow obstruction with connection to neighboring lobules. The red lines respectively dots show the peripheric or local inflow applied by the initial value ∂p_0^{FR} . The outflow pressure is represented by the pressure p^{FR} in the CV and is illustrated by blue lines.

The inflow and outflow conditions of each geometry are again marked by red and blue

lines, respectively. To investigate the influences of different BC on hepatic processes, three different possible pressure conditions are considered. In the first case (a), a classical physiological condition of microperfusion representing a healthy group of lobule is performed. The second example (b) reveals unchanged inflow conditions, but with an outflow obstruction on the left lobule. The last example (c) applies pressure only at the PFs in order to determine the changes of a local inflow at the PF and the distributed inflow through additional venules. In the first two examples, the external concentrations and the pressure are applied at the same location on the lobule periphery. The third condition allows the inflow of external concentrations from the lobule periphery, whereas the pressure is applied only at the PF. Hence, the external concentrations can drain through the adjacent central veins.

7.2 Microscopic Perfusion through Liver Lobules

The previously derived model allows simulation of the spatial distribution of perfusion within a liver lobule coupled with function in liver cells. To investigate these processes, the microperfusion in the liver lobules is analyzed and evaluated in a first step. The permeability is assumed using the anisotropic permeability approach described in Section 5.6.8, which leads to a dependence of the preferred flow direction on the pressure. Different BVPs are considered to evaluate microperfusion, allowing a differentiation of morphology by including vascular septa and calculation of different perturbations of perfusion. Furthermore, the dependence of perfusion on different structural conditions of the initial lobule morphology will be determined. This can be achieved by integrating different lobule geometries or by including exclusively inlets and outlets instead of complete delineations of lobules.

7.2.1 Evaluation of Microperfusion

The microperfusion will be evaluated for the different geometries and boundary conditions presented in Section 7.1. Here, the applied boundary conditions, expressed as Dirichlet values for the in- and outflow, will determine the results for the pressure pattern. Between the inflow and outflow areas, it is anticipated that there is a pressure difference of around 100 Pa. Figure 7.2 evaluates the microperfusion in a

group of seven liver lobules for the three boundary conditions with different inflow and outflow conditions. The pressure p^{FR} is depicted on the left and the seepage velocity \mathbf{w}_{FS} is illustrated on the right. Here the seepage velocity is proportional to the pressure gradient resulting from the applied Darcy formulation of the blood. In the representation of the seepage velocity, the preferred flow direction is represented by streamlines. This direction is mainly influenced by the preferred flow direction of the blood, which results from the pressure gradient, see Section 5.6.8. Besides the applied boundary conditions, permeability is the major factor influencing the seepage velocity. In the first example (a), all liver lobules show a homogeneous distribution of microperfusion with pericentral pressure gradients from the PF to the CV. In the second case, there is an outflow obstruction in the CV of one lobule, so that no pressure gradient forms in the latter. Since there is only pressure at the PF, microperfusion is significantly reduced and no advective processes occur. Since the individual lobules are not connected, there are no changes in the perfusion of the remaining lobules. In the last example (c), the blood inflow occurs only at the corners of the lobule, so that a more physiological example is shown here. Although the outflow in the left lobule is still disturbed, it can rearrange itself over the neighboring lobules. To increase the speed of the blood, the pressure at the inflow is increased by 20%. Here, the streamlines also illustrate the blood flow to the neighboring lobules.

7.2.2 Integration of Realistic Liver Lobule Geometries

To allow a patient-specific and more realistic simulation of hepatic processes, the inclusion of liver lobule morphology in the multiscale and multiphase model is performed. Several factors are important here. The structure of the hepatic lobules mentioned in Section 2.1.3 results in an ideal consideration to a hexagon in two dimensions or a hexagonal prisma in three dimensions. If stained histological sections are examined, a deviating, not ideally hexagonally represented geometry of the liver lobules can be discerned. The heterogeneity of the hepatic lobule geometry has a significant effect on the spatial pressure distribution and the associated perfusion. To include these effects in the simulation, a semi-automatic procedure based on H&E-stained histological sections is used to segment the real lobule geometry and further process it into an input for the calculation as shown in Figure 7.3.

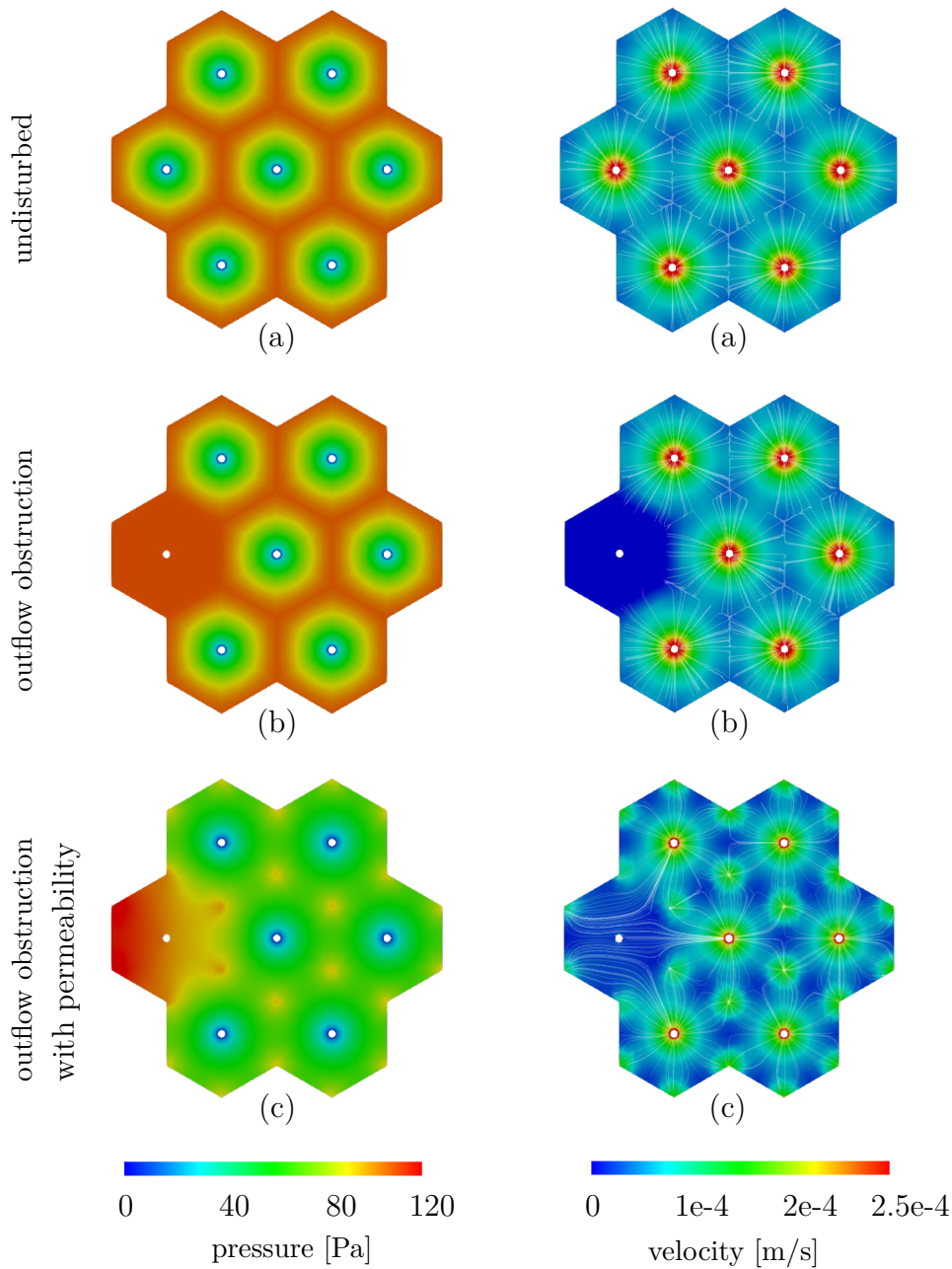


Figure 7.2: Evaluation of microperfusion in a group of liver lobules. Left hand side: Spatial pressure distribution [Pa] with pressure gradient of $\sim 100\text{-}120$ Pa between PF and CV; Right hand side: Spatial velocity distribution [$\frac{\text{m}}{\text{s}}$] with streamlines denoting the preferred flow direction using anisotropic permeability. (a) Undisturbed distribution, (b) Outflow obstruction, (c) Outflow obstruction with permeability.

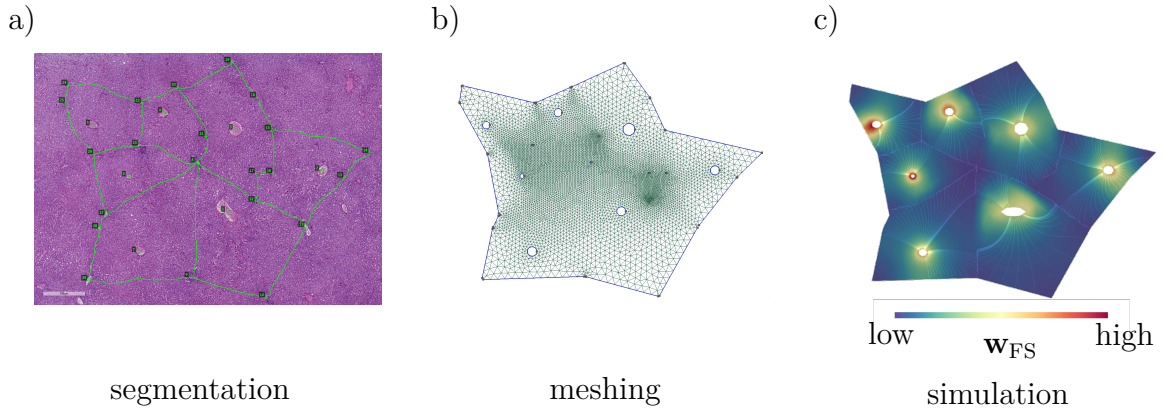


Figure 7.3: Semi-automatic workflow for including realistic liver lobule geometries in the simulation. a) H&E-stained human histological section with manually annotated location of PF and CV¹. b) meshed geometry c) simulation results for heterogeneous blood perfusion w_{FS} .

With the help of the imaging viewing software for pathology slides ImageScope [6] the histological images can be viewed and labeled. The locations of the PF as well as the CV are manually tagged and then automatically exported. Further processing and reformatting into the required format is done with the help of a developed Python script.

This enables the import into the meshing software GMSH [59] as well as the subsequent meshing. The required refinement of the mesh as well as a selection of elements can be specified. The exported input file can be reformatted into the desired format of the simulation program and subsequently applied as input for

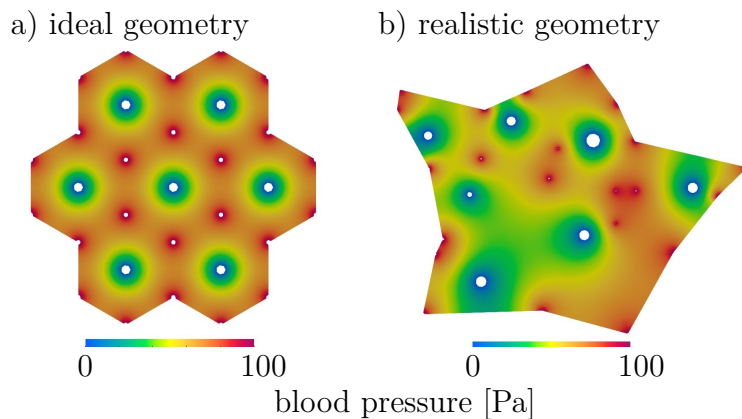


Figure 7.4: Comparison of blood pressure in a group of a) ideally hexagonally and b) a group of realistically shaped liver lobules segmented from a histological section.

the multiphase and multiscale simulation. A pressure gradient between the PF and the CV is again applied as a boundary condition. The resulting spatial perfusion distribution in Figure 7.3 c) displays a significantly less homogeneous distribution

¹© Prof. Dr. med. Uta Dahmen, Jena University Hospital, UKJ_16_016_J-19-0469_HE.ndpi

than the ideal hexagonal structures.

The streamlines illustrate the flow direction of the blood, which deviates markedly from the previous results of an ideal hexagon. Furthermore, if the pressure distribution of the homogeneous and inhomogeneous liver geometry is compared, a discrepancy of the blood pressure is evident as shown in Figure 7.4. Whereas in the ideal hexagon a uniform pressure gradient is established, it varies significantly in the inhomogeneous geometry. Moreover, due to the position of the inflow areas at the PF, it becomes visible that there are also non-perfused or weakly perfused areas within the lobule.

In addition to segmenting clear lobule boundaries, the geometry can also be determined using the sinusoidal remodeling of the sinusoids described in Section 5.6.8 [83]. Here, only the positions of the blood inflows at the PFs and the outflow at the CV are manually determined from a histological image, see Figure 7.5 a). Not a single

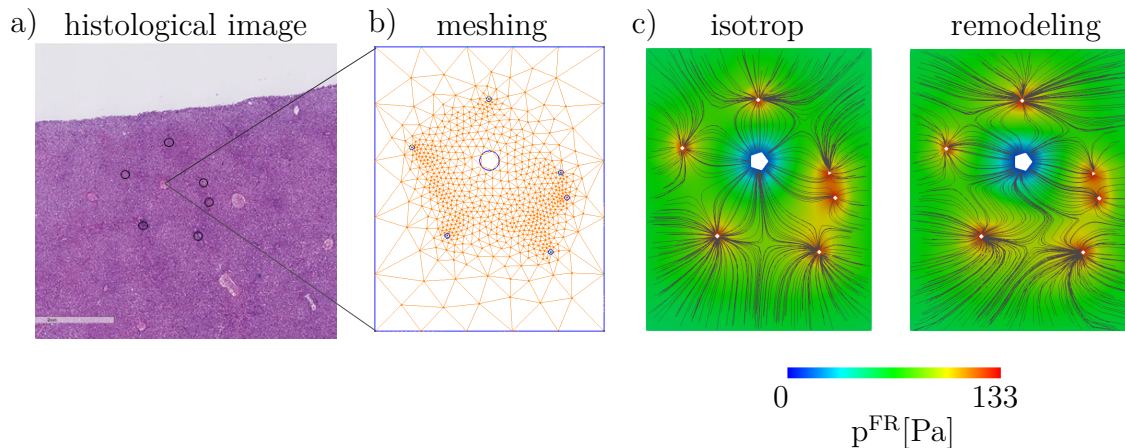


Figure 7.5: Evaluation of lobule geometry using sinusoidal remodeling. a) histological image of a healthy human liver with marked PF ², b) meshing of a finite area around the previously defined PF, c) spatial pressure distribution and blood flow illustrated by streamlines for isotropic and anisotropic tissue permeability

liver lobule is applied, but a finite area around the inflows is applied as a simulation geometry, as Figure 7.5 b) illustrates. The edge of this area has no specific pressure BCs, while at the PFs a pressure of 133 Pa and at the CV a pressure of 0 Pa is predefined. This results in a spatial pressure distribution that regulates the anisotropic blood flow. Figure 7.5 c) shows the resulting pressure distribution p^{FR} as well as the

²© Prof. Dr. med. Uta Dahmen, Jena University Hospital, UKJ_16_016_J-19-0469_HE.ndpi

blood flow characterized by streamlines for the case of an isotropic permeability and an anisotropic permeability specified by the pressure gradient. In the isotropic case, the distribution shows a very regular formation of the flow distribution. However, if anisotropic permeability of the liver tissue is considered, the flow distribution changes compared to the isotropic case. Here, the dependence on the pressure gradient becomes significant, especially at locations where the distance between two PFs is small, as well as when the distance between the PF and the outflow is large. While the preferred flow direction is initially set to a fixed value, it updates over time with the pressure distribution. This temporal evolution of the blood flow is illustrated in Figure 7.6.

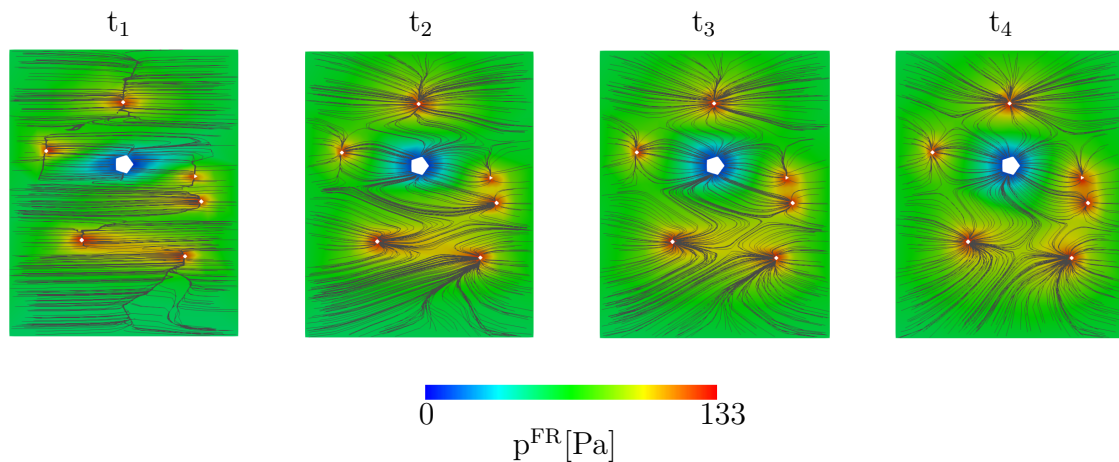


Figure 7.6: Evolution of blood flow distribution over time illustrated by streamlines.

At time t_1 , the flux distribution follows the prescribed direction, while with time the real distribution is established on the basis of the pressure division and the structure of the liver lobules becomes apparent.

7.3 Simulation of Hepatic Diseases

7.3.1 Zonated Accumulation of Steatosis during NAFLD

The simulation of NAFLD using a multiphase and multiscale model contains an approach for lipid development at the cellular level, see Section 6.1.1. The approach by SCHLEICHER et al. [131] is zonated and focuses on the differences in hepatocytes of different zones within the hepatic lobules. The different metabolic conditions will be

extended from the one-dimensional consideration to the spatial distribution within a group of liver lobules with the help of the coupled PDE-ODE model. Here, the focus is also on the different factors influencing fat metabolism and zonation. A coupling of hepatic function and perfusion is also expected to alter fat distribution in the presence of impaired perfusion. This hypothesis will be investigated by using the BVPs presented in Section 7.1. The material parameters are shown in Table 7.2.

Table 7.2: Material parameters of a liver lobule for the simulation of NAFLD

Parameter	Value	Unit	Remark
n_{0S}^S	0.7	-	Initial volume fraction solid
n_{0S}^T	0.05	-	Initial volume fraction fat
n_{0S}^C	0.05	-	Initial volume fraction tumor
n_{0S}^F	0.20	-	Initial volume fraction fluid
μ^S, μ^T	$4 \cdot 10^4$	Pa	Lamé constant
λ^S, λ^T	$3 \cdot 10^4$	Pa	Lamé constant
θ	280	K	Temperature
R	8.3144	J/molK	Gas constant
k_D	$4.5 \cdot 10^{-10}$	m/s	Darcy permeability

Simulation of NAFLD in a single lobule

The implementation of the described metabolic model on the cellular scale leads to a zoned accumulation of fat, depending on the initial BC of concentrations.

This distribution was investigated in a single liver lobule model, cf. Figure 7.7 for two different initial concentrations of FFA and oxygen causing different zonations. The spatial distribution of fat fraction in the left

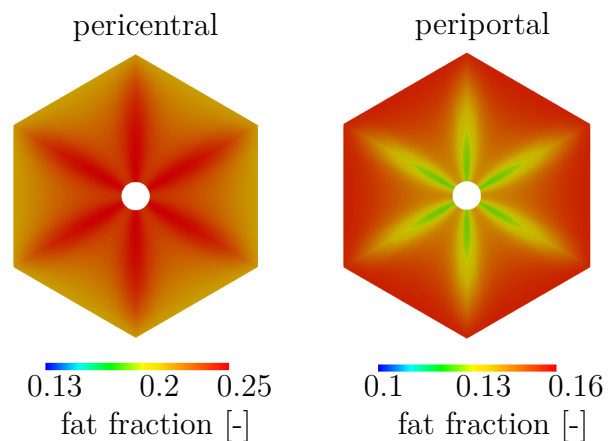


Figure 7.7: Spatial distribution of fat volume fraction with a) periportal zonation, b) pericentral zonation

lobule shows a pericentral zonation whereas the right lobule displays a periportal zonation of fat fraction. By regarding the development of volume fractions over time, high intake of FFA combined with a low oxygen concentration results in a pericentral zonation, see Figure 7.8 a), meaning increased formation of fat vacuoles near the CV. A reduction of FFA intake changes the pattern to a periportal development of steatosis, i.e. at the outer edge of the lobules, shown in Figure 7.8 b). NAFLD development on the lobular scale in humans is mostly characterized by a pericentral zonation, also called zone 3 zonation, of fat distribution with a higher amount of fat near the CV, cf. KLEINER AND MAKHLOUF [78].

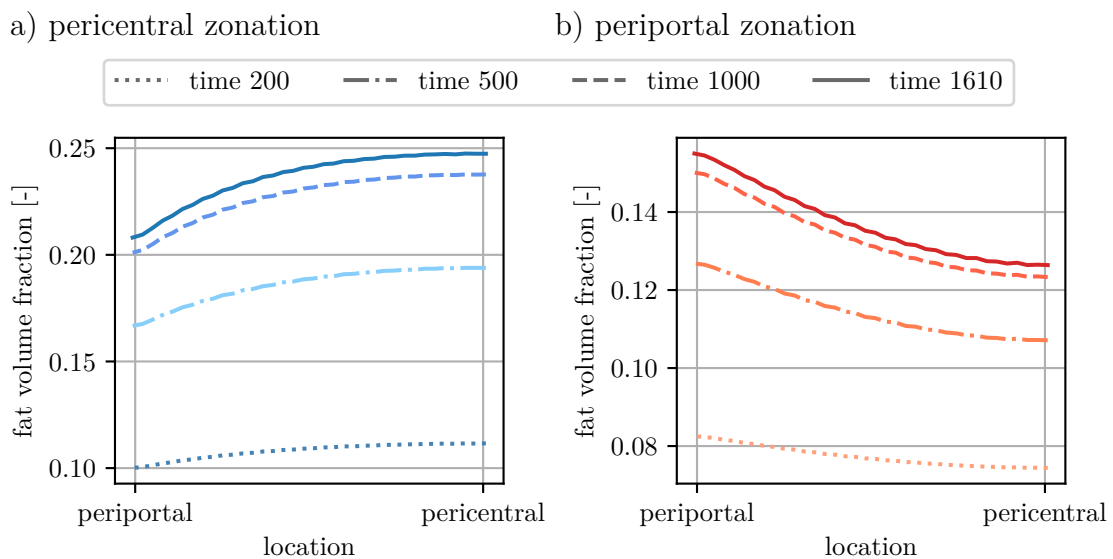


Figure 7.8: Distribution of fat volume fraction along the liver lobule. Fat content is evaluated after 200, 500, 1000 and 1610 seconds during a) pericentral zonation of fat accumulation, b) periportal zonation of fat accumulation.

However, NAFLD may also be associated with periportal fat accumulation, in which fat content is increased in the outer regions of the lobule, cf. LIU ET AL. [92]. Validation of the simulation results is performed using experimentally obtained histological sections of a steatotic rat and human liver, see Figure 7.9. The H&E-stained histological sections show a moderate to severe grade of steatosis and clearly differentiate the white fat vacuoles from the pink appearing liver parenchyma. The fat formation visible in Figure 7.9 a) occurs more frequently in zone 1, i.e., near the PF, which characterizes a periportal zonation. In contrast, Figure 7.9 b) shows an enhanced appearance of white round fat vacuoles in the pericentral region around the CV, whereas the area around the PFs is sparsely. The different fat distributions appearing zoned over the

area of the lobule can thus be represented with the coupled continuum-biomechanical simulation.

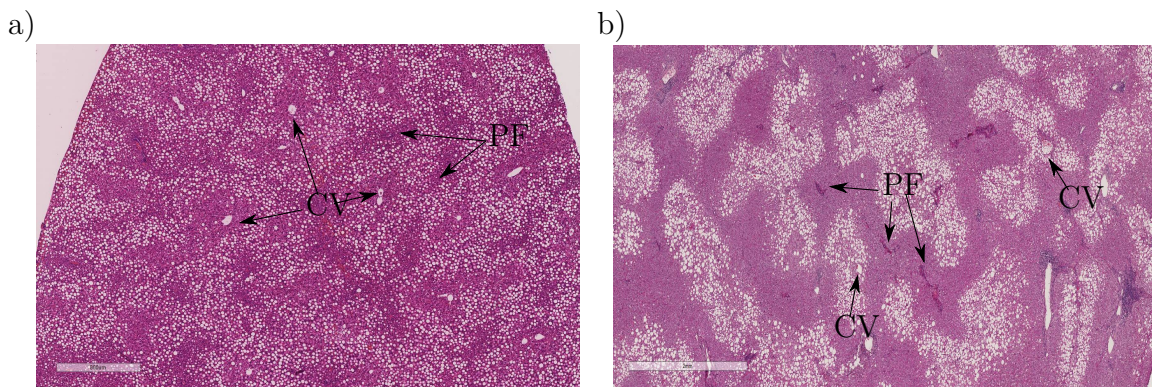


Figure 7.9: Zonated accumulation of fat in histological images with a) periportal zonation of fat accumulation in a steatotic rat liver³, b) pericentral zonation of fat accumulation in steatotic human liver⁴, CV = central vein, PF = portal field

Simulation of NAFLD during different perfusion conditions

The formation of a NAFLD was simulated using the three BVPs in Section 7.1. Due to the different evaluations of the microperfusion, various evaluations of the fat metabolism occur. The first two slots in Figure 7.10 depict the external FFA concentration c^{FFFA} as well as the oxygen concentration c^{FO_2} whereas the last slot illustrates the volume fraction of fat n^{T} . Advection and diffusion are responsible for the transport of external concentration. Here, advection characterizes the transport via the blood velocity. Diffusion transport shows a steady movement from areas with higher concentration to areas with low concentration. Therefore, the periportal pressure gradient (advection) and the periportal external concentration gradients (diffusion) are both necessary for the transfer of FFA and oxygen. Additionally, the degradation rate of the chemicals in the lobule is influenced by the fat buildup, a chemical conversion process. In the first illustration (a), FFA and oxygen concentrations are externally gradients, with higher concentrations at the PF and lower concentrations at the CV. These concentration gradients in the lobule result from altered diffusion conditions and

³© Prof. Dr. med. Uta Dahmen, Jena University Hospital, SFL-074_T-10-169_HE.ndpi

⁴© Prof. Dr. med. Uta Dahmen, Jena University Hospital, UKJ-19_050_Human+_J-19-0712_HE.ndpi

altered blood transport with higher seepage velocity at the CV (outflow). Since FFA esterifies to fat in chemical processes, the concentration of this solute is further reduced. This means that a high concentration of FFA promotes increased accumulation of fat, while a high concentration of oxygen leads to increased fatty acid oxidation and thus to a reduction in fat accumulation. Thus, although both processes work against each other, both are essential for fat metabolism. In the work of SCHLEICHER et al. [131] a high influence of the oxygen gradient on fat accumulation with a pericentral pattern was observed. This zoning pattern results from low oxygen levels at the CV, so fatty acid oxidation is reduced, favoring fat accumulation. This aspect will be investigated in more detail using the PDE-ODE simulation. For this purpose, the zoned distribution of the resulting fat is evaluated temporally as well as spatially for different oxygen gradients. The metabolic rate in the coupled ODE system at the cellular level is modified by a factor, so that a stronger gradient is generated and the oxygen content at the CV is reduced. Figure 7.11 a) depicts the temporal evolution of lipid content at different oxygen gradients. It is clear that the volume fraction of fat tissue increases with an increase in the gradient and thus a reduction in the pericentral oxygen content. While this is still relatively small at low fat contents, deviations of more than 10% occur in a fatty liver. Within a liver lobule, the fat content is also evaluated along a sinusoid from the periportal to the pericentral zone for different oxygen gradients, shown in Figure 7.11 b). Here, the influence of this gradient on the zonation becomes distinctly evident; the pericentral zonation is significantly more pronounced with large gradients than with a more uniform oxygen distribution within a liver lobule.

In the second example (b), there is a clear change in microperfusion with no pressure gradient and therefore no advection in the left lobule. This leads to no mass transfer by advection being observed in this lobule. Although diffusion attempts to balance the concentration gradient towards the CV, the process is too limited to sufficiently initiate mass transport up to the CV. Since the external substances are only present in the periportal zone, a periportal distribution of fat develops. In the area around the CV, there is no formation of fat due to the absence of FFA. Thus, there is an inhomogeneous distribution of fat within the hepatic lobules.

In the last example (c), the boundary conditions of the influence are changed so that the influence can only occur at the PF and the blood can flow between the lobules. This leads to an altered flow of the disturbed lobule to the lobule adjacent above and

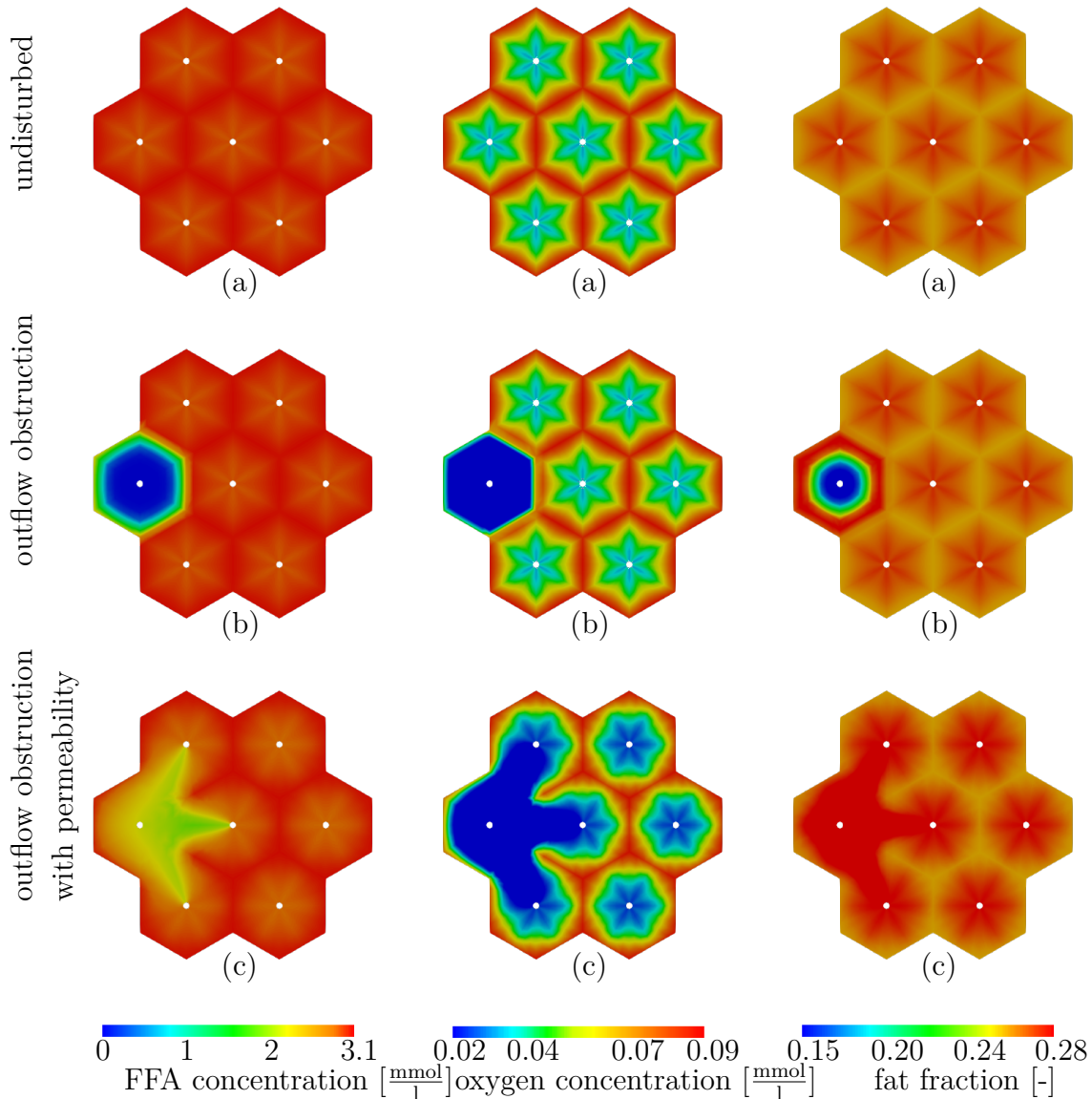


Figure 7.10: Deposition of nutrients and fat accumulation after 1610 seconds of simulation time. First slot: contour plot for FFA concentration $[\frac{\text{mmol}}{\text{l}}]$. Second slot: contour plot for oxygen concentration $[\frac{\text{mmol}}{\text{l}}]$. Third slot: contour plot for fat volume fraction [-]. (a) Undisturbed distribution, (b) Outflow obstruction, (c) Outflow obstruction with permeability.

below, so that higher concentrations of the external substances are present in this area. In the spatial distribution of the fat in this example, the strong influence of the oxygen gradient can be seen. Although the concentration of FFA in the areas

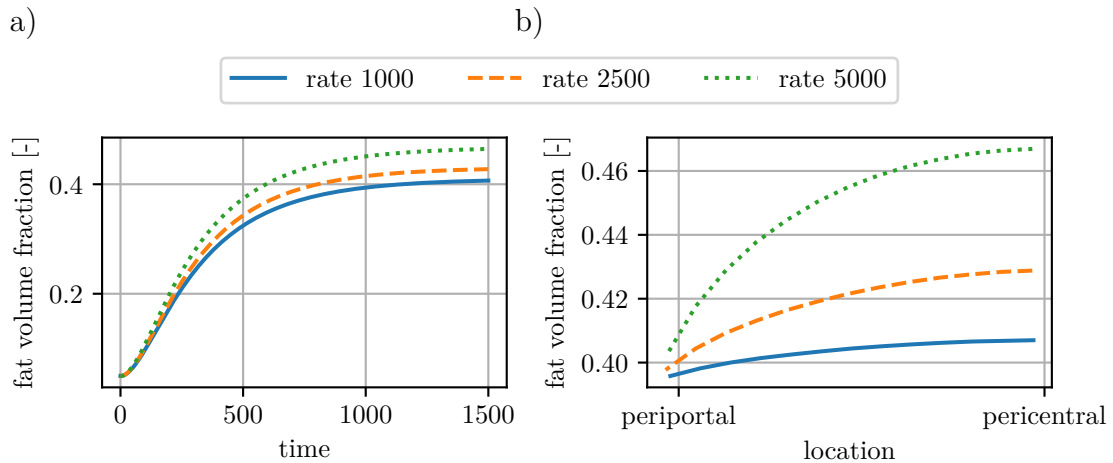


Figure 7.11: Evaluation of fat volume fraction n^T for different rates of oxygen. a) Change of fat volume fraction n^T over 1500 time steps, b) spatial evolution from periportal to pericentral zone of one lobule.

is significantly reduced, there is considerable accumulation of fat in the connections between the disturbed lobules and its neighbors. This can be explained by the significantly reduced amount of oxygen in these areas. These examples illustrate that the oxygen gradient is more influencing than the FFA gradient. There is no fat metabolism if the FFA concentration is insufficient, as in situation (b). Additionally, it is evident that the advective transfer has a higher influence than the diffusive transport, as stated in Section 5.6.7. This suggests that outflow obstructions have a significant impact on the accumulation of hepatic fat. As anticipated, a substantial association between microperfusion and fat metabolism is easily discernible, and the disrupted fat metabolism may be caused by an inhomogeneous perfusion pattern.

7.3.2 Development of Liver Tumor

The development of HCC in the liver is influenced by various risk factors as described in Section 2.2.2. In the following, the formation and development of HCC at the liver lobule level will be investigated numerically. Here, a pre-existing NAFLD is considered as a risk factor from which the tumor develops. The BCs remain unchanged to the consideration of the development of NAFLD, so that a pressure gradient of 133 Pa between PF and CV is set as well as initial chemical potentials for external metabolites. Furthermore, HCC is assumed to form from a progressing NAFLD. For

this purpose, a fat value of 30% is used as a threshold for triggering the carcinogenic processes within the cells. However, since a malignant change of the cell towards a tumor cell does not necessarily occur at this fat content, a random algorithm is also implemented. This algorithm allows triggering the functional processes of tumor formation at the cellular level with a predefined probability. Here, both the triggering itself and the spatial point of the initial tumor are determined.

Development during NAFLD

For the numerical simulation of HCC, not only its time progression and the associated dependencies are important, but also the cause of development is of particular importance. One risk factor is a pre-existing chronic disease such as NAFLD. Due to the accumulation of fat in the hepatocytes, these easily turn into carcinogenic cells, resulting in liver cancer. In order to represent this relationship numerically, the increase of the tumor phase n^T is no longer described only with the help of Monod kinetics but extended by the dependence of the current volume fraction of the fat phase n^T , with $\hat{\rho}^C = \hat{\rho}^C(n^T)$. This dependence is accounted for using the threshold value n_{crit}^T , which represents the critical level of NAFLD and from which carcinogenic processes can be triggered. As described in Section 6.1.2, tumor tissue development requires nutrients, which are present as glucose in this scenario and are consumed during the process.

The process of tumor development resulting from NAFLD is illustrated in Figure 7.12, where the volume fractions of fat n^T and tumor n^C , the concentration of glucose c^{FGl} , and the pressure p^{FR} in a lobule are evaluated. Rotationally symmetric boundary conditions are exploited to consider only one-twelfth of the entire ideal hexagonal lobule for the simulation. The different output values are evaluated at different time points and presented chronologically from left to right. The pressure distribution reveals a pressure gradient of 1 mmHG respectively 133 Pa between the PF and the CV. The material parameters for this simulation are shown in Table 7.3. At the beginning of the calculation, only the development of NAFLD is simulated, with the corresponding metabolism from Section 6.1.1 activated. The first results show the state when the NAFLD is fully developed and the critical threshold is reached. This results in an increase in the volume fraction of fat n^T as well as an increase in geometry due to the growth processes, see Section 5.6.8. Since the tumor metabolism

Table 7.3: Material parameters of a liver lobule for the simulation of tumor development

Parameter	Value	Unit	Remark
n_{0S}^S	0.7	-	Initial volume fraction solid
n_{0S}^T	0.05	-	Initial volume fraction fat
n_{0S}^T	0.05	-	Initial volume fraction tumor
n_{0S}^F	0.2	-	Initial volume fraction fluid
μ^S, μ^T	$4 \cdot 10^4$	Pa	Lamé constant
λ^S, λ^T	$3 \cdot 10^4$	Pa	Lamé constant
θ	280	K	Temperature
R	8.3144	J/molK	Gas constant
k_D	$0.2 \cdot 10^{-8}$	m/s	Darcy permeability
$\hat{\rho}_{\max}^C$	0.3	kg/m ³ s	maximal growth rate
C_x	30	mol/g	growth yield constant
K_C	0.5	mmol/l	Monod constant
m	1	mol/(g s)	maintenance coefficient
Y_G	100	mol/g	growth yield constant

is not yet triggered in this time period, the volume fraction of the tumor n^C as well as the glucose concentration c^{FGl} remain constant, and the pressure distribution is also unaffected. After about 400 time steps, the amount of fat within the lobules reaches the critical value n_{crit}^T and triggers a random algorithm by exceeding this value. This algorithm controls the time at which cancer-inducing processes arise in the hepatocytes and thus, on the cell scale, the metabolism from Section 6.1.2 is activated. In the further course, the volume fraction of the tumor n^C increases steadily. The emerging tumor consumes glucose and thus reduces the concentration c^{FGl} within the lobule, since it can no longer be adequately transported to the CV. Finally, a tumor formation in the periportal zone is recognizable. The volume fraction of the tumor n^T shows a significant increase, which develops due to the supply of nutrients through the portal fields immediately adjacent to them. The associated degradation of glucose in this area as well as the undersupply of the rest of the lobule is evident in the spatial distribution of glucose. This is significantly reduced in the pericentral zone, so that the development of the tumor also progresses with a lower rate $\hat{\rho}^C$. Furthermore, the additional growth processes occurring during tumor formation lead to a significant increase in geometry. Further evaluations of the growth processes during different

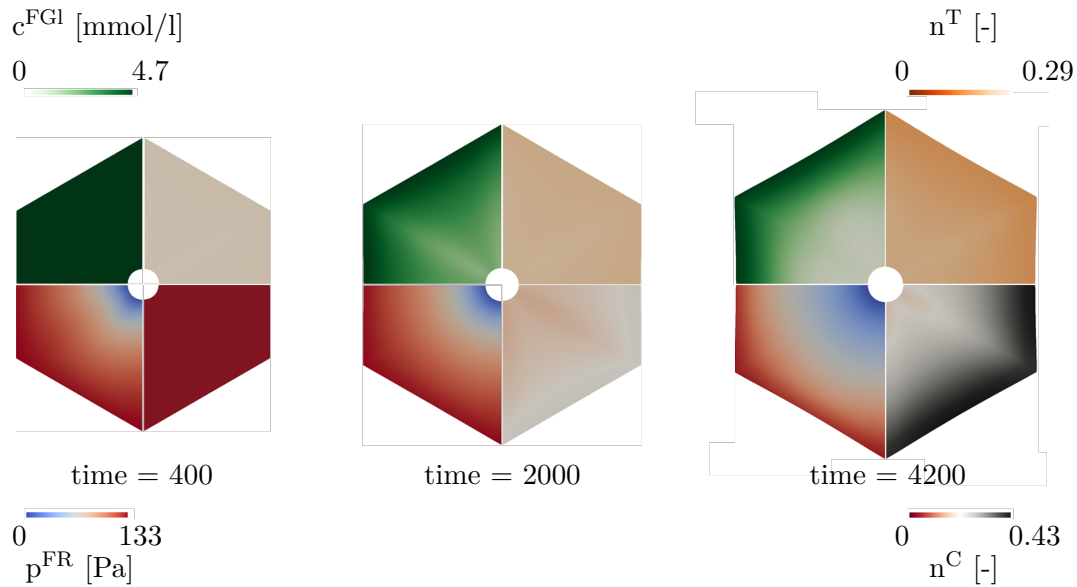


Figure 7.12: Evaluation of combined NAFLD and tumor development at different time points. Each hexagonal liver lobule is divided in four parts, namely the volume fraction of fat tissue n^T (upper right), volume fraction of tumor tissue n^C (lower right), pressure p^{FR} (lower left), and glucose concentration c^{FGl} (upper left)

disease patterns can be found in Section 7.3.3. In the evaluations, the coupling of the hepatic and function and the microcirculation of the liver also becomes clear. As HCC increases, the spatial pressure distribution in the lobule shown in the lower left part changes significantly, due to altered processes on the microscale. Further evaluations of the coupling of function and perfusion in the liver are provided in Section 7.5.

Figure 7.13 shows the progression of the different volume fractions during the development of a liver tumor. Here, Subfigure 7.13 a) considers the results at a point in the pericentral zone, while Subfigure 7.13 b) examines a point in the periportal zone. It becomes apparent that initially the volume fraction of fatty tissue n^T (orange dashed line) increases and as a consequence the healthy liver tissue n^S (blue solid line) decreases, since no tumor growth is activated in this period. This occurs almost identically in both zones, although there is a slight pericentral zonation (see Section 7.3.1). Once the threshold of critical fat content is exceeded, the random algorithm is activated, which allows tumor growth from a certain point. This is clearly visible in the increase of the volume fraction of the tumor tissue n^C (green dotted line).

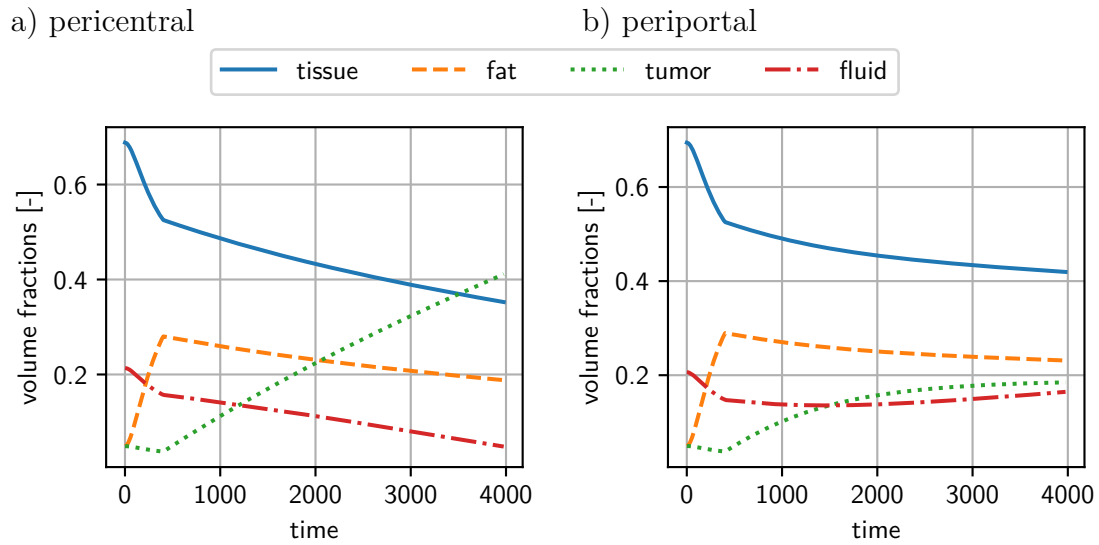


Figure 7.13: Evaluation of volume fractions for liver tissue n^S , fat tissue n^T , tumor tissue n^T and blood n^F during the development of HCC in a) the pericentral zone and b) the periportal zone. Tumor growth is activated after 400 time steps triggered by the critical fat amount.

Due to the coupling of the individual processes, this has a direct effect on the other volume fractions, which decrease accordingly. The development of the tumor occurs predominantly in the pericentral zone. This zonation is due to the dependence of the mass exchange of the tumor phase $\hat{\rho}^C$ on the concentration of glucose c^{FGl} . Glucose is transported in the nutrient-rich blood of the PV from the digestive tract into the liver and flows into the lobules at the PFs. Here, the developing tumor in the pericentral zone is directly and continuously supplied with nutrients. As the HCC consumes the glucose, implemented by the mass exchange of the concentration of glucose $\hat{\rho}^{FGl}$, the concentration of glucose in the blood decreases and fewer nutrients are transported to the pericentral zone of the lobules by advection and diffusion, see Figure 7.14.

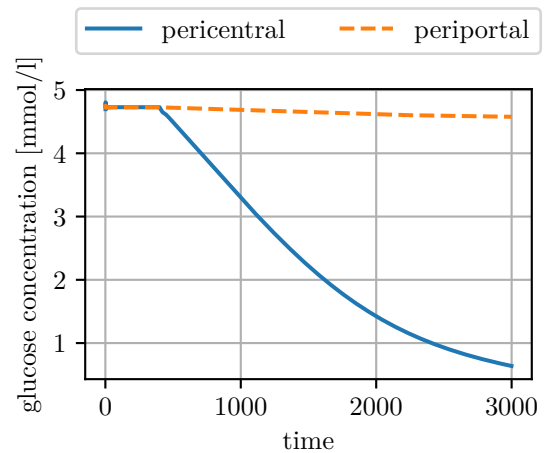


Figure 7.14: Evaluation of glucose concentration c^{FGl} during the development of HCC in a) the pericentral zone and b) the periportal zone.

Considering the glucose concentration c^{FGI} over the time of tumor growth, it is evident that glucose is present almost unaltered in the periportal zone due to the inflow of nutrients and thus promotes tumor growth. In the vicinity of the CV, on the other hand, a significant reduction is apparent, which is induced by processes at the cellular level. A reduced glucose concentration c^{FGI} in this area therefore also reduces tumor mass increase $\hat{\rho}^{\text{C}}$.

Figure 7.15 illustrates two histological images of HCC in human livers. On the left, HCC is developed without an additional NAFLD, whereas the liver on the right shows a clear accumulation of fat next to the tumor tissue.

a) HCC in normal liver

b) HCC during NAFLD

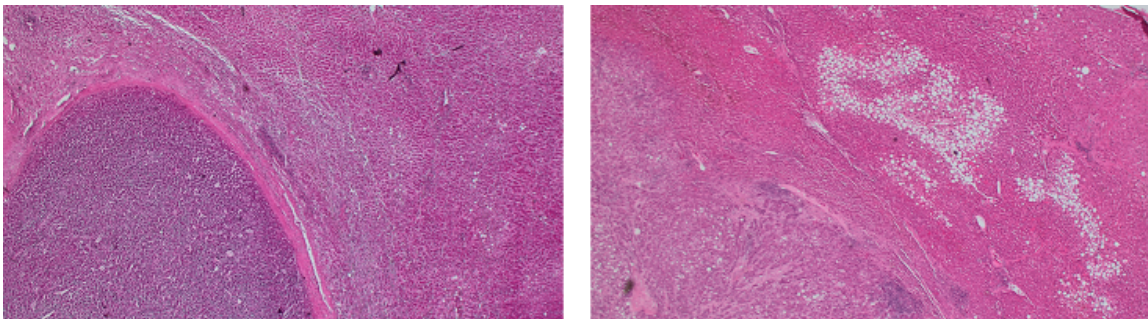


Figure 7.15: Histological images of HCC a) in a healthy human liver, b) in a human liver with additional NAFLD characterized by white fat droplets.⁵

It is clear that the spread of the tumor is well beyond the size of a liver lobule. This is in agreement with the results of the simulation, which show a zoned expansion, but the volume fraction in the entire liver lobule increases significantly. Therefore, due to the functionality of the liver by a structure of identical functional units, the simulation of a single lobule can be assumed characteristic of an area in the liver.

7.3.3 Evaluation of Growth Processes

During the development of NAFLD and liver tumors, mechanical growth processes occur. The growth approach from Section 5.6.8 will now be examined in more detail using these two diseases as examples. The central point of the approach is the splitting of the deformation gradient \mathbf{F}_S into an elastic part \mathbf{F}_{Se} and a growth part \mathbf{F}_{Sg} , the

⁵© PD Dr. med. Hans-Michael Tautenhahn, Jena University Hospital

latter depending on the mass exchange $\hat{\rho}^\alpha$. To evaluate the growth processes in the form of the total deformation gradient and the growth part in both the pericentral and periportal zones are evaluated, as shown in Figure 7.16.

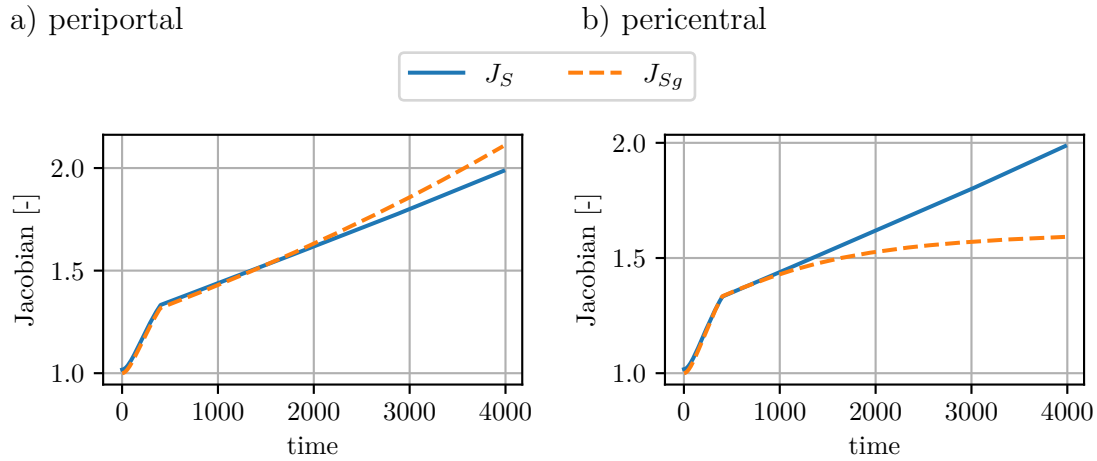


Figure 7.16: Evaluation of Jacobian J_S and its growth part J_{S_g} over time in the a) periportal and b) pericentral zone. In the first 400 time steps, only NAFLD is present, before the growth of the tumor is triggered.

Although in both cases there is inhomogeneous growth with zoned or localized confined processes, at first the two parts of the deformation gradient are located almost atop each other. The difference only becomes larger with increasing time and increasing volume fraction of the tumor n^C . Moreover, despite the opposing zonation of the two processes, it increases significantly more in the periportal zone. These phenomena can be explained by the combination of the two growth approaches in Section 5.6.8. At the beginning, only a NAFLD develops; tumor-initiating processes are not yet activated. The growth fraction of the deformation gradient J_{S_g} depends directly on the mass transfer, so that in the pericentrally zoned process of NAFLD it also increases significantly in this area. Through the subsequent formation of the tumor, the growth fraction is again substantially increased, since here the mass exchange $\hat{\rho}^C$ is summative to that of the fat $\hat{\rho}^T$. The increase in the volume fraction is greater than during NAFLD, which is why there is a bigger increment. However, since this is occurring over a longer period of time, the slope is flatter. The two processes differ greatly in their inhomogeneity. NAFLD forms a zoned pattern in fat distribution, but the inhomogeneity or locality is not as pronounced as in a tumor and fat also develops in the periportal zone. For this reason, the stress distribution is much more homogeneous than during tumor formation. There is therefore less constraint

within the body due to differential growth, which would have to be compensated by the elastic component of the deformation gradient \mathbf{F}_{Se} . This explains the small difference between the total deformation \mathbf{F}_{S} and its growth part \mathbf{F}_{Sg} . However, as the increase in the volume fraction of the tumor n^{C} is much more inhomogeneous, constraints arise in which healthy tissue is displaced by the tumor. These constraints have to be compensated, which is shown by the different values of the Jacobian J_{S} and its growth fraction J_{Sg} . In this example, the tumor grows mainly in the periportal zone, so that the proportion of J_{Sg} is significantly higher in this area. The growth is compensated by a low elastic part \mathbf{F}_{Se} . In the pericentral zone, tumor growth is significantly decreased and thus J_{Sg} is also smaller. However, constraints from the growing tissue have an effect here, which must also be compensated for by the elastic part \mathbf{F}_{Se} , but this time by accretion rather than compression, which leads to an increased elastic fraction \mathbf{F}_{Se} .

7.3.4 Detoxification of Paracetamol and necrosis

By means of the processes on the cellular scale described in Section 6.1.3, the metabolism of paracetamol degradation and the resulting consequences on the function-perfusion relationship can be determined. The paracetamol metabolism is directly dependent on the given dose and thus on the current concentration in the blood.

Paracetamol medication in healthy patients

In this example, the administration of a defined amount of paracetamol, its transport and degradation in a liver lobule is simulated. Figure 7.17 shows the concentration of paracetamol c^{FPara} decreasing over time due to detoxification in the blood. As a result of the existing concentration of paracetamol, the endogenous glutathiones c^{SGt} are decomposed to neutralize the harmful substances shown in Figure 7.17. Consequently, the concentration in the tissues decreases over time. While sufficient glutathiones are still present in a normal dosage, their concentration is exhausted in an overdose and necrotic processes are triggered, resulting in necrotic tissue.

Falling below the critical limit of glutathione concentration c^{SGt} triggers the necrotic processes, which are manifested by the transformation of healthy liver tissue into

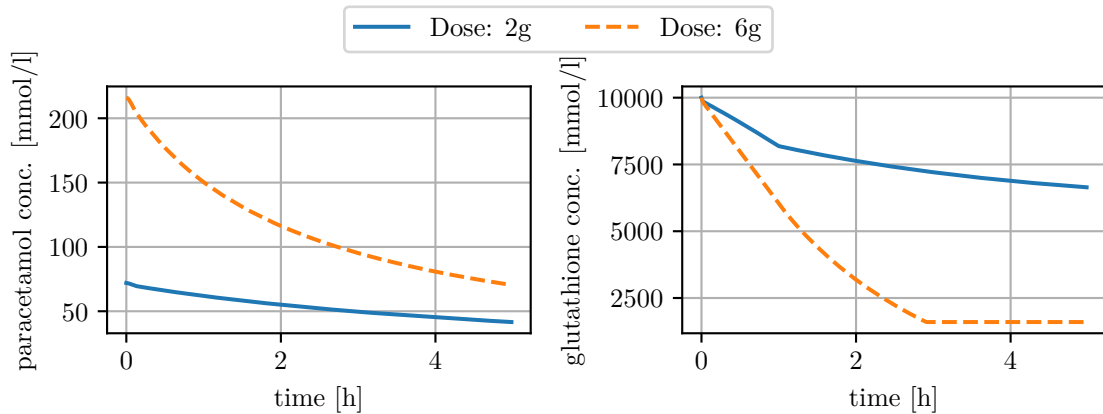


Figure 7.17: Evaluation of paracetamol and glutathione concentration for different doses. Left: Concentration of paracetamol c^{FPara} over time evaluated in the pericentral zone during a dose of 2 g (blue, solid line) and 6 g (orange, dashed line), Right: Concentration of glutathione c^{SGt} over time evaluated in the pericentral zone during a dose of 2 g (blue, solid line) and 6 g (orange, dashed line).

necrotic tissue. Figure 7.18 illustrates the changes in volume fractions at different doses of the analgesic. The evaluation is performed spatially in one liver lobule as well as over time in one point in the pericentral zone. While no changes in the temporal and spatial distribution occur at a dose of 2000mg, there is a transition from healthy liver tissue n^{S} to necrotic cells n^{N} at a higher dose of 6000mg. As described in Section 2.2.3, the processes during paracetamol degradation and the formation of necrotic tissue occur in a zoned pattern due to the heterogeneous distribution of the CYP2E1 enzyme. This is also evident in the spatial distribution of volume fractions in Figure 7.18, where the formation of necrosis is mainly visible around the CV.

Paracetamol medication in patients with NAFLD

During the development of NAFLD, different processes happen that could have an impact on drug degradation, such as the development of NAFLD with a phase transition from healthy tissue n^{S} to fat tissue n^{T} or a change in microcirculation, see Section 7.3.1. Therefore, the interactions of both hepatic processes will be investigated. For this purpose, the formation of a fatty liver is first simulated up to a value of 20% fatty tissue represented by a volume fraction $n^{\text{T}} = 0.2$. Subsequently, the administration of 6g paracetamol - i.e. an overdose - is applied after 42h. For

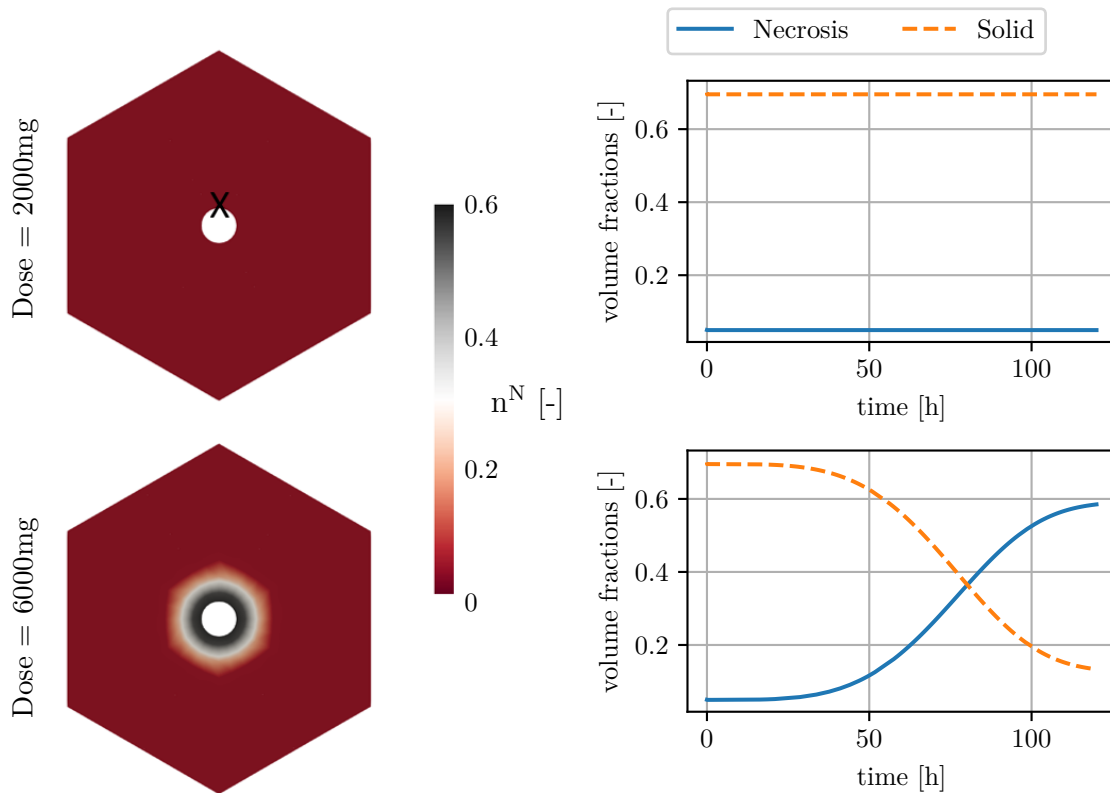


Figure 7.18: Evaluation of volume fractions during necrosis after different doses of paracetamol. Left: Spatial evaluation of volume fraction of necrotic tissue n^N in one liver lobule with a given dose of 2000 mg (top) and 6000 mg (bottom). Right: Evaluation of volume fractions of necrotic tissue n^N (blue, solid line) and healthy tissue n^S (orange, dashed line) in one point at the pericentral zone.

simplification, the fat metabolism is stopped from this point and the previously applied distribution remains constant. Figure 7.19 illustrates the volume fractions over time for the whole period including the development of NAFLD and the time after medication. When examining the volume fraction after medication, it is apparent that the known pattern emerges in which healthy tissue is converted to necrotic tissue.

However, the volume fraction of healthy tissue n^S is already visibly reduced at the time of medication, while necrosis n^N remains absent. This is due to the formation of fatty liver and the associated phase transition $\hat{\rho}^T$. If the development of the volume fractions after drug administration is subsequently compared with the previous courses without NAFLD in Figure 7.19 b), a significant difference becomes evident, which is mainly due to the reduced volume fraction n^S caused by fat formation. However,

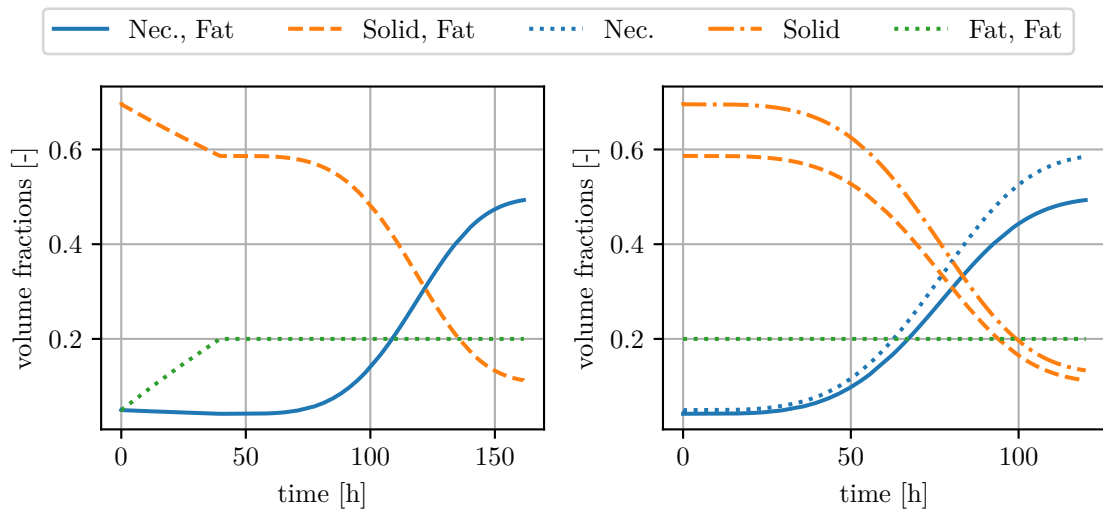


Figure 7.19: Evaluation of volume fractions during necrosis with and without additional NAFLD. Left: Volume fraction for necrosis n^N (blue, solid), healthy tissue n^S (orange, dashed), and fat n^T (green, dotted) with paracetamol administration after 42h. Left: Evaluation over time after medication with additional volume fractions without NAFLD for necrosis n^N (blue, dotted) and healthy tissue n^S (orange, dashdotted).

due to the changed conditions, the development of necrosis n^N is also altered and is weaker under NAFLD, but still reaches a critical final value. The evaluation of

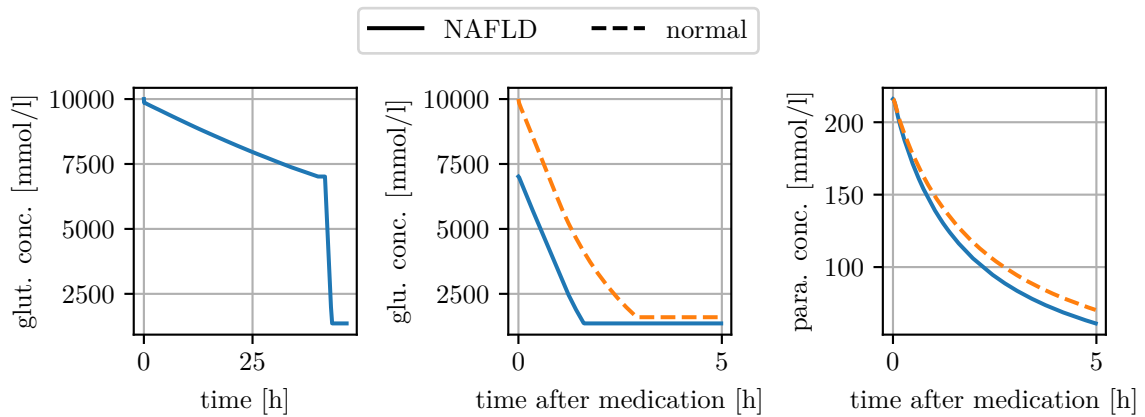


Figure 7.20: Evaluation of paracetamol and glutathione concentration with additional NAFLD. a) Glutathione concentration c^{SGt} for healthy livers and under NAFLD from beginning of fat formation (left) and after medication (right) at one point in the pericentral zone. b) Paracetamol concentration c^{FPara} after medication at one point in the pericentral zone.

the time course of the concentrations of glutathione c^{SGt} and paracetamol c^{FPara} in Figure 7.20 also shows differences between a normal liver and a fatty liver. Here, the critical limit of the glutathione concentration c^{SGt} in the tissue is reached significantly earlier, which leads to an earlier triggering of necrosis and thus to a lower possible dosage of paracetamol. Furthermore, it is shown that the concentration of glutathione c^{SGt} is already reduced before the administration of the drug. Since glutathiones are endogenous substances that are dissolved in the tissue and not in the blood, their concentration in the model depends significantly on the presence of healthy tissue and thus on its volume fraction n^{S} . If this is reduced, it also leads to a reduction in the concentration of glutathione. The altered flow conditions during NAFLD thus also affect the degradation of paracetamol, and differences in the concentration course c^{FPara} compared with administration in healthy patients are evident in Figure 7.20 b).

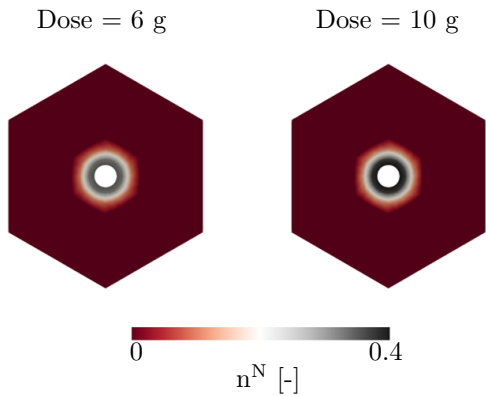
Discussion of results

It is evident that the formation of necrosis occurs primarily around the CV, which is the pericentral zone. This pattern can also be observed in human paracetamol overdoses [54] as well as in animal experiments. Figure 7.21 illustrates the influence of the dose on formation of necrotic tissue, where Figure 7.21 a) shows a lower volume fraction n^{N} during lower doses and b) indicates the same behavior also in temporal evaluation. A pericentral pattern of distribution of necrosis is evident in the simulations. This is also found in animal experiments on mice. In Figures 7.21 c) and 7.21 d), it is clear that the areas around the CV have a lighter hue, representing a structural change of the tissue towards necrosis. In contrast, the tissue around the PFs is intact and no change can be observed. Therefore, the results obtained from the simulation are consistent with the experimentally and clinically observed results.

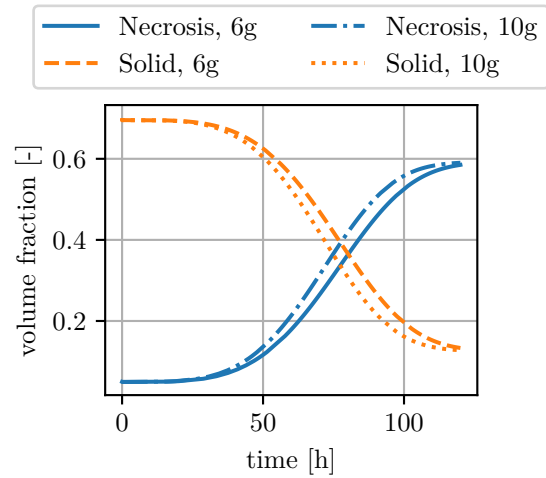
7.4 Simulation of Perfusion Changes after Extended Liver Resection

Severe liver diseases such as tumors can be treated by resection of the damaged liver tissue under specific conditions. This involves severing the blood-carrying vessels

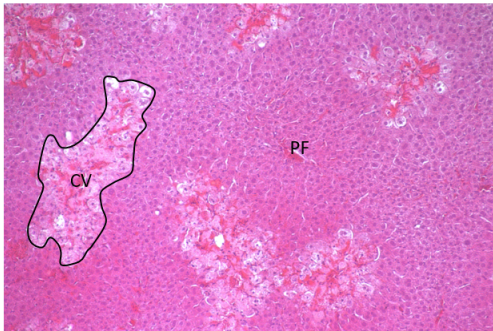
a) Spatial distribution



b) Temporal distribution



c) Histology H&E



d) Histology GS

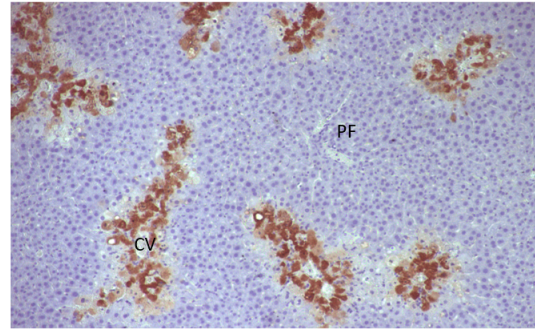


Figure 7.21: Validation of necrosis simulation. a) Spatial distribution of necrotic volume fraction n^N in one liver lobule for a dose of 6g and 10g, b) Evaluation of necrotic n^N and solid n^S volume fraction over time for a dose of 6g and 10g, c) Histological image of a H&E stained tissue of a mice with paracetamol overdose, d) Histological image of a GS parallel section showing the pericentral zone in brown. Histological images reproduced from [142]

and disrupting the perfusion of the entire organ. Since the amount of blood passing through the liver remains nearly identical, there is a change in the flow and pressure conditions in the whole organ and thus also in the microperfusion represented by the pressure at the terminal branches of PV and HA on the lobular scale. Using the model from Section 6.2, the altered pressure, flow and geometric conditions of the vascular vessels during this surgical interventions and adjusting physical conditions can be determined. After surgical interventions, such as (e)PHx, a change in function

can be determined [37, 38]. For this reason, a disturbance of the vascular tree in different generations is applied to investigate changes in the microperfusion. Each of these calculations illustrates a resection of different extent, a disruption of an early generation means more resected mass than a disruption in a later generation. In response to the increased blood flow, the vessels dilate, which also leads to a change in pressure and flow. In order to better take into account individual physical characteristics, three different dilations of 5%, 10% and 15% are assumed.

A resection and thus a disturbance in a certain generation of blood vessels leads to a change in the flow conditions. To determine these, the conditions in the healthy and disturbed strand are approximated by iteration of the conditions and thus the conditions after resection are determined. Two approaches are as followed: one is to approximate the pressure and the other is to approximate the flow velocity, whereas the other parameter is predefined.

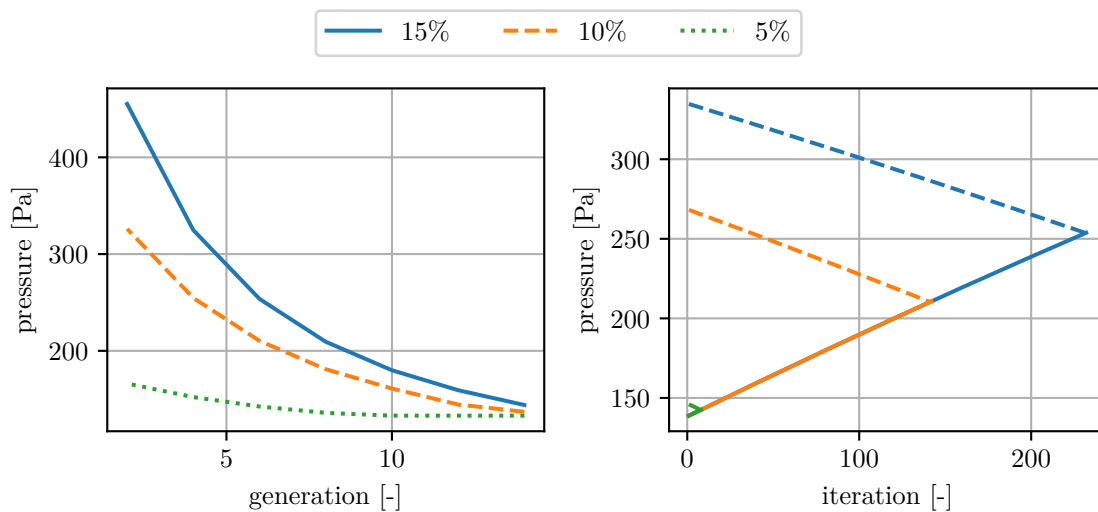


Figure 7.22: Evaluation of pressure over generations and the required number of iterations. Left: Resulting pressure plotted over the generation at which the system is disturbed. Here, different dilations of the vessels of 15% (blue solid line), 10% (orange dashed line) and 5% (green dotted line) are considered. Right: Comparison of iterations to obtain an equilibrium between healthy liver (solid line) and disturbed liver (dashed line).

Figure 7.22 shows the evaluation of the pressure at the terminal branch of the PF during disruptions in different generations with altered widths of the vessels. Here, a resection of larger extent shows a significantly changed pressure and thus a smaller

pressure gradient in the hepatic lobule. A greater widening of the vessels also increases the pressure and results in altered pressure conditions in the lobule, since the flow velocity stays constant. The pressure values are calculated using an iteration scheme for pressure in healthy and disturbed liver, where a larger dilation of the vessel require more iteration and leading to a higher resulting pressure as shown by the larger number of required iterations in Figure 7.22 on the right.

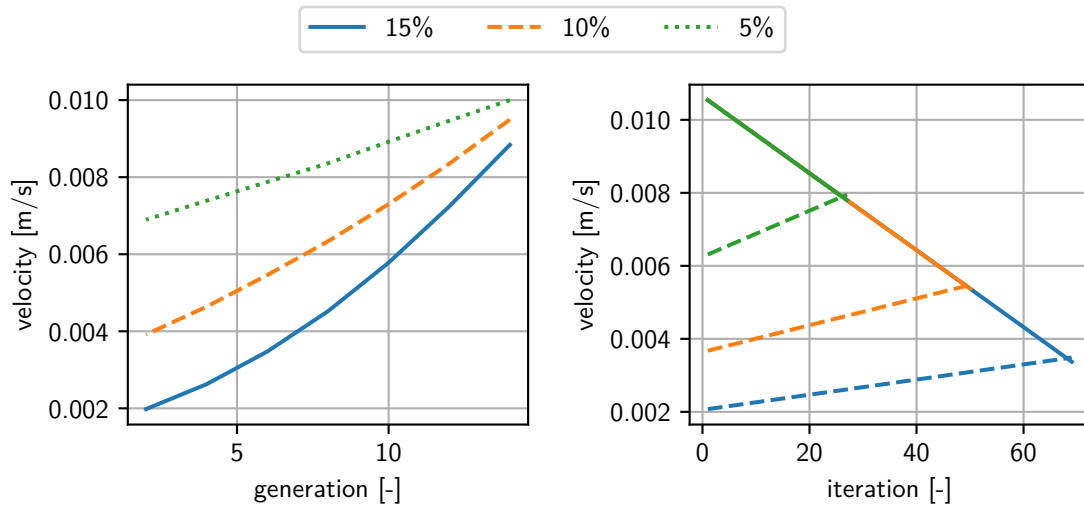


Figure 7.23: Evaluation of the resulting velocity plotted over the generation at which the system is disturbed. Here, different dilations of the vessels of 15% (blue solid line), 10% (orange dashed line) and 5% (green dotted line) are considered.

Additionally, the model can be iterated to approximate the velocity instead of pressure. The evaluation of velocity in Figure 7.23 also shows a greater change in flow ratios with a larger resection and thus disruption in an earlier generation. Here, however, dilatation of the vessels results in a lower velocity within the vessel. This is also evident in the evaluation of the iteration behavior, where more iterations are required under a higher dilation.

These results can also be observed in experiments in rats. DAHMEN et al. [41] showed in their work the correlation between resection extent and the change of blood pressure in the portal vein. To validate the model based on these experiments, a pressure of 11 mmHG is assumed as the initial value, so that a mean pressure of about 8 mmHG is established inside the vascular tree analogous to the baseline pressure in the experiments. Subsequently, disturbances are applied in different generations

representing different stages of resection and the resulting pressure is compared with the experimentally obtained data. The dilation of the vessels is assumed to be 5%, analogous to the experimentally measured change in sinusoidal diameter. Thereby, the

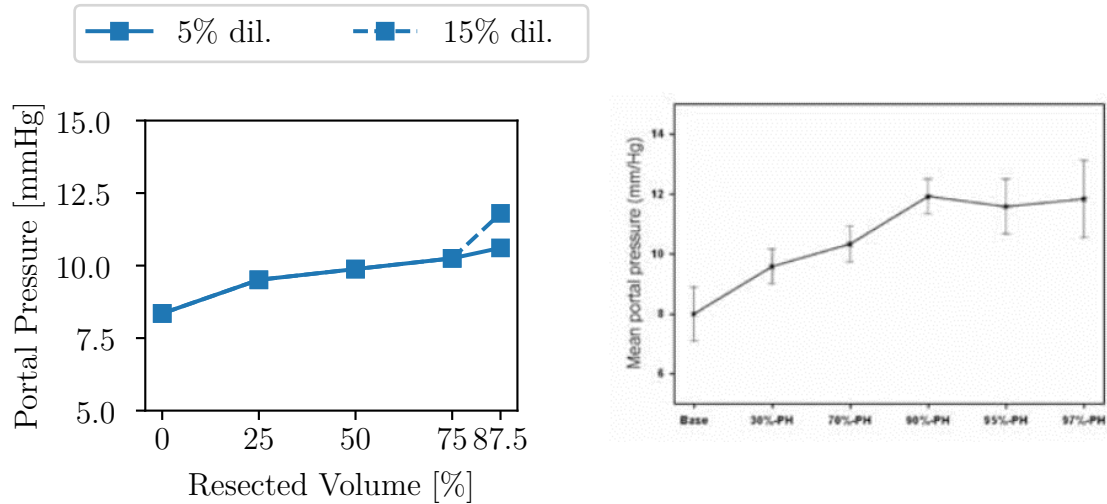


Figure 7.24: Validation of simulation with experimental results for pressure after different resections. Left: Calculated results for mid portal pressure during different stages of liver resection for 5% dilation or 15% dilation in case of 90% resection. Right: Measured values in rats by DAHMEN et al. [41], reproduced with permission.

results in Figure 7.24 show a clear agreement of the computationally determined data with the experiments. Starting from a baseline value of 8 mmHG, the mean portal pressure increases to about 10 mmHG by 70% liver resection. In the calculation, the slope towards 90% resection remains approximately identical, whereas in the experiments a clear elevation can be seen. This is presumably due to the more distinct dilation of the vessels, which was also measured in a clear increase in sinusoidal diameter in the experiments at 90% resection. For this reason, a larger dilation of the vessels was assumed in a further calculation, which leads to a pressure of approximately 12 mmHG and thus to the level of the measured values. When comparing the concrete values, the base value is the one farthest away from the experimental values with a deviation of about 4%; for the other extents of resection, the error is less than 1% in each case.

7.5 Function-Perfusion Relationship

The results of simulations of a fatty liver (Section 7.3.1), tumor growth (Section 7.3.2) and necrosis (Section 7.3.4) already reveal a clear correlation between function and perfusion in the liver. Altered function is assumed to have a direct influence on microperfusion in the liver lobules. In this chapter, the effect of perfusion changes on the hepatic function as well as the effect of hepatic disease on microperfusion will be examined. Therefore, the influence of an outflow obstruction that can for example result from a cardiovascular disease in the patient and its effect on formation of hepatic disease is investigated. Subsequently, the flow behavior of a healthy liver is compared to the one during NAFLD and liver tumors.

7.5.1 Evaluation of Function during Perfusion Changes

Perfusion changes during increased CVP

However, perfusion within the hepatic lobules may not only be affected by surgical procedures, but may also be impaired by outflow disturbances at the CV clinically determined by a changed CVP, see Section 2.2.4.

To describe the phenomena during increased CVP, the outflow boundary conditions at the CV are adjusted to the changed conditions. Under the influence of different outflow pressures, the fat volume fraction n^T within one liver lobule is evaluated.

Figure 7.25 illustrates the evaluation of the fat volume fraction n^T analyzed at a point in the pericentral zone of the lobule where the most fat accumulation is expected. The different lines show the variation in fat volume fraction under different pressures at the CV. The normal CVP in healthy patients is assumed to be 0 Pa, while the increased pressure in the vena cava is simulated by different outflow pressures resulting in a lower pressure gradient along the liver lobule. It becomes visible that the fat volume fraction n^T increases with lower pressure gradient in the lobule. Thereby, the correlation is not linear, but influence of changed CVP increases with decrease of pressure gradient. The influence of the changed CVP can be represented by the coupled approach of the governing equations and the resulting coupling of the perfusion and functional processes. The disturbed microperfusion on lobular scale

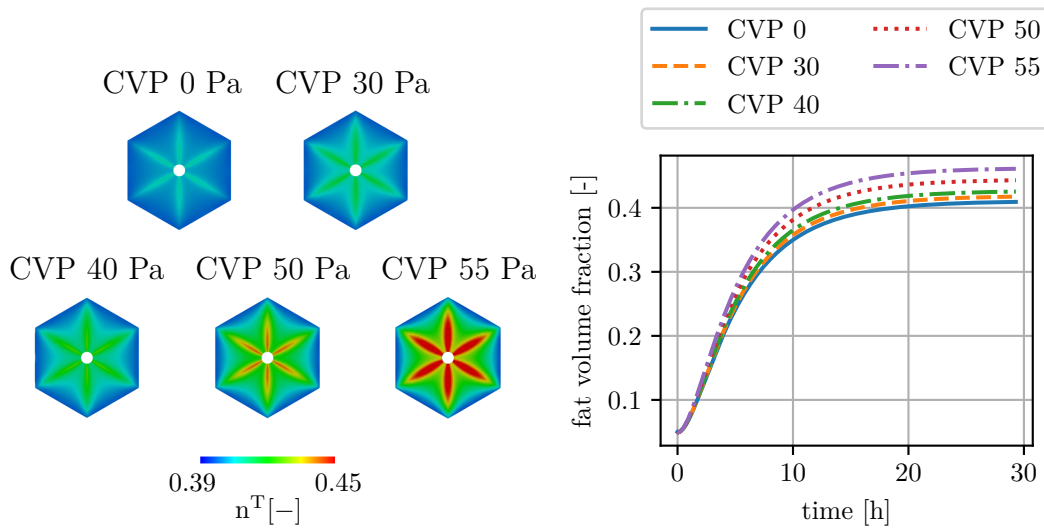


Figure 7.25: Evaluation of fat volume fraction for various CVPs. A CVP of 0 Pa represents the initial condition in a healthy patient. Left: spatial distribution of fat volume fraction n^T [-], Right: temporal development of fat volume fraction n^T [-] over 1750 time steps

and the resulting reduced perfusion gradient thus have a direct influence on hepatic function and of fat metabolism on the microscale.

7.5.2 Evaluation of Microperfusion during Diseases

Evaluation of microperfusion during NAFLD

The formation of fat vacuoles in the hepatocytes of the liver parenchyma also affects the structural allocation at the hepatic lobule level and leads to a change in the liver cell architecture. This also affects blood flow in adjacent capillaries, resulting in altered perfusion during NAFLD.

Therefore, the association between fat content and blood perfusion in the results of the coupled function-perfusion simulation is investigated. Figure 7.26 illustrates the impact of the accumulation of fat on the microperfusion in one lobule over 1610 seconds of simulation time by evaluating the relationship between seepage velocity and fat volume fraction.

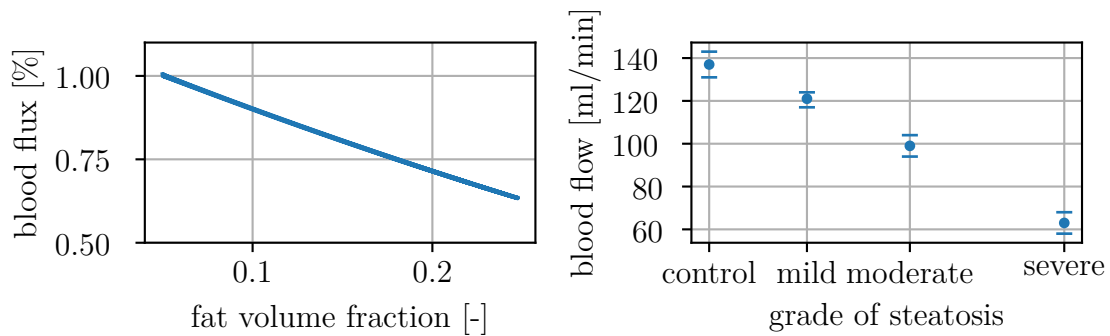
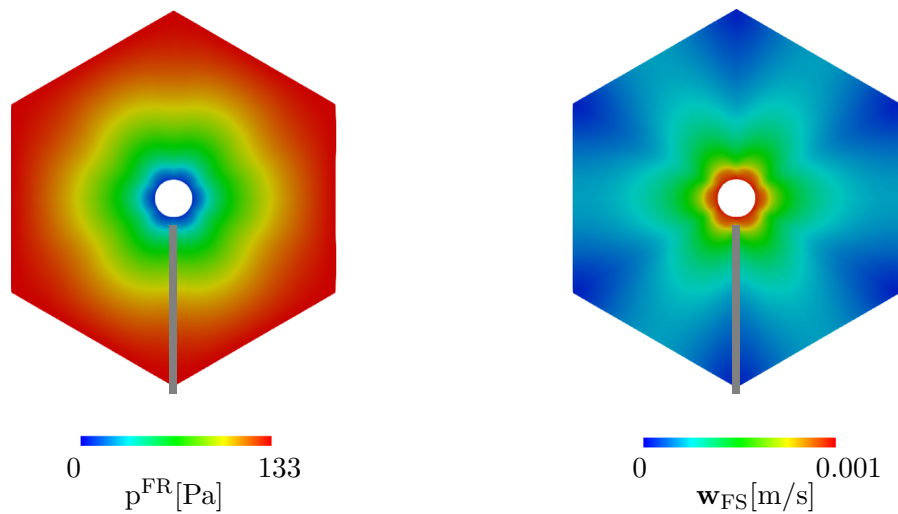


Figure 7.26: Numerical simulation of the relation between the fat accumulation [-] and the seepage velocity in relation to the initial one [%]. The diagram shows the results over 1610 seconds of simulation time at the mid zone of a lobule. Similar results were shown in a study of an animal model which evaluates the *in vivo* effect of steatosis on hepatic blood flow, see SEIFALIAN et al. [135], illustrated in the right diagram.

An increased fat accumulation leads to the reduction of the seepage velocity and therefore the blood flux with a nearly linear relation. This correlation has also been investigated in experiments, where SEIFALIAN et al. [135] determined similar results for the effect of graded steatosis on the blood flow in hepatic microperfusion, see Figure 7.26.

A correlation between the hepatic function of fat metabolism on the cellular scale and the coupled microperfusion is also shown in Figure 7.27. The latter illustrates the evaluation of the spatial distribution for pressure and blood velocity after 1610 time steps. The distribution along a sinusoid (gray line) from the periportal to the pericentral zone is also shown with distinction between the initial values (blue solid line) and the values at the end of the simulation with a present NAFLD (orange dashed line). Figure 7.27 shows the zoned distribution of the blood pressure induced by the applied pressure gradient between the CV and the PF. However, this pressure changes with increasing fat content and there is a pressure drop within the sinusoid, which is caused by the change in geometry and therefore a change of the respective considered length from PF to CV. The coupled relationship between function and perfusion is clearly evident when considering blood velocity. With increasing fat content, the blood velocity also decreases significantly and thus indicates a change in microperfusion due to a change in function.

a) spatial distribution



b) plot over line

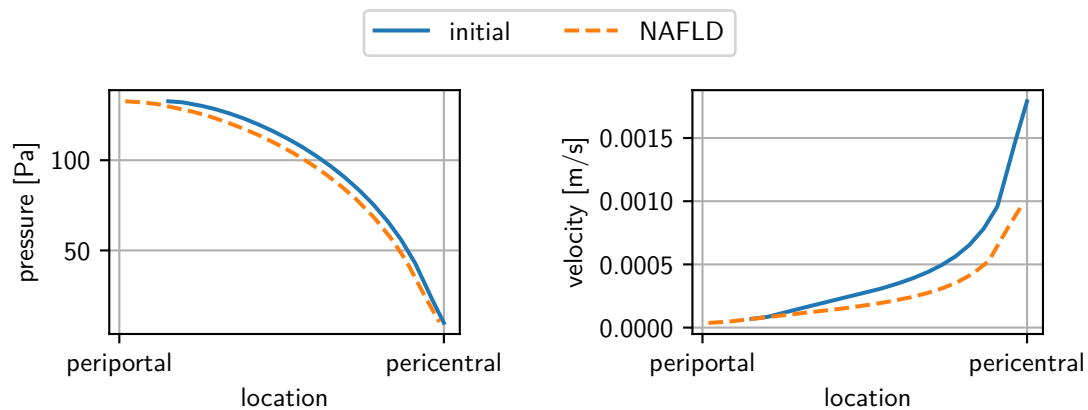
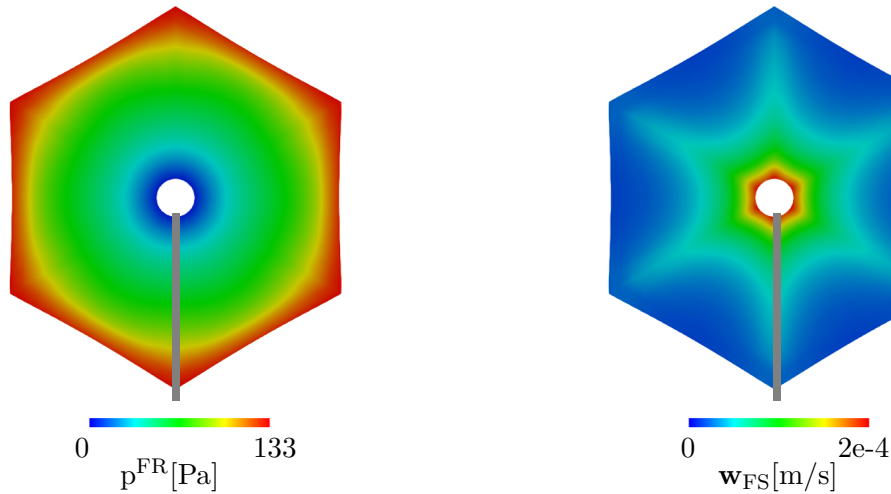


Figure 7.27: Evaluation of relationship between NAFLD and microperfusion. a) spatial distribution of pressure p^{FR} [Pa] and blood velocity w_{FS} [m/s] in one lobule, b) results plotted along one sinusoid represented by gray line. The results compare the evolution along one sinusoid for healthy tissue (blue line) and during NAFLD (orange dashed line)

Evaluation of microperfusion during HCC

After the demonstration of the relationship between the formation of fat in the liver cells and perfusion, it will be determined whether such a function-perfusion relationship also exists in the formation of a tumor. The growth processes and the resulting changes in liver morphology are also expected to alter perfusion.

a) spatial distribution



b) plot over line

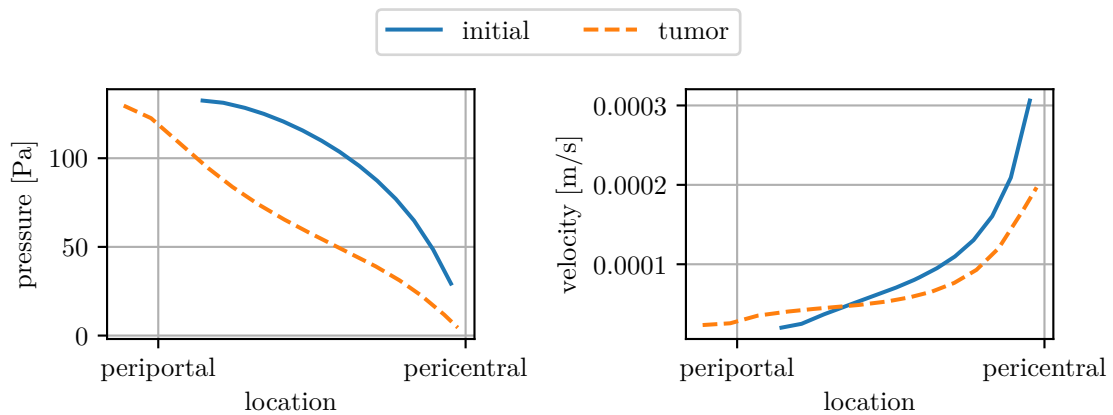


Figure 7.28: Evaluation of relationship between tumor growth and microperfusion. a) spatial distribution of pressure p^{FR} [Pa] and blood velocity w_{FS} [m/s] in one lobule, b) results plotted along one sinusoid represented by gray line. The results compare the evolution along one sinusoid for healthy tissue (blue line) and during tumor (orange dashed line)

Figure 7.28 depicts the spatial distribution of pressure p^{FR} and blood velocity w_{FS} during the development of a tumor after 5000 time steps. In addition, the distribution of both quantities along a sinusoid (gray line) is shown. The initial state represents the liver lobule with a NAFLD right before tumor growth is triggered. Here we compare between the distribution during a liver with NAFLD (blue solid line) and during the development of a tumor (orange dashed line). Clearly, tumor growth has a significant

effect on perfusion. The pressure gradient is no longer homogeneously distributed between CV and PF. The spatial velocity distribution also shows significant differences to the determined microperfusion results in Section 7.2.1. The zoned arrangement of the tumor reveals a significant deviation from the initial state and an influence of a change in function on perfusion. Both pressure and velocity drop significantly during tumor formation. Here, the difference can be seen especially in the pericentral zone, while the area of the tumor continues to be well perfused. These results also show a clear coupling between function (tumor growth) and perfusion in the liver lobule.

However, limitations of the model are still apparent. The pressure is given as a fixed gradient between PF and CV. As a result of the growth of the liver lobule, its geometry changes and thus also the distribution of the pressure. Due to the different growth behavior during NAFLD and tumor growth, which were described and evaluated in section 7.3.3, different pressure changes occur during both disease patterns. In reality, however, a heterogeneous distribution of fat within the whole organ is compensated by pressure adjustments at the terminal ends of the vessel. In perspective, this should be incorporated by coupling a whole organ model, which provides the respective pressures depending on the heterogeneous fat distribution. However, this has not been implemented so far, so that the boundary condition of the pressure was assumed to be constant in a simplified way at first. Therefore, the distribution of the pressure cannot be finally used as evidence of the function-perfusion coupling, whereas the altered perfusion within the liver lobule due to a change in function clearly illustrates this relationship.

7.6 Non-Linear Model Order Reduction

Computer-aided simulations are highly resource intensive and due to the complex model with many degrees of freedom and a multi-scale coupling, a significant amount of computation time is required. To reduce computing time, studies on MOR using ML approaches have been conducted, see LAMBERS et al. [84] and MIELKE et al. [100], where an artificial neural network (ANN) is trained on *in silico* data with a random distribution of selected input variables. Based on a simulation of fat metabolism as a function of FFA and oxygen, the decisive influencing variables on the spatial formation of fat within a liver lobule can be identified.

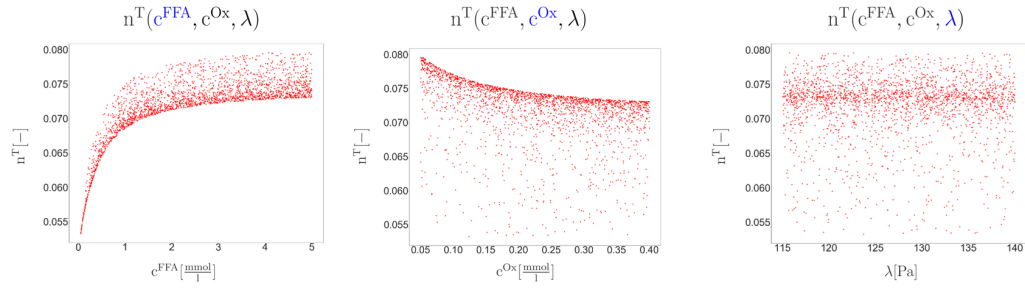


Figure 7.29: Identification of decisive influencing parameters on fat accumulation by plotting all possible solution over one parameter with random distribution of a) FFA concentration with $0.05 < c^{FFA} \leq 5.0 [\frac{mmol}{l}]$, b) oxygen concentration with $0.05 < c^{Ox} \leq 0.4 [\frac{mmol}{l}]$ and c) blood pressure with $115 \leq \lambda \leq 140 [Pa]$. The other parameters in each case are constant.

Figure 7.29 illustrates the fat accumulation in a point when one parameter is randomly distributed over a predefined interval. The remaining parameters are kept constant at their initial values with $c^{FFA} = 3 \frac{mmol}{l}$, $c^{Ox} = 0.091 \frac{mmol}{l}$ and $\lambda = 133 Pa$. Figure 7.29 a) illustrates a higher fat accumulation with an increase in the supplied amount of free fatty acids. In contrast, the volume fraction of fat is reduced with elevated oxygen concentration as seen in Figure 7.29 b). This is explained by the oxidative processes during fat metabolism described in Section 6.1.1. A minor influence on fat accumulation can be detected in the fluctuation of blood pressure illustrated in 7.29 c).

To perform the non-linear MOR using ANN, 2438 *in silico* samples with random distribution of FFA concentration, oxygen concentration and blood pressure served as basis for simulation of fat volume fraction n^T in the area of the lobule. Using these data, a neural network was trained, tested, and validated so that the previously simulated fat evolution is calculated using it alone and without cost- and time-intensive numerical computations. The network consists of 3 inputs namely concentration of FFA and oxygen as well as blood pressure and 85 outputs representing the fat volume fraction at each node of a twelfth lobule. In between the calculation is performed with 2 hidden layers where each contains 30 neurons and an activation function $a(x) = \tanh(x)$.

To evaluate the precision of the developed ANN for calculating fat accumulation, a comparison between the predicted and simulated results is performed. Figure 7.30 shows the evaluated volume fraction of fat at a point within the liver lobule for different

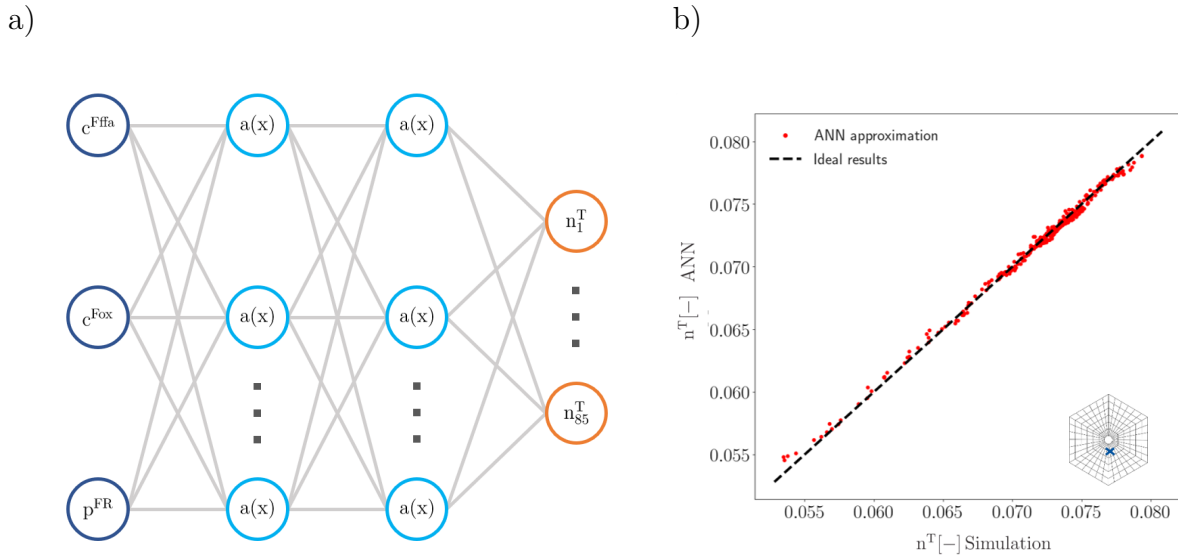


Figure 7.30: Evaluation of lobular processes using an ANN. a) Setup of the ANN with 3 inputs, 2 hidden layers and 85 outputs. b) Comparison of fat volume fraction evaluated at one point of the liver lobule using numerical simulation and ANN.

parameter combinations. The red dots represent the approximation in relation to the simulated result. This leads to an ideal allocation, which is represented by the dashed line. The predicted results differ only marginally from the ideal simulated values and therefore show a high precision. The deviation is increased at lower fat accumulation, which can be explained by the lower number of data in this area. Since most parameter combinations lead to increased fat growth, less data is available for training the neuronal network in the area of a lower volume fraction, so that a prediction becomes less accurate in this region. Spatial prediction in all points of the liver lobule also has a maximum relative error of 0.01 only. This low difference indicates, that the reduced model can serve as a surrogate for the simulation of fat accumulation in one liver lobule.

7.7 Numerical Sensitivity Analysis

When using mathematical models, typically a large number of input parameters play a role. These are easy to incorporate during the model development and allow a broad and complex representation of the simulated processes. However, if these

processes are to be parameterized and validated with clinical and experimental data, a classification of the relevance of individual parameters is essential. The experiments required to determine input values are time- and cost-intensive and therefore their number is limited. In order to make a prediction which parameters are important for the processes and quantities to be investigated and thus should be determined by experiments, a numerical SA is performed.

In general, numerical SAs can be classified into different categories according to PIANOSI et al. [108]. On the one hand, there is the classification into local or global analyses. In a local analysis, the model parameters are varied by a specific value and the resulting influence on the output is determined as uncertainty. The global analysis considers in addition to the model parameters further factors of the calculation like the spatial resolution. The variation of the input parameters takes place in the entire possible space. A further subdivision is made into qualitative and quantitative SA. In qualitative SA, the evaluation is performed with the help of visual assessment or the use of visualization tools, while quantitative SA provides a numerical and reproducible assessment of the influence on the model output. Furthermore, a distinction can be made according to the sampling method. In the One-At-a-Time (OAT) methods, one parameter is varied per sample, the others are left at a fixed value. All-At-a-Time (AAT) methods, on the other hand, vary all parameters at the same time and can therefore determine not only the influence of a single parameter, but also the joint influence of the parameter through interactions with other inputs. OAT methods are mostly used in local SAs, global SAs use both AAT and OAT methods. The type of SA is determined by the overall objective. In a ranking, the selected input parameters are sorted according to their influence on the model output, the screening shows input parameters that have only a negligible influence on the output and the mapping clarifies parameter ranges that have a significant influence.

To perform a SA for the presented model, a workflow according to PIANOSI et al. is applied:

1) Experimental setup

The sensitivity analysis will be performed for the development of NAFLD and tumor growth in one liver lobule. Therefore, the parameters FFA c^{FFFA} and oxygen c^{FOx} concentration as well as glucose concentration c^{FGl} are selected. To capture also influences of mechanical parameters, the initial solid volume

fraction n^S , the Young's modulus for solid E_S and fat/ tumor E_T/ E_C as well as the Poisson's ratio ν will be varied in the SA. In order to incorporate also the microperfusion, the permeability characterized by the Darcy parameter k_D and the initial pressure at the PF p^{FR} are chosen as parameters to be varied. For tumor growth, the growth parameters K_C and μ_{max} will be included in the set of varied parameters. The other parameters are kept constant at the values defined in Table 7.2 and 7.3. With the help of the SA, the influence of the selected parameters on the volume fractions of fat n^T and tumor n^C , blood velocity \mathbf{w}_{FS} and growth J_{Sg} will be determined. For this purpose, the respective values are output after a specified period of time at all nodes. A statistical mean is formed from the nodal values over the area of the liver lobule, which is used as a scalar function in the evaluation.

2) Choice of the SA method

In a first step, a ranking and screening of the parameters will be performed. Due to the relatively high number of parameters and the associated high runtime, the Morris method is suitable for displaying the influence of the parameters on the total output. Subsequently, a Fourier Amplitude Sensitivity Test (FAST) analysis will be conducted with the relevant parameters determined in the Morris method. This variance-based method provides a more precise statement about the sensitivity of the parameters, but requires significantly more samples and therefore runtime. Finally, a Regional Sensitivity Analysis (RSA) will identify regions in the input parameters responsible for a respective output.

3) Choice of variability space, sampling strategy and sampling size

All parameters are varied around a certain value from the literature and/or experiments with the inclusion of the physical proportionality. In the Morris analysis the problem consists of $k=9$ (NAFLD) or $k=10$ (tumor) input parameters. By choosing $r = 15$ model runs the sample size results in $N=r*(k+1) = 150$ resp. 165. For the evaluation of FAST and RSA method, the sample size is set to 2.000 samples.

7.7.1 Morris Method

In order to have a ranking and screening of the relevant parameters for the development of a NAFLD and during tumor growth, the relevance of each selected parameter is determined using the Morris method [101]. Here, parameters for which a certain uncertainty exists are identified and changed stepwise. The Morris method describes a statistical OAT method, which can be applied especially to models with high computation time or many factors. The method is based on two parameters of sensitivity: μ denotes the mean of the distribution and thus the direct influence of the parameter; and σ the standard deviation and thus characterizes higher order effects. Since effects can be truncated in the calculation of the mean μ due to different signs, an alternative evaluation using μ^* was developed [34]. This value is therefore used to evaluate the importance of the parameters. In addition, however, the mean is also considered, since this value and its deviation provide additional information on the sign of the values and thus on possible oscillations. The evaluation of the standard deviation allows a statement about the dependence of the influence on the choice of the other parameters [4]. Thus, with the help of this method, parameters can be divided into negligible, parameters with a linear influence or parameters with a higher dimensional influence.

Morris method for NAFLD

For the SA, the output variables for which the sensitive parameters are to be ascertained were first determined. Here, the volume fraction of fat n^T , the seepage velocity w_{FS} and the growth fraction of the Jacobian J_{Sg} are considered. Table 7.4 shows the input parameters to be varied and their range. The values are determined on the basis of physical and biological boundary conditions so that they represent a realistic spectrum.

Figure 7.31 shows the respective plots of the modified mean μ^* plotted against the standard deviation σ . It becomes clear that in the process of fat formation, the concentration of oxygen c^{FOx} and FFA c^{FFA} have a great influence on the results. As all other parameters have a small to very small influence, will be not be considered in the following analyses. A similar picture emerges when evaluating the sensitivity by considering the Jacobian growth part. Since these growth processes in this model are

Naming	Minimum	Maximum	Unit	Influence		
				fat	flow	growth
n^S	0.4	0.6	-	→	↓	→
k_D	$2 \cdot 10^{-9}$	$1.5 \cdot 10^{-8}$	$[m^2/N/s]$	→	↑↑	→
E_S	7.000	11.000	$[N/m^2]$	→	↓	→
E_F	7.000	11.000	$[N/m^2]$	↓	↓	↓
ν	0.1	0.4	-	→	→	↓
c^{FFFA}	0.1	5	$[mmol/l]$	↑↑	↓	↑↑
c^{FOx}	0.01	0.2	$[mmol/l]$	↑	↓	↑
T_0	260	320	Kelvin	↓	↓	↓
λ	50	400	Pa	→	↑↑	→

Table 7.4: Range of Parameters in Morris Method for fat accumulation

triggered directly by the formation of fat and the growth rate J_{Sg} is directly dependent on the rate of the fat phase $\hat{\rho}^T$, a high influence of the concentrations of oxygen c^{FOx} and FFA c^{FFFA} , which are responsible for the metabolism, also results here. The other parameters have a negligible effect on the model output for growth processes. Additionally, the influence of the different input parameters on the blood flow velocity \mathbf{w}_{FS} is investigated. In particular, the pressure gradient, which is controlled by the initial pressure λ , and the permeability coefficient k_D are decisive.

Morris Method for tumor growth

Also in the sensitivity analysis for tumor growth, the parameters for which the sensitivity analysis is to be performed are first determined. For this purpose, the volume fraction of the tumor tissue n^C , the blood flow velocity \mathbf{w}_{FS} and the growth fraction of the Jacobian J_{Sg} are selected. Table 7.5 shows the input parameters to be varied and their range. The values are determined on the basis of physical and biological boundary conditions so that they represent a realistic spectrum.

The evaluation in Figure 7.32 indicates that especially the concentration of glucose c^{FGI} and the maximum growth rate μ_{max} are accountable for the increase of the tumor tissue. This seems plausible due to the influence of these parameters on metabolism at the cellular level, see Section 6.1. Although this is also true for the growth parameter K_S , its influence is minor, although still noticeable. Overall, there are more parameters that have a noticeable influence than for development of NAFLD. When evaluating

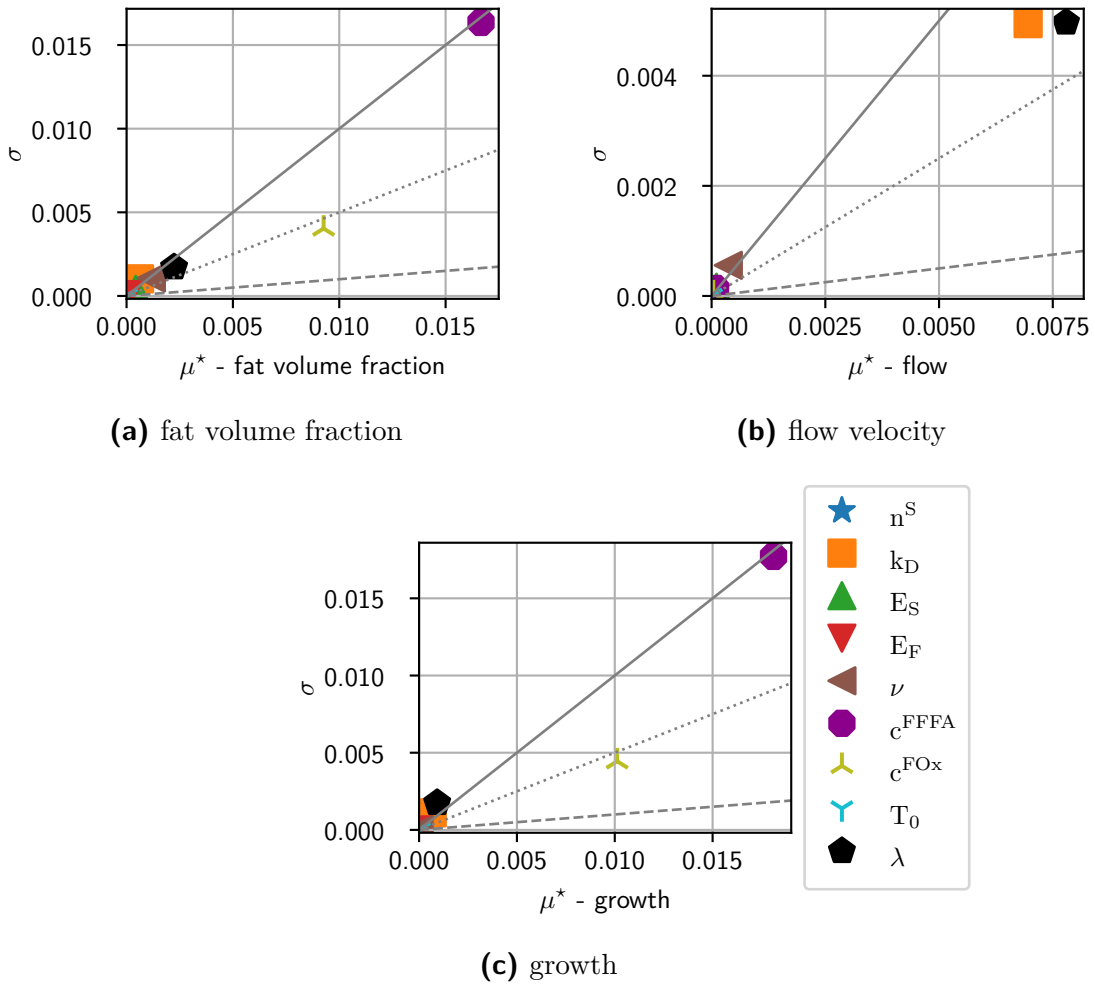


Figure 7.31: Morris Method for NAFLD. Mean μ^* against standard deviation σ for nine input parameters evaluated for a) fat volume fraction n^T , blood velocity w_{FS} and Jacobian growth J_{Sg} . A high mean indicates a high direct influence on the output, whereas a high standard deviation represents a large influence through interactions with other parameters.

the sensitivity to blood flow velocity w_{FS} , permeability k_D and blood pressure λ are again directly identifiable as marked values. The glucose concentration c^{FGl} and the parameters of growth μ_{max} and K_S also show deviations, which can be explained by the triggered growth and the resulting altered pore geometry. Similar to the evaluation of NAFLD, the determination of the marked parameters for the Jacobian J_{Sg} coincides with the identified parameters of the volume fraction of tumor tissue n^C .

Naming	Minimum	Maximum	Unit	Influence		
				tumor	flow	growth
n^S	0.4	0.6	-	↓	↓	↓
k_D	$2 \cdot 10^{-9}$	$1.5 \cdot 10^{-8}$	$[m^2/N/s]$	→	↑↑	→
E_S	7.000	10.000	$[N/m^2]$	↓	↓	↓
E_F	7.000	10.000	$[N/m^2]$	↓	↓	↓
ν	0.1	0.4	-	→	→	→
c^{FGI}	1	10	$[mmol/l]$	↑↑	↑	↑↑
T_0	260	320	Kelvin	↓	↓	↓
λ	50	400	Pa	→	↑	→
μ_{max}	0.02	0.2	-	↑↑	→	↑
K_S	0.4	0.8	-	→	→	→

Table 7.5: Range of Parameters in Morris Method for tumor growth

7.7.2 Extended Fourier Amplitude Sensitivity Test

Another option for analyzing the sensitivity of the problem is the extended Fourier Amplitude Sensitivity Test (eFAST), which belongs to the variance-based methods. It is characterized as an AAT method and provides a global sensitivity analysis, which can be used for screening and ranking [108]. This method requires significantly more samples and thus computational time. In this method, the inputs are considered as stochastic variables whose influence on the output variance is a good measure of sensitivity. Here, first-order indices S_i^F are determined, which reflect the direct influence of a parameter, and total-order indices S_i^T , which describe the total influence of the parameter including its interactions.

eFAST for NAFLD

Using the results of the Morris method, the four most relevant inputs could be determined as permeability factor, FFA and oxygen concentration and blood pressure. To reduce the computing time, the detailed evaluation with the help of the eFAST is carried out with these parameters only, see Table 7.6.

Using 2000 samples, the fat volume fraction n^T , blood velocity \mathbf{w}_{FS} and growth fraction of the Jacobian J_{Sg} are evaluated and the corresponding sensitivities are determined using the sensitivity library SALib [72]. The first order sensitivity indices

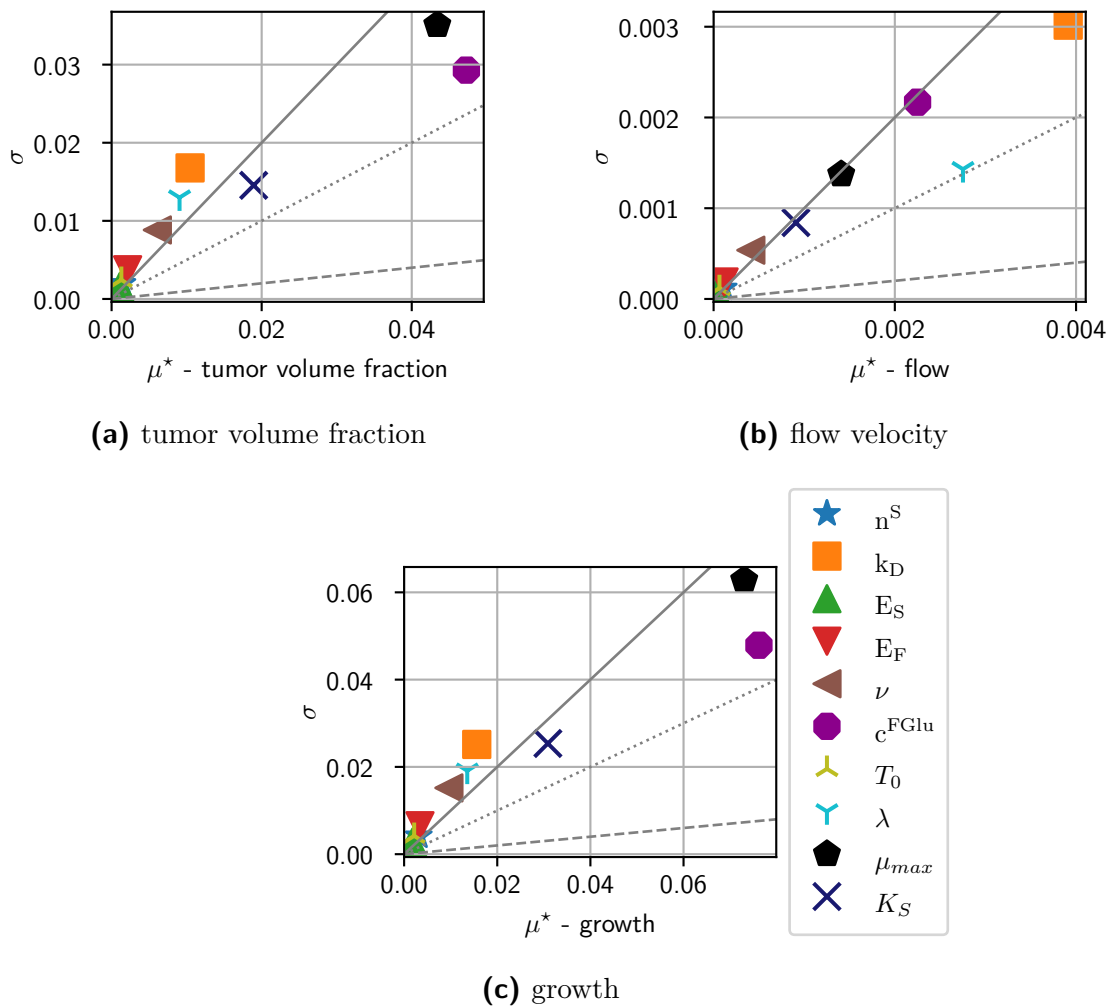
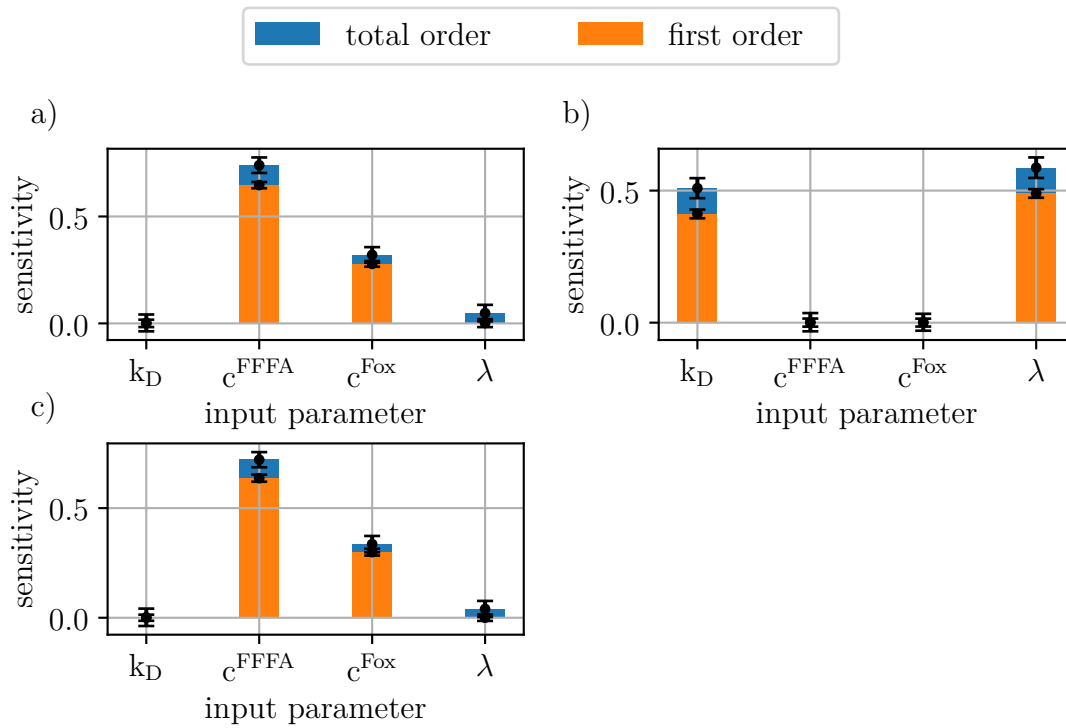


Figure 7.32: Morris Method for tumor growth. Mean μ^* against standard deviation σ for ten input parameters evaluated for a) tumor volume fraction n^C , blood velocity w_{FS} and Jacobian growth J_{Sg} . A high mean indicates a high direct influence on the output, whereas a high standard deviation represents a large influence through interactions with other parameters.

and the total order sensitivity indices as well as their respective confidence intervals are shown in Figure 7.33.

The results of the eFAST evaluation correspond to those from the Morris method, but the individual influences become even clearer here. The increase of the fat phase as well as the growth is significantly influenced by the concentration of FFA and oxygen. Both are directly and indirectly involved in the sensitivity through interactions, whereby the interaction share of the FFA concentration is higher. Both the permeability factor

Parameter	Naming	Minimum	Maximum	Unit
Darcy-Parameter	k_D	$2 \cdot 10^{-9}$	$1.5 \cdot 10^{-8}$	$[\text{m}^2/\text{N}/\text{s}]$
Concentration FFA	c^{FFFA}	2	5	$[\text{mmol}/\text{l}]$
Concentration Oxygen	c^{FOx}	0.01	0.2	$[\text{mmol}/\text{l}]$
Blood Pressure	λ	100	150	Pa

Table 7.6: Range of Parameters in eFAST Method for fat accumulation**Figure 7.33:** eFAST for NAFLD. First order and total order sensitivity for a) fat volume fraction n^T , b) blood flow w_{FS} and c) Jacobian growth J_{Sg} derived using eFAST.

and the blood pressure can be neglected in this analysis. The microperfusion through the lobule is significantly influenced by the permeability and the pressure gradient, this also reflects the expectations as well as the results of the Morris method. The concentrations of solutes do not show an influence on the perfusion.

eFAST for tumor growth

The four most relevant inputs were determined using the results of the Morris method. To reduce the computing time, the detailed evaluation with the help of the eFAST is carried out with these parameters only, see Table 7.7.

Parameter	Naming	Minimum	Maximum	Unit
Darcy-Parameter	k_D	$2 \cdot 10^{-9}$	$1.5 \cdot 10^{-8}$	$[\text{m}^2/\text{N}/\text{s}]$
Concentration glucose	c^{FGI}	1	10	$[\text{mmol}/\text{l}]$
Maximum growth rate	μ_{max}	0.02	0.2	-
Growth Parameter	K_S	0.4	0.8	-

Table 7.7: Range of Parameters in eFAST Method for tumor growth

Evaluation of sensitivity with the eFAST method in Figure 7.34 also confirms the results of the Morris method for tumor growth. For the development of a tumor, the concentration of glucose c^{FGI} and the maximum growth rate μ_{max} are the most influential. Both have a very high first order influence and also an influence by interactions represented by the total order fraction. The other parameters have a considerably lower influence. Since the growth is not accompanied only by the formation of the fat, but also by the growth of the tumor, also in this case the results for the evaluation of the growth fraction of the deformation gradient J_{Sg} are very similar to those of the volume fraction n^C . The same parameters, namely glucose concentration c^{FGI} and maximum growth rate μ_S , are found to be influential. In the case of microperfusion, represented by the flow velocity \mathbf{w}_{FS} , it is clear that the permeability factor k_D plays a major role and also exerts this role directly, which is evident from the high proportion of first order sensitivity. However, since the development of a tumor also influences the microperfusion through the coupled processes and interactions, the glucose concentration c^{FGI} and the growth rate μ_{max} , which significantly cause the increase in volume fraction n^C , are also responsible for changes in perfusion. Although their sensitivity is below the sensitivity of the permeability parameter and they show clear influences both directly (first order) and via coupled processes and interactions (total order).

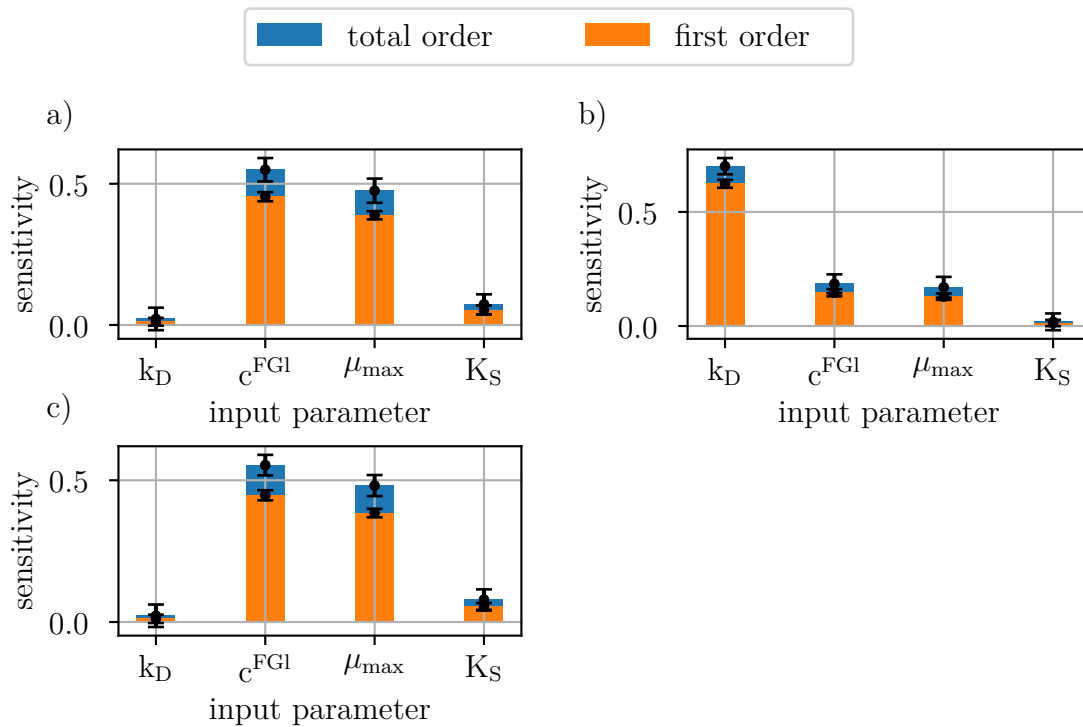


Figure 7.34: eFAST for tumor growth. First order and total order sensitivity for a) tumor volume fraction n^C , b) blood flow w_{FS} and c) Jacobian growth J_{Sg} derived using eFAST.

7.7.3 Regional Sensitivity Analysis

RSA describes a global AAT method for mapping sensitivities and identifying regions that influence a particular behavior [108]. The samples with randomized input parameters and their outputs are thus divided into two groups, so-called behavioral and non-behavioral sets. The selection is based on a set threshold of the output. For evaluation, the respective cumulative distribution functions (CDFs) of both sets are determined and plotted against each other. A visual evaluation can be employed to estimate the sensitivity by determining the distance between the two functions. A large distance indicates a high sensitivity, while curves close to each other represent a lower sensitivity.

RSA for NAFLD

For fat accumulation, the behavioral set describes all inputs that lead to a fat volume fraction greater than 0.15, while non-behavioral sets produce a lower value as output. It becomes apparent that the two curves for behavioral and non-behavioral set for

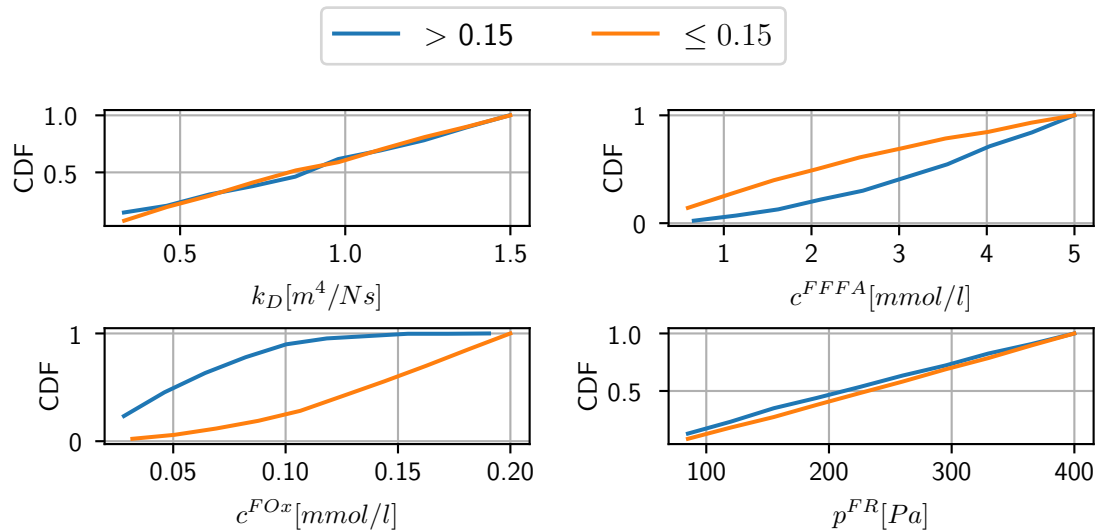


Figure 7.35: Regional Sensitivity Analysis for NAFLD. Evaluation of CDF for behavioral and non-behavioral sets separated for each input parameter evaluated for fat accumulation.

parameters FFA and oxygen deviate most clearly from each other, see Figure 7.35. This can be taken as a measure of a large influence of these parameters, which is also consistent with the results of the previous sensitivity analyses. The curves evaluated according to the parameters k_D and λ deviate only minimally from each other or even overlap in part, so it can also be assumed here that these parameters have a rather small influence on the increase in the volume fraction of fat n^T .

RSA for tumor development

In addition to the sensitivity analysis for the development of hepatic fat, an RSA is also performed for the development of a tumor in the liver. Here, the threshold for the division into behavioral and non-behavioral sets is set to a volume fraction $n^C = 0.1$, which after an analysis of all output values is suitable as a mean and thus a

good threshold. Figure 7.36 illustrates the values of investigated input parameters permeability factor k_D , glucose concentration c^{FGI} , and the growth parameters μ_{max} and K_S over the CDF. The result of the previous sensitivity analyses is also confirmed

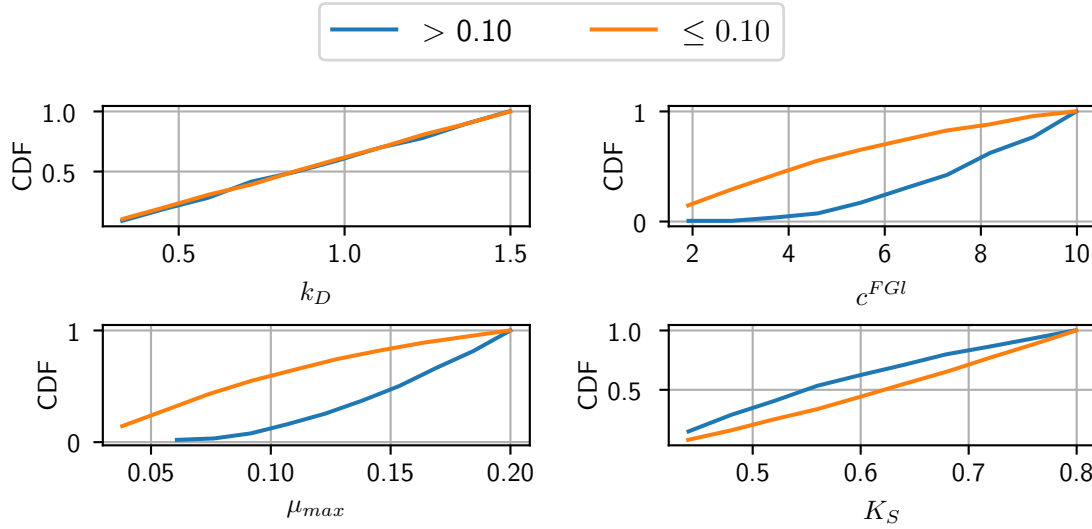


Figure 7.36: Regional Sensitivity Analysis for NAFLD. Evaluation of CDF for behavioral and non-behavioral sets separated for each input parameter evaluated for tumor growth.

since both the glucose concentration c^{FGI} and the maximum growth rate μ_{max} can be identified as the most influential parameters. While the growth parameter K_S also shows a small influence, it is also apparent in this evaluation that the permeability factor k_D almost has no influence on the formation of the tumor, since the curves of the behavioral and the non-behavioral set do not deviate from each other and even overlap at times.

8 Summary, Conclusion, and Future Work

8.1 Summary

This work was designed to develop a multiphasic, multiscale continuum-biomechanical model for the simulation of selected function-perfusion processes in the liver. In chapter 1 the open research questions regarding the simulation of selected processes in the liver were identified and subsequently the goals of the thesis were formulated. Chapter 2 focuses on the biological basis and specific processes of the liver. The relationship between function and perfusion of the physiological and pathophysiological processes addressed in this thesis (steatosis, tumor growth, necrosis) are explained. In chapter 3, relevant mathematical models for simulating the processes in question are presented and analyzed. In chapter 4 the generation of experimental, clinical and *in silico* data needed for the continuum-biomechanical model is presented. Chapter 5 shows the derivation of the multiphase model for simulating function-perfusion processes based on the eTPM on the liver lobule scale. Chapter 6 is devoted to the multiscale model, since the derived model spans multiple scales from liver cells to the total organ. First, approaches to describe the metabolic processes in liver cells, that are responsible for the considered diseases, are presented. Following this, an approach to calculate macroscopic perfusion throughout the total organ is outlined. To simulate the multiscale model using the FEM, the numerical implementation is then presented. In chapter 7 the numerical examples for the different application areas of the model are presented. The model allows the simulation of the progression of selected liver diseases, namely non-alcoholic fatty liver disease, tumor growth and necrosis triggered by paracetamol overdose. Furthermore, perfusion in the hepatic lobules as well as its change as a consequence of a resection or changes in central

venous pressure can be simulated. Moreover, the model allows the simulation of the function-perfusion relationship, disclosing the bilateral relationships of the three disease patterns and perfusion as well as the influence of changes in blood flow, e.g., by resection, on the development of the disease. In order to include realistic medical and biological conditions in the models, first data-driven approaches were developed. Finally, nonlinear model order reduction for the simulation of one liver lobule is performed and sensitivity analysis is applied for screening, ranking, and mapping the parameters.

8.2 Conclusion

The developed model allows the calculation of deformation, flow, and growth processes as well as advection-diffusion-reaction processes in porous media. This model is applied to calculate specific processes in the liver considering liver cells, liver lobules and the whole organ. This allows the simulation of progression of fatty liver, tumor growth and necrosis triggered by an overdose of paracetamol, microperfusion in the liver lobules as well as the interaction between these diseases and perfusion. An important result of this work is the inclusion of the organ scale through a simplified approach of macroscopic perfusion. While models of the individual scales or a coupled lobule-cell scale already exist, models that include all three scales are still rare. However, inclusion of the organ scale is essential for calculating perfusion changes after resection. Another result of this work is the simulation of three different applications in the form of liver disease and the influence on perfusion. Not only selected processes in the course of the diseases individually, but also interactions between these diseases can be included. In addition, the work yielded first approaches for a data-driven approach within the framework of the continuum biomechanical model. In contrast to the so far published mostly knowledge-driven models, this work achieves first approaches to enable a more realistic simulation of the considered processes by using selected medical data.

However, the model still has limitations. Mathematical models always contain assumptions to describe the exact reality. During the development of the continuum-biomechanical model, assumptions were made for simplification, such as neglecting temperature changes in the organ. In order to represent reality more accurately, first

approaches to include medical and biological data for parameterization and validation were shown. These are not yet sufficient to fully represent the complex behavior and processes in the liver, but the model can be combined with additional methods to represent the behavior in more detail.

In addition, the model currently includes only selected diseases and possible forms of therapy. In the clinical setting, however, patients usually suffer from various comorbidities or undergo other forms of therapy, not all of which are yet covered by the model.

Another limitation of the model is the high computational time and required computational power, triggered by the complexity of the model due to many degrees of freedom and the coupling of multiple scales. For this, a first approach for developing a surrogate model on the lobular scale has already been taken, but further adaptations are required to enable a perspective use in clinical practice.

8.3 Future Aspects

In the long term, such a model could be used as a clinical decision support tool, providing clinical staff with an additional method for evaluating specific diseases or forms of therapy. However, to be eligible for such an application, further enhancements and improvements need to be performed.

To enable a patient-specific prediction of certain processes, a further individualization of the model is required. To this end, additional medical data, like perfusion pattern in the lobule or the stiffness of the liver, can be included to improve the accuracy of the model. Processing the large amount of clinical data requires strategic approaches to data preparation, analysis, and integration that take clinical requirements into account, such as anonymization or integration into existing systems.

In order to cover an even broader spectrum of cellular processes and associated diseases, further cellular-level models shall be coupled to the lobular level. For example, the simulation of ischemia-reperfusion injury after liver transplantation can help to quantify the quality of marginal liver donor organs and thus perspectively support the clinical decision whether an organ is suitable for transplantation. The

incorporation of various metabolic processes requires a sustainable and interchangeable model-based software environment for PDE-ODE coupling. This can for example be realized by using coupling libraries.

In addition, the development of surrogate models may significantly reduce the computing time and thus enable near-real-time prediction. The approach developed in this work can be extended to a surrogate model for the cell and the lobule as well as for the coupled system of both scales by using state-of-the-art concepts from the field of physics-aware methods. These surrogates can also be used to better quantify the impact of aleatoric uncertainties and thus make them more tangible for practical use in a clinical setting.

Acknowledgement

This work was funded by Deutsche Forschungsgemeinschaft (DFG, German Research Foundation) under Germany's Excellence Strategy—EXC 2075—390740016 and the Research Unit Programme FOR 5151 QuaLiPerF (Quantifying Liver Perfusion—Function Relationship in Complex Resection—A Systems Medicine Approach) by grant number 436883643.

Figures 2.1, 2.2, 2.5, 2.9, 2.10, 4.1, 5.3, 5.4, 5.5, 5.10, 6.1, 6.2, 6.3, 6.4, 6.7, 6.8, 6.10 are created with BioRender.com.

Bibliography

- [1] ACARTÜRK, AYHAN YUSUF. “Simulation of Charged Hydrated Porous Media”. PhD thesis. Institute of Applied Mechanics (Civil Engineering), Universität Stuttgart.
- [2] Priyom ADHYAPOK et al. “A computational model of liver tissue damage and repair”. In: *PLoS ONE* 15.12 (2020), e0243451. DOI: 10.1371/journal.pone.0243451.
- [3] R. AHMADI-BADEJANI, M. MOSHARAF-DEHKORDI, and H. AHMADIKIA. “An image-based geometric model for numerical simulation of blood perfusion within the liver lobules”. In: *Computer Methods in Biomechanics and Biomedical Engineering* 23.13 (2020), pp. 987–1004. ISSN: 1025-5842. DOI: 10.1080/10255842.2020.1782389.
- [4] ANDREA SALTELLI, STEFANO TARANTOLA, FRANCESCA CAMPOLONGO, MARCO RATTO. *Sensitivity analysis in practice: A guide to assessing scientific models*. Reprinted. Chichester and Weinheim: Wiley, 2007. ISBN: 9780470870938.
- [5] M. Yu. ANTONOV, A. V. GRIGOREV, and A. E. KOLESOV. “Numerical Modeling of Fluid Flow in Liver Lobule Using Double Porosity Model”. In: *Numerical Analysis and Its Applications*. Ed. by Ivan DIMOV, István FARAGÓ, and Lubin VULKOV. Vol. 10187. Lecture Notes in Computer Science. Cham: Springer International Publishing, 2017, pp. 187–194. ISBN: 978-3-319-57098-3. DOI: 10.1007/978-3-319-57099-0{textunderscore}18.
- [6] *Aperio ImageScope*. <https://www.leicabiosystems.com/digital-pathology/manage/aperio-imagescope/>. Accessed: 2021-12-14.
- [7] Jorge ARAMBURU et al. “Liver cancer arterial perfusion modelling and CFD boundary conditions methodology: a case study of the haemodynamics of a patient-specific hepatic artery in literature-based healthy and tumour-bearing liver scenarios”. In: *International Journal for Numerical Methods in Biomedical Engineering* 32.11 (2016), n/a–n/a. ISSN: 2040-7947. DOI: 10.1002/cnm.2764.

- [8] William B. ASHWORTH, Nathan A. DAVIES, and I. David L. BOGLE. “A Computational Model of Hepatic Energy Metabolism: Understanding Zonated Damage and Steatosis in NAFLD”. In: *PLoS Computational Biology* 12.9 (2016), e1005105. DOI: 10.1371/journal.pcbi.1005105.
- [9] Gerard A. ATESHIAN and Tim RICKEN. “Multigenerational interstitial growth of biological tissues”. In: *Biomechanics and Modeling in Mechanobiology* 9.6 (2010), pp. 689–702. ISSN: 1617-7959. DOI: 10.1007/s10237-010-0205-y.
- [10] Chloe AUDEBERT et al. “Partial hepatectomy hemodynamics changes: Experimental data explained by closed-loop lumped modeling”. In: *J Biomech* 50 (2017), pp. 202–208. DOI: 10.1016/j.jbiomech.2016.11.037.
- [11] B. MARKERT. “Porous Media Viscoelasticity with Application to polymeric foams”. PhD thesis. Institute of Applied Mechanics (Civil Engineering), Universität Stuttgart.
- [12] Octavia BANE et al. “Hemodynamic measurements with an abdominal 4D flow MRI sequence with spiral sampling and compressed sensing in patients with chronic liver disease”. In: *Journal of Magnetic Resonance Imaging* 49.4 (2019), pp. 994–1005.
- [13] Hila BARASH et al. “Functional MR imaging during hypercapnia and hyperoxia: noninvasive tool for monitoring changes in liver perfusion and hemodynamics in a rat model”. In: *Radiology* 243.3 (2007), pp. 727–735. ISSN: 0033-8419. DOI: 10.1148/radiol.2433060433.
- [14] N. BARLÉON, R. J. CLARKE, and H. HO. “Novel methods for segment-specific blood flow simulation for the liver”. In: *Computer Methods in Biomechanics and Biomedical Engineering* 21.15 (2018), pp. 780–783. ISSN: 1025-5842. DOI: 10.1080/10255842.2018.1520224.
- [15] Pierre BEDOSSA. “Diagnosis of non-alcoholic fatty liver disease/non-alcoholic steatohepatitis: Why liver biopsy is essential”. In: *Liver international : official journal of the International Association for the Study of the Liver* 38 Suppl 1 (2018), pp. 64–66. DOI: 10.1111/liv.13653.
- [16] Mark BENEDICT and Xuchen ZHANG. “Non-alcoholic fatty liver disease: An expanded review”. In: *World journal of hepatology* 9.16 (2017), pp. 715–732. ISSN: 1948-5182. DOI: 10.4254/wjh.v9.i16.715.
- [17] Nikolaus BERNDT et al. “A multiscale modelling approach to assess the impact of metabolic zonation and microperfusion on the hepatic carbohydrate

- metabolism”. In: *PLoS Comput Biol* 14.2 (2018), e1006005. DOI: 10.1371/journal.pcbi.1006005.
- [18] Nikolaus BERNDT et al. “Characterization of Lipid and Lipid Droplet Metabolism in Human HCC”. In: *Cells* 8.5 (2019). ISSN: 2073-4409. DOI: 10.3390/cells8050512.
- [19] Nikolaus BERNDT et al. “HEPATOKIN1 is a biochemistry-based model of liver metabolism for applications in medicine and pharmacology”. In: *Nat Commun* 9.1 (2018), p. 2386. ISSN: 2041-1723 (Electronic) 2041-1723 (Linking). DOI: 10.1038/s41467-018-04720-9.
- [20] Albrecht BERTRAM. *Elasticity and Plasticity of Large Deformations: An Introduction*. Berlin Heidelberg: Springer-Verlag GmbH, 2005. ISBN: 978-3-540-27525-1. DOI: 10.1007/3-540-27525-8. URL: <http://site.ebrary.com/lib/alltitles/docDetail.action?docID=10228992>.
- [21] Fleurianne BERTRAND, Lena LAMBERS, and Tim RICKEN. “Least Squares Finite Element Method for Hepatic Sinusoidal Blood Flow”. In: *PAMM* 20.1 (2021). ISSN: 16177061. DOI: 10.1002/pamm.202000306.
- [22] Christian BLEILER. “Continuum-mechanical modelling across scales : homogenisation methods and their application to microstructurally-based skeletal muscle modelling”. Dissertation. 2021. DOI: 10.18419/opus-11959. URL: <https://nbn-resolving.de/urn:nbn:de:bsz:93-opus-ds-119761>.
- [23] Edward H. BLOCH. “The Termination of Hepatic Arterioles and the Functional Unit of the Liver as Determined by Microscopy of the Living Organ”. In: *Annals of the New York Academy of Sciences* 170.1 The Hepatic C (1970), pp. 78–87. ISSN: 0077-8923. DOI: 10.1111/j.1749-6632.1970.tb37004.x.
- [24] R. de BOER. *Theory of Porous Media – highlights in the historical development and current state*. Springer-Verlag, 2000.
- [25] Noemie BOISSIER, Dirk DRASDO, and Irene E. VIGNON-CLEMENTEL. “Simulation of a detoxifying organ function: Focus on hemodynamics modeling and convection-reaction numerical simulation in microcirculatory networks”. In: *International Journal for Numerical Methods in Biomedical Engineering* 37.2 (2021), e3422. ISSN: 2040-7947. DOI: 10.1002/cnm.3422.
- [26] Tim BOMBERNA et al. “A Hybrid Particle-Flow CFD Modeling Approach in Truncated Hepatic Arterial Trees for Liver Radioembolization: A Patient-specific Case Study”. In: *Frontiers in Bioengineering and Biotechnology* 10 (2022), p. 914979. ISSN: 2296-4185. DOI: 10.3389/fbioe.2022.914979.

- [27] Andrea BONFIGLIO et al. “Mathematical modeling of the circulation in the liver lobule”. In: *Journal of Biomechanical Engineering* 132.11 (2010), p. 111011. ISSN: 0148-0731. DOI: 10.1115/1.4002563.
- [28] Leopold BÖSWIRTH and Sabine BSCHORER. *Technische Strömungslehre*. Wiesbaden: Springer Fachmedien Wiesbaden, 2014. ISBN: 978-3-658-05667-4. DOI: 10.1007/978-3-658-05668-1.
- [29] Ray M BOWEN. “Continuum physics”. In: *Acad. Press, New York* (1976). DOI: 10.1016/B978-0-12-240803-8.X5001-4.
- [30] Ray M BOWEN. “Incompressible porous media models by use of the theory of mixtures”. In: *International Journal of Engineering Science* 18.9 (1980), pp. 1129–1148. DOI: 10.1016/0020-7225(82)90082-9.
- [31] Freddie BRAY et al. “Global cancer statistics 2018: GLOBOCAN estimates of incidence and mortality worldwide for 36 cancers in 185 countries”. In: *CA: a cancer journal for clinicians* 68.6 (2018), pp. 394–424. DOI: 10.3322/caac.21492.
- [32] C. COUINAUD. “The Liver. Anatomical and surgical investigations”. In: *Le foie. Etudes anatomiques et chirurgicales* (1957).
- [33] Rose CAIRNS et al. “Paracetamol poisoning-related hospital admissions and deaths in Australia, 2004-2017”. In: *The Medical journal of Australia* 211.5 (2019), pp. 218–223. DOI: 10.5694/mja2.50296.
- [34] CAMPOLONGO F, CARIBONI J, and WIM S. *Enhancing the Morris Method*. 2005.
- [35] Laurent CASTERA, Xavier FORNS, and Alfredo ALBERTI. “Non-invasive evaluation of liver fibrosis using transient elastography”. In: *Journal of hepatology* 48.5 (2008), pp. 835–847.
- [36] Naga CHALASANI et al. “The diagnosis and management of nonalcoholic fatty liver disease: Practice guidance from the American Association for the Study of Liver Diseases”. In: *Hepatology* 67.1 (2018), pp. 328–357. ISSN: 1527-3350. DOI: 10.1002/hep.29367.
- [37] Bruno CHRIST et al. “Computational Modeling in Liver Surgery”. In: *Frontiers in Physiology* 8 (2017), p. 906. DOI: 10.3389/fphys.2017.00906.
- [38] Bruno CHRIST et al. “Hepatectomy-Induced Alterations in Hepatic Perfusion and Function - Toward Multi-Scale Computational Modeling for a Better Prediction of Post-hepatectomy Liver Function”. In: *Frontiers in Physiology*

- 12 (2021), p. 2058. ISSN: 1664-042X. DOI: 10.3389/fphys.2021.733868. URL: <https://www.frontiersin.org/article/10.3389/fphys.2021.733868>.
- [39] Bernard D. COLEMAN and Walter NOLL. “The thermodynamics of elastic materials with heat conduction and viscosity”. In: *Archive for Rational Mechanics and Analysis* 13.1 (1963), pp. 167–178. ISSN: 0003-9527. DOI: 10.1007/BF01262690.
- [40] C. J. CYRON, R. C. AYDIN, and J. D. HUMPHREY. “A homogenized constrained mixture (and mechanical analog) model for growth and remodeling of soft tissue”. In: *Biomechanics and Modeling in Mechanobiology* 15.6 (2016), pp. 1389–1403. ISSN: 1617-7940. DOI: 10.1007/s10237-016-0770-9.
- [41] U. DAHMEN et al. “Regulation of hepatic microcirculation in stepwise liver resection”. In: *Acta Gastroenterol Belg* 70.4 (2007), pp. 345–351.
- [42] Henryk DANCYGIER. *Klinische Hepatologie: Grundlagen, Diagnostik und Therapie Hepatobiliärer Erkrankungen*. Berlin, Heidelberg: Springer Berlin / Heidelberg, 2003. ISBN: 9783642559020. URL: <https://ebookcentral.proquest.com/lib/kxp/detail.action?docID=6281706>.
- [43] Charlotte DEBBAUT. “Multi-level modelling of hepatic perfusion in support of liver transplantation strategies”. PhD thesis. Jan. 2013.
- [44] Charlotte DEBBAUT et al. “A 3D porous media liver lobule model: the importance of vascular septa and anisotropic permeability for homogeneous perfusion: the importance of vascular septa and anisotropic permeability for homogeneous perfusion”. In: *Comput Methods Biomech Biomed Engin* 17.12 (2014), pp. 1295–1310. ISSN: 1476-8259 (Electronic) 1025-5842 (Linking). DOI: 10.1080/10255842.2012.744399.
- [45] Charlotte DEBBAUT et al. “Modeling the impact of partial hepatectomy on the hepatic hemodynamics using a rat model”. In: *IEEE transactions on bio-medical engineering* 59.12 (2012), pp. 3293–3303. DOI: 10.1109/TBME.2012.2199108.
- [46] Charlotte DEBBAUT et al. “Perfusion characteristics of the human hepatic microcirculation based on three-dimensional reconstructions and computational fluid dynamic analysis”. In: *Journal of Biomechanical Engineering* 134.1 (2012), p. 011003. ISSN: 0148-0731. DOI: 10.1115/1.4005545.
- [47] Laurie D. DELEVE and Guadalupe GARCIA-TSAO, eds. *Vascular Liver Disease*. New York, NY: Springer New York, 2011. ISBN: 978-1-4419-8326-8. DOI: 10.1007/978-1-4419-8327-5.

- [48] Juan G. DIAZ OCHOA et al. “A multi-scale modeling framework for individualized, spatiotemporal prediction of drug effects and toxicological risk”. In: *Frontiers in pharmacology* 3 (2012), p. 204. DOI: 10.3389/fphar.2012.00204.
- [49] J. R. DIXON. “The International Conference on Harmonization Good Clinical Practice guideline”. In: *Quality assurance (San Diego, Calif.)* 6.2 (1998), pp. 65–74. ISSN: 1052-9411. DOI: 10.1080/105294199277860.
- [50] Wolfgang EHLERS. “Challenges of porous media models in geo-and biomechanical engineering including electro-chemically active polymers and gels”. In: *International Journal of Advances in Engineering Sciences and Applied Mathematics* 1.1 (2009), pp. 1–24. DOI: 10.1007/s12572-009-0001-z.
- [51] Wolfgang EHLERS. “Foundations of multiphasic and porous materials”. In: *Porous Media*. Ed. by Wolfgang EHLERS and Joachim BLUHM. Berlin, Heidelberg: Springer Berlin Heidelberg, 2002, pp. 3–86. ISBN: 978-3-642-07843-9. DOI: 10.1007/978-3-662-04999-0{\textunderscore}1.
- [52] Andrew EVANS et al. “Quantitative shear wave ultrasound elastography: initial experience in solid breast masses”. In: *Breast cancer research* 12.6 (2010), R104.
- [53] J FERLAY et al. *Global Cancer Observatory: Cancer Today*. Lyon, France: International Agency for Research on Cancer. <https://gco.iarc.fr/today>. Accessed: 2022-10-16. 2020.
- [54] Robert J. FONTANA. “Acute Liver Failure including Acetaminophen Overdose”. In: *The Medical clinics of North America* 92.4 (2008), pp. 761–794. ISSN: 0025-7125. DOI: 10.1016/j.mcna.2008.03.005.
- [55] Xiao FU et al. “Modeling of xenobiotic transport and metabolism in virtual hepatic lobule models”. In: *PLoS ONE* 13.9 (2018), e0198060. DOI: 10.1371/journal.pone.0198060.
- [56] Philippe GARTEISER et al. “MR elastography of liver tumours: value of viscoelastic properties for tumour characterisation”. In: *European radiology* 22.10 (2012), pp. 2169–2177.
- [57] Rolf GEBHARDT et al. “Hepatocellular expression of glutamine synthetase: an indicator of morphogen actions as master regulators of zonation in adult liver”. In: *Progress in histochemistry and cytochemistry* 41.4 (2007), pp. 201–266. ISSN: 0079-6336. DOI: 10.1016/j.proghi.2006.12.001.
- [58] Suzanne GEENEN et al. “Multiscale modelling approach combining a kinetic model of glutathione metabolism with PBPK models of paracetamol and the potential glutathione-depletion biomarkers ophthalmic acid and 5-oxoproline

- in humans and rats”. In: *Integrative biology : quantitative biosciences from nano to macro* 5.6 (2013), pp. 877–888. DOI: 10.1039/c3ib20245c.
- [59] Christophe GEUZAIN and Jean-François REMACLE. “Gmsh: A 3-D finite element mesh generator with built-in pre- and post-processing facilities”. In: *International Journal for Numerical Methods in Engineering* 79.11 (2009), pp. 1309–1331. ISSN: 1097-0207. DOI: 10.1002/nme.2579.
- [60] Ahmed GHALLAB et al. “Influence of Liver Fibrosis on Lobular Zonation”. In: *Cells* 8.12 (2019). DOI: 10.3390/cells8121556.
- [61] Christoph GILLE et al. “HepatoNet1: a comprehensive metabolic reconstruction of the human hepatocyte for the analysis of liver physiology”. In: *Molecular Systems Biology* 6 (2010), p. 411. ISSN: 1744-4292. DOI: 10.1038/msb.2010.62.
- [62] Stefano GITTO et al. “Study of the Serum Metabolomic Profile in Nonalcoholic Fatty Liver Disease: Research and Clinical Perspectives”. In: *Metabolites* 8.1 (2018). ISSN: 2218-1989. DOI: 10.3390/metabo8010017.
- [63] Nicolas GOLSE et al. “Predicting the risk of post-hepatectomy portal hypertension using a digital twin: A clinical proof of concept”. In: *Journal of Hepatology* 74.3 (2021), pp. 661–669. ISSN: 0168-8278. DOI: 10.1016/j.jhep.2020.10.036.
- [64] W. GRONER et al. “Orthogonal polarization spectral imaging: a new method for study of the microcirculation”. In: *Nature medicine* 5.10 (1999), pp. 1209–1212. ISSN: 1078-8956. DOI: 10.1038/13529.
- [65] Jan GRZEGORZEWSKI et al. “Pharmacokinetics of Caffeine: A Systematic Analysis of Reported Data for Application in Metabolic Phenotyping and Liver Function Testing”. In: *Frontiers in pharmacology* 12 (2021), p. 752826. DOI: 10.3389/fphar.2021.752826.
- [66] Douglas HANAHAN and Robert A. WEINBERG. “Hallmarks of cancer: the next generation”. In: *Cell* 144.5 (2011), pp. 646–674. DOI: 10.1016/j.cell.2011.02.013.
- [67] Douglas HANAHAN and Robert A. WEINBERG. “The Hallmarks of Cancer”. In: *Cell* 100.1 (2000), pp. 57–70. DOI: 10.1016/S0092-8674(00)81683-9.
- [68] Harvey HO et al. “Modeling the hepatic arterial buffer response in the liver”. In: *Med Eng Phys* 35.8 (2013), pp. 1053–1058. DOI: 10.1016/j.medengphy.2012.10.008.
- [69] Michael J. HODGMAN and Alexander R. GARRARD. “A review of acetaminophen poisoning”. In: *Critical care clinics* 28.4 (2012), pp. 499–516. DOI: 10.1016/j.ccc.2012.07.006.

- [70] Jinrong HU et al. “Flow dynamics analyses of pathophysiological liver lobules using porous media theory”. In: *Acta Mechanica Sinica* 33.4 (2017), pp. 823–832. ISSN: 0567-7718. DOI: 10.1007/s10409-017-0674-7.
- [71] Marijke HUYSMANS and Alain DASSARGUES. “Review of the use of Péclet numbers to determine the relative importance of advection and diffusion in low permeability environments”. In: *Hydrogeology Journal* 13.5-6 (2005), pp. 895–904. ISSN: 1431-2174. DOI: 10.1007/s10040-004-0387-4.
- [72] Takuya IWANAGA, William USHER, and Jonathan HERMAN. “Toward SALib 2.0: Advancing the accessibility and interpretability of global sensitivity analyses”. In: *Socio-Environmental Systems Modelling* 4 (May 2022), p. 18155. DOI: 10.18174/sesmo.18155. URL: <https://sesmo.org/article/view/18155>.
- [73] Etienne JESSEN et al. *Rigorous mathematical optimization of synthetic hepatic vascular trees*. 2022. URL: <https://arxiv.org/pdf/2202.04406>.
- [74] Kyu Sik JUNG and Seung Up KIM. “Clinical applications of transient elastography”. In: *Clinical and molecular hepatology* 18.2 (2012), pp. 163–173. DOI: 10.3350/cmh.2012.18.2.163.
- [75] Takeshi KATSUDA and Toshiro MARUYAMA. “Chemical-Kinetics Model for the Growth of a Multicellular Tumor Spheroid”. In: *JOURNAL OF CHEMICAL ENGINEERING OF JAPAN* 42.3 (2009), pp. 198–203. ISSN: 0021-9592. DOI: 10.1252/jcej.08we229.
- [76] Georgia KERAMIDA et al. “Heterogeneity of intrahepatic fat distribution determined by (18)F-FDG PET and CT”. In: *Annals of nuclear medicine* 30.3 (2016), pp. 200–206. DOI: 10.1007/s12149-015-1045-8.
- [77] Hyunmi KIM et al. “Metabolic Spectrum of Liver Failure in Type 2 Diabetes and Obesity: From NAFLD to NASH to HCC”. In: *International journal of molecular sciences* 22.9 (2021). DOI: 10.3390/ijms22094495.
- [78] David E. KLEINER and Hala R. MAKHLOUF. “Histology of Nonalcoholic Fatty Liver Disease and Nonalcoholic Steatohepatitis in Adults and Children”. In: *Clinics in liver disease* 20.2 (2016), pp. 293–312. DOI: 10.1016/j.cld.2015.10.011..
- [79] Adrian KÖLLER et al. “Prediction of Survival After Partial Hepatectomy Using a Physiologically Based Pharmacokinetic Model of Indocyanine Green Liver Function Tests”. In: *Frontiers in Physiology* 12 (2021), p. 730418. DOI: 10.3389/fphys.2021.730418.

-
- [80] Matthias KÖNIG, Sascha BULIK, and Hermann-Georg HOLZHÜTTER. “Quantifying the contribution of the liver to glucose homeostasis: a detailed kinetic model of human hepatic glucose metabolism”. In: *PLoS Comput Biol* 8.6 (2012), e1002577. DOI: 10.1371/journal.pcbi.1002577.
- [81] Matthias KÖNIG and Hermann-Georg HOLZHÜTTER. “Kinetic modeling of human hepatic glucose metabolism in type 2 diabetes mellitus predicts higher risk of hypoglycemic events in rigorous insulin therapy”. In: *The Journal of biological chemistry* 287.44 (2012), pp. 36978–36989. DOI: 10.1074/jbc.M112.382069.
- [82] Tobias KÖPPL, Ettore VIDOTTO, and Barbara WOHLMUTH. “A 3D-1D coupled blood flow and oxygen transport model to generate microvascular networks”. In: *International Journal for Numerical Methods in Biomedical Engineering* 36.10 (2020), e3386. ISSN: 2040-7947. DOI: 10.1002/cnm.3386.
- [83] Lena LAMBERS, André MIELKE, and Tim RICKEN. “Semi-automated Data-driven FE Mesh Generation and Inverse Parameter Identification for a Multi-scale and Multiphase Model of Function-Perfusion Processes in the Liver”. In: *PAMM* 21.1 (2021). ISSN: 1617-7061. DOI: 10.1002/pamm.202100190.
- [84] Lena LAMBERS, Tim RICKEN, and Matthias KÖNIG. “Model Order Reduction (MOR) of Function-Perfusion-Growth Simulation in the Human Fatty Liver via Artificial Neural Network (ANN)”. In: *PAMM* 19.1 (2019), e201900429. ISSN: 1617-7061. DOI: 10.1002/pamm.201900429.
- [85] Lena LAMBERS, Navina WASCHINSKY, and Tim RICKEN. “On a Multi-Scale and Multi-Phase Model of Paracetamol-induced Hepatotoxicity for Human Liver”. In: *PAMM* 18.1 (2018), e201800454. ISSN: 1617-7061. DOI: 10.1002/pamm.201800454.
- [86] Lena LAMBERS et al. “A Multi-scale and Multi-phase Model for the Description of Toxicity caused by Paracetamol in Biological Tissue using the Example of the Human Liver”. In: *PAMM* 17.1 (2017), pp. 199–200. ISSN: 1617-7061. DOI: 10.1002/pamm.201710069.
- [87] S. LANGER et al. “Orthogonal polarization spectral imaging as a tool for the assessment of hepatic microcirculation: a validation study”. In: *Transplantation* 71.9 (2001), pp. 1249–1256. ISSN: 0041-1337. DOI: 10.1097/00007890-200105150-00012.

- [88] Anne M. LARSON et al. “Acetaminophen-induced acute liver failure: results of a United States multicenter, prospective study”. In: *Hepatology (Baltimore, Md.)* 42.6 (2005), pp. 1364–1372. DOI: [10.1002/hep.20948](https://doi.org/10.1002/hep.20948).
- [89] W. W. LAUTT, J. SCHAFER, and D. J. LEGARE. “Hepatic blood flow distribution: consideration of gravity, liver surface, and norepinephrine on regional heterogeneity”. In: *Canadian journal of physiology and pharmacology* 71.2 (1993), pp. 128–135. ISSN: 0008-4212. DOI: [10.1139/y93-018](https://doi.org/10.1139/y93-018).
- [90] Yvonne LINICUS et al. “Vena cava compression syndrome in patients with obesity presenting with edema and thrombosis”. In: *Obesity (Silver Spring, Md.)* 24.8 (2016), pp. 1648–1652. DOI: [10.1002/oby.21506](https://doi.org/10.1002/oby.21506).
- [91] I. S. LIU. “Method of Lagrange multipliers for exploitation of the entropy principle”. In: *Archive for Rational Mechanics and Analysis* 46 (2) (1972), pp. 131–148.
- [92] Weilin LIU et al. “Effective treatment of steatosis and steatohepatitis by fibroblast growth factor 1 in mouse models of nonalcoholic fatty liver disease”. In: *Proceedings of the National Academy of Sciences* 113.8 (2016), pp. 2288–2293. ISSN: 0027-8424. DOI: [10.1073/pnas.1525093113](https://doi.org/10.1073/pnas.1525093113).
- [93] Xijiao LIU et al. “Gadoxetic acid disodium-enhanced magnetic resonance imaging outperformed multidetector computed tomography in diagnosing small hepatocellular carcinoma: A meta-analysis”. In: *Liver transplantation : official publication of the American Association for the Study of Liver Diseases and the International Liver Transplantation Society* 23.12 (2017), pp. 1505–1518. DOI: [10.1002/lt.24867](https://doi.org/10.1002/lt.24867).
- [94] Sylvie LORENTE, Mathieu HAUTEFEUILLE, and Aczel SANCHEZ-CEDILLO. “The liver, a functionalized vascular structure”. In: *Scientific Reports* 10.1 (2020), p. 16194. DOI: [10.1038/s41598-020-73208-8](https://doi.org/10.1038/s41598-020-73208-8).
- [95] Renfei MA et al. “Modeling the hepatic arterial flow in living liver donor after left hepatectomy and postoperative boundary condition exploration”. In: *International Journal for Numerical Methods in Biomedical Engineering* 36.3 (2020), e3268. ISSN: 2040-7947. DOI: [10.1002/cnm.3268](https://doi.org/10.1002/cnm.3268).
- [96] Roderick N. M. MACSWEEN, Bernard PORTMANN, and Linda D. FERRELL. *MacSween’s pathology of the liver*. 6th ed. [Oxford?]: Churchill Livingstone Elsevier, 2007. ISBN: 978-0-7020-3398-8.
- [97] Adil MARDINOGLU et al. “Genome-scale metabolic modelling of hepatocytes reveals serine deficiency in patients with non-alcoholic fatty liver disease”.

- In: *Nat Commun* 5 (2014), p. 3083. ISSN: 2041-1723 (Electronic) 2041-1723 (Linking). DOI: 10.1038/ncomms4083.
- [98] Bernd MARKERT. *Weak or strong: On coupled problems in continuum mechanics: Zugl.: Stuttgart, Univ., Habil., 2010*. Vol. 20. Report / Institut für Mechanik (Bauwesen) Lehrstuhl II. Stuttgart: Institut für Mechanik (Bauwesen) Lehrstuhl II, 2010. ISBN: 3937399208. URL: <http://nbn-resolving.de/urn:nbn:de:bsz:93-opus-54539>.
- [99] Muriel MESCAM, Marek KRETOWSKI, and Johanne BEZY-WENDLING. “Multiscale model of liver DCE-MRI towards a better understanding of tumor complexity”. In: *Medical Imaging, IEEE Transactions on* 29.3 (2010), pp. 699–707. ISSN: 0278-0062. DOI: 10.1109/TMI.2009.2031435.
- [100] André MIELKE and Tim RICKEN. “Evaluating Artificial Neural Networks and Quantum Computing for Mechanics”. In: *PAMM* 19.1 (2019), e201900470. ISSN: 1617-7061. DOI: 10.1002/pamm.201900470.
- [101] Max D. MORRIS. “Factorial Sampling Plans for Preliminary Computational Experiments”. In: *Technometrics* 33.2 (1991), p. 161. ISSN: 00401706. DOI: 10.2307/1269043.
- [102] Ingo MÜLLER. *Thermodynamik: Die Grundlagen d. Materialtheorie*. Düsseldorf: Bertelsmann-Universitätsverlag, 1973. ISBN: 357109185X.
- [103] Raja MUTHUPILLAI and Richard L EHMAN. “Magnetic resonance elastography”. In: *Nature medicine* 2.5 (1996), pp. 601–603.
- [104] Kenichiro NISHII et al. “Multiscale computational model of fluid flow and matrix deformation in decellularized liver”. In: *Journal of the Mechanical Behavior of Biomedical Materials* 57 (2016), pp. 201–214. ISSN: 1751-6161. DOI: 10.1016/j.jmbbm.2015.11.033.
- [105] O. C. ZIENKIEWITZ and R. L. TAYLOR. *The Finite Element Method - Its Basis and Fundamentals*. 6th ed. Butterworth-Heinemann, 2005.
- [106] “Perioperative use of the LiMON method of indocyanine green elimination measurement for the prediction and early detection of post-hepatectomy liver failure”. In: *European journal of surgical oncology : the journal of the European Society of Surgical Oncology and the British Association of Surgical Oncology* 35.9 (2009), pp. 957–962. DOI: 10.1016/j.ejso.2009.02.003.
- [107] PETER WRIGGERS. *Nonlinear Finite Element Methods*. Springer-Verlag Berlin Heidelberg, 2008.

- [108] Francesca PIANOSI et al. “Sensitivity analysis of environmental models: A systematic review with practical workflow”. In: *Environmental Modelling & Software* 79 (2016), pp. 214–232. ISSN: 13648152. DOI: 10.1016/j.envsoft.2016.02.008.
- [109] D. M. PIERCE, T. RICKEN, and Gerhard A. HOLZAPFEL. “Modeling sample/patient-specific structural and diffusional responses of cartilage using DT-MRI”. In: *International Journal for Numerical Methods in Biomedical Engineering* 29.8 (2013), pp. 807–821. ISSN: 2040-7947. DOI: 10.1002/cnm.2524.
- [110] Monica PIERGIOVANNI et al. “Microcirculation in the murine liver: a computational fluid dynamic model based on 3D reconstruction from in vivo microscopy”. In: *J Biomech* 63 (2017), pp. 125–134. DOI: 10.1016/j.jbiomech.2017.08.011.
- [111] F. PISCAGLIA et al. “Influence of the spleen on portal haemodynamics: a non-invasive study with Doppler ultrasound in chronic liver disease and haematological disorders”. In: *Scandinavian journal of gastroenterology* 37.10 (2002), pp. 1220–1227. ISSN: 0036-5521. DOI: 10.1080/003655202760373452.
- [112] H. P. RANI et al. “Numerical investigation of non-Newtonian microcirculatory blood flow in hepatic lobule”. In: *Journal of Biomechanics* 39.3 (2006), pp. 551–563. ISSN: 0021-9290. DOI: 10.1016/j.jbiomech.2004.11.029.
- [113] A. M. RAPPAPORT et al. “Subdivision of hexagonal liver lobules into a structural and functional unit; role in hepatic physiology and pathology”. In: *The Anatomical record* 119.1 (1954), pp. 11–33. ISSN: 0003-276X. DOI: 10.1002/ar.1091190103.
- [114] *Reprinted from WHO Map Gallery, 2017.* https://www.who.int/images/default-source/maps/global_obesity_2016_male.png?sfvrsn=ee61225b_0. Accessed: 2022-10-15.
- [115] *Reprinted from WHO Map Gallery, 2017.* https://www.who.int/images/default-source/maps/global_obesity_2016_female.png?sfvrsn=8e0dfc1d_0. Accessed: 2022-10-15.
- [116] Vahid REZANIA, Dennis COOMBE, and Jack A. TUSZYNSKI. “A physiologically-based flow network model for hepatic drug elimination III: 2D/3D DLA lobule models: 2D/3D DLA lobule models”. In: *Theoretical Biology and Medical Modelling* 13.1 (2016), p. 9. ISSN: 1742-4682. DOI: 10.1186/s12976-016-0034-5.

-
- [117] T. RICKEN and J. BLUHM. “Remodeling and growth of living tissue: a multi-phase theory”. In: *Archive of Applied Mechanics* 80 (5) (2010), pp. 453–465. ISSN: 0939-1533.
- [118] T. RICKEN et al. “Modeling function-perfusion behavior in liver lobules including tissue, blood, glucose, lactate and glycogen by use of a coupled two-scale PDE-ODE approach”. In: *Biomech Model Mechanobiol* 14.3 (2015), pp. 515–536. ISSN: 1617-7940 (Electronic) 1617-7940 (Linking). DOI: 10.1007/s10237-014-0619-z.
- [119] Tim RICKEN, Uta DAHMEN, and Olaf DIRSCH. “A biphasic model for sinusoidal liver perfusion remodeling after outflow obstruction”. In: *Biomechanics and Modeling in Mechanobiology* 9.4 (2010), pp. 435–450. ISSN: 1617-7959. DOI: 10.1007/s10237-009-0186-x.
- [120] Tim RICKEN and Lena LAMBERS. “On computational approaches of liver lobule function and perfusion simulation”. In: *GAMM-Mitteilungen* 42.4 (2019), e201900016. DOI: 10.1002/gamm.201900016.
- [121] Tim RICKEN, Navina WASCHINSKY, and Daniel WERNER. “Simulation of Steatosis Zonation in Liver Lobule—A Continuummechanical Bi-Scale, Tri-Phasic, Multi-Component Approach”. In: *Simulation of Steatosis Zonation in Liver Lobule—A Continuummechanical Bi-Scale, Tri-Phasic, Multi-Component Approach*. Ed. by Tim RICKEN, Navina WASCHINSKY, and Daniel WERNER. Vol. 84. Springer International Publishing, 2018, pp. 15–33. ISBN: 978-3-319-59547-4. DOI: 10.1007/978-3-319-59548-1{\textunderscore}2.
- [122] E. K. RODRIGUEZ, A. HOGER, and A. D. McCULLOCH. “Stress-dependent finite growth in soft elastic tissues”. In: *Journal of Biomechanics* 27 (4) (1994), pp. 455–467. ISSN: 0021-9290.
- [123] E. ROEB et al. “S2k-Leitlinie nicht alkoholische Fettlebererkrankungen”. In: *Zeitschrift für Gastroenterologie* 53.7 (2015), pp. 668–723. DOI: 10.1055/s-0035-1553193.
- [124] Eduard ROHAN, Jana CAMPROVÁ TURJANICOVÁ, and Václav LIŠKA. “Geometrical model of lobular structure and its importance for the liver perfusion analysis”. In: *PLoS ONE* 16.12 (2021), e0260068. DOI: 10.1371/journal.pone.0260068.
- [125] Eduard ROHAN, Vladimír LUKEŠ, and Alena JONÁŠOVÁ. “Modeling of the contrast-enhanced perfusion test in liver based on the multi-compartment flow

- in porous media”. In: *Journal of mathematical biology* 77.2 (2018), pp. 421–454. DOI: 10.1007/s00285-018-1209-y.
- [126] Alejandro ROLDÁN-ALZATE et al. “In vivo validation of 4D flow MRI for assessing the hemodynamics of portal hypertension”. In: *Journal of magnetic resonance imaging* 37.5 (2013), pp. 1100–1108.
- [127] W. M. S. RUSSELL. *The principles of humane experimental technique*. Special ed. Wheathampstead: Universities Federation for Animal Welfare, 1999. ISBN: 0900767782.
- [128] Abdus SATTER and Ghulam M. IQBAL. “Reservoir rock properties”. In: *Reservoir Engineering*. Vol. 45. Elsevier, 2016, pp. 29–79. ISBN: 9780128002193. DOI: 10.1016/B978-0-12-800219-3.00003-6.
- [129] Fridtjof SCHIEFENHÖVEL et al. “High Central Venous Pressure after Cardiac Surgery Might Depict Hemodynamic Deterioration Associated with Increased Morbidity and Mortality”. In: *Journal of clinical medicine* 10.17 (2021). ISSN: 2077-0383. DOI: 10.3390/jcm10173945.
- [130] J. SCHLEICHER et al. “A theoretical study of lipid accumulation in the liver—implications for nonalcoholic fatty liver disease”. In: *Biochimica et Biophysica Acta (BBA) - Molecular and Cell Biology of Lipids* 1841.1 (2014), pp. 62–69. ISSN: 1388-1981. DOI: 10.1016/j.bbailip.2013.08.016.
- [131] Jana SCHLEICHER et al. “Zonation of hepatic fat accumulation: insights from mathematical modelling of nutrient gradients and fatty acid uptake”. In: *Journal of the Royal Society, Interface / the Royal Society* 14.133 (2017). ISSN: 1742-5662. DOI: 10.1098/rsif.2017.0443.
- [132] Andreas A. SCHNITZBAUER et al. “Right portal vein ligation combined with in situ splitting induces rapid left lateral liver lobe hypertrophy enabling 2-staged extended right hepatic resection in small-for-size settings”. In: *Annals of surgery* 255.3 (2012), pp. 405–414. DOI: 10.1097/SLA.0b013e31824856f5.
- [133] Daniel SCHOLZ. *Numerik interaktiv*. Berlin, Heidelberg: Springer Berlin Heidelberg, 2016. ISBN: 978-3-662-52939-3. DOI: 10.1007/978-3-662-52940-9.
- [134] Lars Ole SCHWEN et al. “Algorithmically generated rodent hepatic vascular trees in arbitrary detail”. In: *Journal of Theoretical Biology* 365.0 (2015), pp. 289–300. ISSN: 0022-5193. DOI: 10.1016/j.jtbi.2014.10.026.
- [135] Alexander M SEIFALIAN et al. “THE EFFECT OF GRADED STEATOSIS ON FLOW IN THE HEPATIC PARENCHYMAL MICROCIRCULATION¹,

- 2". In: *Transplantation* 68.6 (1999), pp. 780–784. DOI: 10.1097/00007890-199909270-00009.
- [136] Seyed M. SEYEDPOUR et al. “Application of Magnetic Resonance Imaging in Liver Biomechanics: A Systematic Review”. In: *Frontiers in Physiology* 12 (2021), p. 733393. DOI: 10.3389/fphys.2021.733393.
- [137] Tsuyoshi SHIINA et al. “WFUMB guidelines and recommendations for clinical use of ultrasound elastography: Part 1: basic principles and terminology”. In: *Ultrasound in medicine & biology* 41.5 (2015), pp. 1126–1147.
- [138] J. H. SIGGERS et al. “Mathematical model of blood and interstitial flow and lymph production in the liver”. In: *Biomechanics and Modeling in Mechanobiology* (2013). ISSN: 1617-7959.
- [139] Herbert SIGLOCH. *Technische Fluidmechanik: Mit 40 Tabellen, sowie 114 gelösten Berechnungsbeispielen*. 6., neu bearb. Aufl. Berlin, Heidelberg: Springer-Verlag, 2008. ISBN: 978-3-540-44633-0. DOI: 10.1007/978-3-540-44635-4. URL: <http://dx.doi.org/10.1007/978-3-540-44635-4>.
- [140] James P. SLUKA et al. “A Liver-Centric Multiscale Modeling Framework for Xenobiotics”. In: *PLoS ONE* 11.9 (2016), e0162428. DOI: 10.1371/journal.pone.0162428.
- [141] Bharath SRINIVASAN. “A guide to the Michaelis-Menten equation: steady state and beyond”. In: *FEBS Journal* (2021). ISSN: 1742-4658. DOI: 10.1111/febs.16124.
- [142] Peggy STOCK et al. “Human bone marrow mesenchymal stem cell-derived hepatocytes improve the mouse liver after acute acetaminophen intoxication by preventing progress of injury”. In: *International journal of molecular sciences* 15.4 (2014), pp. 7004–7028. DOI: 10.3390/ijms15047004.
- [143] Martin STOCKMANN et al. “Prediction of postoperative outcome after hepatectomy with a new bedside test for maximal liver function capacity”. In: *Annals of surgery* 250.1 (2009), pp. 119–125. DOI: 10.1097/SLA.0b013e3181ad85b5.
- [144] Stein K.F. STOTER et al. “A diffuse interface method for the Navier–Stokes/Darcy equations: Perfusion profile for a patient-specific human liver based on MRI scans”. In: *Computer Methods in Applied Mechanics and Engineering* 321 (2017), pp. 70–102. ISSN: 0045-7825. DOI: 10.1016/j.cma.2017.04.002.
- [145] S. Kim SUVARNA, Christopher LAYTON, and John D. BANCROFT. *Bancroft’s Theory and Practice of Histological Techniques*. 8th ed. Elsevier, 2019. ISBN: 978-0-7020-6864-5.

- [146] A. C. SWIFT. “Upper airway obstruction, sleep disturbance and adenotonsillectomy in children”. In: *The Journal of laryngology and otology* 102.5 (1988), pp. 419–422. ISSN: 0022-2151. DOI: [10.1017/s0022215100105249](https://doi.org/10.1017/s0022215100105249).
- [147] Amirtahà TAEBI, Catherine T. VU, and Emilie RONCALI. “Multiscale Computational Fluid Dynamics Modeling for Personalized Liver Cancer Radioembolization Dosimetry”. In: *Journal of Biomechanical Engineering* 143.1 (2021). ISSN: 0148-0731. DOI: [10.1115/1.4047656](https://doi.org/10.1115/1.4047656).
- [148] C. TAYLOR and P. HOOD. “A numerical solution of the Navier-Stokes equations using the finite element technique”. In: *Computers & Fluids* 1.1 (1973), pp. 73–100. ISSN: 0045-7930. DOI: [10.1016/0045-7930\(73\)90027-3](https://doi.org/10.1016/0045-7930(73)90027-3).
- [149] A. THELEN et al. “Liver resection for hepatocellular carcinoma in patients without cirrhosis”. In: *The British journal of surgery* 100.1 (2013), pp. 130–137. DOI: [10.1002/bjs.8962](https://doi.org/10.1002/bjs.8962).
- [150] Andrea THOM. *Theory and model implementation of gaseous transport and reaction processes in porous media applied to methane oxidation in landfill cover layers*. 2022. DOI: [10.18419/opus-12685](https://doi.org/10.18419/opus-12685).
- [151] Michael Z. TONG et al. “Severe Outflow Obstruction After Liver Transplantation: Rescue Stapled Cavo-Cavostomy via the Right Atrial Approach and Hypothermic Circulatory Arrest”. In: *Liver transplantation : official publication of the American Association for the Study of Liver Diseases and the International Liver Transplantation Society* 27.5 (2021), pp. 763–766. DOI: [10.1002/lt.25954](https://doi.org/10.1002/lt.25954).
- [152] Clifford TRUESDELL. *Rational Thermodynamics*. 2nd ed. Springer-Verlag, Berlin - Heidelberg - New York, 1984.
- [153] Clifford TRUESDELL and Richard TOUPIN. “The classical field theories”. In: *Principles of classical mechanics and field theory/Prinzipien der Klassischen Mechanik und Feldtheorie*. Springer, 1960, pp. 226–858.
- [154] Costin D. UNTAROIU et al. “Modeling the biomechanical and injury response of human liver parenchyma under tensile loading”. In: *Journal of the Mechanical Behavior of Biomedical Materials* 41 (2015), pp. 280–291. ISSN: 1751-6161. DOI: [10.1016/j.jmbbm.2014.07.006](https://doi.org/10.1016/j.jmbbm.2014.07.006).
- [155] Sudhakar K VENKATESH, Meng YIN, and Richard L EHMAN. “Magnetic resonance elastography of liver: technique, analysis, and clinical applications”. In: *Journal of magnetic resonance imaging* 37.3 (2013), pp. 544–555.

-
- [156] Brigitte VOLLMAR and Michael D. MENGER. “The hepatic microcirculation: mechanistic contributions and therapeutic targets in liver injury and repair”. In: *Physiological reviews* 89.4 (2009), pp. 1269–1339. ISSN: 0031-9333. DOI: 10.1152/physrev.00027.2008.
- [157] WAGNER, A. “Extended Modelling of the Multiphasic Human Brain Tissue with Application to Drug-Infusion Processes”. PhD thesis. Institute of Applied Mechanics (Civil Engineering), Universität Stuttgart.
- [158] Christin WALLSTAB et al. “A unifying mathematical model of lipid droplet metabolism reveals key molecular players in the development of hepatic steatosis”. In: *FEBS Journal* 284.19 (2017), pp. 3245–3261. ISSN: 1742-4658. DOI: 10.1111/febs.14189.
- [159] Jianzhong WANG et al. “A modified FCM algorithm for MRI brain image segmentation using both local and non-local spatial constraints”. In: *Computerized medical imaging and graphics : the official journal of the Computerized Medical Imaging Society* 32.8 (2008), pp. 685–698. DOI: 10.1016/j.compmedimag.2008.08.004.
- [160] Daniel WERNER. *Two Scale Multi-component and Multi-phase Model for the Numerical Simulation of Growth Processes in Saturated Porous Media under Consideration of Bio-chemical Processes - at the Example of the Human Liver*. 1. Auflage. Berichte aus der Biomechanik. Aachen: Shaker, 2017. ISBN: 3844054626.
- [161] Christopher P. WILD, Elisabete WEIDERPASS, and Bernards W. STEWART. “World Cancer Report: Cancer Research for Cancer Prevention.” In: *Lyon, France: International Agency for Research on Cancer* (2020).
- [162] “World Medical Association Declaration of Helsinki: ethical principles for medical research involving human subjects”. In: *JAMA* 310.20 (2013), pp. 2191–2194. DOI: 10.1001/jama.2013.281053.
- [163] Benjamin C. YAN et al. “Arginase-1: A New Immunohistochemical Marker of Hepatocytes and Hepatocellular Neoplasms”. In: *The American journal of surgical pathology* 34.8 (2010), pp. 1147–1154. ISSN: 0147-5185. DOI: 10.1097/PAS.0b013e3181e5dfffa.
- [164] Zobair M. YOUNOSSI et al. “Global epidemiology of nonalcoholic fatty liver disease-Meta-analytic assessment of prevalence, incidence, and outcomes”. In: *Hepatology* 64.1 (2016), pp. 73–84. ISSN: 1527-3350. DOI: 10.1002/hep.28431.

- [165] Drazen ZEKANOVIC et al. “Doppler ultrasound of hepatic and system hemodynamics in patients with alcoholic liver cirrhosis”. In: *Digestive diseases and sciences* 55.2 (2010), pp. 458–466. DOI: 10.1007/s10620-009-0760-1.
- [166] Yingzhen N. ZHANG et al. “Liver fat imaging-a clinical overview of ultrasound, CT, and MR imaging”. In: *The British journal of radiology* 91.1089 (2018), p. 20170959. DOI: 10.1259/bjr.20170959.

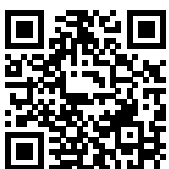


Lena Lambers

The human liver is a unique organ and primarily responsible for the metabolic processes in the body. These processes are enabled by a relationship of perfusion in the tissue and function in the liver cells and can be harmed by various diseases. Due to a significant increase in risk factors, such as alcohol consumption, obesity, and diabetes, the number of chronic liver diseases has been steadily increasing in recent years and represents an enormous social and economic problem worldwide. This requires an optimal decision-making of diagnosis, prognosis, and therapy by clinicians, which is increasingly supported by computational continuum-biomechanical modeling.

In this thesis, a multiscale and multiphase continuum-biomechanical model is developed based on the Theory of Porous Media (TPM) to describe the coupled function-perfusion relationship in the liver. This model enables a numerical simulation of macroperfusion in the total organ, microperfusion in the liver lobules and function in the cells as well as their interaction. Selected liver diseases like non-alcoholic fatty liver disease, a liver tumor or necrosis after paracetamol overdose serve as application. Furthermore, perfusion changes due to surgical interventions such as a resection are simulated.

However, purely knowledge-based models are too generic to provide individual, reliable and efficient clinical predictions. For this reason, patient-specific data of different origins and formats are used to parameterize and validate the model. Finally, first steps to improve clinical usability like a non-linear model order reduction and a sensitivity analysis are performed.



Institut für Statik und Dynamik
der Luft- und Raumfahrtkonstruktionen
Univ.-Prof. Dr.-Ing. Tim Ricken

